

**OPTICAL PARAMETRIC OSCILLATORS : A
COMPARISON OF NEW MATERIALS**

GORDON ROBERTSON

**A Thesis Submitted for the Degree of PhD
at the
University of St Andrews**



1993

**Full metadata for this item is available in
Research@StAndrews:FullText
at:**

<http://research-repository.st-andrews.ac.uk/>

Please use this identifier to cite or link to this item:

<http://hdl.handle.net/10023/6487>

This item is protected by original copyright

**This item is licensed under a
Creative Commons Licence**

Optical Parametric Oscillators: A Comparison of New Materials

A thesis presented by

Gordon Robertson

to the

University of St. Andrews

in application for the degree of

Doctor of Philosophy.

May 1993



Declarations

I, Gordon Robertson, hereby certify that this thesis has been composed by myself, that it is a record of my own work, and that it has not been accepted in partial or complete fulfilment of any other degree of professional qualification.



Gordon Robertson

May 1993

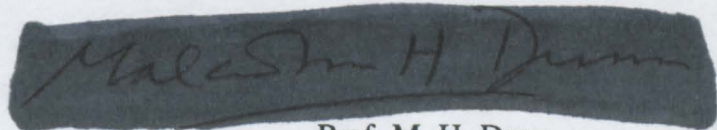
I was admitted to the Faculty of Science of the University of St. Andrews under Ordinance No. 12 on 1st October 1989 and as a candidate for the degree of PhD on October 1990.



Gordon Robertson

May 1993

I hereby certify that the candidate has fulfilled the conditions of the Resolution and Regulations appropriate to the Degree of Ph.D.



Prof. M. H. Dunn

Research supervisor

May 1993

Abstract

A study of new materials for optical parametric oscillators (OPOs) was carried out using an XeCl excimer laser as a pump source. The three non-linear optical materials studied were lithium borate (LBO), deuterated L-arginine phosphate (d-LAP) and β -barium borate (BBO). These optical parametric oscillators were characterised for oscillation thresholds, tuning ranges, linewidths and efficiencies.

A novel device in LBO was demonstrated, using the non-critically phase matched type II geometry. The device displayed a low oscillation threshold, which was independent of pump beam area thus made it attractive for use with low energy pump sources. The device was also shown to have a narrow inherent linewidth, oscillating on only one or two axial modes.

Other geometries in LBO were also explored. The type I critical geometry displayed a very large tuning range covering the near ultra-violet, the visible and the near infra-red spectral regions. The type II yz geometry was also studied.

An OPO in d-LAP was demonstrated for the first time. The device was tunable in the blue/green spectral region and also in the near infra-red. A low threshold was observed for large beam sizes. Optically induced damage caused by the ultra-violet pump was also encountered.

A comparison of the thresholds, efficiencies and tuning ranges of the three materials, LBO, d-LAP and BBO, was made and the suitability of each material for use in a line-narrowed oscillator discussed. Although possessing the largest linewidth, BBO was found to be the best suited due to its low oscillation threshold and large tunability. A single axial mode BBO OPO was demonstrated that was tunable from 385 nm to 560 nm and from 2300 nm to 684 nm. The line-narrowed OPO was then used for linewidth control of other devices. Firstly, an injection seeded OPO was demonstrated and the device was characterised for threshold and linewidth. Secondly, the line-narrowed OPO was used to seed an optical parametric amplifier (OPA). Single pass gains of ~ 20 were observed from the OPA.

Nomenclature

In the field of optical parametric oscillators (OPOs) the terms commonly used for the two generated waves are 'signal' and 'idler'. The literature is, in general, not specific in its use of these terms and their meanings are often vague. In many cases no distinction is required between the two generated waves, and the phrase 'signal and idler' is freely used to refer to the resultant beams leaving the OPO.

An early, although somewhat unsatisfactory definition (N. Kroll, Phys. Rev. 127, 1207 (1962) seems to be that the signal is the high frequency wave and the idler the low frequency wave. The names 'signal' and 'idler' are obscure when used in this way and can be misleading. A superior definition would be that the signal wave is the resonant wave which builds up within the OPO cavity (or in the case of an injection signal is imposed on the OPO from outside). The idler is not constrained by the cavity but is instead free to select the wavelength and phase that will produce maximum gain. This definition is frequently implied or used in a theoretical context when the signal is deemed to be present initially and thus uniquely determines the operational characteristics of the OPO. In conclusion the terms 'signal' and 'idler' are confusing in many cases. They have, however, been used for nearly 30 years and will probably continue to be used in the future. In this thesis the definition will be that:

At any given instant the beam that extrinsically constrains the operation of the device will be called the 'signal' and the beam that is intrinsically constrained by the parametric process (i.e. the beam that is defined by $\omega_i = \omega_p - \omega_s$) will be called the idler.

Generally this implies that the signal is the resonant wave and the idler is the non-resonant wave. This definition can lead to difficulties when discussing doubly resonant OPOs (DROs) where both waves are resonant. In this case, both waves are signal waves in the sense that neither is free to take on any wavelength or phase but are instead constrained by the cavity. It is this over-constraining of the cavity in a DRO that leads to the erratic mode-hopping of these devices. At no point are DROs discussed in connection with signal and idler so no conflict will arise. In the case of injection seeding, the seeding beam will be called the 'signal' since its purpose is to constrain the operation of the OPO. The other wave, whether resonant or not will be called the 'idler'.

Acknowledgements

I would like to thank my supervisor, Prof. Malcolm H. Dunn, for his help, advice and encouragement during my PhD. Thanks are also due to Dr John Kirton at the Royal Signals and Radar Establishment (DRA Malvern) for his enthusiastic discussions.

I am grateful for the financial support of the Science and Engineering Research Council, (SERC), The Royal Signals and Radar Establishment, (DRA, Malvern), the physics department, in particular Malcolm Dunn, and my parents.

Thanks to Jim Clark in the physics workshop for turning the plans into mounts, and to the rest of the technical staff for their services over the years.

Credit where credit's due to Majid Ebrahimzadeh and Angus Henderson for their help and advice on all things non-linear.

Hello and best wishes to Gordon, Sara, Jonny, Jason, Greg, Neil Z. Macignonn and of course Suzanne.

Publications

'Excimer-pumped LiB_3O_5 optical parametric oscillators'.

M. Ebrahimzadeh, G. Robertson, M. H. Dunn and A. J. Henderson. Conference on lasers and electro-optics, Technical Digest vol 7, paper CPD26 (Optical Society of America, Washington D. C. 1990).

'Efficient Ultraviolet LiB_3O_5 Optical Parametric Oscillator'.

M. Ebrahimzadeh, G. Robertson and M. H. Dunn. Opt. Lett. 16, 767 (1991).

'Highly Efficient optical parametric oscillator for the UV'.

Gordon Robertson, Malcolm H. Dunn and Majid Ebrahimzadeh. Conference on lasers and electro-optics, Technical Digest vol 10, paper CFM2 (Optical Society of America, Washington D. C. 1991).

'Attainment of High Efficiencies in Optical Parametric Oscillators'.

G. Robertson, A. Henderson and M. Dunn. Opt. Lett. 16, 1584 (1991).

'Efficient line narrowing of an excimer-pumped β -barium borate optical parametric oscillator'.

Angus J. Henderson, Gordon Robertson and Malcolm H. Dunn. Conference on lasers and electro-optics, Technical Digest vol 12, paper CTuR2 (Optical Society of America, Washington D. C. 1992).

'Broadly Tunable LiB_3O_5 Optical Parametric Oscillator'.

Gordon Robertson, Angus Henderson and Malcolm H. Dunn. Appl. Phys. Lett. 60, 271 (1992).

'Efficient, Single Axial Mode Oscillation of a Beta Barium Borate Optical Parametric Oscillator pumped by an Excimer Laser'.

Gordon Robertson, Angus Henderson and Malcolm H. Dunn. Appl. Phys. Lett. 62, 123 (1993).

'Deuterated L-arginine phosphate optical parametric oscillator'.

Gordon Robertson and Malcolm H. Dunn. Conference on lasers and electro-optics, Technical Digest vol 11, paper CThS27 (Optical Society of America, Washington D. C. 1993).

'An excimer pumped deuterated L-arginine phosphate optical parametric oscillator'.

Gordon Robertson and Malcolm H. Dunn. To be published in Appl. Phys. Lett. June 28th 1993.

'Comparison of lithium triborate and beta barium borate as nonlinear media for optical parametric oscillators'.

Dominic E. Withers, Gordon Robertson, Angus J. Henderson, Yan Tang, Yong Cui, Wilson Sibbett, Bruce D. Sinclair and Malcolm H. Dunn. To be published in J. Opt. Soc. Am. B September 1993.

Declaration	ii
Abstract	iii
Nomenclature	iv
Acknowledgements	v
Publications	vi
Contents	vii

Chapter 1 - Introduction

1.1 Introduction	1
1.2 Background	2
1.3 Basic Principles.....	5
1.4 Historical Review	8
1.5 Modern OPOs.....	9
1.6 Figures of Merit	16
1.7 Thesis Layout.....	16
References.....	17

Chapter 2 - Theory

2.1 Three Wave Non-linear Interactions	20
2.2 The Effective Non-linear Coefficient.....	24
2.3 Crystallographic Conventions	26
2.4 Phase-matched Interactions in Non-linear Media.....	30
2.5 The Effect of Momentum Mis-match on Phase-matching	34
2.6 Prediction of Inherent OPO Linewidths	35
2.7 Poynting vector Walk-off in Birefringent Crystals.....	37
2.8 Comparison of Walk-off and Acceptance Angles	38
2.9 Oscillation Threshold	39
2.10 Dispersion of $\chi^{(2)}$	40
References	41

Chapter 3 - Lithium Borate

3.1 General Orientations	43
3.2 Non-linear Coefficient	45
3.3 Phase-matching.....	46
3.4 Acceptance Angle.....	50
3.5 Acceptance Bandwidth.....	53
3.6 Signal Linewidth	55
3.7 Poynting Vector Walk-off.....	56
3.9 Selection of Suitable Crystal Cuts.....	58
References.....	59

Chapter 4 - Non-critically Phase Matched LBO

4.1 Introduction	61
4.2 Pump Lasers	61
4.3 Experimental Set-up.....	63
4.4 9 mm Crystal.....	67
4.5 16 mm Crystal – Tuning Range	72
4.6 Oscillation Threshold Measurements.....	75
4.7 Pump Depletion.....	75
4.8 Crystal Degradation/ Measurements of Scattering & Absorption.....	77
4.9 Ratio of Signal to Idler Energies.....	79
4.10 IR Resonant NCPM LBO.....	83
4.11 Inherent NCPM LBO Linewidths.....	84
4.12 Type II yzLBO	89
4.13 Conclusions	92
Reference.....	93

Chapter 5 - Type I LBO in the xy Plane

5.1 Experimental Set-up.....	95
5.2 Tuning Range.....	97
5.3 Oscillation Threshold	98
5.4 Pump Depletion vs. Beam Size.....	101
5.5 Pump Depletion vs. Wavelength	102
5.6 External Efficiency	103
5.7 Inherent Linewidth	105
5.8 Conclusions.....	106
Reference	106

Chapter 6 - Deuterated L-Arginine Phosphate

6.1 Introduction	107
6.2 Linear and Non-linear Optical Properties of d-LAP	107
6.3 OPO Set-up	113
6.4 Experimental Results.....	116
6.5 Conclusions.....	124
References.....	124

Chapter 7 - Comparison of non-linear materials

7.1 Introduction	126
7.2 A review of Excimer Pumped BBO OPOs	127
7.3 Comparison of Tuning Ranges	129
7.4 Comparison of Thresholds.....	130
7.5 Comparison of Efficiencies	134
7.6 Comparison of Inherent Linewidths	138
7.7 Implications for Line-narrowing in OPOs.....	139
References.....	140

Chapter 8 - Line-narrowed OPOs

8.1 Introduction	141
8.2 Background	143
8.3 Etalon Insertion Losses.....	145
8.4 Experimental Set-up.....	146
8.5 Experimental Results.....	148
8.6 Characterisation of the line-narrowed OPO	154
8.7 Conclusions.....	163
References	165

Chapter 9 - Injection Seeding

9.1 Introduction	166
9.2 Historical Perspective.....	167
9.3 Injection Seeding Experimental Set-up	168
9.4 Injection Seeding Results.....	171
9.5 Optical Parametric Amplifier	175
9.6 Optical Parametric Amplifier Results.....	177
9.7 Conclusions.....	180
References	180

Chapter 10 - Conclusions

10.1 Summary.....	182
10.2 Conclusions	184
10.3 Future Work.....	186
References.....	187

Appendix A - Sellemeier Equations

- A1 Lithium Borate
- A2 Deuterated L-Arginine Phosphate
- A3 β -Barium Borate

Appendix B - Computer Programs For Calculating Tuning Ranges

- B1 Critical LBO (xyLBO)
- B2 LBOyz (NCPM LBO)
- B3 dLAP
- B4 BBO

This definition can lead to difficulties when discussing doubly resonant OPOs (DROs) where both waves are resonant. In this case, both waves are signal waves in the sense that neither is free to take on any wavelength or phase but are instead constrained by the cavity. It is this over-constraining of the cavity in a DRO that leads to the erratic mode-hopping of these devices. Further difficulties arise in the case of an injection seeded OPO where the cavity is resonant for say, the long wavelength and the injection signal is the short wavelength. Initially the OPO will be constrained by the injection signal, although in this case the choice of 'idler' is not truly free but is determined by the cavity. Later, when the seed pulse has ceased, the OPO will be constrained by the cavity. Then the beams to which signal and idler refer will change over.

Introduction

In this chapter the basic principles of the optical parametric oscillator are introduced and some applications highlighted. A short summary of the early work in non-linear optics and optical parametric oscillators is provided and a detailed review of work using β -barium borate, lithium borate and L-arginine phosphate (which are the three materials studied in this thesis) is given.

1.1 Introduction

The field of optical parametric oscillators (OPOs) is now about thirty years old¹. After an initial period of rapid development in the late 1960's, the pace of research into OPOs slowed and the OPO failed to fulfilled its early promise. This was mainly because materials did not possess the right combinations of non-linear coefficient, damage threshold and other key parameters that determine the performance of an OPO. However with the introduction of some new non-linear optical materials in the late 1980's^{2,3} there has been an upsurge of interest in the OPO as a viable tunable source. Access to the ultraviolet and blue spectral regions has been permitted by new materials like BBO and LBO, which are transparent down to ~200 nm and also well into the infrared, and yet have moderate non-linear coefficients. Coupled with the improvement in non-linear materials and crystal growth was the improvement in viable pump lasers. For broad tunability in the visible it is necessary to pump the OPO in the ultraviolet and to this end the development of frequency tripled Nd:YAG systems⁴ and, in particular, diode pumped sources⁵ was instrumental in the resurgence of interest in OPOs. However, a more direct method of obtaining ultraviolet light is to use an excimer laser⁶. This approach also brings the added benefit of high energies. The excimer laser makes an excellent, highly-efficient pump source for an OPO and it is the excimer pumped OPO that is the topic of this thesis. This, however, does not limit the application of the work presented here to only excimer pump devices. The excimer system provides an excellent test bed for materials and device characteristics and the results are equally applicable to any pumping system, as will be shown in chapter 7 when the excimer system is compared to a diode pumped system.

The results presented in this thesis are centred on the new non-linear materials, namely LBO, d-LAP and BBO, which have been pumped by an XeCl excimer laser. An exploration of oscillation thresholds, efficiencies and in particular linewidths is presented. Ultimately operation of a single-axial mode OPO and an amplifier/OPO combination are reported.

1.2 Background

There are at present a multitude of lasers and other optical devices capable of producing coherent high energy pulses or CW high power radiation at many discrete wavelengths across the visible spectrum. These have been developed in the thirty years following the demonstration of the first laser, a ruby laser⁷, in 1961. In this time many new wavelengths have been added to the palette of colours available from coherent laser sources, which, in turn, has led to the emergence of many applications for them. Alongside the evolution of the laser has been the growth of non-linear optics and many novel devices have been demonstrated, such as frequency doublers⁸ and sum⁹ and difference¹⁰ frequency mixers. The attraction of these devices is that they provide a whole new range of accessible wavelengths to complement those of the laser. Although discrete wavelengths are of great interest in many applications, there remains the desire to provide a coherent optical source that is tunable, while retaining all the advantages of a fixed frequency, narrow linewidth laser. This problem has been tackled from both the laser and the non-linear optical point of view. The former has produced devices like the dye laser^{11,12} and the Ti:sapphire laser¹³. The main contender from non-linear optics is the optical parametric oscillator with its ability to produce broadly tunable light from a single laser pump source. It is this device that is the subject of this thesis and it is the most recent developments that are the main thrust of this first chapter.

Early OPOs were confined to the infrared and red spectral regions¹⁴⁻¹⁸ and, with advances in pump sources including diode pumped devices, the IR OPO¹⁹ has continued to be a major area of research due to its application in communications and in infrared spectroscopy and chemistry²⁰. The extension of the OPO into the visible required the use of both UV pump sources and materials with transparency ranges covering the UV, visible and IR^{21,22}. The result was a device that is capable of covering a very large range of wavelengths with a resulting wide diversity of applications. The majority of OPOs to date are pulsed devices due to the high pump powers required for their operation. The use of nanosecond laser pulses has for a long time been the easiest way to reach oscillation threshold in a pulsed OPO which typically is $\sim 20 \text{ MWcm}^{-2}$. The pulsed nature clearly limits the applications of such devices. An equally great limitation is imposed by the broad inherent linewidths typical of many OPOs (see table 8.1). In such

devices there is a direct trade-off between broad tunability and narrow linewidth. In general, the more broadly tunable the device, the greater its inherent linewidth will be. A major application of a broadly tunable device is in the field of spectroscopy where narrow linewidth light is required to probe atomic transitions in gases. It is therefore necessary to line narrow OPOs if their great potential as spectroscopic tools is to be realised. For this reason the later part of this thesis concentrates on the construction of a narrow linewidth OPO which would make a useful spectroscopic tool.

However, many applications do exist for which the broad linewidth OPO may still be useful. Examples that do not require particularly narrow linewidths, but which do benefit from the tunable, high power, directable beam of an OPO, are photo-acoustic spectroscopy, medical applications and light sources in the entertainment industry. As an example of a realised application, experiments have been carried out using the broad band BBO OPO (described later in this thesis) to measure low concentrations of impurities in liquids using photo-acoustic spectroscopy²³. In the experiment, low concentrations of oil were detected in water (of the order of 1 ppm). Originally the experiment had been carried out using an IR continuum generated by Raman scattering in fibres. The selection of the desired wavelength was made using a monochromator. This led to low probe energies being used. Using an OPO, higher pulse energies could be obtained thus increasing the signal to noise ratio. The pulses were weakly focused into a cell of distilled water into which a known concentration of the impurity had been added. The OPO was tuned to operate in the 1.6–1.8 μm region where the level of the photoacoustic response from benzene is an order of magnitude greater than that from water. The phonons created by the absorption were detected by a microphone attached to the cell. Measurement of the concentration was made by comparison of the contaminated sample with a pure sample. This technique can also be used to detect glucose concentrations in human blood in an in-vivo system for the study of diabetes.

Medical applications are also not dependent on the source being of narrow linewidth. For example, laser surgery²⁴, treatment of skin colouration defects²⁵ and tumour treatment²⁶ all benefit from the tunability of the light source, usually to control the penetration depth/ absorption level in tissue. Selective absorption in cells can be produced by using dyes that become concentrated in certain cells, for example cancer cells²⁷. Laser fragmentation of gallstones²⁸ benefits from the tunability of the light source as the different chemical composition of each stone leads to different absorption peaks in the stones. By tuning to an absorption peak the minimum energy can be used while treating the patient. Other applications do have a greater need for narrow linewidth tunable light, for example, the implementation of frequency standards, where a chain of

referenced frequencies at integral ratios to each other can be locked together by harmonic generation effects, such as frequency doubling, ($\omega_o=2\omega_p$). The OPO can add to this frequency chain by providing the $\omega_o=\frac{1}{2}\omega_p$ option, when it is operating at degeneracy, and $\omega_o=\frac{1}{3}\omega_p$ when the signal frequency $\omega_s=2\omega_i$. (The idler can be frequency doubled and locked to the signal frequency to control the exact ratio).

Process	Tuning range	Comments	Ref
colour centre laser	NaCl:OH ⁻ 1.4–1.85 μ m KCl:Ti ⁰ (1) 1.4–1.65 μ m LiF 0.8–1.01 μ m	Cryogenic temperatures required	29
Er Doped Optical Fibre Lasers	1.52–1.62 μ m	May require long lengths of fibre	30
Semi-conductor Lasers	Temperature tuning around 0.8, 0.95, 1.1, 1.3, 1.5 μ m depending on materials	Small tuning range typically 790–830 nm or 940–960 nm	31
LiCaAlF ₆ :Cr ³⁺ (Cr:LiCAF)	720–840 μ m	Forerunner to LiSAF see below	32
LiSrAlF ₆ :Cr ³⁺ (Cr:LiSAF)	780–1010 nm flash lamp pumped	Can be pumped by diode	33
Ti:sapphire	0.68–1.1 μ m	Broadest laser tuning range	34
Cr ⁴⁺ YAG	1.037–1.510 μ m	A promising new solid state laser material	35
Alexandrite (Cr:BeAl ₂ O ₄)	0.70–0.82 μ m	Can be diode pumped	36
Co:MgF ₂	1.5–2.3 μ m	Must be operated at cryogenic temperatures	37
Dye laser	9 dyes required for 400–1023 nm range	Needs many dyes to cover range	38

Table 1.1. Tunable Laser Sources

With current advances in laser sources, in terms of diode pumping and the growth techniques of non-linear optical materials, becoming more refined, the OPO is becoming a serious option for generating tunable coherent output. The new materials possess higher non-linear coefficients and higher optical damage thresholds, which enables more efficient devices with lower oscillation thresholds to be built. OPOs are now approaching a level where they can compete with other tunable laser sources in applications like spectroscopy, Lidar and range finding. Table 1.1 lists some of the other ways of generating coherent tunable light over the region accessible by an ultraviolet (UV) to near infrared (NIR) OPO. The Ti:sapphire and the dye lasers are the two main rivals to the broadly tunable, infrared, visible and ultraviolet OPO. The sum frequency mixing and frequency doubling³⁹ can be used to extend the tuning ranges of these lasers, in particular by frequency doubling to cover the blue/UV spectral region. The advantage of OPOs is that they are capable of tuning over larger ranges than either of these lasers (or any other laser) using only one efficient conversion step.

So far only pulsed OPOs have been discussed, although many of the lasers mentioned can be operated in CW mode. For this reason perhaps a few words about CW OPOs are appropriate. In the realm of CW coherent light, lasers, such as the Ti:sapphire and the dye laser, are still more powerful and more broadly tunable than any CW OPO. CW OPOs using materials such as $\text{BaNaNb}_5\text{O}_{15}$ ⁴⁰ and LiNbO_3 ⁴¹, which have large non-linear coefficients, have been constructed to provide tunable output over small ranges. Construction of CW OPOs relies heavily on the use of non-critically phase-matched crystals and on doubly or triply resonant cavities. Recently thresholds of the order of 50 mW have been obtained using LBO pumped at 514 nm by an argon laser⁴². The cavities used lead to unstable oscillation and active stabilisation is required to keep both (or all three) waves resonant simultaneously. The need for temperature tuning rather than angle tuning in the non-critical phase-matching geometry leads to further stabilisation problems associated with achieving and maintaining steady and often high temperatures.

1.3 Basic Principles

Figure 1.1 shows a schematic diagram of the configuration of a typical OPO. The crystalline gain media is always anisotropic, has a non-centrosymmetric symmetry, and is transparent over a wide range, (including the pump laser wavelength). In the case of the ideal OPO, it also possesses a large non-linearity, is resistant to optical damage, is mechanically hard and chemically stable. In reality, some of the latter criteria may be compromised somewhat.

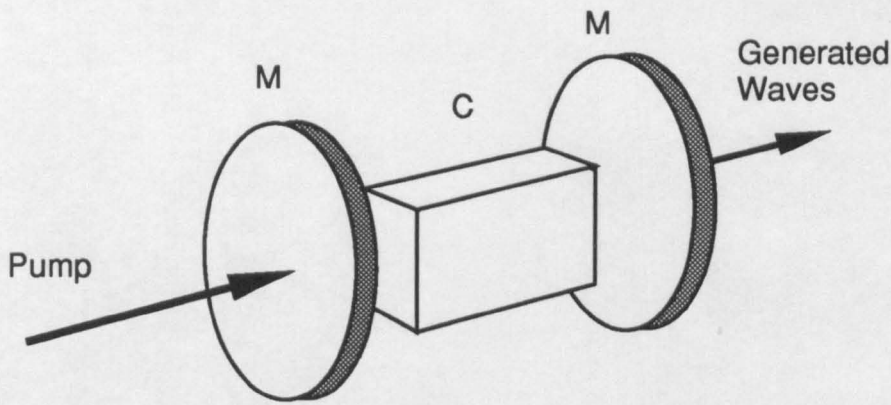


Figure 1.1 The Optical Parametric Oscillator showing the mirrors (M), which are reflecting for one or both of the generated waves; and the non-linear crystal (C).

Optical parametric amplification (the gain process in an OPO) makes use of the third rank tensor property of the material, namely the second order non-linear susceptibility $\chi^{(2)}$. This allows the amplification of an optical field E_n , at a frequency ω_n , by the non-linear interaction of two other fields E_l and E_m , at frequencies ω_l and ω_m respectively. The only constraint on this is that $\omega_l = \omega_m + \omega_n$, which is required for energy conservation. The magnitude of $\chi^{(2)}$ is typically ~ 1 pm/V although certain materials exhibit much higher values, for example in cadmium selenide $\chi^{(2)} = 54$ pm/V. ($\chi^{(2)}$ is also quoted in mks and cgs units. The conversion factors between the S.I. system and these systems are [mks] = [m/V] ϵ_0 and for cgs, [m/V] = $\frac{3}{4}\pi \times 10^4$ esu, which derive from the different definitions of $\chi^{(2)}$). Optical powers of a few 10s of MWcm⁻² are required to obtain reasonable gains within a typical crystal length of 1 cm. Using high peak power beams, for example, with the short pulses obtained from mode-locked lasers, it is possible to observe parametric superfluorescence⁴³ when sufficient gain is obtained. Parametric superfluorescence is the spontaneous creation of two photons at frequencies ω_m and ω_n , (obeying the energy conservation rule $\omega_l = \omega_m + \omega_n$) from one photon of frequency ω_l , on a single pass of the non-linear gain medium. In general the efficiency of such a device would be low as in the case of the first experiment demonstrating second harmonic generation (ref 8) since the three waves propagating within the material will have different phase velocities due to the dispersion of the refractive index in the material. For maximum efficiency, the three interacting waves must have the same phase relationship throughout the length of the crystal. Fortunately, non-linear materials are birefringent, so the refractive index is dependent on the directions of propagation and on the polarisations of the three waves. Using the birefringence it is possible to maintain the relative phase between the waves and produce efficient operation. This technique is called phase-matching and can be written as

$$k_l = k_m + k_n + \Delta k$$

where k_l , k_m and k_n are the wavevectors of the three fields E_l , E_m and E_n respectively. The term Δk is called the phase (or momentum) mismatch. This is zero in the case of perfect phase-matching but will become non-zero in the presence of beam divergence, multi-mode pump sources and cavity mis-alignment. For values of $\Delta k \neq 0$, the efficiency of the device will drop by an amount given by⁴⁴

$$\sin^2(\Delta k l / 2) / (\Delta k l)^2$$

where l is the length of the crystal. Observations of parametric fluorescence show the generated waves emanating in a cone from the material. The actual wavelength generated differs with angle around the cone due to the variation in the wavevectors k_l , k_m and k_n .

When the power density of the pump pulses is insufficient to generate the required output on a single pass it is usual to resonate one (or both) of the generated optical fields and turn the device into an oscillator (see fig 1.1). In the case of a simple OPO the resonator is formed by plane parallel reflectors for one or both of the generated waves. When only one wave is resonant, the device is called a singly resonant oscillator (SRO) and when both waves are resonant, it is called a doubly resonant oscillator (DRO). There are advantages and disadvantages to both designs. The DRO has a lower oscillation threshold, but it is susceptible to instabilities due to the requirement that both waves be resonant simultaneously in the cavity, which lead to mode-hopping and cluster effects⁴⁵. An SRO has a higher threshold than a DRO but will be more stable.

The phase-matching condition $k_l = k_m + k_n$ determines the wavelength pair that will be generated. All three wavevectors are assumed to be collinear with the cavity axis. The wavelength pair that oscillates will be the one with the smallest Δk and hence the highest gain. The wavelength pair can be tuned by rotating the crystal or in some cases by changing the temperature of the crystal. Both these methods change the relative refractive indices of the materials and thus the wavelength pair that experience highest gain due to the reduction of Δk . OPOs can be extremely broadly tunable devices depending on the birefringence of the material. In general the larger the birefringence, the greater is the tuning range.

1.4 Historical Review

The optical parametric oscillator (OPO) developed from the demonstration of optical non-linearity by Franken et al (ref 8) in 1961. They were able to produce the second harmonic of 694 nm radiation from a ruby laser using crystalline quartz as the non-linear medium. The non-linear coefficient of quartz is ~ 0.3 pm/V and the device was not phase matched, therefore, the efficiency of the device was low. In fact, for a pump energy of 3J in 4 ms pulse at 694 nm, an estimated 10^{11} photons were observed at 347 nm, corresponding to an efficiency of $10^{-6}\%$. By using potassium dihydrogen phosphate (KDP), and the concept of phase-matching discussed above, Giordmaine⁴⁶ was able to obtain more efficient second harmonic generation (SHG). He recognised that the phase velocities of the interacting waves could be made equal in certain propagation directions in anisotropic media by using their birefringence. The theory of phase-matching was extended to include phase mismatch Δk , caused by finite bandwidth and divergence of the pump beam, by Maker et al⁴⁷. In 1962, Armstrong et al⁴⁸ published a paper containing detailed calculations of three wave non-linear interactions in crystalline media. They also proposed various frequency mixing experiments using the second order non-linearity. In their suggested experiments and in all previous experiments, there were always two of the three waves present in the interaction either as the pump (SHG) or as the pump and signal beam (sum frequency mixing, difference frequency mixing). Amplification of the third beam then occurred through the coupling provided by $\chi^{(2)}$. At about the same time Kroll⁴⁹ calculated that optical parametric oscillators would be possible and would be capable of generating broadly tunable radiation in the visible and infrared. In an OPO only one of the three waves is present, namely the pump wave, and the parametric process relies on the zero point energy of one photon per mode as the starting point in the amplification of the other two waves. This very weak signal requires many round-trips to build up and thus a resonator is required. It was not until 1965 however, that Giordmaine and Miller (ref 1) reported the first optical parametric oscillator. The non-linear gain medium for their device was a lithium niobate (LiNbO_3) crystal (lithium niobate had already been used for difference frequency generation, and was to become one of the most widely used non-linear materials), and the pump source was a frequency doubled $\text{CaWO}_4:\text{Nd}^{+3}$ laser, doubled in lithium niobate to $0.529 \mu\text{m}$. The OPO was temperature tunable from 0.97 to $1.15 \mu\text{m}$.

The early work on OPOs, from this first device until the development of the new range of non-linear optical materials such as (in chronological order of discovery), urea, β -barium borate, lithium borate and L-arginine phosphate, is well documented in review

papers, and books. In particular, a chapter in the book 'Lasers' by R. G. Smith ref(44) and a review paper by Harris⁵⁰ contain reviews of many of the early experiments carried out before 1974. Details of later work may be found in reference 51. Two Russian papers provide a good source of information on the non-linear materials^{52,53} as does a paper by Eckardt et al⁵⁴ and a book on non-linear materials by Dmitriev et al⁵⁵.

1.5 Modern OPOs

In recent years, the development of new non-linear materials has lead to a resurgence of interest in OPOs. These OPOs taken together span the entire spectral region from the ultraviolet to the infrared. The performance of an OPO in terms of tunability and efficiency are determined by parameters such as transparency range, non-linear coefficient, Poynting vector walk-off angles and optical damage thresholds of the non-linear materials. Unfavourable combinations of these parameters may exclude materials under certain application conditions.

Crystal	LBO ^{56,57}	BBO ⁵⁵	d-LAP ⁵⁸
Crystal and point groups	Orthorhombic, mm2	Trigonal, 3m	Monoclinic, 2
Optical Crystal Class	Biaxial	Uniaxial	Biaxial
Non-linear coefficient	$d_{31} = 1.24 \text{ pm/V}$ $d_{32} = 1.15 \text{ pm/V}$ $d_{33} = 0.1 \text{ pm/V}$	$d_{11} = 1.8 \text{ pm/V}$	$d_{23} = -0.8 \text{ pm/V}$ $d_{16} = d_{21} = 0.48 \text{ pm/V}$ $d_{14} = d_{25} = d_{36} = -0.22 \text{ pm/V}$
Transparency	0.16-2.6 μm	0.19-2.6 μm	0.3-1.3 μm
Figure of Merit	1.2	5.0	1.0
Damage Threshold	25 GW/cm ²	5GW/cm ²	35GW/cm ²
Walk-off Angle	NCPM = 0° Type I = 1.1°	4.63°	3.3°
Stability	Non-hygroscopic	~Non-hygroscopic	Hygroscopic

Table 1.2. A comparison of LBO, BBO and d-LAP. The figure of merit is defined in S1.6. The values of optical damage threshold vary according to pump wavelength and pulse duration and these figure are to be taken only as guide. The material with the best value in each category is highlighted.

Table 1.2 lists some important properties of three non-linear optical crystals suitable for pumping in the ultraviolet, namely β -BaB₂O₄ (BBO), LiB₃O₅ (LBO) and deuterated L-arginine phosphate (d-LAP). Other materials such as KTP, KNbO₃, LiNbO₃ which are commonly used OPO materials do not transmit far enough into the ultraviolet to be pumped by an XeCl excimer laser and are not considered here. Although KDP and its isomorphs do transmit down to 308 nm, their non-linear coefficients are too small to be of any practical use in an OPO. The figure of merit, given in the table, is a function of the single pass gain in the crystal when pumped at 308 nm to generate 616 nm. The definition of the figure of merit is given in section 1.6.

Compared to many other non-linear materials, LBO has the advantage of being mechanically hard, which is necessary if the crystal is to be polished to good optical quality; and of being chemically stable and non-hygroscopic, which are necessary for easy handling and use. It also has a high optical damage threshold and can be grown to adequate sizes, in terms of aperture for tunability and length for parametric gain. It is transparent between 160 nm and 2.6 μ m and has a relatively large birefringence resulting in a large tuning range, (357 nm to 2.2 μ m). The non-linear coefficients are not large but are sufficient for use in an OPO, particularly since a non-critical phase-matched option is available, permitting low threshold operation.

LBO OPOs have been successfully pumped by both Nd:YAG and excimer lasers, see table 1.3 for a list of experiments. The most popular and widely tunable variant of Nd:YAG pumping is to pump with the third harmonic of Nd:YAG. Pumped at 355 nm, the tuning range of the device has been reported (ref 63) as 435 nm to 1922 nm, with efficiencies of around 20%. Pumping with the fourth harmonic has also been demonstrated (ref 61), using the non-critically phase-matched geometry. Efficiencies of around 25% have been reported for this configuration with a limited temperature tuned wavelength range. Narrow linewidth operation was also observed.

Excimer lasers make attractive pump sources for OPOs offering high energies and a selection of pump wavelengths in the ultraviolet, namely XeF at 351 nm, XeCl at 308 nm, KrF at 249 nm and ArF at 198 nm. Using a XeCl laser, very large tuning ranges in LBO have been observed (357 nm to 2.2 μ m). The overall efficiency of the device is also high with pump depletions in the OPO of around 30% and electrical to optical efficiencies of a few percent in the excimer laser. Details of the excimer lasers used in this thesis are given in chapter 4.

Pump/nm	Pulse Duration	PM Type	Tuning	Crystal Length	Tuning Range/nm	Resonator	Pump Energy	Efficiency or output energy	Linewidth	Reference
355	9 ps	Type I $\theta=90^\circ$ $\phi=39^\circ$	Angle	5x5x10.5	452-690	Synch pumped SRO	2 mJ	P.D.=26% idler=10% @3x th	Not Given	59
532.5	55 ps	Type I $\theta=90^\circ$ $\phi=0^\circ$	Temp	3x3x12	652-890 and 1270- 2650	SRO	90 mW ave	P.D.=20% @2x th	1 nm to 11 nm (D)	60
266	10 ns	NCPM z-axis	Temp	3x3x16	311.5-314 and 1821-1740	SRO	0.5 mJ	P.D.=25% @3x th	2-3 axial modes	61
532	15 ps	Type I $\theta=90^\circ$ $\phi=11.5^\circ$	Angle and Temp	6x6x10	650- 2500	OPA	5 mJ pump 0.3 μ J sig	450 μ J signal	Not Given	62
354.7	10 ns	Type I $\theta=90^\circ$ $\phi=33.4^\circ$	Angle	6x3x15.9	435-1922	SRO	12 mJ	P.D.=22% o/p= 2.7 mJ	0.2nm to 'large' @ D.	63
532	35 ps	Type I z-axis NCPM	Temp	3x3x15	750-1800	OPA	2-5 mJ	20%	Not Given	64
355	10 ns	NCPM z-axis	Temp	5x3x12	470-487	SRO	90 mJ	9% @ 480 nm	0.02 nm	65
355	15 ps	Type I $\theta=90^\circ$ $\phi=35^\circ$	Angle	16 mm long	460-1600	OPA	2.3 mJ pump 10 μ J sig	1 mJ signal	Not Given	66

Table 1.3 LiB₃O₅ Experiments. Key and Continuation of table overleaf..

Pump/nm	Pulse Duration	PM Type	Tuning	Crystal Length	Tuning Range/nm	Resonator	Pump Energy	Efficiency/ Output Energy	Linewidth	Reference
532	10 ns	Type II NCPM	Temp	4x5x8	950-1000 and 1130-1210	SRO	18 mJ	S+I o/p =1 mJ	0.4 nm	67
308	10 ns	type II NCPM z-axis	Angle and Temp	3x3x16	383-387 nm	SRO	20 mJ	P.D=35%	2 axial modes	68
308	17 ns	Type I $\theta=90^\circ$ $\phi=40^\circ$	Angle	6x3x15	357-500 and 2244-802	SRO	80 mJ	Not Given	0.3 nm	69
355	30 ps	II NCPM	Temp	3x3x10	415.9-482.6	Not Given	4.8 mJ	p to s 37.7% o/p=1.5 mJ	0.15 nm	70

Table 1.3 Continued. OPO experiments in LiB_3O_5 . KEY:- abbreviations: D=degeneracy. NCPM= non-critically phase-matched. OPA = optical parametric amplifier. 'p' = pump. PD= pump depletion. PM= phase-matching. sig or 's' = signal. SRO= singly resonant oscillator. synch= synchronously. th=threshold. θ and ϕ are angles measured within the crystal (see chapter 2.3).

Due to the broad tunability of LBO, the linewidth of such a device can be large, especially close to degeneracy, ~ 11 nm (ref 60). For many applications, the linewidth of the OPO is an important issue and the inherent linewidth of an OPO can be a problem, particularly in singly resonant OPOs pumped by multi-mode pumps. It is thus necessary to line-narrow these devices if they are to be useful in major applications such as spectroscopy. At the other extreme the NCPM geometry in LBO provides tunable light over a small range by temperature tuning. The slow rate of angle tuning around this point indicates that the linewidth might be narrow and this is in fact the case. References 61 and 68 in table 1.3 report operation of an OPO on two or three axial modes. No line-narrowing elements are used and only the phase-matching determines the size of the gain bandwidth. For stable operation on a single axial mode, it may only be necessary to use short stabilised cavities. In between the extremes of the broadly tunable and NCPM (non-critically phase-matched) geometries is the type II geometry. It is characterised by a moderate angle tuning rate and a linewidth somewhere between that of the other two geometries. Other geometries exist in LBO at other pump wavelengths, but only the three mentioned above are discussed in this thesis.

BBO is another excellent material for OPOs and is the forerunner of LBO. Some of the OPO experiments that have been reported to date are listed in table 1.4 . BBO is characterised by its large non-linear coefficient, enabling low threshold devices to be built in broadly tunable critically phase-matched geometries. It is mechanically hard and only slightly hygroscopic. It is also transparent from 190 nm to 2.6 μm . These attributes are offset by an extremely large linewidth, particularly near degeneracy, when it is pumped by a multi-mode laser. BBO also has a large Poynting vector walk-off angle, which effectively restricts the interaction length of the three waves within the material. Despite this, efficiencies of more than 60% have been obtained by excimer pumping.

Both BBO and LBO are inorganic materials. However, not all of the new non-linear materials are. Urea and d-LAP, both of which are organic non-linear materials, make useful gain media in OPOs. Organic materials unfortunately tend to be highly hygroscopic. This means they require careful handling and must be kept away from the moisture in the air. Experiments on urea have shown it to possess a multi-shot damage problem, which manifests itself as clouding of the pumped volume within the crystal. The effect is apparently irreversible and unavoidable in material grown to date. Experimental results on urea OPOs can be found in ref (51). The non-linear material d-LAP (Deuterated L-arginine phosphate) was first reported in 1989 by Eimerl⁸³. To date very few experiments on d-LAP have been reported. To my knowledge the d-LAP OPO presented in this thesis is the first.

Pump/nm	Pulse Duration	PM Type	Crystal Dimension s/mm ²	Tuning Range/nm	Resonator	Pump Energy	Efficiency / output energy	Linewidth	Ref
355	Not Given	I+II	6x7x8	500-2000 and 400-2000	Parametric Fluorecence	Not Given	Not Given	Not Given	71
532	85 ps	I	4.5x4.5x7.2	680-2400	Synch pumped SRO	40 mJ	~40%	Not Given	72
308	12 ns	I $\theta=36^\circ$	4x4 x7	422-477 and 1140-869	SRO	10 mJ	P.D.=30%	Not Given	73
355	6 ns	I $\theta=25^\circ+$ $\theta=35^\circ$	6x6x12	412-2550	SRO	30 mJ	o/p=140 mW ave	single mode by i. s.	74
532	12 ns	I	9 mm	940-1220	SRO	10 mJ	1 mJ o/p	Not Given	75
355	6 ns	I $\theta=37.5^\circ$	10x10x11 and 10x10x9.5	420-2300	SRO 2 crystals	21 mJ	32%	2.5 nm near D.	76
360	20 ps	I $\theta=35^\circ$	6x6x12	406-3170	SRO	2.2GW cm ⁻²	P.D.=30%	Not Given	77
355	65 ps	I $\theta=35^\circ$	11.8 mm	590-890	Synch SRO	280kW	15kW o/p	Not Given	78
355	10 ns	I	8x6x10	415-2411	SRO double pass	th=13mJ	P.D.=41%	Not Given	79

Table 1.4. OPO experiments in β -BaB₂O₄. Continued overleaf.

Pump/nm	Pulse Duration	PM Type	Crystal Dimension/mm	Tuning Range/nm	Resonator	Pump Energy	Efficiency or Output Energy	Linewidth	Ref
308	10 ns	I	6x3x20	400-560 and 1339-684	SRO	11MW/cm ² Threshold	9%	Single mode with etalons	80
355	8 ns	II	10x8x20 and 8x8x17	480-630 and 1360-810	SRO	38MW/cm ² Threshold	12%	0.05-0.3 nm	81
355	Not Given	I	5x9x10	450-1680	SRO	15mJ max	efficiency =9.4%	Not Given	82

Table 1.4 OPO experiments in β -BaB₂O₄. KEY:- abbreviations: D=degeneracy. eff= efficiency i. s.= injection seeding. o/p= output power 'p' = pump. PD= pump depletion. PM= phase-matching. SRO= singly resonant oscillator. synch= synchronously. th=threshold.

1.6 Figures of Merit

In table 1.2, a figure of merit was given for the three non-linear materials LBO, BBO and d-LAP. This was defined in terms of the effective non-linear coefficient, crystal length and the wavelengths of interaction. Finally, it was normalised to the smallest of the three, which occurred in d-LAP. The values used were appropriate for the phase-matching conditions used experimentally in this thesis. From the table it can be seen that the figure of merit of BBO is 5 times that of d-LAP and 4 times that of LBO. From experimental results to be presented later, it will become clear that other important factors must be taken into account before a reliable figure of merit can be obtained for a particular application. One such factor is the Poynting vector walk-off angle which was given in table 1.2. The effect of walk-off is to limit the interaction length by reducing the overlap of the three waves. A more appropriate figure of merit might therefore be given by introducing a term dependent on the Poynting vector walk-off, for example, the oscillation threshold. Similarly, other factors such as tuning range, damage properties and crystal aperture limitations may determine the material of choice but these are more difficult to include in a figure of merit.

1.7 Thesis Layout

The second chapter provides details of some of the more general theory and ideas used throughout the remainder of the thesis. Additional theory is included in later chapters where it is of particular relevance. Chapters 3 and 6 contain detailed calculations on the predicted performance of LBO and d-LAP and chapters 4, 5, and 6 contain the experimental results on LBO and d-LAP. These materials are compared with BBO in chapter 7, which contains the experimental results obtained for threshold and efficiency measurements on LBO, d-LAP and BBO. All three materials are considered for suitability in a line-narrowed OPO system. The theory and experimental results of the line-narrowing work is given in chapter 8 and its application in injection seeding an OPO and an OPA is given in chapter 9. Finally, the conclusions of the work and a discussion of future work is given in chapter 10.

REFERENCES

- 1 'Tunable Coherent Parametric Oscillation in LiNbO₃ at Optical Frequencies'. J.A. Giordmaine and Robert L. Byer. *Phys. Rev. Lett.* 14, 973 (1965).
- 2 'Widely Tunable parametric generation in beta barium borate'. Herman Vanherzeele and Chuangtian Chen. *Appl. Opt.* 27, 2634 (1988).
- 3 'New nonlinear-optical crystal:LiB₃O₅'. Chuangtian Chen, Yicheng Wu, Aidong Jiang, Bochang Wu, Guiming You, Rukang Li and Shujie Lin. *J. Opt. Soc. Am. B.* 6, 616 (1989).
- 4 '354.7 nm Pumped Parametric Oscillation in RD*A'. K. Kato *IEEE J. Quantum Electron.* 11, 939 (1975).
- 5 'Y. Cui, M. H. Dunn, C. J. Norrie, W. Sibbett, B. D. Sinclair, Y. Tang, J. A. C. Terry. Conference on Lasers and Electro-Optics (1992). paper CTuR1.
- 6 M. Ebrahimzadeh and M. H. Dunn. Conference on Lasers and Electro-Optics (1988). paper PD30
- 7 'Stimulated Optical Radiation in Ruby'. T. H. Maiman. *Nature* 187, 493 (1960).
- 8 'Generation of Optical Harmonics'. P. A. Franken, A. E. Hill, C. W. Peters and G. Weinreich'. *Phys. Rev. Lett.* 7,118 (1961).
- 9 'Optical Mixing'. M. Bass, P. A. Franken, A. E. Hill, C. W. Peters and G. Weinreich. *Phys. Rev. Lett.* 8, 18 (1962).
- 10 'Measurement of Parametric gain accompanying optical difference frequency generation'. C. C. Wang and C. W. Racette. *Appl. Phys. Lett.* 6, 169 (1965).
- 11 'Optical Maser Action in Europium Benzolacetone'. A. Lempicki and H. Samelson. *Phys. Lett.* 4, 133 (1963).
- 12 'Flashlamp-excited Organic Dye Lasers'. B. B. Snavely. *Proc. IEEE.* 57, 1374 (1969).
- 13 *Laser Focus World*, February 1989, p23.
- 14 'Optical Parametric Oscillation in the Visible Spectrum'. J. A. Giordmaine and R. C. Miller. *Appl. Phys. Lett.* 9, 298 (1966).
- 15 'Tunable LiNbO₃ Optical oscillation with external mirrors'. Robert C. Miller and W. A. Nordland. *Appl. Phys. Lett.* 10, 53 (1967).
- 16 'Ruby-laser-pumped optical parametric oscillator with electro-optic tuning'. L. B. Kreuzer. *Appl. Phys. Lett.* 10, 336 (1967).
- 17 'Continuous Optical Parametric Oscillator in Ba₂NaNb₅O₁₅'. R. G. Smith, J. E. Geusic, H. J. Levinstein, J. J. Rubin, S. Singh and L. G. Van Uiterl. *Appl. Phys. Lett.* 12, 308 (1968).
- 18 'Efficient Optical Parametric Oscillation using Doubly and Singly resonant Cavities. J. E. Bjorkholm. *Appl. Phys. Lett.* 13, 53 (1968).
- 19 'Transverse parametric intensity distribution of optical parametric oscillation in Mg:LiNbO₃ crystal'. D. Wang, X. Long, F. Wu and J. Yao. Conference on Lasers and Electro-Optics (1992) paper CTuR6
- 20 'High-power LiIO₃ optical parametric oscillator for infrared laser chemistry applications'. I. I. Ashmarin, Yu. A. Bykovshii, V. A. Ukraintsev, A. A. Christyakov and L. V. Shishonkov. *Sov. J. Quantum Electron.* Qu E-14, 1237 (1984).
- 21 'Efficient High-gain Parametric generation in ADP Continuously Tunable across the Visible Spectrum'. J. M. Yarborough and G. A. Massey. *Appl. Phys. Lett.* 18, 438 (1971).
- 22 'Some Recent Advances and Applications of Optical Parametric Oscillators'. R. W. Wallace. *IEEE J. Quantum Electron.* Qu. E-7, 307 (1971).
- 23 'A laser photoacoustic sensor for analyte detection in aqueous systems'. H. A. Mackenzie, G. B. Christison, P. Hodgson and D. Blanc. to be published in *Sensors and Actuators B*.
- 24 'Optical Fibre Delivery and Tissue Ablation Studies Using a Pulsed Hydrogen Fluoride Laser'. P. E. Dyer, M. E. Khosroshahi and S. J. Tuft. *Lasers in Medical Science* 7, 331 (1992).
- 25 'The Frequency-doubled Nd:YAG Laser with Automatic Scanning in the Treatment of Port Wine Stains: A Preliminary Report'. F. Laffitte, S. Mordon, J. P. Chavoain, J. L. Bonafe, D. Rouge and M. Costagliula. *Lasers in Medical Science* 7, 341 (1992).
- 26 'Laser Interstitial Thermotherapy in Stereotactical Neurosurgery'. F. X. Roux, L. Merienne, B. Leriche, S. Lucerna, B. Turak, B. Devraux and J. P. Chodkiewicz. *Lasers in Medical Science* 7, 121 (1992).
- 27 'Chromophores in tissue for laser medicine and laser surgery'. Leon Goldman. *Lasers in Medical Science* vol 5, 289 (1990).
- 28 'Wavelength Dependence of Laser Fragmentation of Gallstones'. N. F. Mitchell, R. Novak. M. McLoughlin. *Lasers in Medical Science* vol 7, 427 (1992).
- 29 'Color center lasers'. Werner Gellerman. *J. Phys. Chem. Solids.* 52, 249 (1991).

- 30 David Burns PhD Thesis St Andrews 1991.
- 31 Laser Focus Buyers Guide 1993, p118.
- 32 'A Promising New Solid State Laser Material'. Stephen A. Payne, L. L. Chase, Herbert W. Newkirk, Larry Smith and William F. Krupke
- 33 'Flashlamp pumped Cr:LiSrAlF₆ laser'. M Staider, B. H. T. Chai and M. Bass. *Appl. Phys. Lett.* 58, 216 (1991).
- 34 'Titanium Sapphire Laser Characteristics'. W. R. Rappaport and Chandra P. Khattak. *Appl. Opt.* 27, 2677 (1988).
- 35 'Continuous wave mode locked Cr⁴⁺YAG laser'. P. M. W. French, N. H. Rizvi, J. R. Taylor and A. V. Shestakov. *Opt. Lett.* 18, 39 (1993).
- 36 Richard Scheps, Bernard M. Gately, Joseph F. Myers, Jerzy S. Krasinski and Donald F. Heller. 'Alexandrite laser pumped by semiconductor lasers'. *Appl. Phys. Lett.* 56, 2288 (1990).
- 37 Peter F. Moulton. 'An investigation of the Co:MgF₂ laser system'. *IEEE J. Quantum Electron.* 21, 1582 (1985).
- 38 Exciton Dye Laser Wavelength Chart. Exciton inc. P.O. Box 31126, Dayton Ohio.
- 39 'Resonant frequency doubling of a self-starting, coupled cavity mode-locked Ti:AL₂O₃ laser'. P. F. Curley and A. I. Ferguson. *Opt. Lett.* 16, 321 (1991).
- 40 'Continuous Optical Parametric Oscillation in Ba₂NaNb₅O₁₅'. R. G. Smith, J. E. Geusic, H. J. Levinstein, J. J. Rubin, S. Singh and L. G. Van Uitert. *Appl. Phys. Lett.* 12, 308 (1968).
- 41 'Visible CW Parametric Oscillator'. R. L. Byer, M. K. Oshman, J. F. Young and S. E. Harris. *Appl. Phys. Lett.* 13, 109 (1968).
- 42 'Continuous-wave parametric oscillation in lithium triborate'. Finlay G. Colville, Angus J. Henderson, Miles J. Padgett, Jun Zhang and Malcolm H. Dunn. *Opt. Lett.* 18, 205 (1993).
- 43 'Parametric superfluorescence in KTiOPO₄ crystals pumped by 1 ps pulses'. Tadashi Nishikawa, Naoshi Uesugi and Junji Yumoto. *Appl. Phys. Lett.* 58, 1943 (1991).
- 44 'Lasers'. R. G. Smith. Editors A. K. Levine and A. J. DeMaria. Marcel Dekker New York (1976).p
- 45 'Lasers' R. G. Smith. Editors A. K. Levine and A. J. DeMaria. Marcel Dekker New York (1976). p247
- 46 'Mixing of light beams in crystals'. J. A. Giordmaine. *Phys. Rev. Lett.* 8, 19 (1962).
- 47 'Effects of dispersion and focusing on the production of optical harmonics'. P. D. Maker, R. W. Terhune, M. Nisenoff and C. M. Savage. *Phys. Rev. Lett.* 8, 21 (1962).
- 48 'Interactions between light waves in a non-linear dielectric'. J. A. Armstrong, N. Bloembergen, J. Ducuing and P. S. Pershan. *Phys. Rev.* 127, 1918 (1962).
- 49 'Parametric Amplification in Spatially Extended media and Application to the Design of Tuneable Oscillators at Optical Frequencies'. Norman M. Kroll. *Phys. Rev.* 127, 1207 (1962).
- 50 'Tunable Optical Parametric Oscillators'. Stephen E. Harris. *Proc. of IEEE* 57, 2096 (1969).
- 51 'Optical Parametric Oscillators pumped by an Excimer Laser'. Majid Ebrahimzadeh. PhD Thesis, St Andrews University 1989.
- 52 'Non-linear Optics Crystals (review and summary of data)'. D. N. Nikogosyan. *Sov. J. Quantum Electron.* 7, 1 (1977).
- 53 'Crystals for non-linear optics'. D. N. Nikogosyan and G. G. Gurzadyan. *Sov. J. Quantum Electron.* 17, 970 (1987).
- 54 'Absolute and Relative Non-linear Optical Coefficients of KDP, KD*P, BaB₂O₄, LiIO₃, Mg:LiNbO₃ and KTP Measured by Phase-matched Second Harmonic Generation' Robert C. Eckardt, Hisashi Masuda, Yuan Xuan Fan and Robert L. Byer. *IEEE J. Quantum Electron.* 26, 922 (1990).
- 55 'Handbook of Nonlinear Optical Crystals'. V. G. Dmitriev, G. G. Gurzadyan, D. N. Nikogosyan. Springer Series in Optical Sciences.
- 56 'Temperature tuned noncritically phase-matched frequency conversion in LiB₃O₅ crystal'. J. T. Lin, J. L. Montgomery. *Opt Comm.* 80, 159 (1990).
- 57 'New nonlinear-optical crystal: LiB₃O₅'. Chuangtian Chen, Yicheng Wu, Aidong Jiang, Bochang Wu, Guiming You, Rulcang Li and Shujie Lin. *J. Opt. Soc. Am. B* 6, 616 (1989).
- 58 'Deuterated L-Arginine Phosphate: A New Efficient Nonlinear Crystal'. D. Eimerl, S. Velsko, L. Davis, F. Wang, G. Loiacono and G. Kennedy. *IEEE J. Quantum Electron.* Qu. E-25, 179 (1989).
- 59 'Lithium triborate picosecond optical parametric oscillator'. V. Kubecek, Y. Takagi, K. Yoshihara and G. C. Reali. *Opt. Comm.* 91, 93 (1992).

- 60 'Singly resonant, all solid state, mode-locked LiB_3O_5 optical parametric oscillator tunable from 652 nm to 2.65 μm '. M. Ebrahimzadeh, G. J. Hall and A. J. Ferguson. *Opt. Lett.* 17, 652 (1992).
- 61 'Lithium triborate optical parametric oscillator pumped at 266 nm'. Y. Tang, Y. Cui and M. H. Dunn. *Opt. Lett.* 17, 192 (1992).
- 62 'Optical parametric amplification in a lithium triborate crystal tunable from 0.65 μm to 2.5 μm '. Shujie Lin, J. Y. Huang, J. W. Ling, Chuangtian Chen and Y. R. Shen. *Appl. Phys. Lett.* 59, 2805 (1991).
- 63 'Visible optical parametric oscillation in LiB_3O_5 '. Yunping Wang, Zuyan Xu, Daoqun Deng, Wanhua Zheng, Baichang Wu and Chuangtian Chen. *Appl. Phys. Lett.* 59, 531 (1991).
- 64 'Noncritically phase-matched second-harmonic generation and optical parametric amplification in a lithium triborate crystal'. J. Y. Huang, Y. R. Shen, Chuangtian Chen and Bochang Wu. *Appl. Phys. Lett.* 58, 1579 (1991).
- 65 'Blue parametric generation from temperature-tuned LiB_3O_5 '. Frank Hanson and David Dick. *Opt. Lett.* 16, 205 (1991).
- 66 'Picosecond optical amplification in lithium triborate'. J. Y. Huang, Y. R. Shen, Chuangtian Chen and Bochang Wu. *Appl. Phys. Lett.* 58, 213 (1991).
- 67 'Parametric Oscillation in LiB_3O_5 Pumped at 0.532 μm '. K. Kato. *IEEE J. Quantum Electron.* Qu. E-26, 2043 (1990).
- 68 'Efficient ultraviolet LiB_3O_5 optical parametric oscillation'. Majid Ebrahimzadeh, Gordon Robertson and Malcolm H. Dunn. *Opt. Lett.* 16, 769 (1991).
- 69 'Broadly tunable LiB_3O_5 optical parametric oscillator'. Gordon Robertson, Angus Henderson and Malcolm H. Dunn. *Appl. Phys. Lett.* 60, 271 (1992).
- 70 'Picosecond optical parametric generation and amplification in LiB_3O_5 and $\beta\text{-BaB}_2\text{O}_4$ '. Fang Huang, Liu Huang. *Appl. Phys. Lett.* 61, 1769 (1992).
- 71 'Widely tunable parametric generation in beta barium borate'. Herman Vanherzeele and Chuangtian Chen. *Appl. Opt.* 27, 2634 (1988).
- 72 'Synchronously pumped optical parametric oscillation in beta-barium borate'. L. J. Bromley, A. Guy and D. C. Hanna. *Opt. Comm.* 67, 316 (1988).
- 73 'Optical parametric oscillator in a beta-barium borate crystal pumped by an XeCl excimer laser'. Hiroshi Komine. *Opt. Lett.* 13, 643 (1988).
- 74 'Visible BaB_2O_4 optical parametric oscillator pumped at 355 nm by a single-axial- mode pulsed source'. Y. X. Fan, R. C. Eckardt, R. L. Byer, J. Nolting and R. Wallenstein. *Appl. Phys. Lett.* 53, 2014 (1988).
- 75 'Barium Borate Optical Parametric Oscillation'. Y. X. Fan, R. C. Eckardt, Robert L. Byer, Chuangtian Chen and A. D. Jiang. *IEEE J. Quantum Electron.* Qu. E-25, 1196 (1989).
- 76 'High-efficiency and narrow linewidth operation of a two crystal $\beta\text{-BaB}_2\text{O}_4$ optical parametric oscillator'. W. R. Bosenberg, W. S. Pelouch and C. L. Tang. *Appl. Phys. Lett.* 55, 1952 (1989).
- 77 'Visible optical parametric oscillation in synchronously pumped beta-barium borate'. S. Burdulis, R. Grigonis, A. Piskarskas, G. Sinkevicius, V. Sirutkatus, A. Fix, J. Nolting and R. Wallenstein. *Opt. Comm.* 74, 398 (1990).
- 78 'Parametric Oscillation in Beta-Barium Borate Synchronously pumped by the third harmonic of a continuously mode-locked and Q switched Nd:YAG laser'. A. Piskarskas, V. Smilgevičius, A. Umbrasas, A. Fix and R. Wallenstein. *Opt. Comm.* 77, 335 (1990).
- 79 'Highly efficient visible and infrared $\beta\text{-BaB}_2\text{O}_4$ optical parametric oscillator with pump reflection'. Yunping Wang, Zuyan Xu, Daoqun Deng, Wanhua Zheng, Xiang Liu, Baichang Wu and Chuangtian Chen. *Appl. Phys. Lett.* 58, 1461 (1991).
- 80 'Efficient, single-axial mode oscillation of a beta barium borate optical parametric oscillator pumped by an excimer laser'. Gordon Robertson, Angus Henderson and Malcolm H. Dunn. *Appl. Phys. Lett.* 62, 123 (1993).
- 81 'Type II phase-matching in a β -barium borate optical parametric oscillator'. W. R. Bosenberg and C. L. Tang. *Appl. Phys. Lett.* 56, 1819 (1990).
- 82 'Broadly tunable optical parametric oscillation in $\beta\text{-BaB}_2\text{O}_4$ '. L. K. Cheng, W. R. Bosenberg and C. L. Tang. *Appl. Phys. Lett.* 53, 175 (1988).
- 83 'Deuterated L-Arginine Phosphate: A New Efficient Non-linear Crystal'. D. Eimerl, S. Velsko, L. Davis, F. Wang, G. Loiacono and G. Kennedy. *IEEE J. Quantum Electron.* QE-25, 179 (1989).

Theory

This chapter contains an overview of the basic OPO theory which is used throughout this thesis. It also discusses less well documented issues, such as crystallographic conventions, phase-matching in biaxial crystals, acceptance bandwidths and acceptance angles of OPOs.

2.1 Three Wave Non-linear Interactions

In an optically transparent material, the electron polarisation, P , in the medium can be regarded as linearly dependant on the electric field, $E(\omega_1)$, at the frequency ω_1 , that drives it, provided that the intensity of the field is low. A feel for what intensities can be considered low or high will develop as the chapter progresses. The polarisation at frequency ω_1 can be written

$$P(\omega_1) = \epsilon_0 \chi^{(1)} E(\omega_1) \tag{2.1}$$

where $\chi^{(1)}$ is the linear susceptibility and ϵ_0 is the free space permittivity. When the light intensity is strong, the linear approximation given above breaks down and higher order terms must be included, thus

$$P(\omega_1) = \epsilon_0 \chi^{(1)} E(\omega_1) + \epsilon_0 \chi^{(2)} E(\omega_m) E(\omega_n) + \epsilon_0 \chi^{(3)} E(\omega_q) E(\omega_r) E(\omega_s) + \text{higher order terms} \tag{2.2}$$

where ω denotes the frequency of the field and $\omega_1 = \omega_m + \omega_n = \omega_q + \omega_r + \omega_s$. The higher intensities required to observe the non-linearities are obtainable only with the use of laser light and although the concept of optical non-linearity has long been known, it is only since the demonstration of the first laser that experimental non-linear optics has been possible. In this analysis, only the first and second order terms are required since it is the $\chi^{(2)}$ term that is responsible for the parametric generation process as well as second harmonic generation and sum frequency mixing. For the even order term to be present, the medium must lack a centre of inversion. Thus only non-centrosymmetric crystals are useful for optical parametric oscillators. (The $\chi^{(3)}$ term is responsible for intensity

dependent refractive index processes such as self-focusing and also four wave mixing). From equation 2.2, we can see that the field at ω_1 can be driven by the other two fields at ω_m and ω_n via $\chi^{(2)}$. Polarisation at ω_m and ω_n can be driven in a similar way using the same $\chi^{(2)}$ as follows

$$\begin{aligned} P(\omega_m) &= \chi^{(1)}E(\omega_m) + \chi^{(2)}E(\omega_1)E^*(\omega_n) \\ P(\omega_n) &= \chi^{(1)}E(\omega_n) + \chi^{(2)}E(\omega_1)E^*(\omega_m) \end{aligned} \quad (2.3)$$

The stars denote complex conjugates. By inserting the non-linear polarisation into Maxwell's equations, it is possible to derive the wave-equation in a non-linear medium¹, namely for the case of plane waves

$$\frac{d^2E}{dz^2} = \frac{1}{c^2} \frac{d^2E}{dt^2} + \frac{1}{c^2} \frac{d^2P}{dt^2} \quad (2.4)$$

where P is defined in equation 2.3. Equation 2.4 is solved by assuming the appropriate forms for the three waves at ω_1 , ω_m , and ω_n , which are

$$\begin{aligned} E_1 &= \mathcal{E}_1(z) \exp(i\{\omega_1 t - k_1 z + \phi_1\}) \\ E_{m,n} &= \mathcal{E}_{m,n}(z) \exp(i\{\omega_{m,n} t - k_{m,n} z + \phi_{m,n}\}) \end{aligned} \quad (2.5)$$

where $\phi_{1,m,n}$ are the phases of the waves, $k_{1,m,n}$ are the wavevectors and $\mathcal{E}_{1,m,n}(z)$ are the slowly varying amplitudes associated with the fields $E_{1,m,n}$. The solution of equation 2.5 is derived by Yariv (ref 1), Armstrong et al² and Smith³. Three coupled differential equations result which connect the three fields via the second order non-linear susceptibility, $\chi^{(2)}$. These determine the growth of each wave as a function of the other two interacting fields. These are

$$\begin{aligned} \frac{d\mathcal{E}_1}{dz} &= iK_1 \mathcal{E}_m \mathcal{E}_n e^{i(\Delta k z + \phi_1)} \quad ; \quad K_1 = 2\pi \left[\frac{\omega_1 \chi^{(2)}}{n_1 c} \right] \\ \frac{d\mathcal{E}_m}{dz} &= iK_m \mathcal{E}_1 \mathcal{E}_n^* e^{i(\Delta k z + \phi_m)} \quad ; \quad K_m = 2\pi \left[\frac{\omega_m \chi^{(2)}}{n_m c} \right] \\ \frac{d\mathcal{E}_n}{dz} &= iK_n \mathcal{E}_1 \mathcal{E}_m^* e^{i(\Delta k z + \phi_n)} \quad ; \quad K_n = 2\pi \left[\frac{\omega_n \chi^{(2)}}{n_n c} \right] \end{aligned} \quad (2.6)$$

where

$$\Delta k = k_1 - k_m - k_n$$

In the terminology of OPOs, the field E_p is considered to be the 'pump' field and the two fields that are generated the 'signal' and 'idler'. The fields will from now on be denoted as E_p , E_s and E_i and the frequencies by ω_p , ω_s and ω_i . The three coupled equations 2.6 can be solved analytically to find the single pass gain and hence the resulting power densities providing that some assumptions are made to simplify the calculation. Generally it is assumed that the pump depletion is small thus $dE_p/dz = 0$. The solution is then a pair of simultaneous differential equations, the solution of which is given by Smith (ref 3) and Shen⁴ and results in the following equation for the signal power density

$$S_s = \frac{S_0}{\Gamma^2} \left\{ \left[\Gamma \cosh(\Gamma z) + \Gamma_0 r \sin \phi \sinh(\Gamma z) \right]^2 + \left[\frac{\Delta k}{2} - \Gamma_0 r \cos \phi \right]^2 \sinh^2(\Gamma z) \right\} \quad (2.7)$$

where r is the ratio of idler to signal in the initial conditions, S_0 is the initial signal power density and $\phi = \phi_p - \phi_s - \phi_i$. The single pass gain, Γ is defined as

$$\Gamma^2 = \Gamma_0^2 - \left(\frac{\Delta k}{2} \right)^2$$

where

$$\Gamma_0^2 = \kappa S_p \quad (2.8)$$

and

$$\kappa = \frac{\omega_s \omega_i \chi^2}{\epsilon_0 c^3 n_p n_s n_i}$$

where the superscript (2) has been dropped from $\chi^{(2)}$ for clarity. It is interesting to note that the dependence on the signal and idler frequencies of κ means that close to degeneracy, the gain will be greater than the gain at larger frequency separations, i.e. further from degeneracy. Simplifications to 2.7 can be made for specific cases. In the case where only the signal is resonant, i.e. in a singly resonant oscillator (SRO), and there is no injected field, then one can assume $r = 0$. If the momentum mis-match, Δk , is also taken to be zero, as is the case for perfect phase-matching, then we find the signal power, as a function of crystal length, z , is

$$S_s = S_0 \cosh^2(\Gamma z) = S_0 + S_0 \sinh^2(\Gamma z) \quad (2.9)$$

Inserting typical values into the equation gives $\Gamma_0^2 = 3 \times 10^{-8} S_p (\text{Wm}^{-2})$. For a typical pump power density of 50 MWcm^{-2} in a 20 mm crystal, the single pass gain, G ($= S_s/S_0$) is ~ 100 . For parametric amplification of noise, as in the case of an OPO,

it will be necessary to resonate at least one of the waves in order to achieve useful pump depletions. There are two kinds of pulsed OPOs: SROs as mentioned above and DROs (doubly resonant oscillators) where both generated waves are resonant. From equation 2.7 it is clear that the gain of a DRO will be higher and as a result the oscillation threshold will be lower. However, these devices suffer from stability problems caused by the constraint of having two waves resonant simultaneously within one cavity.

The three coupled equations (2.6) can also be solved numerically to find the signal energy density. The Pascal program in appendix C was used to generate the data in figure 2.1. The figure shows how the signal beam depletes the pump beam in the presence of a momentum mis-match Δk . The initial conditions in the program are: pump =1, signal =0.01 and idler =0, $\Delta k=2/L$, where L is the crystal length. The phase term $\theta=i(\Delta kz + \phi)$ is initially zero but changes instantaneously to $-\pi/2$ when the parametric process begins. When the sign of θ changes from negative to positive the direction of the parametric process reverses. This results in the signal and idler being depleted and the pump being amplified.

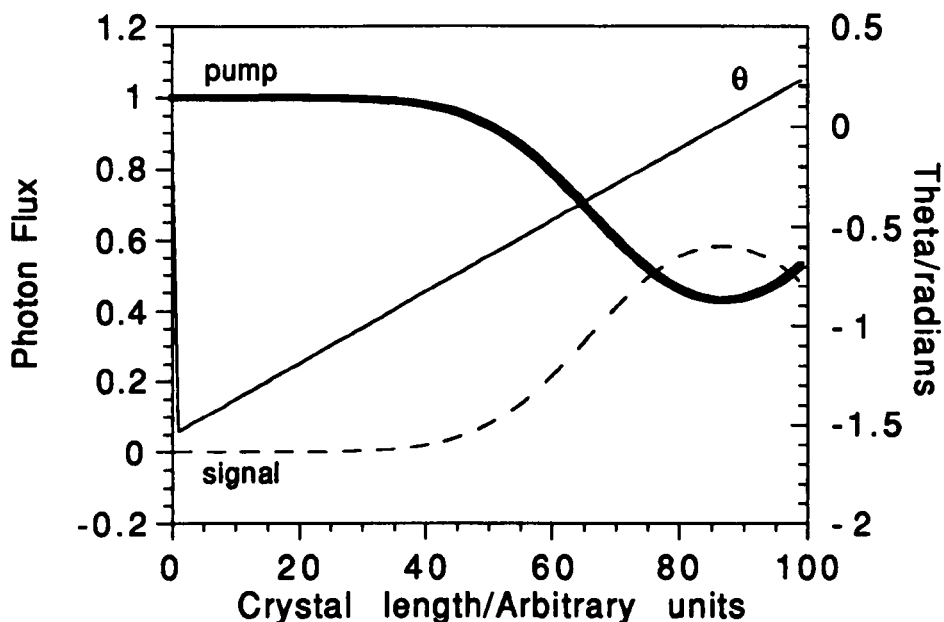


Figure 2.1. Photon flux between pump and signal when $\Delta kl/2=1$. Initially the pump and signal photon levels are 1.00 and 0.01 respectively. The evolution of $\theta = (\Delta kz + \phi)$ is also shown.

Momentum or phase mis-match, Δk , should ideally be zero, but in practical systems it may be large. Contributing factors to Δk are pump beam divergence, pump beam bandwidths, cavity mis-alignment and non-uniformity of the pump beam.

2.2 The Effective Non-linear Coefficient

In the last section, we examined the non-linear response of a medium with a second order non-linear susceptibility, $\chi^{(2)}$, in the presence of three scalar fields obeying the parametric equation $\omega_p = \omega_s + \omega_i$. In this section, the full tensor properties of the second order non-linear coefficient are examined. A spatial component of the second order non-linear polarisation, $P(\omega_l)$, in the presence of two fields, $E(\omega_m)$ and $E(\omega_n)$ can be written

$$P_i(\omega_l) = \epsilon_0 \chi_{ijk}^{(2)} E_j(\omega_m) E_k(\omega_n)$$

where $\chi_{ijk}^{(2)}$ is the second order non-linear susceptibility which is a tensor of rank 3. The second order non-linear susceptibility is normally quoted in the principal axis system of the piezoelectric coefficients. The reason for this is that they share the same symmetry, although they are different in magnitude, so historically they were determined with reference to the same XYZ axis set. The Z axis of the XYZ system is usually taken as the polar axis. The components of $\chi^{(2)}$ are 27 in number and are labelled $\chi_{ijk}^{(2)}$. The subscripts i, j, and k take the values 1, 2, and 3 which refer to the axis X, Y, and Z respectively and summation over repeated indices is assumed. In any given material, many of the components are zero, greatly simplifying the task of any calculations involving $\chi^{(2)}$. In addition, it was shown by Kleinman⁵ that in most cases, when well away from absorption features, there is a symmetry in $\chi^{(2)}$ which further reduces the number of available components. The Kleinman symmetry has the effect that $P(\omega_1) = \epsilon_0 \chi_{123}^{(2)} E_2 E_3 = \epsilon_0 \chi_{132}^{(2)} E_3 E_2$. In order to highlight this symmetry and to simplify calculations, it is usual to define the non-linear coefficient, $d_{i\mu}$, which is defined by

$$\begin{bmatrix} P_X(\omega_l) \\ P_Y(\omega_l) \\ P_Z(\omega_l) \end{bmatrix} = 2\epsilon_0 \begin{bmatrix} d_{11} & d_{12} & d_{13} & d_{14} & d_{15} & d_{16} \\ d_{21} & d_{22} & d_{23} & d_{24} & d_{25} & d_{26} \\ d_{31} & d_{32} & d_{33} & d_{34} & d_{35} & d_{36} \end{bmatrix} \begin{bmatrix} E_X(\omega_m)E_X(\omega_n) \\ E_Y(\omega_m)E_Y(\omega_n) \\ E_Z(\omega_m)E_Z(\omega_n) \\ E_Y(\omega_m)E_Z(\omega_n)+E_Z(\omega_m)E_Y(\omega_n) \\ E_X(\omega_m)E_Z(\omega_n)+E_Z(\omega_m)E_X(\omega_n) \\ E_X(\omega_m)E_Y(\omega_n)+E_Y(\omega_m)E_X(\omega_n) \end{bmatrix}$$

The non-linear coefficient, $d_{i\mu}$, defined in this way takes into account the symmetry in the second order non-linear susceptibility. The second index of $d_{i\mu}$, running from 1 to 6, refers to the double index of the second order non-linear susceptibility, χ_{ijk} , such that μ from 1 to 6 maps to $jk = 11, 22, 33, 23, 13, 12$. In general many of the components of $d_{i\mu}$ will be zero due to symmetry relations within the crystal and it is usual for the effective non-linear coefficient to be dependent on only a few terms. This will limit the number of interactions possible.

The effective non-linear coefficient is a measure of the coupling between the three fields that a wave of a given polarisation and propagation direction will experience on travelling through a material in the presence of two other intense fields. The value of effective non-linear coefficient, d_{eff} , can be calculated by multiplying the direction cosine matrices for the three polarisations present with the matrix of $d_{i\mu}$. A full description is given in papers by Yao and Sheng⁶ and also by Roberts⁷. These authors include extra terms for dispersion due to birefringent effects, which are in general small and are not included in the equations below. We can write the effective non-linear coefficient for type I phase matching as

$$d_{\text{eff}} = \begin{bmatrix} a_1(2) \\ a_2(2) \\ a_3(2) \end{bmatrix} \cdot d_{ijk} \cdot \begin{bmatrix} a_1(1) \cdot a_1(1) \\ a_2(1) \cdot a_2(1) \\ a_3(1) \cdot a_3(1) \\ 2a_2(1) \cdot a_3(1) \\ 2a_1(1) \cdot a_3(1) \\ -2a_1(1) \cdot a_2(1) \end{bmatrix} \quad (2.11a)$$

and for type II phase matching as

$$d_{\text{eff}} = \begin{bmatrix} a_1(2) \\ a_2(2) \\ a_3(2) \end{bmatrix} \cdot d_{ijk} \cdot \begin{bmatrix} a_1(1) \cdot a_1(2) \\ a_2(1) \cdot a_2(2) \\ a_3(1) \cdot a_3(2) \\ a_2(1) \cdot a_3(2) + a_2(2) \cdot a_3(1) \\ a_1(1) \cdot a_3(2) + a_1(2) \cdot a_3(1) \\ a_1(1) \cdot a_2(2) + a_1(2) \cdot a_2(1) \end{bmatrix} \quad (2.11b)$$

where the terms $a_i^{(n)}$ ($n=1,2$) are the two direction cosines of the two orthogonal polarisation eigenstates, e^1 and e^2 , associated with a particular propagation direction (Θ , Φ) within the crystal. Thus in the type I phase-matching above, the pump is polarised as $n=1$ and the signal and idler as $n=2$. The direction cosines for the two polarisations in the XYZ axis system are as follows

$$a_i^{(1)} = \begin{bmatrix} -\cos\Theta\cos\Phi\cos\Delta + \sin\Phi\sin\Delta \\ -\cos\Theta\sin\Phi\cos\Delta - \cos\Phi\sin\Delta \\ \sin\Theta\cos\Delta \end{bmatrix}$$

$$a_i^{(2)} = \begin{bmatrix} -\cos\Theta\cos\Phi\sin\Delta - \sin\Phi\cos\Delta \\ -\cos\Theta\sin\Phi\sin\Delta + \cos\Phi\cos\Delta \\ \sin\Theta\sin\Delta \end{bmatrix}$$
(2.12)

where the angle, Θ , is measured from the Z axis to the X,Y plane, Φ is measured from axis X to Y and Δ is the polarisation angle in the XYZ system (see equation 2.15). To use the equations above to predict non-linear coefficients, it is first necessary to transform them into a new axis system, xyz. More details are given later in this chapter after a discussion on crystallographic conventions and nomenclature.

2.3 Crystallographic Conventions

2.3.1 Introduction

It is necessary to state here some of the conventions used in the nomenclature of crystals used in optical parametric oscillators and amplifiers before discussing the topic of phase-matching. The materials dealt with in this thesis are barium borate (BBO), lithium borate (LBO) and deuterated L-arginine phosphate (d-LAP). The crystal groups, point groups and optical classification of these materials are shown in table 2.1⁸. The optical classification of crystals falls into three categories. These are isotropic (anaxial), uniaxial and biaxial. The terms refer to the number of optic axes the index ellipsoid has. (An optic axis has the property that a plane section at right angles to it through the centre of the index ellipsoid is a circle). Isotropic materials such as sodium chloride have a spherical index ellipsoid so there is no preferred axis of symmetry thus a unique optic axis cannot be defined. They do not possess a second order non-linear coefficient due to this symmetry.

2.3.2 Uniaxial Crystals

The optic axis in a uniaxial crystal, like BBO, is the crystallographic c axis, as shown in figure 2.2. The index ellipsoid is a spheroid with rotational symmetry around the c axis. Thus the refractive indices perpendicular to the optic axis are equal and independent of the direction of propagation. This is called the ordinary refractive index, n_o .






Crystal Group	Index Ellipsoid Axes	Optical Classification	Optic Axes	Examples (and point groups)
Cubic $\alpha=\beta=\gamma=90^\circ$ $a=b=c$		Isotropic (Anaxial)	Undefined	Yttrium Aluminium Garnet (YAG)
Trigonal Tetragonal Hexagonal		Uniaxial	z (+ve) x(-ve) along c axis (shown vertical)	BBO (3m) Urea (42m) Cadmium Selenide (6mm)
Orthorhombic $\alpha=\beta=\gamma=90^\circ$ $a\neq b\neq c$		Biaxial	In xz plane at angle Ω to z axis	LBO (mm2) α -Iodic acid (222)
Monoclinic $\alpha=\gamma=90^\circ$ $\beta>90^\circ$ $a\neq b\neq c$		Biaxial	In xz plane at angle Ω to z axis (y/b axis common to both)	d-LAP (2) MNA (m)
Triclinic $\alpha\neq\beta\neq\gamma$ $a\neq b\neq c$		Biaxial	In xz plane at angle Ω to z axis	No known examples of triclinic (1) crystals used in NLO.

Table 2.1. The crystallographic and optical classifications of some non-linear materials.

The circles in the 'index ellipsoid axes' column denote rotational symmetry about the enclosed axes. The thick lines indicate that the crystallographic (abc) and optical (xyz) axis coincide. Where the abc and xyz axis systems do not coincide i.e. in monoclinic and triclinic crystals, there may be dispersion associated with the xyz axes. In all cases the permutations of axes is dependent on the material and also on the conventions used. The angles α, β, γ are measured between the a axis and bc plane, the b axis and ac plane, and the c axis and the ab plane respectively. In general the XYZ axes are used to report the non-linear coefficients and the xyz axis are used for phase-matching calculations. To correlate the two, it is necessary to rotate the XYZ axis system until the polar axes of the two systems coincide.

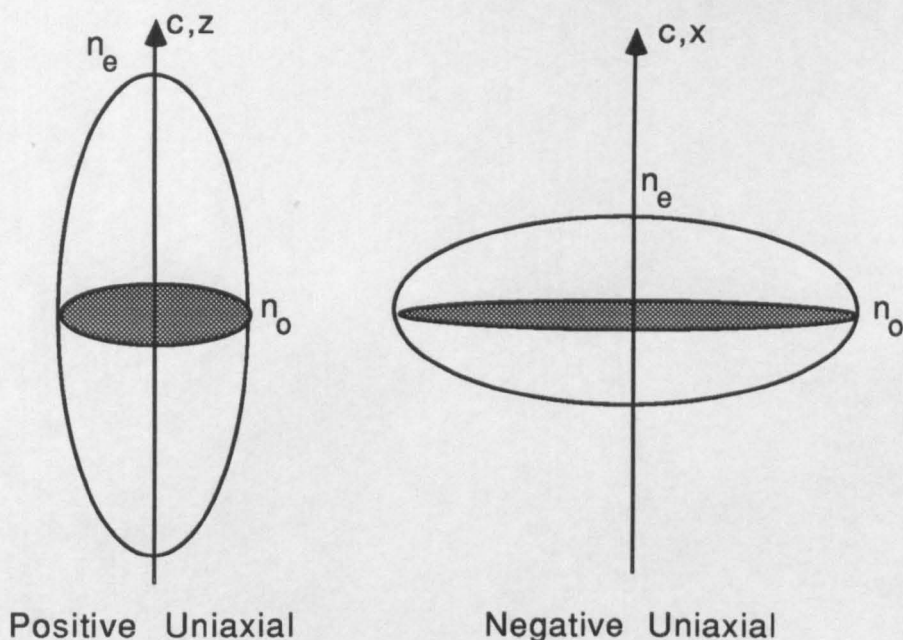


Figure 2.2. Positive and negative uniaxial index ellipsoids. The shaded area shows circular cross-section in positive and negative uniaxial crystals. The c axis is the optic axis and (x,y,z) is defined such that $n_x < n_y < n_z$.

The index of refraction along the optic axis is called the extraordinary refractive index, n_e . For propagation at an arbitrary angle through the material, the refractive index will be a combination of n_o and n_e . The crystal is defined as positive uniaxial if $n_o < n_e$ and negative uniaxial if $n_o > n_e$. This has repercussions in the identification of the optic axis with respect to the xyz axis system and the subsequent definitions of angles measured in the index ellipsoid. The z axis is the optic axis in positive uniaxial crystals and θ is defined as the angle between the optic axis and the direction of propagation. In negative uniaxials, the x axis is the optic axis and θ is again measured from the optic axis to the direction of beam propagation. A beam entering a positive (or negative) uniaxial crystal at an angle θ to the z axis (or x axis) will be split into two orthogonal polarisations. One will be polarised in the n_o plane and is called the 'ordinary wave'. The refractive index of the ordinary wave is n_o . The second polarisation is at right angles to the propagation direction and the n_o plane and is called the 'extraordinary wave'. The refractive index of this wave is dependent on n_e and n_o .

2.3.3 Biaxial Crystals

Biaxial materials have two optic axes. These are at an angle Ω to the z axis. In fact, the uniaxial crystal is just a special case of a biaxial crystal where the two optic axes are coincident and $\Omega = 0$. Figure 2.3 shows the index ellipsoid for positive and negative

biaxial crystals. The two shaded areas represent the two circular planes within the ellipsoid. The normals to these two planes are the optic axes (O.A.). The optic axes are in the xz plane and are at an angle Ω to the z axis in positive biaxials and at an angle Ω to the x axis in negative biaxials.

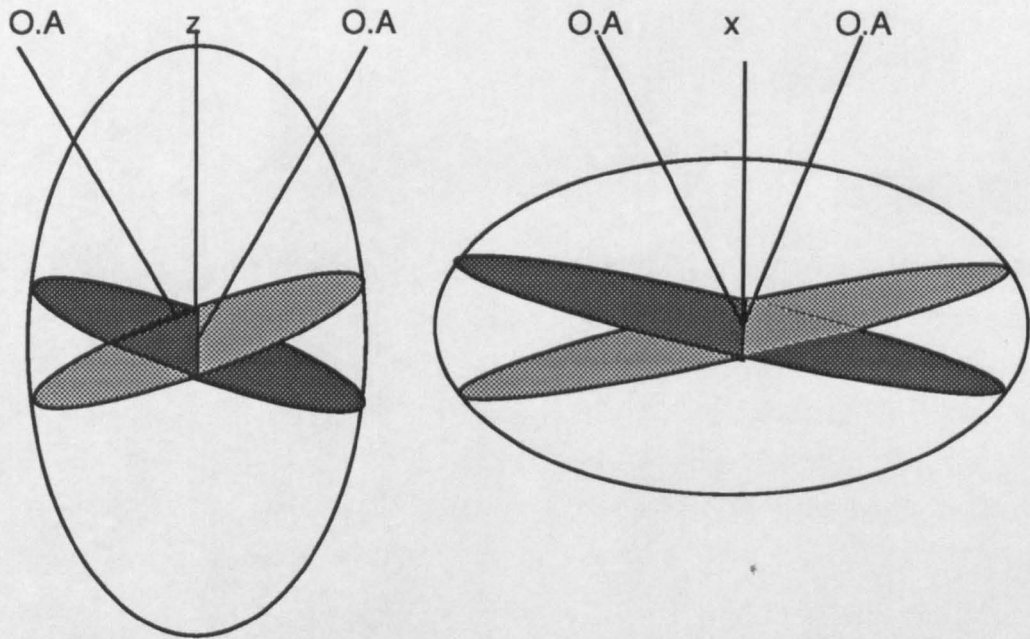


Figure 2.3. Positive (right) and Negative (left) Biaxial Index Ellipsoids. The axes of the ellipse are defined such that $n_z > n_y > n_x$. The shaded areas represent the two possible circular cross-sections through the centre of the ellipsoid. The normals to these circles are the optic axes (O.A.)

It should be noted that the xyz axes of the index ellipsoid do not necessarily coincide with the XYZ axis system which is the reporting frame of the non-linear coefficient. In general, it is necessary to rotate the XYZ axes, in order that the two axis sets are coincident, before calculation of the effective non-linear coefficient can be made. This is the case for monoclinic crystals such as d-LAP. In some crystals, the optical axis system is 'clamped' to the crystallographic and piezoelectric systems (i.e. the abc , XYZ and xyz axes are coincident). This is the case in many biaxial materials of which LBO is an example. The order of the axes varies depending on material parameters and conventions. In LBO abc maps to xzy and XYZ . A paper by Roberts (ref 7) recommends standards for all the crystal groups. In this thesis the axis labelling system used is dependent on the material in question and conforms to the conventions used in the literature for that material. For example in LBO the convention that abc maps to XYZ which maps to xzy with the z axis as the polar axis is universal in the literature⁹⁻¹¹. The conversion of the non-linear coefficients d_{311} and d_{322} of LBO into the xyz system

traditionally used for LBO, is achieved by rotating the XYZ system through -90° about the X axis, (which is parallel to the x axis). The angle is said to be positive if the rotation is clockwise when viewed along the axis, away from the origin. The rotation matrix for LBO is (ref 7)

$$R_{ab}^{13} = \begin{bmatrix} 1 & 0 & 0 \\ 0 & 0 & -1 \\ 0 & 1 & 0 \end{bmatrix}$$

and

$$d_{ijk}^{xyz} = (R_{il} \cdot R_{jm} \cdot R_{kn} \cdot d_{lmn}^{XYZ})$$

This results in $d_{311}^{(XYZ)}$ mapping to $d_{211}^{(xyz)}$ and $d_{322}^{(XYZ)}$ mapping to $d_{233}^{(xyz)}$. (From now on the non-linear coefficient in the xyz system will be written using x, y and z in place of 1, 2 and 3 for the indices. The numbers 1, 2 and 3 will be reserved for the XYZ system. The superscript axis system notation will be dropped). All calculations are from now on carried out in the xyz system using the angles θ and ϕ . The angle θ in LBO is measured from the z axis to the xy plane and the angle ϕ is measured from the x axis to the y axis in the yz plane.

In d-LAP the crystallographic axis system is not orthogonal, however, the b, Y and y axes all coincide. By convention, the negative biaxial system, yzx, is used to perform phase-matching calculations. The non-linear coefficients, quoted in the XYZ system must be transformed into the yzx system before the effective non-linear coefficient can be calculated in terms of θ and ϕ . The rotations are more complex and are dealt with in chapter 6.

2.4 Phase-matched Interactions in Non-linear Media

In general, three waves of different frequencies will not propagate in a medium at the one phase velocity, c/n , due to the dispersion of the refractive index, n , in the media. This, however, can be compensated for by using the birefringence present in some crystals. By using polarised pump light and propagating the beam at an appropriate angle, it is often possible to propagate the three waves with the same phase velocity through the medium. This is possible in all non-linear materials to some degree depending on the birefringence of the crystal. In the presence of phase mis-match Δk , the maximum obtainable efficiency will decrease.

The origin of birefringence is due to the anisotropy of some materials where the electric displacement vector, D , is no longer necessarily parallel to the electric field vector, E ,

but is related by the third rank tensor relation ϵ . This is the simplest relation that can account for anisotropic behaviour¹²:

$$\begin{bmatrix} D_x \\ D_y \\ D_z \end{bmatrix} = \begin{bmatrix} \epsilon_{xx} & \epsilon_{xy} & \epsilon_{xz} \\ \epsilon_{yx} & \epsilon_{yy} & \epsilon_{yz} \\ \epsilon_{zx} & \epsilon_{zy} & \epsilon_{zz} \end{bmatrix} \begin{bmatrix} E_x \\ E_y \\ E_z \end{bmatrix}$$

This also results in the refractive index, n , being dependent on the direction of propagation within the crystal since $n = 1/(\epsilon\mu)^{1/2}$ and is the origin of the index ellipsoid.

In general, the refractive index can be described by the surface of an ellipsoid constructed from the matrix above. This can be transformed so that only the diagonal components remain, i.e. by eliminating the cross product terms through successive rotations. This defines the unique ellipsoid known as the index ellipsoid or optical indicatrix, the axes of which form the principal refractive indices n_x , n_y , and n_z . These refractive indices are defined by convention such that $n_z > n_y > n_x$. Any beam propagating at an angle ϕ to the x axis in the xy plane and at an angle θ to the z axis in a biaxial material can be described by two independent, orthogonal, plane polarised waves (polarisation eigenmodes e^1 and e^2) which have refractive indices n^1 and n^2 found from the following equations (ref 7):

$$\begin{aligned} \frac{1}{n^{(1)2}} &= \left[\left(\frac{a_x^{(1)}}{n_x} \right)^2 + \left(\frac{a_y^{(1)}}{n_y} \right)^2 + \left(\frac{a_z^{(2)}}{n_z} \right)^2 \right] \\ \frac{1}{n^{(2)2}} &= \left[\left(\frac{a_x^{(2)}}{n_x} \right)^2 + \left(\frac{a_y^{(2)}}{n_y} \right)^2 + \left(\frac{a_z^{(2)}}{n_z} \right)^2 \right] \end{aligned} \quad (2.13)$$

where the direction cosines $a_i^{(n)}$ for a wave propagating in the direction $\mathbf{k}(\theta, \phi)$ are

$$\begin{aligned} a_i^{(1)} &= \begin{bmatrix} -\cos\theta\cos\phi\cos\delta^{(1)} + \sin\phi\sin\delta^{(1)} \\ -\cos\theta\sin\phi\cos\delta^{(1)} - \cos\phi\sin\delta^{(1)} \\ \sin\theta\cos\delta^{(1)} \end{bmatrix} \\ a_i^{(2)} &= \begin{bmatrix} -\cos\theta\cos\phi\sin\delta^{(2)} - \sin\phi\cos\delta^{(2)} \\ -\cos\theta\sin\phi\sin\delta^{(2)} + \cos\phi\cos\delta^{(2)} \\ \sin\theta\sin\delta^{(2)} \end{bmatrix} \end{aligned} \quad (2.14)$$

which are the same as the direction cosines used previously for the calculation of the effective non-linear coefficient. The term $\delta^{(n)}$ is the polarisation angle and is defined as

the angle between the polarisation eigenmodes, namely e^1 and e^2 given by the direction cosines $a_i^{(n)}$, and the x - k plane. The angle, $\delta^{(1)}$, between e^1 and the x - k plane is shown in figure 2.4. The polarisation eigenmodes are defined as the internal/external bisectors of the two planes (triangular shaded planes in figure 2.4) formed by the wavevector k and one of the optic axes (O.A.) located at $\pm\Omega$ to the z axis in the xz plane. In negative biaxial crystals where the angle, Ω , between the optic axes and the z axis is greater than 45° , then δ is given by

$$\tan 2\delta = \frac{\sin 2\phi \cdot \cos \theta}{\sin^2\phi - \cos^2\theta \cdot \cos^2\phi + \cot^2\Omega \cdot \sin^2\theta} \quad (2.15)$$

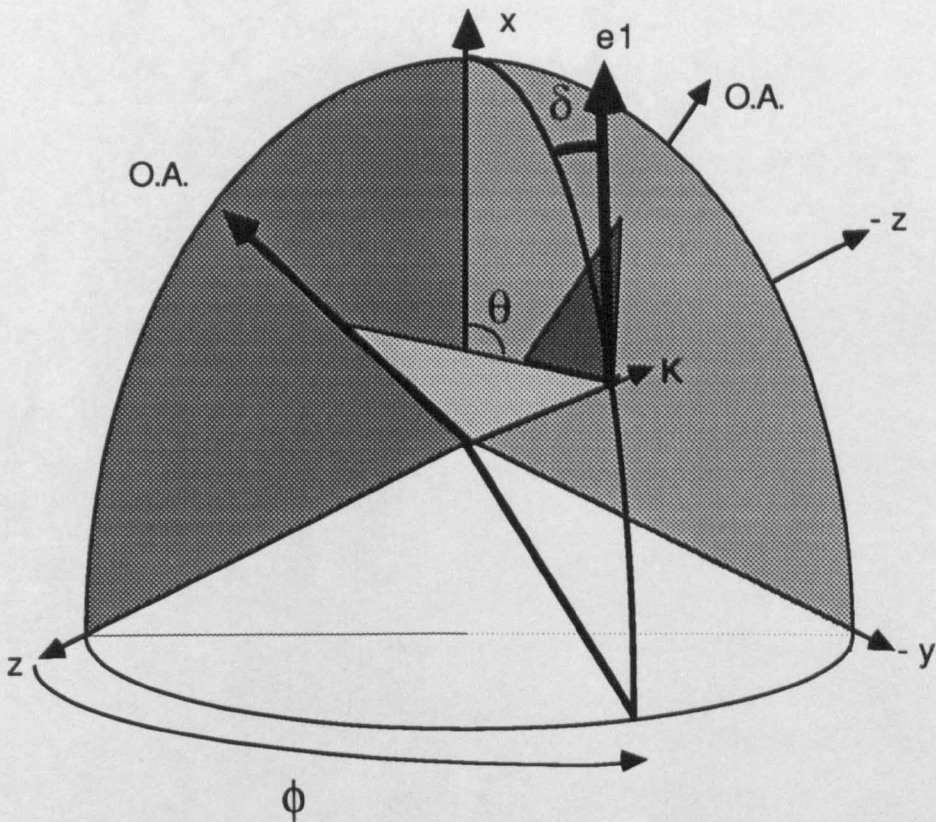


Figure 2.4. The polarisation angles $\delta^{(n)}$. The definition of e^1 and e^2 is given in the text. e^2 is not shown in the diagram but is at an angle $90^\circ + \delta$ to the k - x plane. Both e^1 and e^2 are perpendicular to the propagation direction, k . KEY:- k is the wavevector, δ is the polarisation angle, θ is the polar angle (measured from the x axis in negative biaxials and from the z axis in positive biaxials), ϕ is the azimuthal angle. The two optic axes O. A. lie at an angle, Ω , to the z axis in a positive biaxial and to the x axis in a negative biaxial.

For positive biaxials, where, Ω is less than 45° , the polarisation angle is given by

$$\tan 2\delta = \frac{-\sin 2\phi \cdot \cos \theta}{\cos^2\phi - \cos^2\theta \cdot \sin^2\phi + \tan^2\Omega \cdot \sin^2\theta} \quad (2.16)$$

For monoclinic and triclinic crystals, the principal axes of the index ellipsoid are not fixed to the crystallographic axes but rotate about the b axis, which is parallel to the Y axis in monoclinic crystals. In practise however, the dispersion of the axes is often small over the transparent range of the material and may be ignored.

The equations for the refractive indices can be simplified in some cases, i.e. for propagation in the three principal planes defined by n_x , n_y , and n_z . In the xy plane, for example, the azimuthal angle θ is equal to 90° which implies that $\cos \theta = 0$. Putting this into equation 2.15 or 2.16 we find that $\delta=0$. The simplified direction cosines for beams confined to the xy plane are thus

$$\begin{aligned} \mathbf{a}_i^{(1)} &= \begin{bmatrix} 0 \\ 0 \\ 1 \end{bmatrix} \\ \mathbf{a}_i^{(2)} &= \begin{bmatrix} -\sin\phi \\ \cos\phi \\ 0 \end{bmatrix} \end{aligned} \quad (2.17)$$

This has then reduced to a situation analogous to phase matching in uniaxial crystals, where we would define $\mathbf{a}_i^{(1)}$ as an ordinary wave (o), which is not dependent on the angle of propagation, and $\mathbf{a}_i^{(2)}$ as an extraordinary wave (e), which is dependent on the angle of propagation. Similar simplifications can be made for the other two principal planes. Phase matching calculations for tuning within a principal plane are relatively simple using these specific direction cosines.

Phase matching requires that the three interacting waves satisfy two parametric equations. The first is the energy conservation equation, $\omega_p = \omega_s + \omega_i$, and the second is $k_p = k_s + k_i$. (The momentum mismatch Δk is zero for perfect phase-matching). The momentum equation may be written alternatively as

$$n_p \omega_p = n_s \omega_s + n_i \omega_i$$

where $n_{p,s,i}$ are calculated from equation 2.13. Phase-matching nomenclature for OPOs, which was borrowed from SHG, is as follows: when the pump, signal and idler (p,s,i) are polarised as (a^1, a^2, a^2) or (a^2, a^1, a^1) it is termed type I phase matching and when (p,s,i) are polarised (a^1, a^1, a^2) or (a^2, a^2, a^1) then it is termed type II. (Note there is no real distinction between signal and idler when Kleinman's symmetry holds). In the simplification of phase-matching described by eqn 2.17, the two polarisations $a^{(1)}$ and $a^{(2)}$ may be denoted as o and e, as demonstrated above. Using the convenient notation, pump \rightarrow signal + idler and e and o to denote extraordinary and ordinary refractive indices respectively, the type I phase-matching options are $e \rightarrow o+o$ and $o \rightarrow e+e$ and the type II options are $e \rightarrow o+e$, $e \rightarrow e+o$, $o \rightarrow o+e$ and $o \rightarrow e+o$.

2.5 The Effect of Momentum Mismatch on Phase-matching

It was assumed in the previous section that the phase mismatch, Δk , was zero. However in general this will not be true due to finite laser linewidths and divergences. It is therefore of interest to see the extent to which the pump beam can differ from the ideal yet still provide gain at the signal and idler wavelength. Starting from the momentum equation, but now including the term Δk , defined as

$$\Delta k = \frac{1}{c}(n_p \omega_p - n_s \omega_s - n_i \omega_i) \quad (2.18)$$

we can derive expressions for the acceptance angle and the acceptance bandwidth of a crystal. We start by taking the derivative with respect to angle assuming that the frequency of all three waves is fixed and that k_s is constrained by the OPO cavity, i.e. $dn_s/d\theta = 0$, and get

$$\frac{d(\Delta k)}{d\theta} = \frac{1}{c} \left[\omega_p \frac{dn_p}{d\theta} - \omega_i \frac{dn_i}{d\theta} \right]$$

Noting that $\omega = 2\pi c/\lambda n$ allows us to rewrite this in terms of wavelength, giving

$$\frac{d(\Delta k)}{d\theta} = 2\pi \left[\frac{1}{\lambda_p} \frac{dn_p}{d\theta} - \frac{n_p}{n_i \lambda_i} \frac{dn_i}{d\theta} \right]$$

This can be re-arranged to give the acceptance full angle, $d\theta$

$$d\theta_p = \frac{1}{2\pi} \left[\frac{1}{\lambda_p} \frac{dn_p}{d\theta} - \frac{n_p}{n_i \lambda_i} \frac{dn_i}{d\theta} \right]^{-1} (\Delta k) \quad (2.19)$$

It is usual to assume a value of π/L for the momentum mismatch, Δk , since this corresponds roughly to a halving of the single pass gain¹³. It is interesting to note that if the phase matching is $o \rightarrow e + o$ then the right hand side of the equation becomes undefined since both the pump and idler are ordinary waves. In this case a second order analysis is required. This is treated in chapter 4 for the case of LBO.

The equations for the acceptance bandwidth are calculated in the same way starting from equation 2.18. The signal wavevector is again assumed constant and the derivative of Δk is taken with respect to dv . The variables are then changed to $d\lambda$ and the resultant equation for the acceptance bandwidth, dv_p , is

$$dv_p = \frac{1}{L} \left[(n_p - n_i) - \lambda_p \frac{dn_p}{d\lambda_p} + \lambda_i \frac{dn_i}{d\lambda_i} \right]^{-1} \quad (2.20)$$

where again $\Delta k = \pi/L$. Equations (2.19) and (2.20) define the acceptance angle and bandwidth respectively. These two parameters of an OPO limit the usable crystal length for a given pump beam divergence and linewidth. Exceeding these values leads to back conversion as shown in figure 2.1.

2.6 Prediction of Inherent OPO Linewidths

There are three independent contributions to the linewidth of an OPO. Firstly, there is the effect of the phase-matching bandwidth. Using a similar argument to the above, the signal frequency can be changed from the optimum, given by $k_p = k_s + k_i$, until $\Delta k = \pi/L$. In this case it is assumed that the pump wavevector, k_p , is fixed and the signal frequency variation with respect to Δk is investigated. Starting from the momentum conservation equation 2.18 and taking the derivative with respect to $d\omega_s$ gives

$$\frac{d(\Delta k)}{d\omega_s} = -\frac{1}{c} \left[n_s + \omega_s \frac{dn_s}{d\omega_s} + n_i \frac{d\omega_i}{d\omega_s} + \omega_i \frac{dn_i}{d\omega_s} \right]$$

This can be simplified if it is noted that $(d\omega_i / d\omega_s) = -(d\omega_s / d\omega_s)$ and the variables are changed to λ , giving

$$dv_{s1} = \frac{c}{L} \left[(n_i - n_s) + \lambda_s \frac{dn_s}{d\lambda_s} - \lambda_i \frac{dn_i}{d\lambda_i} \right]^{-1} \quad (2.21)$$

where the usual substitution of $\Delta k = \pi/L$ is made (L is the crystal length). From this equation it is clear that at and near degeneracy, where $n_i \approx n_s$, the linewidth will be large and as the OPO is tuned further from degeneracy, the linewidth will decrease.

The second contribution to the signal comes from the angular spread of wavevectors in the pump beam. This is given by

$$dv_{s2} = \frac{c}{2L} \frac{\partial n_p}{\partial \theta} \Delta \theta_p \left[(n_i - n_s) + \lambda_s \frac{dn_s}{d\lambda_s} - \lambda_i \frac{dn_i}{d\lambda_i} \right]^{-1}$$

where $\Delta \theta_p$ is the pump beam divergence. Again the dependence on $(n_i - n_s)$ ensures that the linewidth will be largest close to degeneracy.

The third contribution is due to the finite spread of frequencies in the pump beam. This contribution is usually much smaller than the other two since the pump linewidth is narrow, typically ~ 0.002 nm (0.2 cm^{-1}), compared to the OPO linewidths, ~ 1 nm. This contribution can be shown to be

$$dv_{s3} = \Delta v_p \left[(n_p - n_i) + \lambda_i \frac{dn_i}{d\lambda_i} - \lambda_p \frac{dn_p}{d\lambda_p} \right] \left[(n_i - n_s) + \lambda_s \frac{dn_s}{d\lambda_s} - \lambda_i \frac{dn_i}{d\lambda_i} \right]^{-1}$$

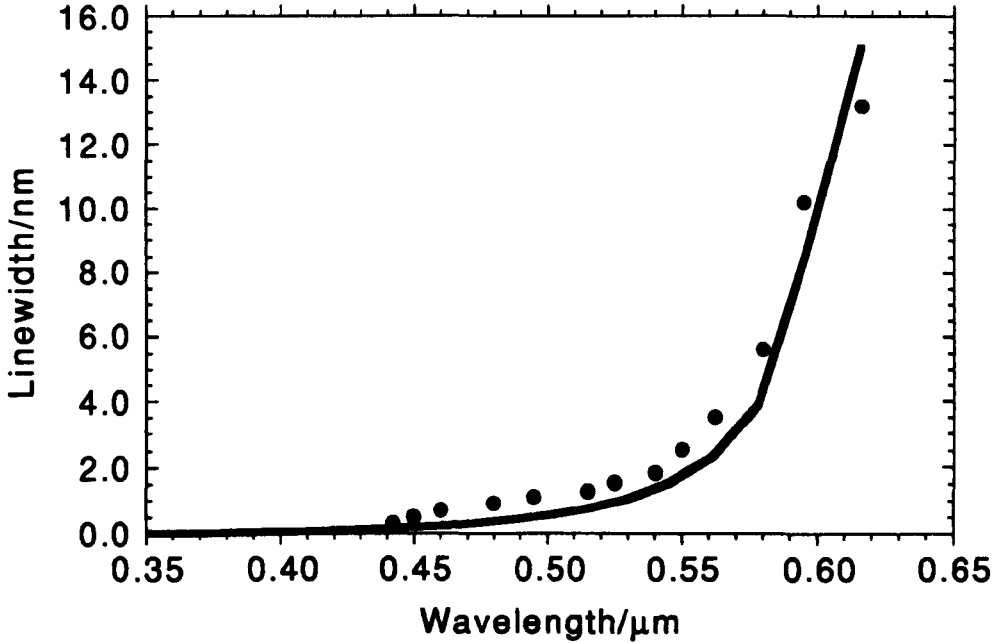


Figure 2.5 The theoretical and experimental linewidth of BBO.

Figure 2.5 shows a plot of theoretical linewidth for BBO, calculated by summing the contributions from dv_{s1} , dv_{s2} , and dv_{s3} . The figure also shows some experimental points taken using a monochromator. Clearly there is a good fit between the theory and experiment. The linewidth close to degeneracy is ~ 14 nm, which is very large. This falls rapidly as the separation in signal and idler wavelengths increases. Work on reducing the large linewidths of OPOs is reported in chapters 8 and 9. In chapter 7, a detailed comparison of the inherent linewidths of LBO and BBO is given including a comparison of the different contributions to linewidth from dv_{s1} , dv_{s2} and dv_{s3} .

2.7 Poynting Vector Walk-off in Birefringent Crystals

It was mentioned in section 2.3 that the directions of the electric displacement vector D and the electric field vector E were not, in general, in the same direction in an anisotropic media. It is therefore a consequence that the wavevector direction, k , and the energy propagation direction, given by the Poynting vector $S=ExH$, are also not in the same direction since k is perpendicular to both B and D , see figure 2.6. It can be shown that the walk-off angle, ρ : the angle between the energy propagation direction S and the wavevector direction k , as shown in figure 2.7, is given by

$$\tan \rho = \frac{1}{n} \left(\frac{dn}{d\theta} \right) \quad (2.22)$$

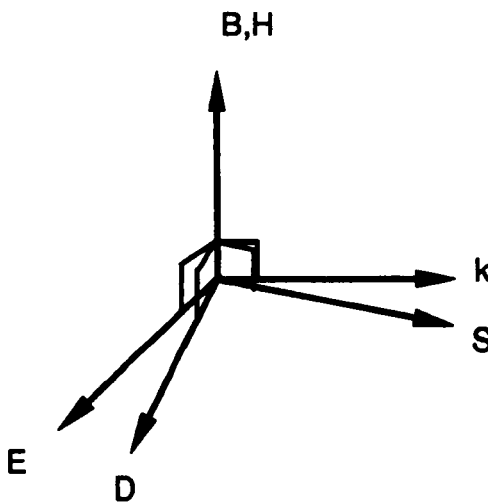


Figure 2.6. The relationship between k and S with respect to E and D

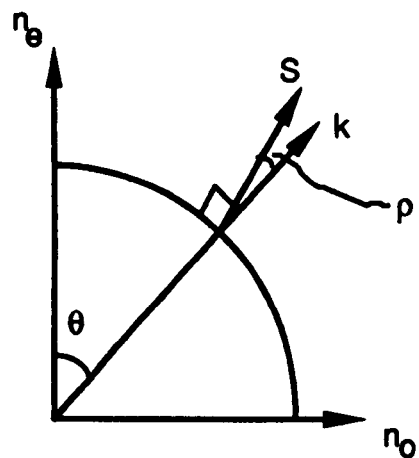


Figure 2.7. The index ellipsoid with the wavevector, k and the Poynting vector, S .

For a uniaxial crystal or within the principal plane of a biaxial crystal where the identification of the principal refractive indices with n^e and n^o can be made, equation 2.22 can be solved in terms of n^e and n^o to give

$$\tan \rho = \frac{1}{2} \sin 2\theta (n^o)^2 \left\{ \frac{1}{(n^e)^2} - \frac{1}{(n^o)^2} \right\} \quad (2.23)$$

In the biaxial case, it is a relative walk-off of all the waves from each other rather than one wave from the other two that takes place. In practise, it will often be possible to identify "ordinary-like" and "extraordinary-like" waves from consideration of the polarisation angles, δ . For example in d-LAP the polarisation angles for the pump, signal and idler are 5° , 87° and 88° respectively and walk-off angles for the three waves are 57, 2 and 4 mR. (see section 2.4).

The implication of the walk-off angle is that it defines a maximum interaction length, $L_w (= W/\tan \rho)$, within the crystal where W is the beam width. Beyond this length there is no further interaction between the extraordinary and ordinary waves. In chapter 7, using experimental data from d-LAP, LBO and BBO, it will be shown that there is a near constant rise in oscillation threshold of 2.3 times, in crystals where complete walk-off occurs, compared with those where little or no walk-off occurs. Clearly the advantage to NCPM is that there is no limit to the crystal length imposed by Poynting vector walk-off. However, there is still the consideration of acceptance bandwidth, which will limit the crystal length for any given pump laser characteristics.

2.8 Comparison of Walk-off and Acceptance Angles

In section 2.4, we developed the concept of acceptance angles, which limit the useful length of crystal that can be used as a gain medium. In the last section, 2.7, we followed the argument of the walk-off angle, which limited the maximum usable crystal length due to walk-off of the extraordinary wave(s) from the ordinary wave(s), an effect caused by the birefringence of the material. In this section, we examine the possibility of the equivalence of the two phenomena in the case of diffraction limited beams, as suggested by Boyd et al¹⁴.

Experimentally it can be shown, see chapter 7, that the effect of walk-off becomes significant when the beam size W_b becomes comparable with the amount of walk-off, W_w

$$W_w = L \tan \rho = W_b \quad (2.24)$$

where ρ is the walk-off angle and L is the crystal length. For BBO, this gives a value of $W_w = 2\text{mm}$. If instead, we treat the problem in terms of acceptance angles, we can show that the width of a beam, W_θ , which is diffraction limited, with a divergence of Θ , is

$$W_\theta = \frac{\lambda}{n\Theta} \quad (2.25)$$

where λ is the pump wavelength and n is the refractive index at the pump wavelength. If we then set the pump beam divergence equal to the acceptance angle in equation 2.25, we will find the smallest pump beam size that will not exceed the crystal acceptance angle. For BBO we find that $W_\theta = 2\text{ mm} = W_w$. This equivalence can also be displayed analytically by considering the forms of the two equations.

Simplifying equation 2.19 for a type I interaction in a negative uniaxial or biaxial crystal (i.e. $e \rightarrow o+o$) and substituting it into equation 2.25, we get

$$W_\theta = \frac{L}{n_p} \frac{dn_p}{d\theta}$$

where it has been assumed that $\Delta k = \pi/L$. Similarly, substituting equation 2.22 into equation 2.24 leads to the expression

$$W_w = \frac{L}{n_p} \frac{dn_p}{d\theta}$$

which is identical to W_θ .

Notice that when propagation is along one of the principal axes, both ρ and $d\theta_p$ become undefined and a second order analysis involving $d^2n/d\theta^2$ is required. The second order analysis in terms of acceptance angle is dealt with by J. Yao et al (ref 6), for the case of biaxial crystals.

2.9 Oscillation Threshold

The threshold of an optical parametric oscillator can be derived from a gain/loss argument, using the gain that was given in equation 2.6 or 2.7. A good theoretical study is given by Brosnan and Byer¹⁵. They derive a value for the threshold of a singly resonant oscillator for the case of Gaussian beams. They use the criteria that threshold is

reached when the oscillator build up time is comparable to the full pump pulse duration with 100 μJ of pump energy converted to signal. This derivation is modified by Ebrahimzadeh et al¹⁶ for the case of a "top hat" spatial intensity pump profile which is more suited to the excimer pump beam. The equation for threshold, J , is then given by

$$J = \frac{2.25\tau}{\kappa l^2} \left\{ \frac{L \cdot \ln(P_n/P_0)}{2\tau c} + 2\alpha l - 0.5 \cdot \ln R + \ln 2 \right\}^2 \quad (2.26)$$

where τ is the pulse length, l is the crystal length, L is the cavity length, κ is defined in equation 2.8, R is the mirror reflectivity and α is the crystal absorption per unit length (αl can be replaced by the Fresnel reflection loss per single pass if the crystals are uncoated, since this will be considerably larger than the absorption of the crystal). The term with $\ln(P_n/P_0)$ is determined by the noise level that the signal builds up from. A value of 100 μJ is taken as the threshold level and this provides a good fit with their experimental results. The first term in the brackets, taken as a whole, treats the build up time as a loss which can be treated like the other losses within the cavity.

This equation is used later to predict the thresholds of OPOs and for comparison with measured values. However, it has been noted^{17,18} that the model can predict thresholds up to twice the measured values. In reference 17, the discrepancy is attributed to the multi-mode OPO pump source. The non-linear coefficient was measured using a single mode pump. The threshold of the OPO may, thus, be lower than predicted using the measured non-linear coefficient. In reference 18, the discrepancy is again blamed on the non-linear coefficient. The thresholds reported in this thesis are consistently lower than the predicted thresholds. As well as a multi-mode pump source, the use of uncoated crystal faces may also lead to a reduction in the measured threshold. The uncoated crystal faces will reflect the pump, signal and idler and will result in essentially double-pass operation or even doubly resonant operation. This will result in a reduction in the thresholds from the purely singly resonant case. Thus the Brosnan and Byer model used here is only for a rough guide to the expected threshold.

2.10 Dispersion of $\chi^{(2)}$

Like the linear susceptibility $\chi^{(1)}$, the second order susceptibility exhibits dispersion. This can be calculated empirically using Miller's rule¹⁹. This expresses the $\chi^{(2)}$ in terms of the linear susceptibility

$$\chi_{ijk}^{(2)}(\omega_p = \omega_s + \omega_i) = \chi_i^{(1)}(\omega_p) \chi_j^{(1)}(\omega_s) \chi_k^{(1)}(\omega_i) \Delta_{ijk}$$

where Δ_{ijk} is Miller's delta. The rule states that all non-zero Δ_{ijk} should be roughly constant. Thus it is possible to write

$$\frac{\chi_{ijk}^{(2)}(\omega_p = \omega_s + \omega_i)}{\chi_i^{(1)}(\omega_p) \chi_j^{(1)}(\omega_s) \chi_k^{(1)}(\omega_i)} = \frac{\chi_{ijk}^{(2)}(\omega_l = \omega_m + \omega_n)}{\chi_i^{(1)}(\omega_l) \chi_j^{(1)}(\omega_m) \chi_k^{(1)}(\omega_n)} \quad (2.27)$$

The value of $d_{ij\mu}$ quoted for a material is generally measured by frequency doubling 1.064 μm radiation. Thus it is necessary to calculate the non-linear coefficient for parametric oscillation using the above equation. This allows the dispersion in $d_{ij\mu}$ to be calculated from the Sellmeier equations of the material. The reported $d_{ij\mu}$ of BBO is 1.8 pm/V but for an OPO pumped at 308 nm and operating near degeneracy, $d_{ij\mu} = 2$ pm/V.

REFERENCES

- 1 'Optical Electronics'. Amnon Yariv. CBS Publishing, New York. p236
- 2 'Interactions between Light Waves in a Non-linear Dielectric'. J. A. Armstrong, N. Bloembergen, J. Ducuing and P. S. Pershan. Phys. Rev. 127, 1918 (1962).
- 3 'Effects of Momentum Mismatch on Parametric Gain'. R. G. Smith. J. Appl. Phys. 41, 4121 (1970).
- 4 'The Principles of Nonlinear Optics'. Y. R. Shen. John Wiley & Sons. New York.
- 5 'Nonlinear Dielectric Polarization in Optical Media'. D. A. Kleinman. Phys. Rev. 126, 1977 (1962).
- 6 'Accurate Calculations of the Optimum Phase Matching Parameters in Three Wave Interactions with Biaxial Nonlinear Optical Crystals'. Jianquan Yao and Weidong Sheng. J. Opt. Soc. Am. B. 9, 891 (1992).
- 7 'Simplified Characterization of Uniaxial and Biaxial Nonlinear Optical Crystals: A Plea for Standardization of Nomenclature and Conventions'. David Roberts. IEEE J. Quantum Electron. 28, 2057 (1992).
- 8 'Physical Properties of Crystals'. J. F. Nye. Oxford Univ. Press, New York. (1957).
- 9 'Tunable UV Generation to 0.2325 μm in LiB_3O_5 '. K. Kato. IEEE J. Quantum Electron. 26, 1173 (1990).
- 10 'Blue Parametric Generation From Temperature Tuned LiB_3O_5 '. Frank Hanson and David Dick. Opt. Lett. 16, 205 (1991).

- 11 'Evaluation of LiB_3O_5 for second harmonic generation of femtosecond optical pulses'. W. S. Pelouch, T. Ukachi, E. S. Wachman and C. L. Tang. *Appl. Phys. Lett.* 57, 111 (1990).
- 12 'Optical Electronics'. Amnon Yariv. CBS Publishing, New York. p11
- 13 'Lasers: a series of advances, vol 4'. R. G. Smith. Eds. A. K. Levine and A. J. DeMaria Pub. Marcel Dekker, New York (1976).p 197
- 14 'Second-Harmonic Generation of Light with Double Refraction'. G. D. Boyd, A. Ashkin, J. M. Dziedzic and D. A. Kleinman. *Phys. Rev.* 137, A1305 (1965).
- 15 'Optical Parametric Oscillation Threshold and Linewidth Studies'. Stephen J. Brosnan and Robert L. Byer. *IEEE J. Quantum Electron.* 15, 415 (1979).
- 16 'An Excimer-Pumped $\beta\text{-BaB}_2\text{O}_4$ Optical Parametric Oscillator Tunable from 354 nm to 2.37 μm '. M. Ebrahimzadeh, A.J. Henderson and M. H. Dunn. *IEEE J. Quantum Electron.* 26, 1241 (1990).
- 17 'Barium Borate Optical Parametric Oscillator'. Y. X. Fan, R. C. Eckardt, Robert L. Byer, Chuangtian Chen, and A. D. Jiang. *IEEE J. Quantum Electron.* 25, 1196 (1989).
- 18 'Visible BaB_2O_4 optical parametric oscillator pumped at 355 nm by a single-axial-mode pulsed source'. Y. X. Fan, R. C. Eckardt, R. L. Byer, J. Nolting and R. Wallenstein. *Appl. Phys. Lett.* 53, 2014 (1988).
- 19 'Lasers: a series of advances, vol 4'.R. G. Smith. Eds. A. K. Levine and A. J. DeMaria Pub.. Marcel Dekker, New York (1976).p 263

Lithium Borate

In this chapter, calculations of phase-matching, effective non-linear coefficients, acceptance angles, acceptance bandwidths and linewidths for LBO are presented, making full use of the equations developed in the previous chapter. The Sellmeier equations for LBO are listed in appendix A.

3.1 General Orientations

The new non-linear material, lithium borate (LiB_3O_5), was first reported by Chen et al¹ in 1989. Lithium borate was 'engineered' in an attempt to improve on barium borate ($\beta\text{-BaB}_2\text{O}_5$), which had been developed a few years previously². In terms of transparency, lithium borate (or LBO as it is known) is very similar to barium borate (BBO). However, in addition to having similar type I and II critical phase-matching geometries to BBO, (offering similar extensive tuning ranges), LBO exhibits type I and II non-critical phase-matching geometries. Further, unlike BBO, it exhibits temperature tuning.

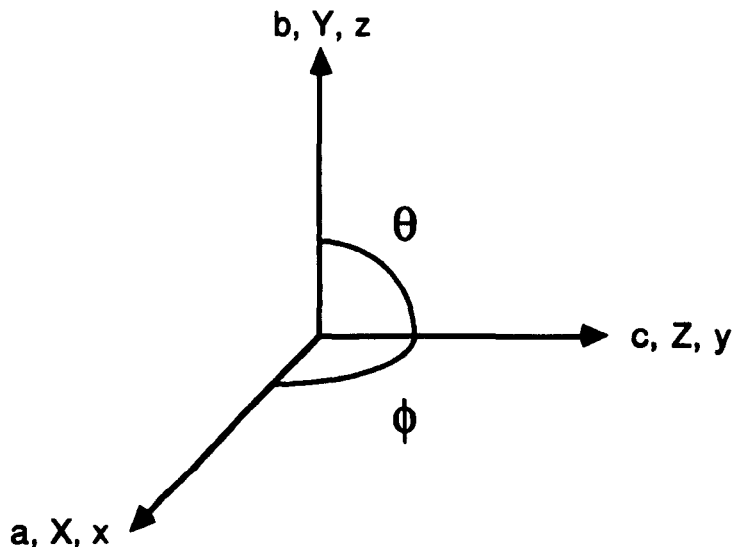


Fig 3.1: The three axis systems (a,b,c), (X,Y,Z) and (x,y,z) and the polar angles θ and ϕ . The angle θ is measured from the z axis to the xy plane and the angle ϕ is measured from x to y.

LBO also differs from BBO in other important aspects, although not always favourably. LBO has improved chemical stability and a higher optical damage threshold than BBO (ref 1). It also has a larger acceptance angle, acceptance bandwidth and a smaller walk-off angle. These plus points are offset by a smaller non-linear coefficient which leads to higher oscillation thresholds in many cases. These differences lead to interesting choices when deciding between the two materials for optical parametric oscillators. Experimental and theoretical evidence shows that the material of choice is strongly dependent on the pump energy available. This is discussed in chapter 7.

LBO is a biaxial crystal belonging to the point group $mm2$. Following the crystallographic convention, the crystal diad is called the c axis and the other two axes, which are orthogonal, are called a and b , such that $|a| < |b|$. The piezoelectric axes X, Y , and Z coincide with the crystallographic axes a, b , and c such that X maps to a , Y to b and Z to c . The axes of the index ellipsoid x, y , and z , which are defined such that the principle refractive indices are ordered $n_z > n_y > n_x$, map to the crystallographic axes as x to a , y to c and z to b . The orientation of the three co-ordinate sets (a,b,c) , (X,Y,Z) and (x,y,z) , in LBO, are shown in figure 3.1. The angles shown in the diagram, θ and ϕ , are measured with respect to the xyz axis set. The angle θ is measured from z to the xy plane and ϕ is measured from x to y in the xy plane. The non-linear coefficients d_{ijk} are determined relative to the XYZ axis set. To calculate the effective non-linear coefficients at a propagation angle, (θ, ϕ) , it is necessary to transpose the XYZ system. Thus the axes XYZ map to xzy , as shown in figure 3.1. The rotation matrices were given in chapter 2.

Chemically, the crystal is very stable and not hygroscopic, unlike BBO. The ease of handling is a great asset of the material. LBO is also highly resistant to optically induced damage with a reported damage threshold of 25 GWcm^{-2} for 10 ns pulses (ref 1). The quality of the material is also in general good with a high optical transmission. The transparency range reported by Chen (ref 1), is 190 nm to 2600 nm, making it an ideal crystal for work in the ultra-violet. For example, we measured the single pass loss to be $\sim 13\%$ in a 15 mm crystal, of which 11.2% is attributable to Fresnel reflection losses at the crystal surfaces. The high reflection losses are due to the high principal refractive indices of the material which are ~ 1.6 . This leads to Fresnel losses at normal incidence of $\sim 5.6\%$ per face. During the period of experimentation, coatings for LBO were available, however the deposition of coatings onto the faces would be likely to reduce the tuning range of the OPO due to the damage threshold/ wavelength range trade-off. For this reason, the faces of the crystal were left uncoated.

3.2 Non-linear Coefficient

LBO has three non-linear coefficients, namely d_{31} , d_{32} , and d_{33} , of which d_{33} is small, ~ 0.2 pm/V, and may be ignored. Initial measurements for the other two coefficients given by Chen et al (ref 1) were $d_{31} = -1.1$ pm/V and $d_{32} = 1.46$ pm/V at $1.064 \mu\text{m}$. More recent measurements³ obtained values of $d_{31} = 1.15$ and $d_{32} = 1.24$ pm/V, again at $1.064 \mu\text{m}$. It should be noted that the subscripts refer to the piezoelectric co-ordinate system, XYZ, and not the xyz system. (See figure 3.1). Writing the two useful coefficients in d_{ijk} notation, they are d_{311} and d_{322} . Translation into the axis system of the index ellipsoid maps d_{311} to d_{yxx} and d_{322} to d_{yzz} . This was confirmed in chapter 2 using a rotation about the X axis. In addition to transforming between the XYZ and xyz axis systems, it is also necessary to take into account the dispersion in d_{ijk} for the particular wavelengths of interaction. This is carried out later for each specific case using Miller's rule (see chapter 2.10 for the definition of Miller's rule).

By inspection, the direction of maximum coupling can be found for both coefficients, assuming that there is no point where the two coefficients add to produce a larger effective non-linear coefficient. (This will be shown to be true later). For d_{yxx} , the maximum will occur when one wave is polarised along the y axis and the other two waves along the x axis. This is only possible for propagation along the z axis. For d_{yzz} , the maximum coupling will occur when one wave is polarised along y and the other two are polarised along z, i.e. propagation along the x-axis. This can be verified theoretically using equation 2.11 with the coefficients d_{yxx} and d_{yzz} . For the case $e \rightarrow o + o$ the effective non-linear coefficient is

$$d_{\text{eff}} = (-\cos\theta\sin\phi\sin\delta + \cos\phi\cos\delta)[d_{yxx}(-\cos\theta\cos\phi\cos\delta + \sin\phi\sin\delta)^2 + d_{yzz}(\sin\theta\cos\delta)^2] \quad (3.1)$$

which is shown graphically in Figure 3.2 for various values of θ and ϕ . Similar expressions can be derived for other phase-matching options. The expressions for d_{eff} can be greatly simplified if propagation is confined to one of the principal planes. Then the polarisation angle, δ , becomes zero and either θ or ϕ can be eliminated.

It is, however, not just sufficient to demonstrate the existence of a significant non-linearity. It is also necessary to determine if phase-matching is possible in such a way as to utilise the non-linear coefficients.

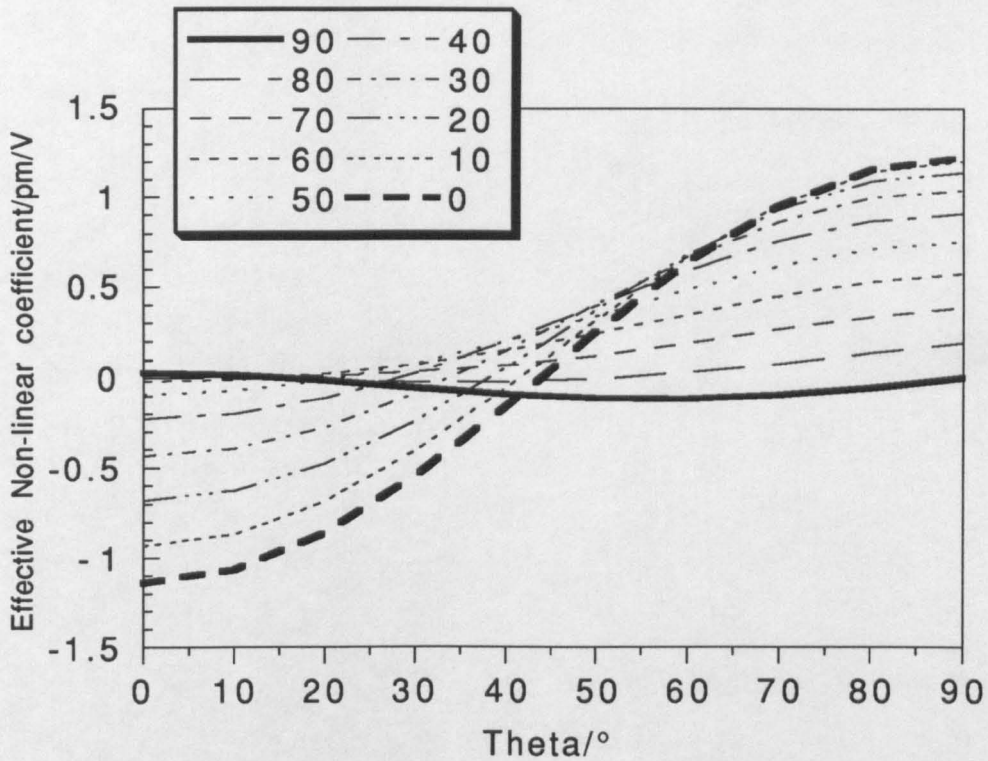


Figure 3.2. $e \rightarrow o+o$ non-linear coefficient in LBO. Each line represents a different angle, ϕ , shown in the key above. The two maxima occur at $\theta=90^\circ$, $\phi=0^\circ$ and at $\theta=0^\circ$, $\phi=0^\circ$. The former corresponds to propagation along the x axis and the later to propagation along the z axis.

3.3 Phase-matching

Since LBO was first reported (ref 1), there have been a number of sets of Sellmeier equations published, each providing progressively improved fits to the measured OPO tuning ranges, particularly in the ultra-violet. The Sellmeier equations that have been reported to date are listed in appendix A. Figure 3.3 provides a comparison between the tuning curves calculated by the different Sellmeier equations and our experimentally measured values. The Sellmeier equations derived by Kato⁴, (k5 in figure 3.3) provide the best fit for our application and are used in theoretical calculations for LBO.

3.3.1 Non-critically Phase-matched LBO

In section 3.2, it was shown that the maximum non-linear coefficients were obtainable along the x and z axes. Equations 2.13 in chapter 2 for the refractive indices of biaxial materials, are used to calculate if phase-matching is possible at a given wavelength along a principal axis or within a given principal plane. The two programs entitled

'yzlbo' and 'xzlbo' in appendix B calculate the angles at which phase-matching ($\omega_p = \omega_s + \omega_i$ and $k_p = k_s + k_i$) will occur for a range of wavelengths, along the z axis and

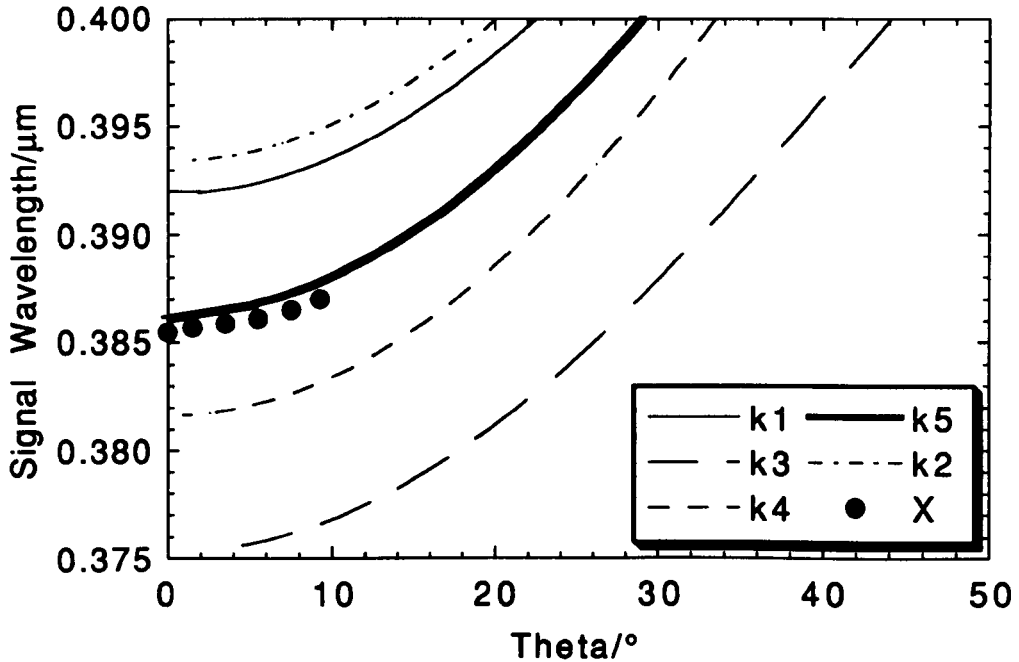


Figure 3.3. A comparison of the predicted tuning ranges of the published Sellmeier equations for LBO. The calculations are for 308 nm pumped LBO in the yz plane. k_1, k_2, k_3, k_4 and k_5 refer to references 1, 5, 6, 7 and 4 respectively. The dots, marked x in the key, represent our experimental data for comparison.

in the neighbouring planes, namely the xz and yz planes. Figures 3.4 and 3.5 show the theoretical tuning ranges of LBO in the xz and yz planes when pumped at 308 nm.

Notice that the phase-matching loci of the xz and yz planes meet along the z axis. This is called "non-critical phase matching" (NCPM) and is especially important because the pump, signal and idler are polarised along the principal axes of the index ellipsoid. The high frequency generated wave is polarised along the y axis and the pump and the other generated wave are polarised along x. In this geometry, the walk-off angle, ρ , and the acceptance angle, $d\theta$, to first order become zero and undefined respectively, (see section 2.7) which has obvious advantages in terms of the maximum crystal length that will be useful. This geometry, with the pump propagating along the z axis, uses the peak value of the non-linear coefficient d_{yxx} and was first demonstrated by Ebrahimzadeh et al⁸ using an excimer pumped system. The results of this system are given in chapter four.

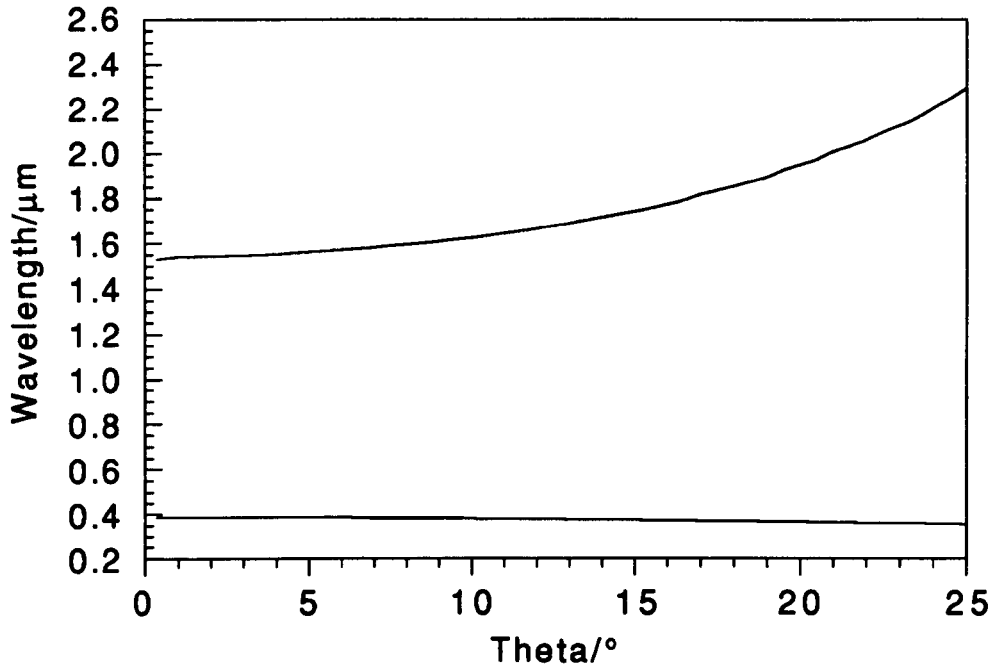


Figure 3.4. The theoretical tuning ranges of LBO when pumped at 308 nm in the xz plane. θ is the angle between the pump beam propagation direction and the z axis.

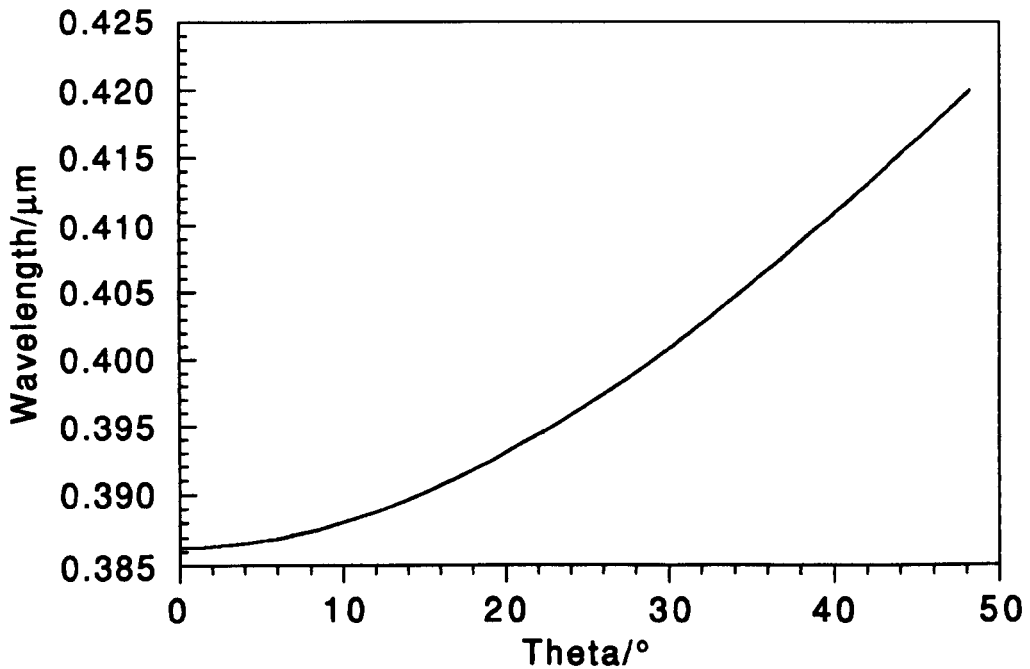


Figure 3.5 The theoretical UV tuning range of LBO when pumped at 308 nm in the yz plane. θ is the angle between the pump beam propagation direction and the z axis. The IR wave has been omitted to show in more detail the tuning range of yz LBO. The IR tuning range extends from 1540 nm to 1155 nm over the angular range 0° to 50° .

The effective non-linear coefficients for the phase-matching loci in the xz and yz planes can be determined by inspection. In the xz plane

$$d_{\text{eff}} = d_{yxx}\cos^2\theta + d_{yzz}\sin^2\theta \quad (3.2)$$

where θ is the angle between the z axis and the xy plane, and in the yz plane

$$d_{\text{eff}} = d_{yxx}\cos\theta \quad (3.3)$$

In the case where $\theta = 0^\circ$, the effective non-linear coefficient $d_{\text{eff}} = d_{yxx}$ as expected. When $\theta = 90^\circ$ in the xz plane, (i.e. propagation along the x axis) the non-linear coefficient $d_{\text{eff}} = d_{yzz}$, however phase-matching is not possible here because the idler wavelength is greater than $2.6 \mu\text{m}$, which is the infrared absorption cut-off in LBO.

The NCPM phase-matched geometry in LBO using propagation along the x axis has been demonstrated by Ebrahimzadeh et al⁹, in an infrared OPO pumped at 532.5 nm . It has also been used in a CW OPO¹⁰ pumped at 514 nm .

3.3.2 The xy Plane

In section 3.2, the non-linear coefficient of a type I interaction, namely $e \rightarrow o+o$, was calculated for various values of θ and ϕ . So far two non-critically phase-matched geometries have been discussed, only one of which can be phase-matched with a 308 nm pump. The tuning range of this device is small and is in the xz and yz planes. The remaining principal plane, the xy plane, contains a type I phase-matching loci. This is calculated by the program 'criticallbo' in appendix B, and is shown graphically in figure 3.6. The tuning range extends from $2.6 \mu\text{m}$, which is the infrared absorption band edge in LBO, down to 350 nm , which is the corresponding wavelength to $2.6 \mu\text{m}$ when an OPO is pumped at 308 nm . To tune over this large range, the crystal must be rotated through an angle of nearly 35° . The non-linear coefficient varies over this range from 0.94 pm/V to 0.58 pm/V . The relation of effective non-linear coefficient with angle can again be determined by inspection to be

$$d_{\text{eff}} = d_{32}\cos\phi \quad (3.4)$$

where ϕ is the angle from the x axis to the y axis. This can be calculated from equation 3.1 by setting $\theta = 90^\circ$ and $\delta = 0^\circ$.

The characteristics of the two OPOs outlined above, namely the type I xy plane OPO and the z axis NCPM OPO, which can be phase-matched when pumping at 308 nm, can now be calculated using the theory set out in chapter 2. This provides useful insight into the expected performance of these devices.

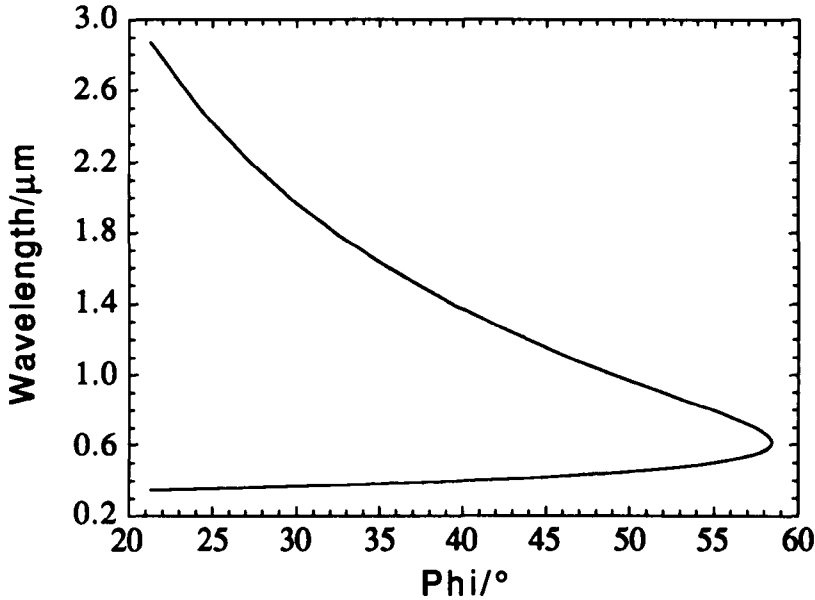


Figure 3.6. Theoretical calculation of the phase matchable tuning range of LBO in the xy plane at 308 nm.

3.4 Acceptance Angle

The Sellmeier equations can be used to calculate acceptance angles and acceptance bandwidths as shown in chapter 2. This gives a guide to the tolerance of the OPO to the beam divergence and linewidth of the pump laser for a given crystal length. The general equation given in chapter 2 for the acceptance angle for a crystal of length, L , was

$$\Delta\theta = \frac{1}{L} \left(\frac{1}{\lambda_p} \frac{dn_p}{d\theta} - \frac{1}{\lambda_p} \frac{n_p}{n_i} \frac{dn_i}{d\theta} \right)^{-1} \quad (3.5)$$

which may be simplified in specific cases as follows.

3.4.1 xy Plane

In rotating the crystal in the xy plane (i.e. about the z axis), any wave polarised along the z axis will see a constant refractive index throughout the tuning range. Thus the signal and idler waves, which are both polarised along z can be thought of in terms of

the uniaxial nomenclature, as ordinary waves. The refractive index of the pump wave, polarised in the xy plane, will be dependent on the angle of propagation and can be thought of as an extraordinary wave. Changing the general variable θ to ϕ , in equation 3.4, since propagation is in the xy plane, and noting that $dn/d\phi$ will be zero since the idler is an ordinary wave, we can write the acceptance angle

$$\Delta\phi = \frac{1}{L} \left(\frac{1}{\lambda_p} \frac{dn_p}{d\phi} \right)^{-1} \quad (3.6)$$

The assumptions made above are not entirely true and the acceptance angle has two components associated with any propagation direction, namely $\Delta\phi$ and $\Delta\theta$. The justification for ignoring the other component of the acceptance angle is that it will be very large and therefore not a constraint on the system. This is the case because $dn/d\theta$ is at its smallest near a principal axis.

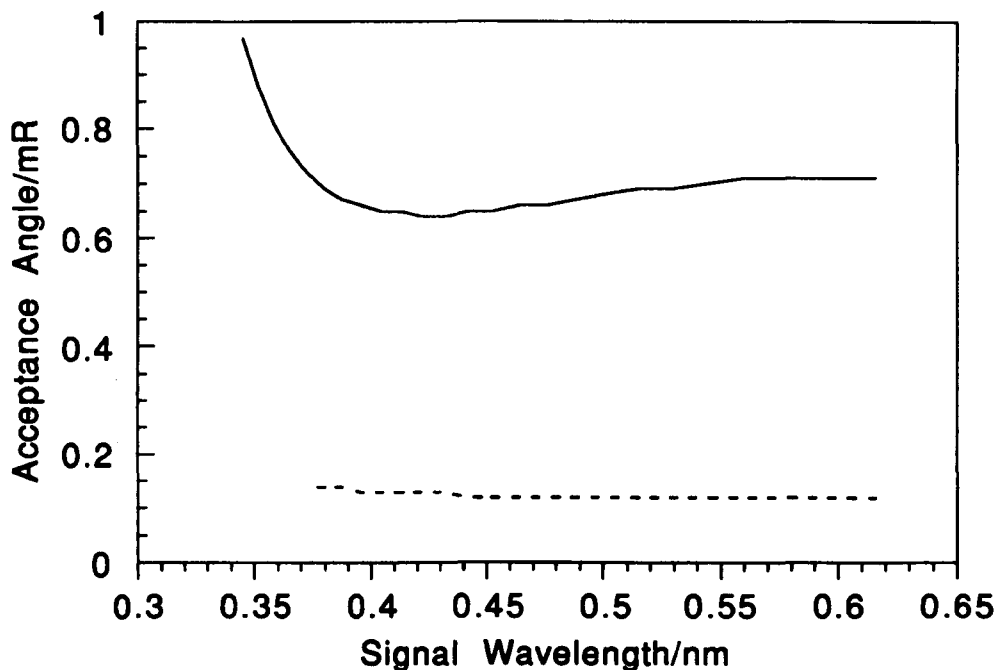


Figure 3.7 The acceptance full angle of LBO (solid line) in the xy plane for a 15 mm crystal. The dotted line is the acceptance angle in type I BBO, again for a 15 mm crystal.

The acceptance angle calculated in eqn 3.6 for a 308 nm pump is shown in figure 3.7. The minimum is at 40° . Referring to fig 3.6 it will be noticed that this is in the middle of the possible tuning range. The acceptance angle is calculated for a crystal of 15 mm. At this length, the acceptance angle equals the beam divergence of the pump beam

when the beam size is $5 \times 2.5 \text{ mm}^2$. This effectively limits the useful length of crystal that may be employed.

3.4.2 xz Plane

Again the assumption that the wave polarisations may be treated as ordinary and extraordinary waves providing tuning is confined to the xz plane, is made. The phase-matching criterion in this plane is $e \rightarrow o + e$ and so the form of equation 3.5 will depend on whether the ordinary or extraordinary wave is resonant. The ordinary wave is the short wavelength. When the ordinary wave is resonant, the pump and idler are both extraordinary waves and so both $dn_p/d\theta$ and $dn_i/d\theta$ are included. When the extraordinary wave is resonant then the pump wave is extraordinary and the idler wave is not. In this case only $dn_p/d\theta$ is included. The result is that when the UV wave is resonant, the acceptance angle is larger than when the IR wave is resonant. The two cases are illustrated in figure 3.8

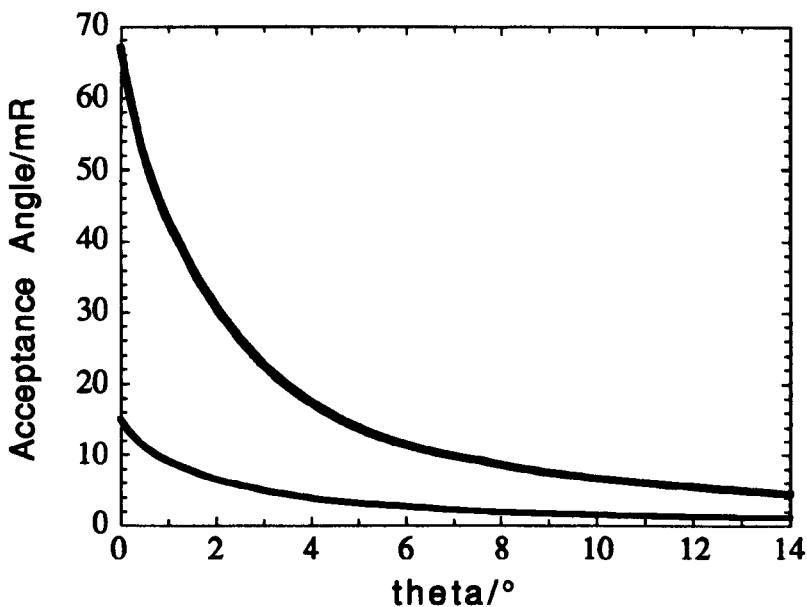


Figure 3.8 The full acceptance angle of a UV resonant (thick line) and IR resonant (thin line) LBO OPO in the xz plane. The crystal length is 16 mm.

The acceptance angle rises sharply near the principal axis and becomes undefined at $\theta = 0^\circ$. The value shown in figure 3.8 is calculated using a second order analysis. This leads to a value of 67 mR for the UV resonant cavity and 15 mR for the IR resonant cavity. Since the acceptance angle is large, it does not impose a practical limit on the maximum crystal length that can be used.

3.4.3 yz Plane

In the yz plane, the phase-matching criterion is $o \rightarrow e+o$. Thus in the case where the extraordinary wave is resonant, the acceptance angle becomes undefined as both $dn_p/d\theta$ and $dn_i/d\theta$ are zero. In this case, a second order analysis using $d^2n_p/d\theta$ and $d^2n_i/d\theta$ is required. This leads to $\Delta\theta \sim 15\text{mR}$ at NCPM.

When the extraordinary wave is the idler, the acceptance angle is as shown in figure 3.9.

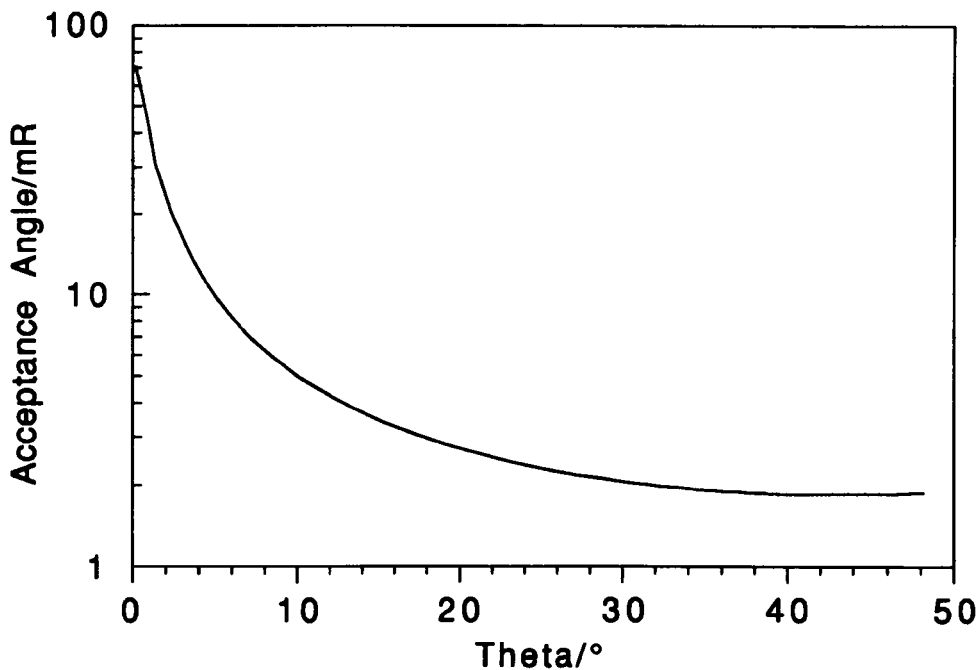


Figure 3.9. The full acceptance angle of a 16 mm yzLBO crystal with the infrared wave resonant

Clearly the acceptance angles associated with the NCPM geometry are large when compared to the divergence of the pump beam which is, for a $4 \times 2 \text{ mm}^2$ beam, $\sim 1 \text{ mR}$. In the absence of walk-off, that is at $\theta=0^\circ$, the maximum crystal length will be set by the crystal growth technique or by financial constraints.

3.5 Acceptance Bandwidth

The derivation of the equation of acceptance bandwidth was given in chapter two and is reproduced here for completeness

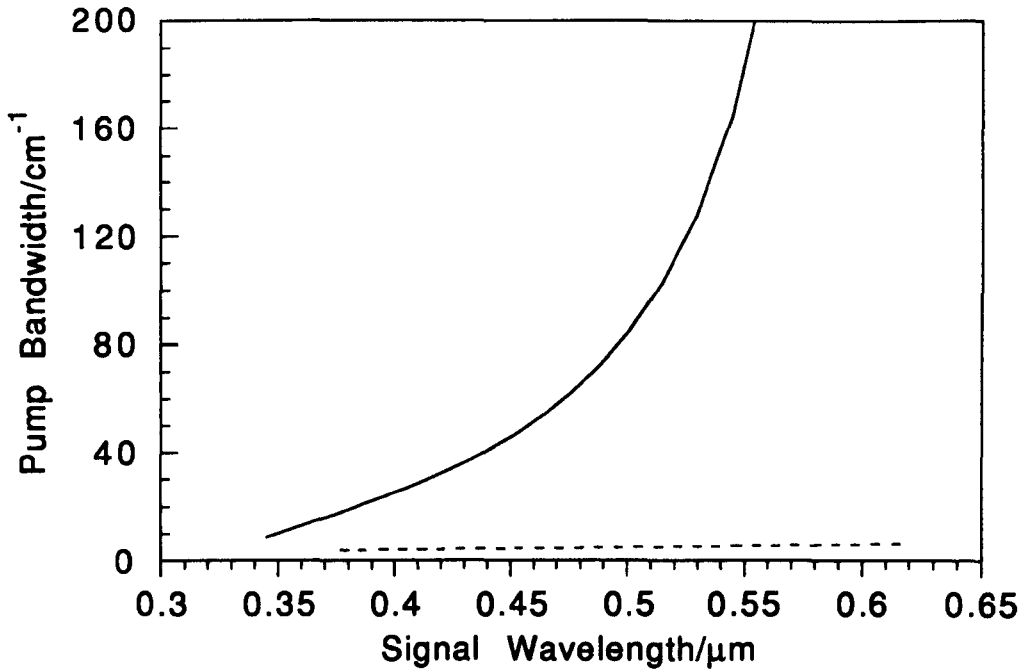


Figure 3.10(a). The acceptance bandwidth across the tuning range of a 15 mm xyLBO crystal. The dotted line represents the acceptance bandwidth in BBO.

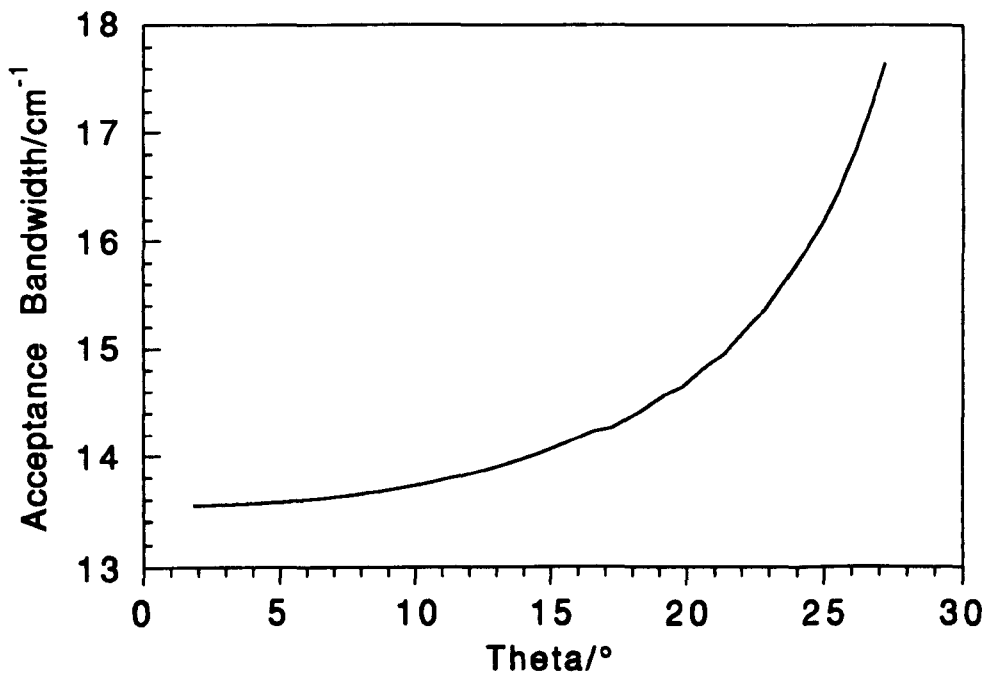


Figure 3.10(b). The acceptance bandwidth vs. angle of a 16 mm xz LBO crystal. Theta is the angle between the propagation direction and the z axis.

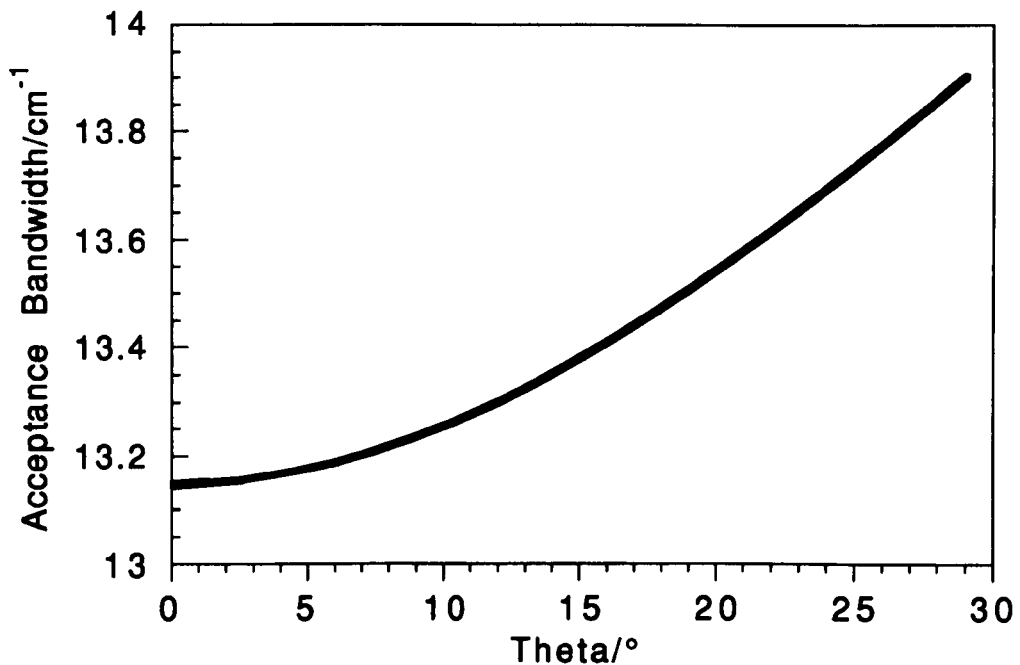


Figure 3.10(c). The acceptance bandwidth of a 16 mm yz LBO crystal. Theta is the angle between the propagation direction and the z axis.

$$\Delta\nu = \frac{1}{L} \left[(n_p - n_i) - \lambda_p \frac{dn_p}{d\lambda_p} + \lambda_i \frac{dn_i}{d\lambda_i} \right]^{-1} \quad (3.7)$$

The differential can be calculated by differentiation of the Sellmeier equations and the graphs of the acceptance bandwidths for the three planes are given in figure 3.10. The acceptance bandwidth is well above the linewidth of the line-narrowed excimer laser. However, it would not be possible to pump the OPO using the excimer without any line-narrowing elements.

3.6 Signal Linewidth

3.6.1 xy Plane

The inherent signal linewidth, as derived in section 2.6, can be calculated from the Sellmeier equations (see figure 3.3 and Appendix A). Figure 3.11 shows the inherent linewidth expected from an LBO OPO operating in the broadly tunable xy plane. The range of linewidths is very large indeed as would be expected from the different tuning rates across the accessible wavelength range. The largest linewidths occur at

degeneracy where the signal and idler wavelengths are degenerate and the tuning rate is fastest. Close to degeneracy, the linewidth is ~ 7 nm. Further from degeneracy, the linewidth falls sharply as the tuning rate steadily slows. The need for linewidth control in such a device is obvious and these techniques are discussed in chapter 8. Comparison of the linewidth of LBO, figure 3.11, with that of BBO, fig 2.5 shows that the type I LBO geometry has a narrower linewidth at a given wavelength.

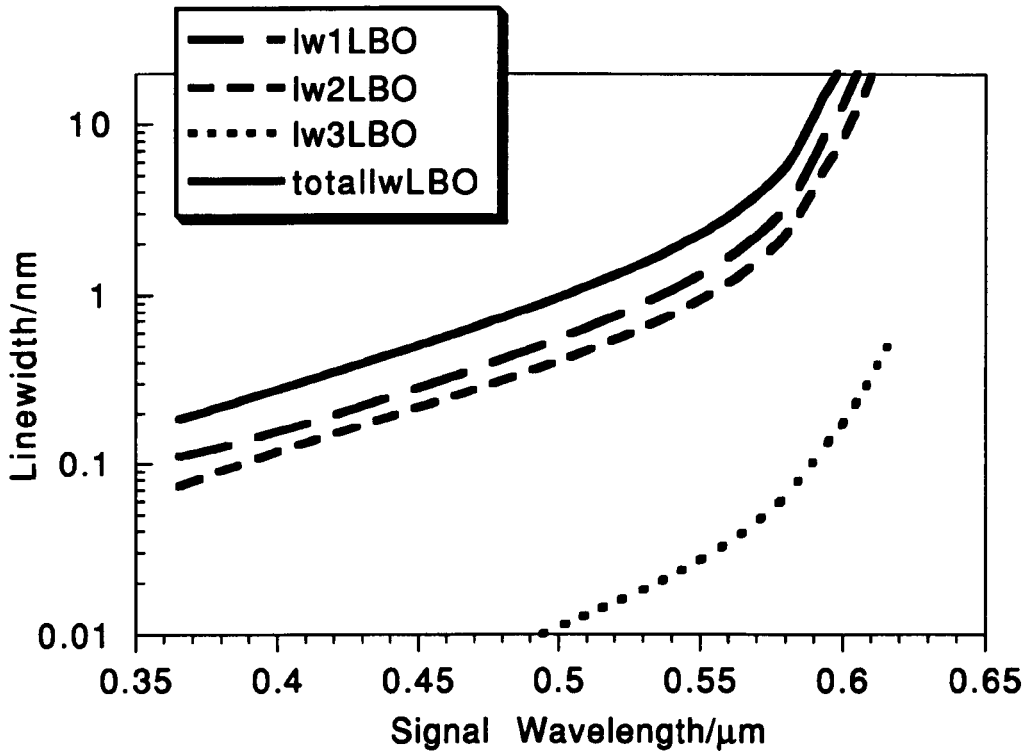


Figure 3.11. The linewidth of the signal wave from LBO in the xy plane. KEY:- $lw1LBO$ = linewidth contribution from the phase-matching bandwidth. $lw2LBO$ = linewidth contribution from pump divergence. $lw3LBO$ = linewidth contribution from pump bandwidth. Total $lwLBO$ = the sum of the three contributions.

3.6.2 NCPM Geometry

The linewidth of the NCPM OPO can be calculated in the same way. Here, due to the slower rate of tuning, the inherent linewidth turns out to be very much narrower ~ 0.09 nm (see figure 3.12). For a typical OPO cavity (20 mm long), this linewidth corresponds to approximately 20 axial cavity modes.

3.7 Poynting Vector Walk-off

3.7.1 xy Plane

In the xy plane, the maximum walk-off angle, which occurs at 45° , is 1.1 mR (see figure 3.13). This corresponds to the minimum acceptance angle in this plane. (See the

discussion on the equivalence of the walk-off angle and the acceptance angle in chapter 2.)

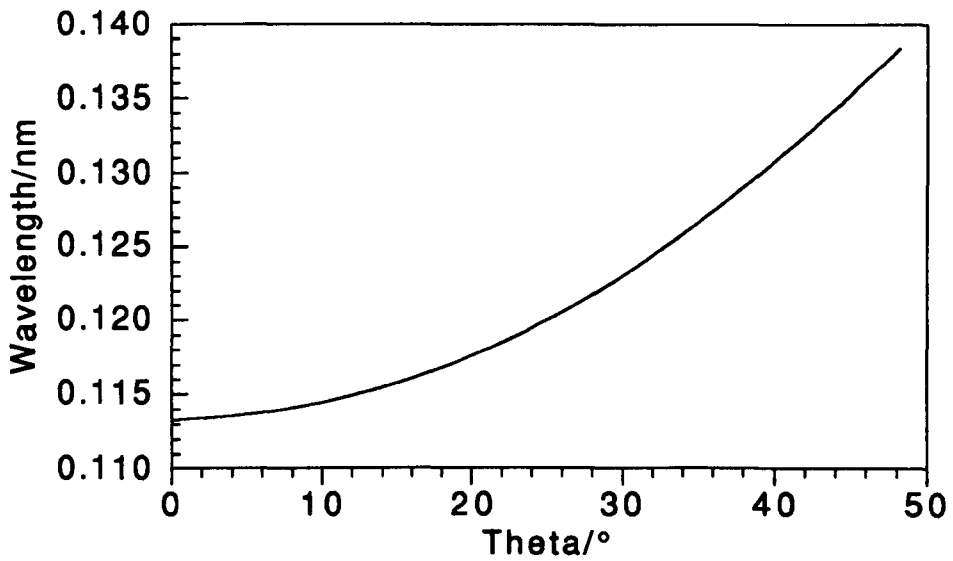


Figure 3.12. The linewidth of the signal wave from yz LBO, showing the linewidth at the NCPM point (385 nm). The linewidth is predominantly due to dV_1 , the other two, dV_2 and dV_3 , being much smaller.

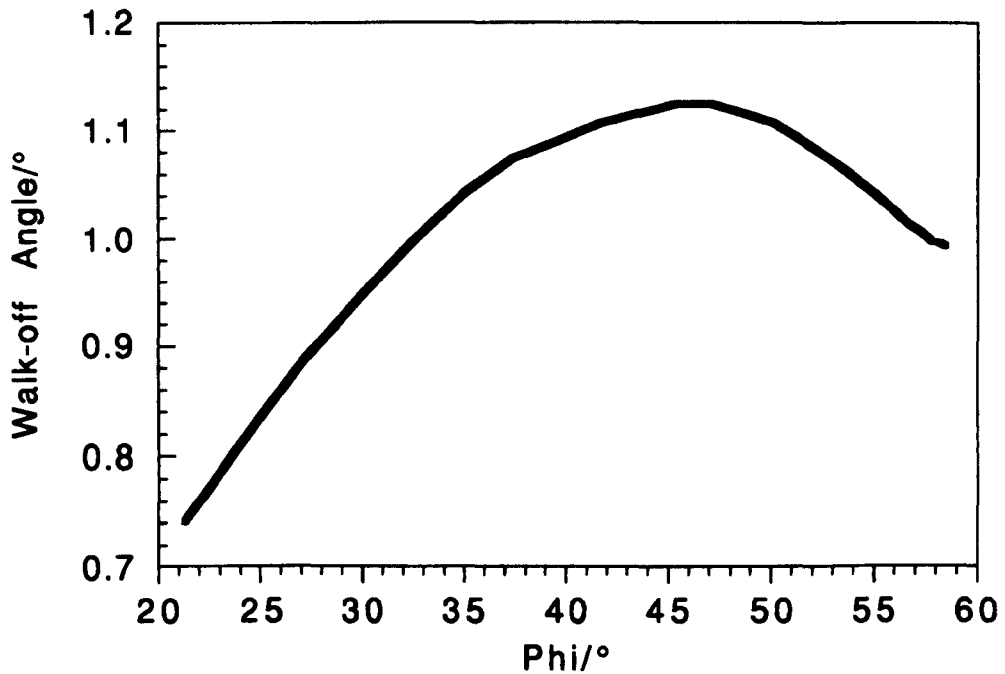


Figure 3.13. Poynting vector walk-off angle, ρ , in the xy plane of a 15 mm LBO crystal.

3.7.2 NCPM Geometry

As can be seen from equation 2.22, the walk-off angle, ρ , falls to zero when the pump beam is propagated along one of the principal axes of the index ellipsoid. A device that operates in this kind of geometry has the advantage that the interaction between the three waves is not diminished by the extraordinary wave (or waves) "walking-off" from the ordinary waves (or wave). In LBO, the xz and yz planes are degenerate when the pump is propagated along the z axis. In the case where the walk-off is non-zero, the maximum useful crystal length is given by $l = w/\tan\rho$, where w is the beam width. Beyond this length, no further interaction between the three waves takes place. Clearly there will be a loss in interaction between the three waves well before they become completely separated. However, the effect that this will have on the threshold and efficiency of the device is hard to estimate quantitatively. In chapter 7, an empirical relation between the increase in threshold and the beam overlap is demonstrated using experimental data. Figure 3.14 shows the variation in walk-off angle across the yz plane.

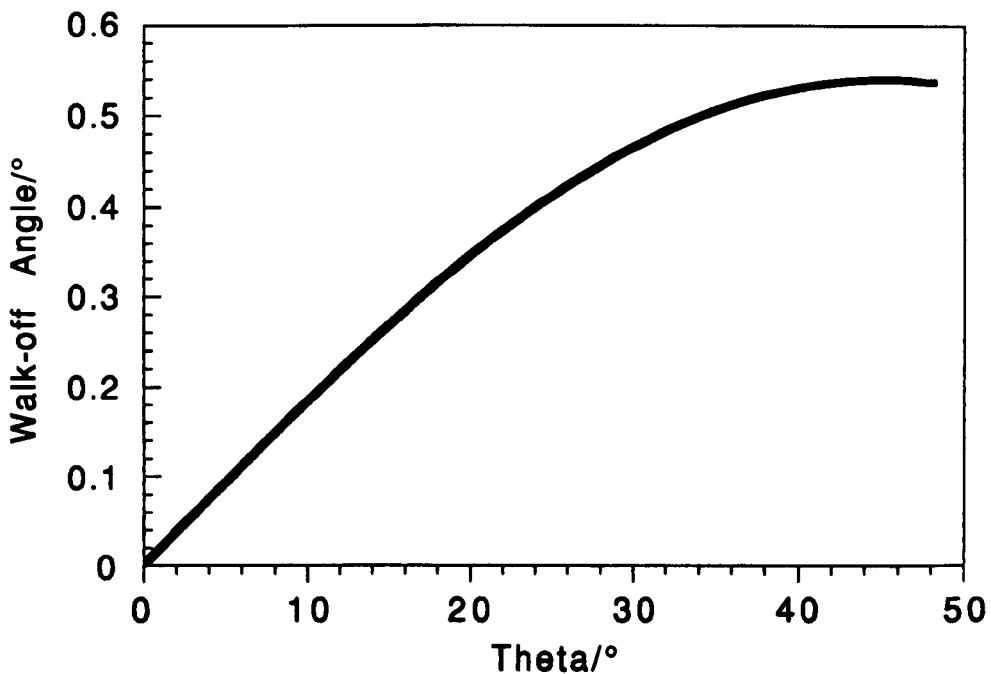


Figure 3.14. Variation in walk-off angle, ρ , in the yz plane.

3.8 Selection of Suitable Crystal Cuts

Using the information laid out in the previous sections, a reasonable estimate of the performance of any given cut can be made. The NCPM geometry is of particular

interest due to the absence of walk-off and the large acceptance angles and bandwidths. It also makes full use of the available non-linear coefficient. It is also worth noting that LBO can be temperature tuned, which is of great interest in an NCPM geometry. Temperatures exceeding 300°C ¹¹ can safely be accessed without fear of damage. Due to the absence of walk-off in this geometry, the selection of crystal length must be determined by factors such as the acceptance angle and acceptance bandwidth. On examination even these parameters permit long crystal lengths, far in excess of anything that can be grown at present. So finally, it is limitations in the crystal growth techniques that constrain the maximum crystal length to $\sim 16\text{ mm}$ ¹².

The other phase-matching option is the xy plane, type I device, which is of interest because of its broad tuning range. To access as much of the tuning range as possible the crystal should be cut at an angle in the middle of the range. For this reason, the crystal used to carry out this work, was cut at $\phi = 40^{\circ}$. Theoretically this restricts the useful crystal length to approximately 15 mm due to the acceptance angle. As will be explained in chapter 7, the acceptance angle is not as restrictive in practice as in theory.

The experimental results on the NCPM and xy geometries are given in the next two chapters.

REFERENCES

- 1 'New nonlinear-optical crystal: LiB_3O_5 '. Chuangtian Chen, Yicheng Wu, Aidong Jiang, Bochang Wu, Guiming You, Rukang Li and Shujie Lin. *J. Opt. Soc. Am. B* 6, 616 (1989).
- 2 ' β - BaB_2O_4 optical parametric oscillator'. Y. X. Fan, R. C. Eckardt, R. L. Byer. C. Chen and A. D. Jiang. Conference on Lasers and Electro-optics (1986). Postdeadline paper ThT4.
- 3 'Temperature-tuned noncritically phase-matched frequency conversion in LiB_3O_5 crystal'. J. T. Lin, J. L. Montgomery and K. Kato. *Opt. Comm.* 80, 159 (1990).
- 4 'Tunable UV Generation to $0.2325\ \mu\text{m}$ in LiB_3O_5 '. K. Kato. *IEEE J. Quantum Electron.* 26, 1173 (1990).
- 5 'Highly Efficient Ultraviolet Generation at 355 nm in LiB_3O_5 '. Baichang Wu, Nong Chen, Chuangtian Chen, Daoqun Deng and Zuyan Xu. *Opt. Lett.* 14, 1080 (1989).
- 6 'Blue parametric generation from temperature-tuned LiB_3O_5 '. Frank Hanson and David Dick. *Opt. Lett.* 16, 205 (1991).

- 7 'Optical parametric amplification in a lithium triborate crystal tunable from 0.65 μm to 2.5 μm '. Shujie Lin, J. Y. Huang, Jiwu Ling, Chuangtian Chen and Y. R. Shen. *Appl. Phys. Lett.* 59, 2805 (1991).
- 8 M. Ebrahimzadeh, G. Robertson, M. H. Dunn and A. J. Henderson. Conference on Lasers and Electro-optics (1990) paper CPD26.
- 9 'Singly resonant all-solid-state mode-locked LiB_3O_5 optical parametric oscillator tunable from 652 nm to 2.65 μm '. M. Ebrahimzadeh, G. J. Hall and A. I. Ferguson. *Opt. Lett.* 17, 652 (1992).
- 10 'Continuous-wave parametric oscillation in lithium triborate'. Finlay G. Colville, Angus J. Henderson, Miles J. Padgett, Jun Zhang and Malcolm H. Dunn. *Opt. Lett.* 18, 205 (1993).
- 11 'Generation of tunable coherent vacuum ultraviolet radiation in LiB_3O_5 crystal'. Baichang Wu, Fali Xie, Chuangtian Chen, Daoqun Deng and Zuyan Xu. *Opt. Comm.* 88, 451 (1992).
- 12 C. Chen. private communication. (1990) via Photox Optical Systems P.O. Box 274, Headington, Oxford OX3 OBJ.

Non-critically Phase-matched LBO

In this chapter, the experimental results for a non-critically phase-matched type II lithium borate (LBO) optical parametric oscillator are reported. The work follows on from the theoretical predictions of tuning ranges, efficiencies and linewidths made in the previous chapter. Experimental results for a crystal cut for propagation in the yz plane (type II critically phase-matched) are also presented. Initially, a description of the experimental set-up is given.

4.1 Introduction

In the previous chapter, the possible phase-matching loci of LBO were calculated and the expected characteristics of the resulting OPOs were presented. Following these theoretical predictions, experiments were undertaken on a number of crystals of LBO. This chapter deals with three of these crystals, two cut in the non-critically phase-matched geometry (NCPM), first reported by us¹, where the pump beam propagates along the z-axis, and a third crystal cut for propagation in the yz plane. The NCPM geometry is merely the special case of $\theta = 0^\circ$ in the yz plane and the majority of this chapter deals with this special case. These results are presented immediately after a description of the pump lasers used for the experimental work.

4.2 Pump Lasers

At this point it is convenient to give details of the two pump lasers used in the experiments in this thesis. Both were XeCl excimer lasers operating at 308 nm, one with a peak output energy of ~20 mJ per pulse, the other with a peak output energy of ~100 mJ per pulse. The 20 mJ laser was a 'home-built' laser constructed specifically to pump BBO and LBO OPOs. Full details of the construction of this device can be found in reference 2.

The design of the 20 mJ laser is shown in figure 4.1. This laser operated on a master/slave oscillator principle, with the master oscillator controlling the linewidth and the slave oscillator supplying the high energy pulses. The linewidth in the master oscillator was controlled by two etalons, of free spectral range 6.7 cm^{-1} and 40 cm^{-1} , both with finesses of 25. The resonator was a simple plane-plane mirror design and the

gas chamber had windows at Brewster's angle to control the polarisation of the beam. An aperture was placed within the master oscillator to control the transverse mode structure.

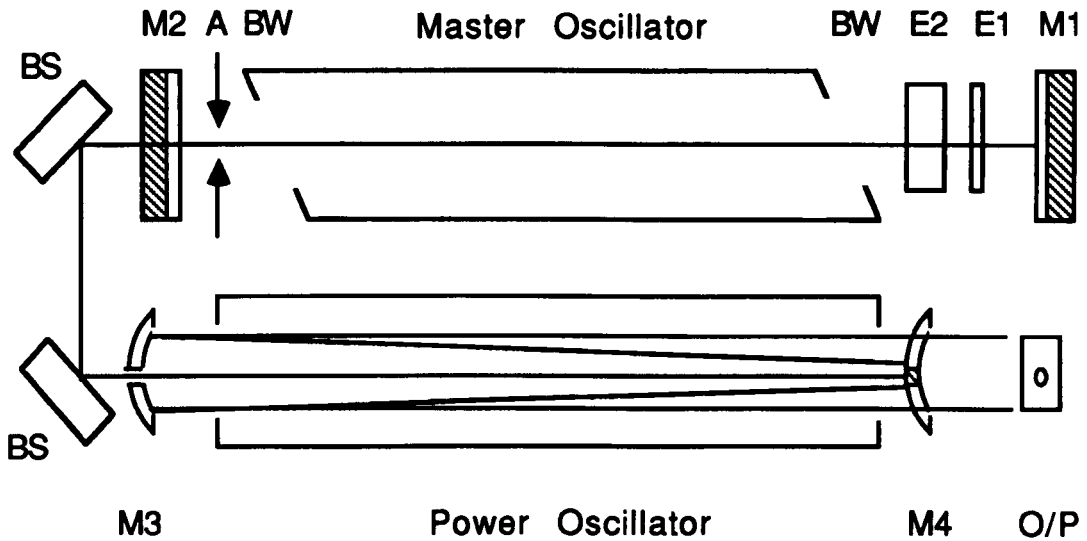


Figure 4.1. The 20 mJ laser. M1 to M4 are laser mirrors. BS are beam steering mirrors. BW are Brewster angled windows. E1 and E2 are etalons. A is an aperture. O/P is the profile of the beam output.

The beam from the master oscillator is fed into the power or slave oscillator via two beam steering mirrors and a hole in the rear mirror of the cavity. The power oscillator cavity is a confocal unstable resonator of length 80 cm. The radius of curvature of M3 and M4 are 180 cm and 20 cm respectively. The beam divergence is $60 \mu\text{R}$ in a $2 \times 1 \text{ cm}^2$ beam and the linewidth is 0.2 cm^{-1} . The pulse duration of the laser is 10 ns (FWHM) giving peak powers of 2 MW. The output was vertically polarised to $>95\%$. The control over the bandwidth, polarisation and spatial quality is necessary for pumping OPOs, as was shown in the preceding two chapters. The maximum permissible bandwidth of the laser is determined by the acceptance bandwidth of the OPO. For example, the minimum acceptance bandwidth in LBO, of 13.5 cm^{-1} , occurs in the yz plane at 0° . Clearly the bandwidth of the laser is significantly less than this value.

Electrically, both laser heads were triggered by a single spark gap, the delay between the two heads being controlled by the pin separation within the laser head and by the relative gas pressures of the two laser heads.

The laser used in the later experiments was a commercially available Lambda Physik EMG150. Typically, it delivered 100 mJ pulses of 17 ns (FWHM) duration. The design

of the laser was very similar to the 20 mJ laser described above, and is shown in figure 4.2. The main differences between this laser and the 20 mJ laser were that the master oscillator was controlled by a diffraction grating and three beam expanding prisms instead of etalons, and the laser was triggered by a thyatron instead of a spark gap. Repetition rates of up to 10 Hz were obtainable from this device. The beam divergence and linewidth were 0.2 mR and 0.3 cm^{-1} respectively and the beam size was again $2 \times 1 \text{ cm}^2$. The addition of two polarising plates, one between the two oscillators and a second after the power oscillator, was required to control the polarisation of the laser, which was $\sim 95\%$. A half wave plate was used to rotate the polarisation from the horizontal to the vertical because this made rotation of the crystal simpler.

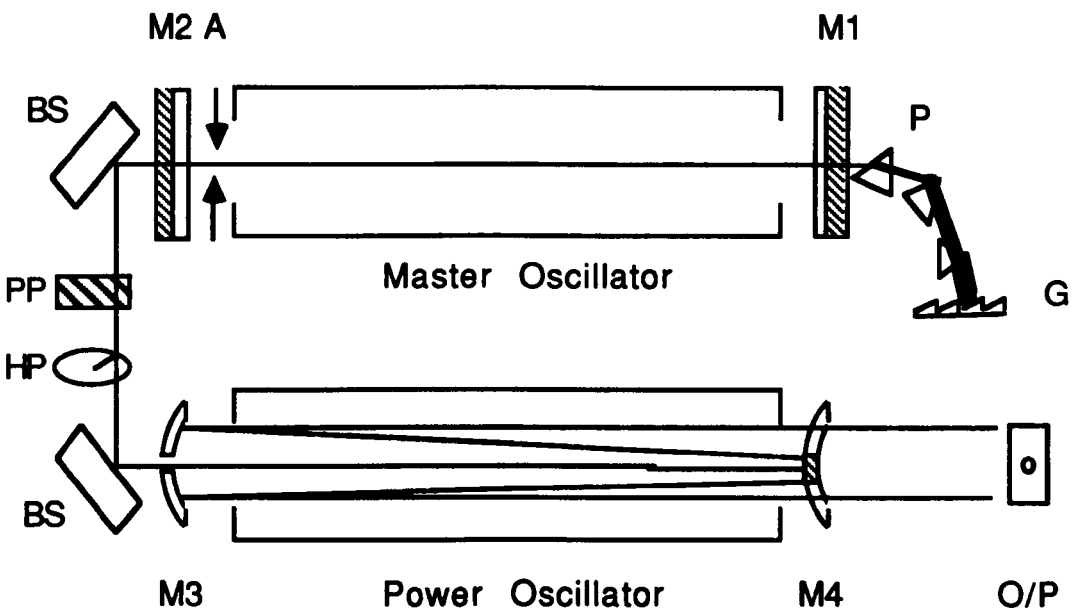


Figure 4.2. The 150 mJ laser. M1 to M4 are laser mirrors. BS are beam steering plates. G is a diffraction grating. P is a set of three prisms. A is an aperture. PP is a polarising plate. HP is a half-wave plate. O/P is the profile of the output beam.

4.3 Experimental Set-up

4.3.1 Cavity Design

The design of the OPO cavity is shown in figure 4.3. From the theoretical tuning range, calculated in the last chapter, the non-critically phase-matched output is expected to be at 386.5 nm and 1516 nm. The plane parallel mirrors selected for the initial experiments were coated for 95% reflectivity between 370 nm and 420 nm and were designed to be highly transmitting at the pump wavelength and also around $1.5 \mu\text{m}$. The OPO was thus operated as a singly resonant device with the shorter wavelength resonant. The longer wavelength, between 1.4 and $1.6 \mu\text{m}$, could be resonated instead by using a pair of

mirrors that had a reflectivity of 95% over this range. A comparison between the infrared and ultra-violet resonant cavities is made in section 4.10.

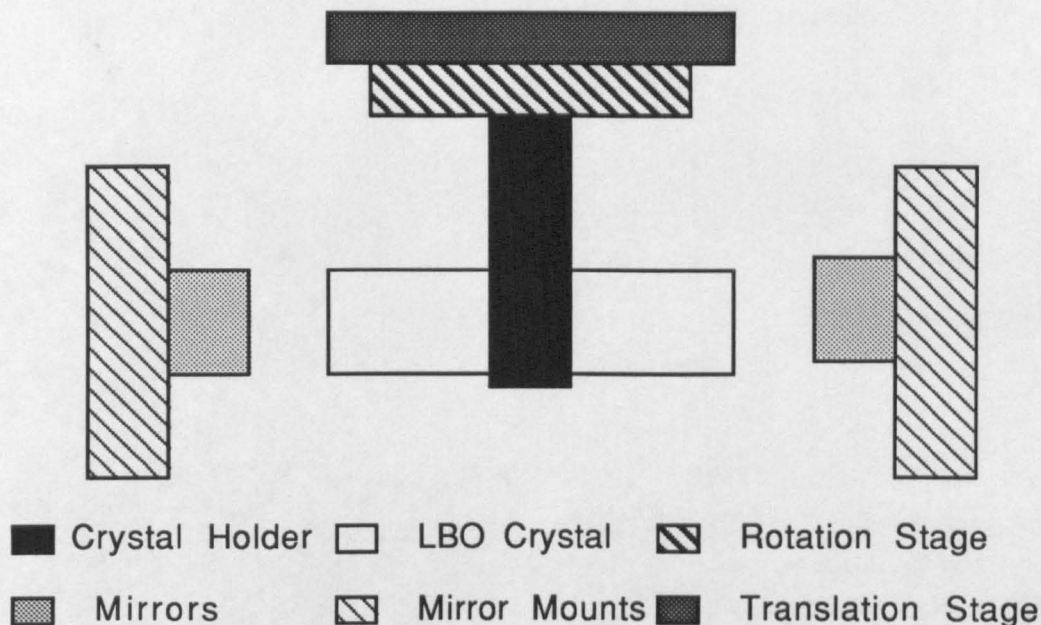


Figure 4.3. The OPO cavity.

Two LBO crystals were used during the course of experimentation; one was 9 mm long, the second was 16 mm long. The initial experiments were carried out on the 9 mm crystal. Both crystals were cut along the z axis allowing non-critically phase-matched operation at normal incidence. The crystals had polished, but uncoated, end faces and were mounted on a translation/ rotation stage to facilitate alignment of the crystal with the pump beam.

4.3.2 Beam Compression Optics

The pump beam, from the 20 mJ laser, entered the OPO cavity via beam compression optics, consisting of a 2 m converging lens and a -25 cm diverging lens, mounted on a rail system. This permitted continuous variation of the lens separation to change the position of the focus of the system. Ideally, the pump beam would have been collimated to keep the beam divergence within the crystal to a minimum. However, all the experiments in this chapter were made using the 20 mJ laser, and to reach the pump powers required, it was necessary to focus the pump beam into the crystal. By varying the position of the diverging lens it was possible to vary the pump energy density within the crystal by changing the beam size. The beam size could then be measured either directly using burn paper or by inferring the spot size from the separation of the

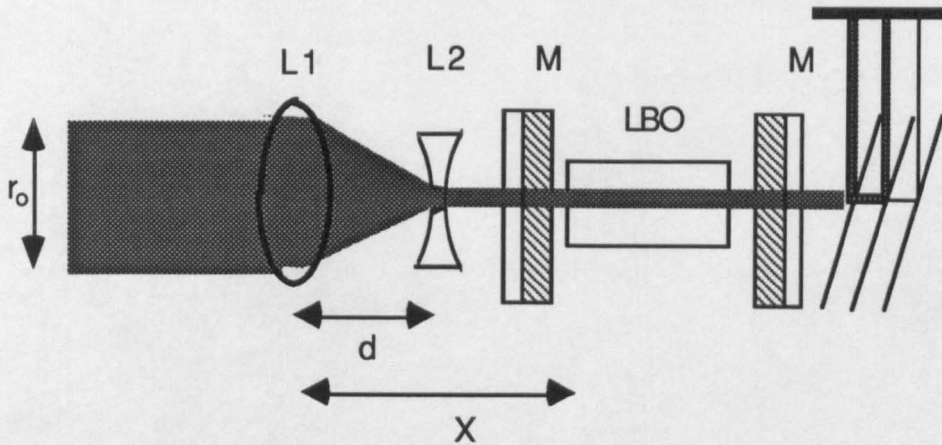


Figure 4.4 System Layout, showing the two lenses separated by a distance, d . KEY:– M 's are mirrors, $L1$ and $L2$ form the beam compressor. X , d and r_0 are dimensions in equation 4.1. The three plates on the right are for deflecting the pump beam.

two lenses in the beam compressor. By inference, it can be calculated by considering the ABCD matrices of the beam compressor. Figure 4.4 shows the set up of the beam compressor, where r_0 is the pump beam diameter at the laser (20 mm x 10 mm), r_1 is the beam diameter at the OPO, d is the distance between the converging lens and the diverging lens and X is the distance between the converging lens and the OPO. The beam size at the OPO is given by

$$r_1 = \left(r_0 - \frac{dr_0}{f_1} \right) - (X-d) \left[\frac{1}{f_2} \left(r_0 - \frac{dr_0}{f_1} \right) + \frac{r_0}{f_1} \right] \quad (4.1)$$

and the divergence, r' , is

$$r' = -\frac{1}{f_2} \left[r_0 - \frac{dr_0}{f_1} \right] - \frac{r_0}{f_1} \quad (4.2)$$

where $f_1=2$ m and $f_2= -25$ cm are the focal lengths of the converging and diverging lenses respectively and $X=207.5$ cm is the distance between the fixed first lens and the OPO. Figure 4.5 shows the variation of beam size with lens separation and the associated change in beam divergence calculated at the crystal. The divergence due to focusing the pump beam clearly has implications in terms of the acceptance angle of the OPO. The assumption made in the following experiments is that the added beam divergence due to focusing is sufficiently less than the acceptance angle of the NCPM device that it may be ignored. The acceptance angle of NCPM LBO was shown to be ~ 65 mR (see figure 3.9).

Experimentally, the beam size was measured using burn paper. The burn mark caused by the beam was measured using a travelling microscope. The agreement between this method and the one described above was good.

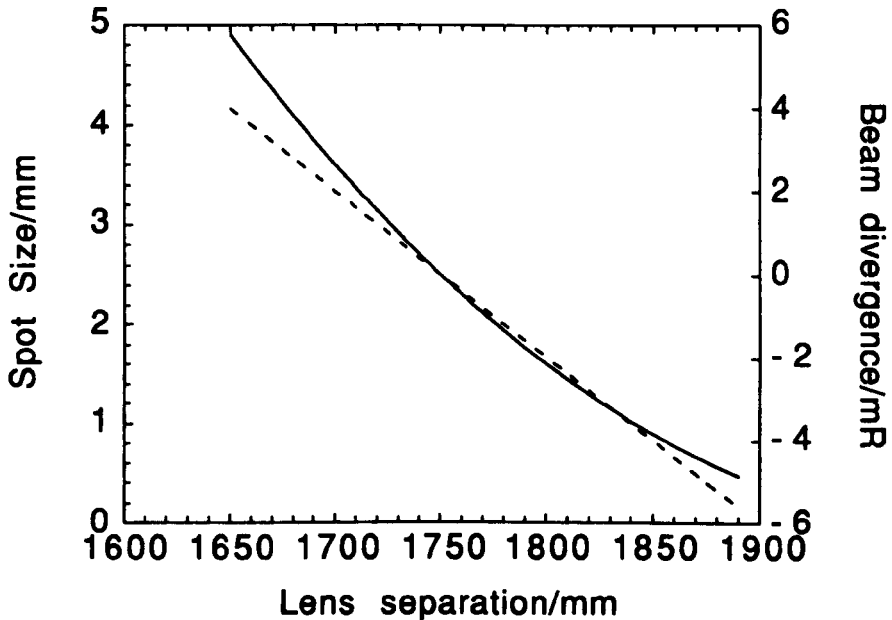


Figure 4.5 The variation of the pump spot size at the crystal face with change in the separation of the two lenses, d , is shown by the dotted line. The beam divergence is shown as the solid line. Note that the acceptance angle of NCPM LBO is 65 mR.

4.3.3 OPO Alignment

The OPO was aligned using a HeNe laser, which was used as a CW spatial reference beam. Two pin holes were placed in the excimer beam, one just after the converging lens and the other just after the diverging lens. The hole in the centre of the excimer beam was used to aid alignment by centring it on the pinholes. The HeNe beam was then passed through the pinholes, ensuring that it was collinear with the pump beam, and into the OPO cavity. The cavity mirrors were partially reflecting at 632 nm and the back reflections from the mirror were sent through the pin holes. This provided coarse alignment of the mirrors. Finally, the interference fringes formed by the two cavity mirrors were centred onto the pinhole thus completing the alignment of the cavity. The crystal could also be aligned so that its faces were normal to the pump beam direction by using the back reflections of the HeNe beam from the faces. This assured non-critically phase-matched operation, i.e. at $\theta = 0^\circ$ (assuming of course that the crystal faces are polished perpendicular to the z axis. This was confirmed during experimentation.

4.4 9 mm OPO Crystal

4.4.1 Tuning Range

The initial experiments were carried out using the 9 mm LBO crystal. The crystal was cut for propagation along the z axis, with an aperture of $5 \times 5 \text{ mm}^2$. As mentioned in the last chapter, the NCPM geometry is in fact a common point between the xz and yz planes. Experiments were therefore not just confined to propagation along the z axis but extended out into the two adjacent principal planes. The OPO was set up using the 370 nm to 420 nm mirrors to resonate the lower of the two expected wavelengths. (The other case is dealt with later). The OPO cavity was 15 mm long. Phase-matching in the xz and yz planes requires that the pump is polarised along the x axis. The pump beam entered the crystal with its polarisation vertical so the crystal was mounted with the x axis vertical. Angle tuning could be achieved in both principal planes by rotation about either a horizontal or vertical axis. As an initial step to measuring the tuning range, the NCPM wavelengths were measured using a monochromator (Rank Hilger monospec 1000) and photomultiplier tube (R931A) connected to a chart recorder, which plotted out the wavelength of oscillation. The signal wave was measured at normal incidence to be 385.0 nm. Tuning of the device was measured by angle tuning the OPO crystal about the optical x and y axes, corresponding to tuning in the yz and xz planes respectively. The angle of rotation of the crystal in the mount, ψ , could be read from the rotation stage. This angle must be corrected for the deflection of the pump at the dielectric interface, to find the angle θ measured with respect to the optical axis system xyz . This is calculated using Snell's law.

Rotating the crystal about the y axis using the rotation stage corresponds to tuning in the xz plane where the pump is an extraordinary wave and the phase matching is type II (see chapter 3.3.1). While the OPO was being pumped at 0.8 Jcm^{-2} , it was observed to tune from 385 nm (normal incidence) to 375 nm by tilting the crystal through an angle $\psi = 11.5^\circ$, which corresponds to an internal crystal angle of $\theta = 7.0^\circ$. The idler wavelength varied from 1573 nm to 1724 nm. The measured xz tuning range is shown in figure 4.6. The tuning range was limited by the increase in oscillation threshold, which was probably caused by three factors, namely a decreasing effective non-linear coefficient, increasing end-face reflections and increasing Poynting vector walk-off, as a result of the increasing angle, θ . Figure 4.6 shows the theoretically predicted tuning ranges. These ranges were obtained from the Sellmeier equations listed in appendix A. The Sellmeier equations published by Kato provide the best fit with the results below. There is however still a discrepancy of 1.5 nm between theoretical and experimental signal wavelengths. There are

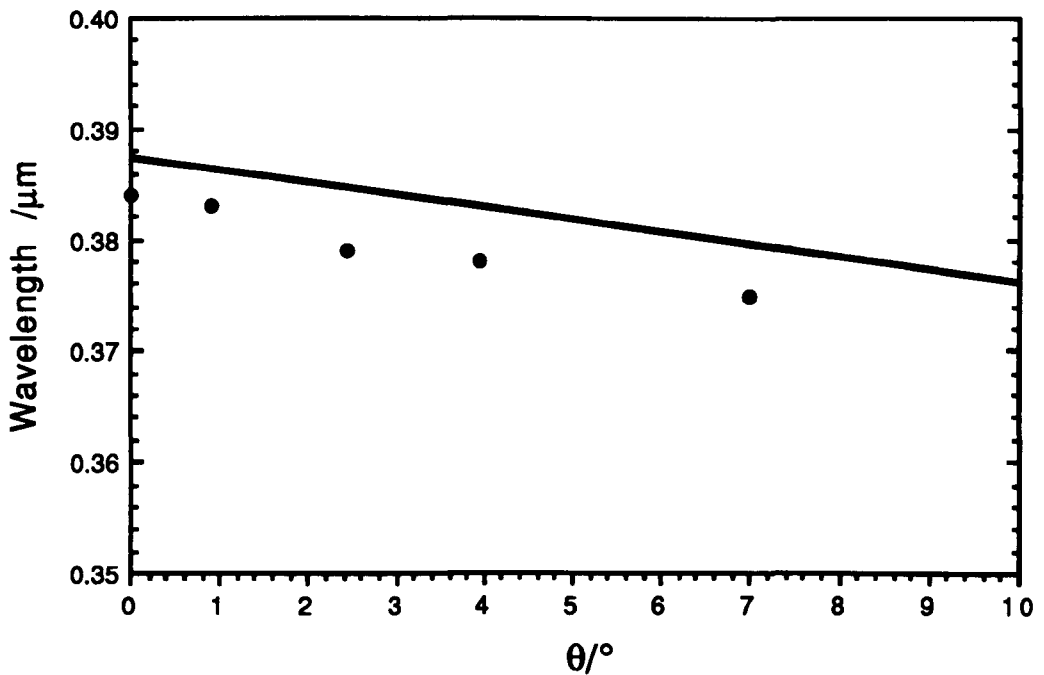


Figure 4.6. *xz* tuning range of 9 mm LBO crystal. The solid line represents the theoretical results as calculated in chapter 3 and the dots represent the experimental data.

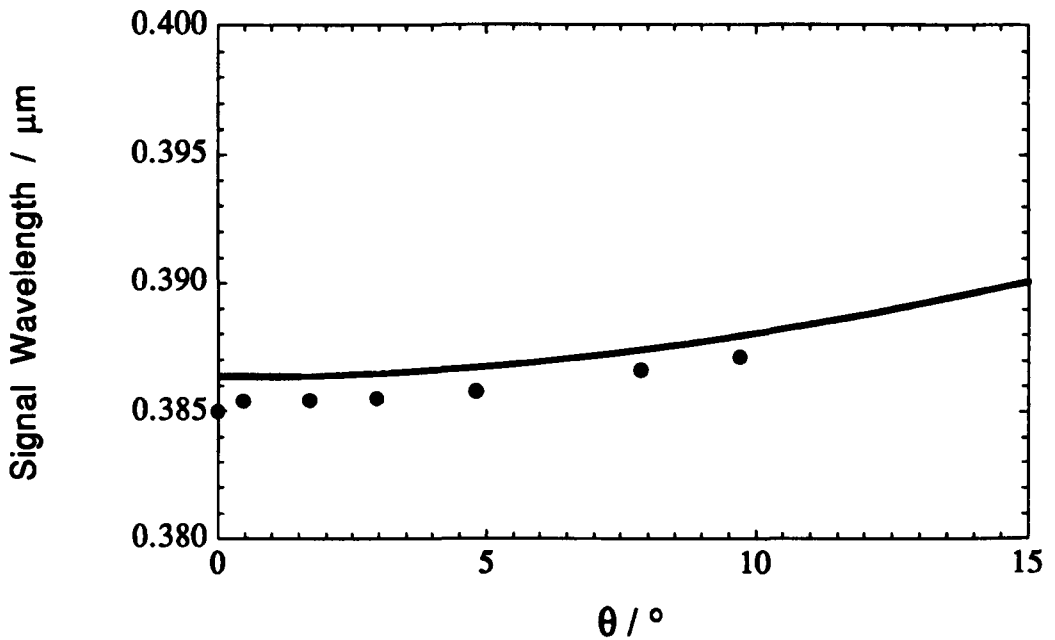


Figure 4.7. The *yz* tuning range of LBO, where θ is the internal crystal angle measured from the *z* axis to the *xy* plane. The solid line represents the theoretical tuning range as calculated in chapter 3. The dots are measured points.

two possible causes for this. One is the temperature tunability of LBO but this is unlikely because, as will be seen later, the tuning rate is $-0.07 \text{ nm}/^\circ\text{C}$. The second, and more likely, cause is inadequacies in the Sellmeier data in the UV.

When the crystal is mounted with the x axis vertical (and the pump polarisation is vertical) and then tuned about this axis, then tuning is in the yz plane. The measured tuning range is shown in figure 4.7. The pump energy density was again 0.8 Jcm^{-2} . This tuning range extended from 385 nm (normal incidence) to 387 nm when the crystal was rotated through an external angle of 15.8° . This corresponds to an internal angle of 9.7° as shown in figure 4.7. Again, the tuning range was limited by the increase in oscillation threshold as the crystal was rotated. There is a discrepancy between the theoretical and experimental signal wavelengths in this tuning range similar to that which was noted in the xz plane.

4.4.2. Threshold

The operation of the OPO close to threshold is generally erratic due to pump energy fluctuations, which result in a distribution of shots above and below threshold. This behaviour was used to measure the threshold by varying the pump energy density until the OPO oscillated only occasionally with the maximum and minimum pump energies straddling the threshold energy. A bench mark of 1 shot in 5 was taken as a measure of threshold. At threshold, the pump energy was measured to be 13 mJ at the laser, before it passed through any optics. Allowing for Fresnel reflection losses at two lens surfaces this, drops to 12 mJ. The beam size was measured to be 0.02 cm^2 (2 mm x 1 mm) using burn paper. This corresponds to an experimental threshold of 0.6 Jcm^{-2} . The pump beam divergence in this case was calculated, using equation 4.2, to be 2 mR which is well within the acceptance angle of the NCPM LBO crystal.

It is possible to calculate the expected threshold for the 9 mm crystal using the expression derived by Brosnan and Byer³ and discussed in chapter 2. The equation is repeated for convenience

$$J = \frac{2.25\tau}{Kl^2} \left[\frac{L}{2\tau c} \ln\left(\frac{P_n}{P_0}\right) + 2\beta - 0.51\ln R + \ln 2 \right]^2 \quad (4.3)$$

and

$$K = \frac{2\omega_s\omega_i d^2}{n_s n_i n_p \epsilon_0 c^3}$$

where the variables are as defined in chapter 2. β is the single pass loss due to Fresnel reflections, which are dominant when the crystal is uncoated. If we insert the suitable values as shown in table 4.1

Variable	τ	l	β	R	d_{eff}	λ_p	λ_s	λ_i	n_p	n_s	n_i
Units	ns	mm	%	%	pm/V	nm	nm	μm	–	–	–
Value	17	9	0.13	0.9	1.15	308	385	1.5	1.60	1.55	1.50

Table 4.1. Parameters for calculating the oscillation threshold

then the threshold energy fluence $J = 2.5 \text{ Jcm}^2$. Clearly there is not very good agreement between theory and experiment in this case. This can be partly explained by noting that the crystal is at normal incidence and that the reflection losses will be greatly reduced by resonant effects between the polished crystal faces and the cavity mirrors. Figure 4.8 depicts a cavity with a high refractive index crystal. The mirrors are 90% reflecting at the signal and the crystal faces are

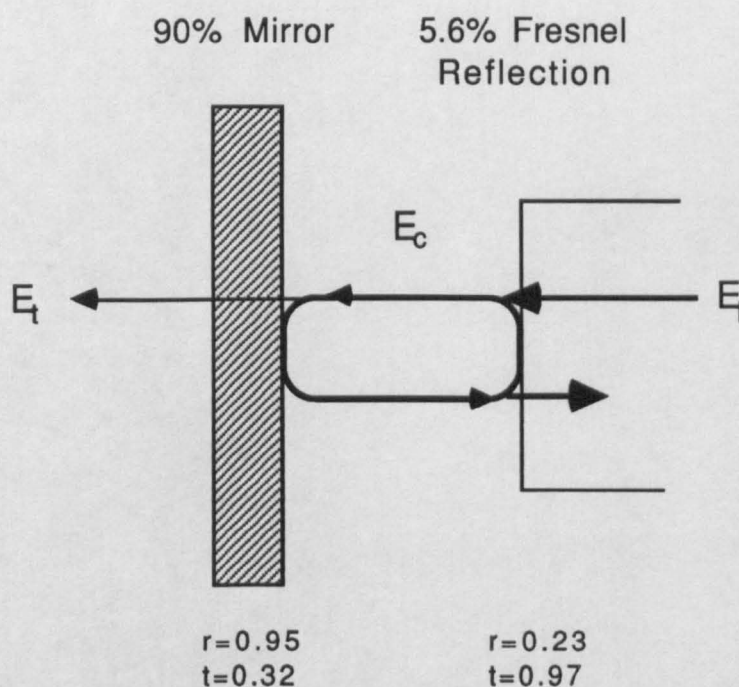


Figure 4.8. Normal incidence reduction in reflection losses. The $R=90\%$ mirror and on-axis crystal face together act like a mirror of reflectivity $R=94\%$ (see text). The ratio of the transmitted field at each surface to the incident field is denoted by t and the ratio of the reflected fields to the incident fields is denoted by r .

5.6% reflecting due to the Fresnel reflection from a dielectric interface of refractive index ~ 1.6 . When the crystal faces are aligned parallel to the mirrors, the signal is not lost on

reflection but is reflected off the mirrors and is re-incident on the crystal. In effect, an on-axis etalon has been introduced into the cavity. It is possible to calculate⁴ the effective transmission and reflectivity of the etalon from considerations of the amplitude reflectivity and transmission, r and t , respectively, for the crystal surface and the cavity mirror. The internal cavity field, E_c , can be written as

$$E_c = [0.95 \times 0.23 \times E_c e^{2i\phi} + 0.97 E_i]$$

which can be re-arranged to give

$$E_c = \frac{0.97 \times E_i}{[1 - 0.95 \times 0.23 \times e^{2i\phi}]}$$

Assuming that the OPO selects the phase, ϕ , to minimise transmission (i.e. for maximum gain) then the transmitted field can be calculated to be

$$E_{t,\min} = \frac{0.32 \times 0.97 \times E_i}{[1 + 0.95 \times 0.23]} = 0.25 E_i$$

thus

$$T_{\min} = \left(\frac{E_{t,\min}}{E_i} \right)^2 = 0.06 \quad (4.4)$$

The reflectivity, $(1 - T_{\min})$, of the etalon is thus 94%. The effect of the crystal face being at normal incidence is thus two-fold. Firstly, the reflectivity of the mirror is enhanced. Secondly, the reflection loss of the crystal surface is removed, assuming, of course, that the phase of the fields is such that the mirror reflectivity is maximised. This is a safe assumption since the OPO will naturally select the modes with highest gain. Using equation 4.3 the theoretical threshold is reduced by a factor of 2.3 to 1.3 Jcm^{-2} , which more closely approaches the measured value of 0.6 Jcm^{-2} . Experimentally, the reduction in threshold due to the normal incidence effect was measured to be ~ 1.4 times. This was achieved by rotating the crystal away from normal incidence by 1.5° . The discrepancy may be due to the surface quality and flatness of the crystal faces reducing the 'etalon' finesse. This effect occurred in all the crystals at normal incidence and further experimental evidence demonstrating this is presented later in this chapter and also in the following chapters.

By decreasing the beam area in the crystal, the OPO was taken to 2.1 times oscillation threshold. The beam size was measured to be $2.0 \text{ mm} \times 0.76 \text{ mm}$ or 0.015 cm^2 , with a pump pulse energy at the OPO of 11 mJ. At this energy density, 0.73 Jcm^{-2} , damage was seen to occur to the rear OPO mirror. Although the energy density in the crystal was

only $\sim 0.73 \text{ Jcm}^{-2}$, the beam size at the back mirror was smaller because the beam was focused down. From equation 4.1, the beam size can be estimated as 0.011 cm^2 . This implies that the energy density at the back mirror was $\sim 1 \text{ Jcm}^{-2}$, which is the damage threshold of the mirrors. Measurement of the efficiency of the device was therefore not practical.

4.5 16 mm LBO Crystal-Tuning Ranges

4.5.1 Angle Tuning Ranges

As a follow up to the 9 mm crystal, a second, longer LBO crystal was used. This crystal, which measured $x \times y \times z = 3.7 \text{ mm} \times 3.5 \text{ mm} \times 16 \text{ mm}$, had the same orientation as the 9 mm crystal, i.e. cut for propagation down the optical z axis. Using

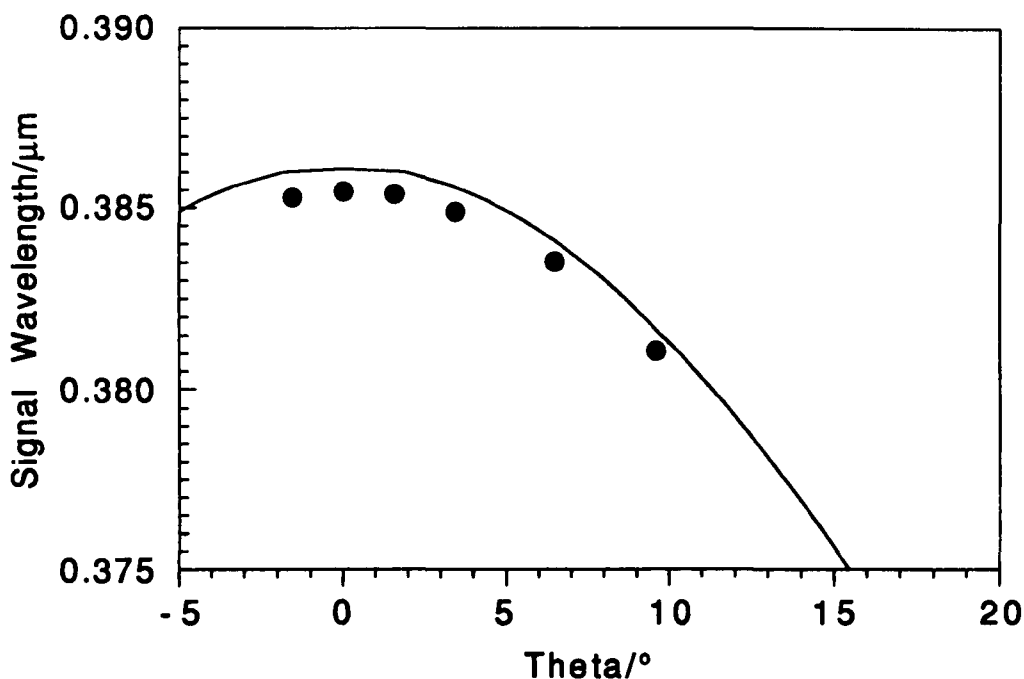


Figure 4.9 a. *xz* tuning range. KEY:- solid line = theoretical tuning range, showing the symmetry about $\theta = 0^\circ$. dots = experimental points taken with the 16 mm LBO crystal.

the 370 nm to 420 nm mirrors, the OPO cavity was made as short as possible and measured only 20 mm. The tuning range, which is shown in figure 4.9, was measured in an identical way to that of the 9 mm crystal. In the *xz* plane the tuning range is measured to be 385.6 nm at normal incidence to 381.0 nm, obtained by rotating the crystal through an angle $\psi = 15.5^\circ$. This corresponds to an internal angle, θ , of 9.5° . The idler wave was calculated to tune from $1.53 \mu\text{m}$ to $1.6 \mu\text{m}$. In the *yz* plane, signal wavelengths from 385.6 nm to 387 nm were generated by tilting the crystal by 15° from

normal incidence. This corresponds to an internal crystal angle, θ , of 9.2° . The idler was calculated to tune from $1.53 \mu\text{m}$ to $1.5 \mu\text{m}$. Thus, taking both tuning ranges together this

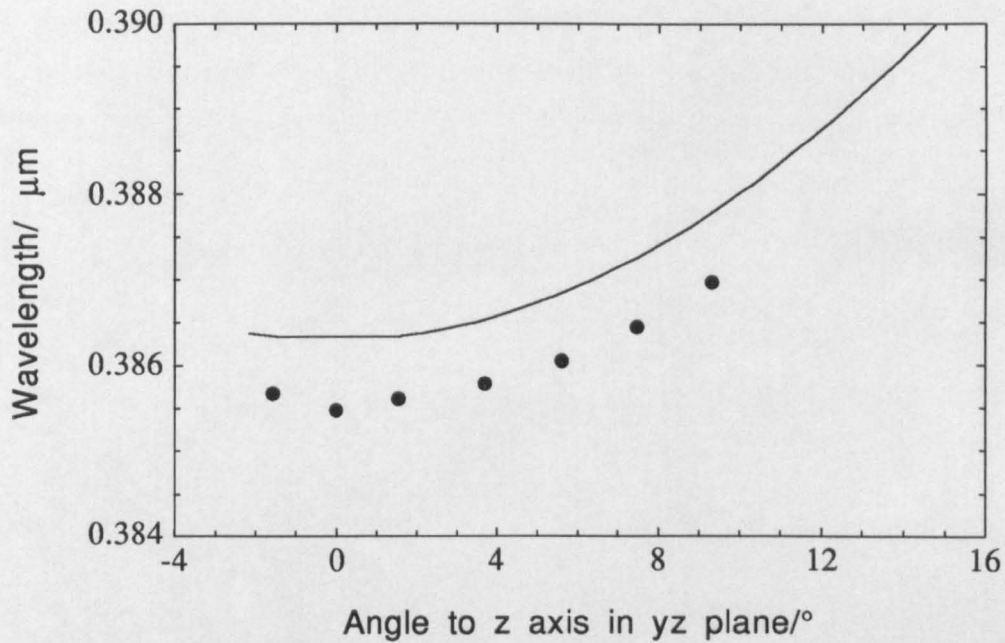


Figure 4.9b. yz tuning range of a 16 mm LBO crystal. KEY:- solid line = theoretical tuning range, dots = measured tuning range. Tuning is symmetric about 0° implying that the crystal faces are cut perpendicular to the z axis.

crystal cut was tunable from 381 nm to 387 nm in the ultraviolet and $1.5 \mu\text{m}$ to $1.6 \mu\text{m}$ in the infrared. The observed tuning ranges in both planes were limited by the crystal aperture. By tuning in both directions from normal incidence, in the xz plane and in the yz plane, it was possible to confirm that the 16 mm crystal was polished with its end faces accurately perpendicular to the optic z axis. This is shown in figures 4.9a and 4.9b by the two data points symmetrically placed on either side of the NCPM point ($\theta=0^\circ$). As the OPO was operating more efficiently with the 16 mm crystal than the one with the 9 mm crystal, and the monochromator slits could therefore be much closer together, the wavelength measured at normal incidence (385.6 nm), was considered to be more

$\theta \setminus \phi$	90	89.56	88.85	86.04	84.50
0	385.58	385.58	385.59	385.67	385.70
2	385.42	385.42	385.44	385.51	385.63
3	385.25	385.28	385.30	385.35	385.50
4	385.11	385.11	385.13	385.18	/

Table 4.2. Tuning out of the principal planes in LBO

accurate than the value obtained using the 9 mm crystal (385.0 nm). Tuning out of the principal planes was also possible in LBO. Table 4.2 shows the measured signal wavelengths for different crystal angles (θ, ϕ). As can be seen from the table, tuning out of the principal plane in LBO revealed no new wavelengths. Furthermore, the effect on parameters such as walk-off and effective non-linear coefficient are detrimental. Thus, the best performance can be expected from operation within one of the principal planes in LBO.

4.5.2 Temperature Tuning Range

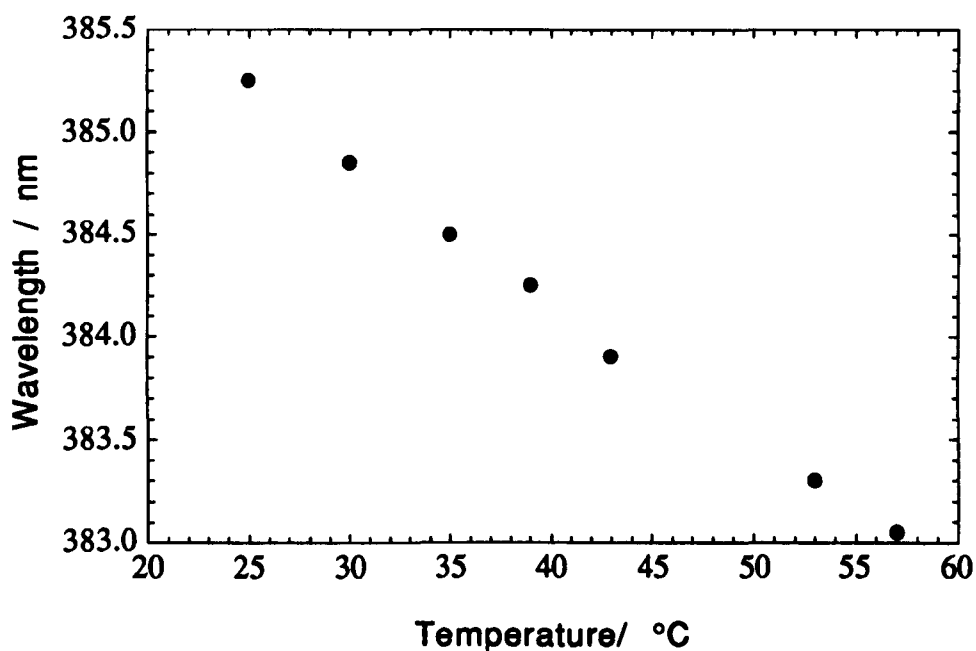


Figure 4.10. Temperature tuning range of NCPM LBO.

In chapter 3, it was stated that LBO was temperature tunable, i.e. the relative values of the principal refractive indices change with changing temperature. In order to investigate this effect, an oven was built to hold the 16 mm crystal. Resistance wire was wound around the oven and this assembly was encased in a PTFE holder to provide insulation. A thermocouple was used to sense the temperature in the oven and this provided feedback to a temperature controller which powered the oven. The temperature in the oven could be raised to 100°C. The temperature stability was good around room temperature but at higher temperatures, near 60°C, the stability decreased due to rapid heat loss from the oven. The experiments were thus confined to between 25°C and 57°C. Figure 4.10 shows the measured temperature tuning range of LBO, at $\theta=0^\circ$, as 385.3 nm to 383 nm. The wavelength variation over this range can be approximated by a linear fit, from which the tuning rate for the signal can be calculated to be $-0.07 \text{ nm}/^\circ\text{C}$. The variation in the idler wave can be inferred from the measured value of the signal wave.

The tuning range was deduced to be from 1.53 μm to 1.57 μm , which implies a tuning rate of $\sim 1 \text{ nm}/^\circ\text{C}$. At this time, no data on the rate of change of the principal refractive indices is available. However, similar temperature tuning rates of $-0.11 \text{ nm}/^\circ\text{C}$, for the short wavelength wave, have been demonstrated by Hanson and Dick⁵ for a 355 nm pumped NCPM device. Operating temperatures as high as 320°C have been reported in LBO⁶, which implies that a considerable extension to this tuning range could be made with the appropriate temperature control unit and suitable precautions against heat loss.

4.6 Oscillation Threshold Measurements

We have already calculated the normal incidence threshold for a 9 mm LBO crystal, and it is easy to calculate the threshold for the 16 mm crystal. Using the same values as in table 4.1 but increasing the length to 16 mm, the threshold can be calculated, using the Brosnan and Byer model, to be $J = 0.79 \text{ Jcm}^{-2}$. The measured threshold, slightly off normal incidence, was 0.34 Jcm^{-2} . Again, the calculated threshold is approximately twice the measured threshold (see chapter 2). The same argument holds for the reduction in threshold at normal incidence. The calculated reduction factor, using the different mirror reflectivities in the Brosnan and Byer model, is 2.3 times, which implies that the theoretical threshold is $J = 0.34 \text{ Jcm}^{-2}$. The measured threshold for the 16 mm crystal at normal incidence was 0.27 Jcm^{-2} . The experimental reduction factor is thus 1.3. The actual mirror enhancement due to the crystal faces is thus less than predicted. This may be due to either the quality, or the flatness of the crystal surfaces.

4.7 Pump Depletion

Following measurements of the oscillation threshold at normal incidence, the OPO was operated at several times above threshold and the efficiency of parametric conversion from pump to signal and idler was measured. The power meter was placed after the first pump deflecting mirror shown in figure 4.4. A diverging lens was placed after the deflecting mirror to reduce the energy density at the power meter head. Readings were taken when the OPO was aligned and when it was mis-aligned, i.e. when the OPO was oscillating and when it was not. This allowed the pump depletion to be calculated. It is defined as

$$\text{P.D.} = \frac{(\text{Energy out when mis-aligned}) - (\text{Energy out when aligned})}{\text{Energy out when mis-aligned}}$$

$$= \frac{E_u - E_d}{E_u} \quad (4.5)$$

where E_u is the undepleted pump and E_d is the depleted pump. Since the pump beam travels along the same path in both cases, all the linear losses due to reflection, absorption and scattering in the crystal and mirrors may be ignored. The resulting pump depletions are shown in figure 4.11. The peak pump depletion achieved was 35% when operating at 3.3 times threshold, which was limited by mirror damage. As can be seen from the graph there is a possible roll-off in efficiency at higher pump energy densities. The roll-off in the pump depletion could be due to the onset of unobserved mirror damage.

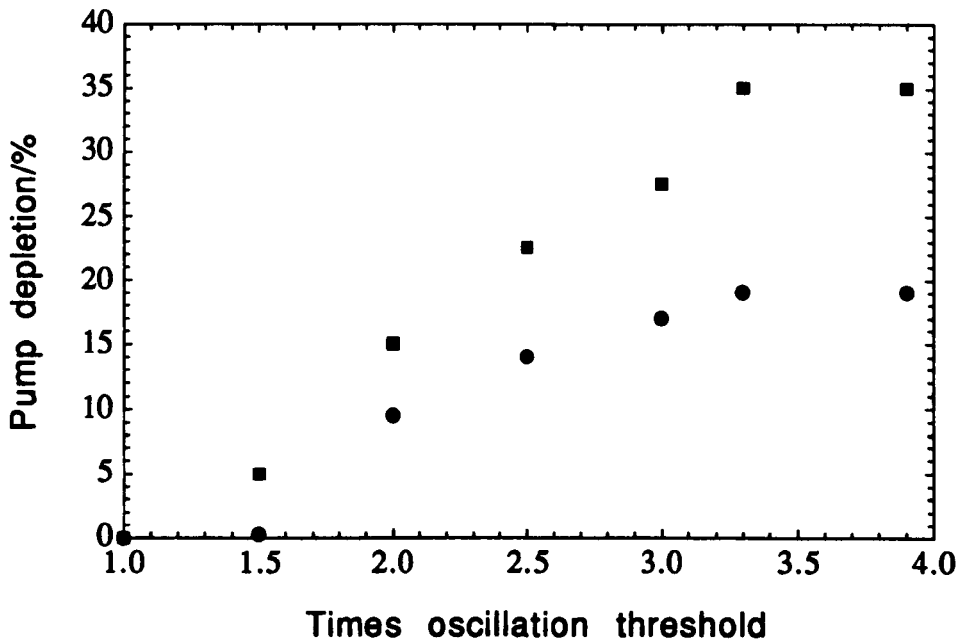


Figure 4.11. Pump depletion in 16 mm LBO crystal. KEY:- The squares depict the pump depletion and the circles the external efficiency (defined later).

Temporal measurements of the depletion of the pump were also made. These were taken using the 100 mJ laser described earlier in this chapter. The unused pump beam after the OPO was propagated through an aperture, into a distant room to avoid noise pick-up from the excimer laser. A photodiode and an oscilloscope were used to record the pulses. Depleted and undepleted pulses were recorded and are shown in figure 4.12. The level of pump depletion, measured as before using the technique of aligning and mis-aligning the cavity, was ~35 %. The build up time of the OPO is clearly visible at the start of the pulse where the pump is undepleted. The build-up time is ~3 ns. This corresponds to approximately 22 OPO cavity round trips. Figure 4.11 also shows the

external efficiency of the NCPM LBO OPO. This is defined as the ratio of the energy in the signal and idler, E_o , to the energy in the pump, E_p . Allowances are made for the signal and idler lost at the pump reflector plates and also for the signal that exits the OPO on the pump laser side through the R=95% mirror. The

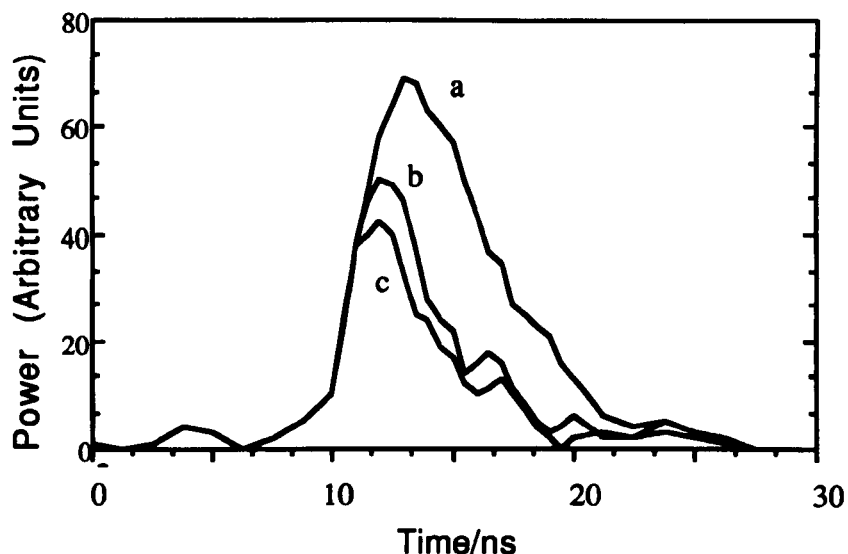


Figure 4.12. Temporal pump depletion. Pulse a is the undepleted pump. The other two are characteristic of ~35% pump depletion.

energy in the signal and idler was measured using a Scientech power meter with the laser operating at 1 Hz. Typical output energies of 0.5 mJ were obtained from the OPO, in the forward direction, in the signal and idler combined. From the output energy, the percentage of energy in the signal could be calculated from the ratio of the frequencies of the two output waves, $\omega_s/\omega_i = 4$. Thus, $4/5E_o$ is the signal energy that exits the cavity in the forward direction. This equals the energy that exits the cavity in the opposite direction, towards the pump laser, because the cavity is symmetric for the signal beam. Thus, the total energy exiting the cavity is equal to $2 \times (4/5E_o) + 1/5E_o = 9/5E_o$. The peak external efficiency, calculated in this manner, is 19%, which is obtained when the pump depletion is 35%. Thus, 54% of the parametrically generated energy is coupled out of the cavity in the signal and idler. The remaining 46% is lost from the cavity, mainly as reflected and scattered light.

4.8 Crystal Degradation/ Measurements of Scattering and Absorption

During the course of experimentation with the LBO crystal, a gradual decrease was observed in the peak pump depletion and external efficiency that could be obtained from the OPO. Over time, the pump depletion had fallen to a level of about only 5%. A typical

set of results is shown in figure 4.13. During this period of decline in performance, the threshold was observed to increase only slightly. To estimate the size of the intra-cavity losses, the optical transmission of the crystal was measured at two wavelengths at the

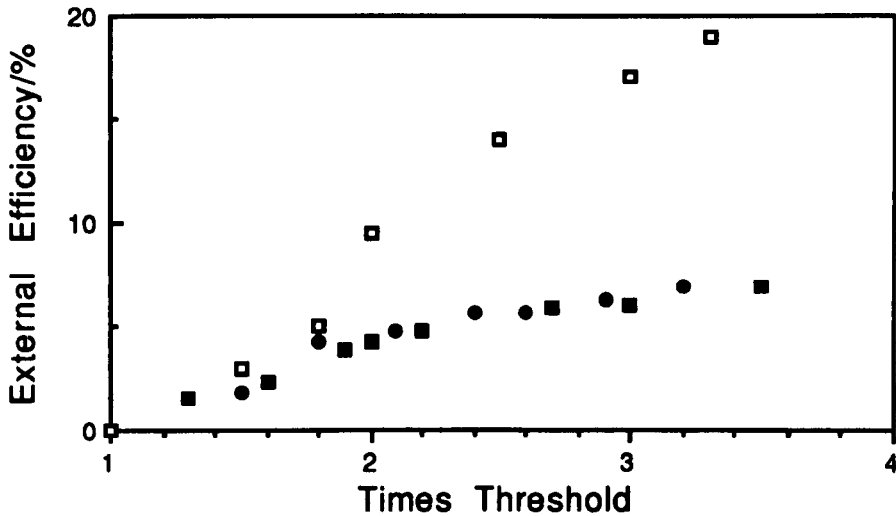


Figure 4.13. Decline in external efficiency. The white squares represent data taken 11/5/90. The black squares and circles represent data taken on 6/7/90 and 12/7/90.

extremes of the tuning range, i.e. 308 nm and 1540 nm. Initially measurements were taken at 308 nm using the pump laser as a probe. The pump beam was left unfocused but was routed through a pin-hole aperture to provide a 2 mm beam of low intensity, $\sim 0.03 \text{ Jcm}^{-2}$. It was important to maintain a low probe energy to avoid losses due to the parametric process. The crystal was mounted on a rotation stage and could be easily removed to allow the absorption of the other components in the system to be measured. The transmitted energy was measured with a power meter. The set up is shown in figure 4.14. The transmission of both the 9 mm and 16 mm crystals was tested to provide a comparison. If, for example, there had been a degradation of the crystal with use, it would be likely that the 16 mm crystal would have a lower transmission due to its more prolonged use. The average transmission levels for the two crystals, taken over many shots were 85% for the 9 mm crystal and 74% for the 16 mm crystal. The single pass Fresnel losses can be shown to be 11.2% in both cases⁷, so the single pass absorption or scattering loss in each crystal was, thus, 4% and 15% respectively. Clearly the losses in the 16 mm crystal are exceedingly high.

Using an erbium fibre laser operating at 1.56 μm , the absorption of the IR in the crystal was measured. Using a set-up similar to that described above for the excimer laser, the transmission of the two crystals was measured to be $\sim 78\%$ for the 16 mm crystal and 86% for the 9 mm crystal. Again, accounting for the Fresnel loss leaves the

absorption/scattering losses as, 11% and 2% for the 16 mm and 9 mm crystals respectively. During the course of the measurements it was noticed that a cloudy film could be seen on the surface of the 16 mm crystal when viewed under a fluorescent light. The crystal was cleaned using methanol and the transmission at 308 nm retaken. The

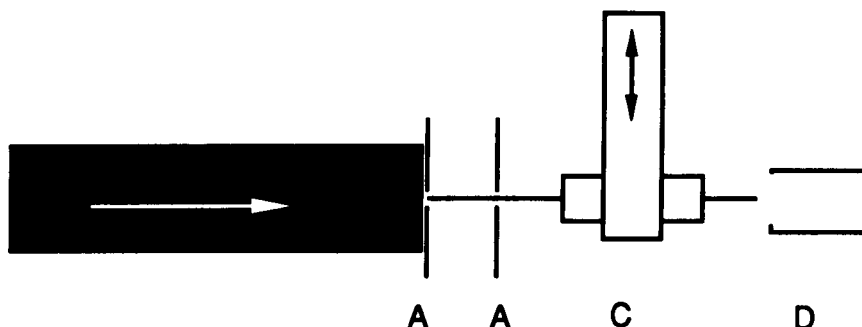


Figure 4.14. Measurement of the crystal transmission. The pump beam is shown in white on the left. A: apertures, C: crystal in translation stage which allows the crystal to be moved to the side, D: detector

transmission was now $\sim 87\%$. Measurements of the pump depletion showed that it had returned to its previous value of $\sim 35\%$. During further use of the LBO crystals, the same clouding returned frequently but could be removed using methanol, without apparent damage to the crystal.

4.9 Ratio of Signal to Idler Energies

In assessing the performance of the OPO, it is important to measure not just the efficiency of the device in terms of pump depletion (the efficiency of conversion from pump to signal and idler), but also in terms of the external efficiency. This can be described as the ratio of the energy coupled out of the cavity in the signal and idler beams to the energy of the pump beam. As an experimental complication, it is necessary to have up to three pump deflector plates between the OPO and the energy meter to remove the undepleted pump. It is thus important to know the transmission of these plates for both of the generated waves. It is also necessary to know the transmission of the other components of the OPO, such as the mirrors and the crystal. By adding a fourth pump deflector plate, after the other three, the loss due to one plate can be measured. In the UV at 385 nm, the transmission of the plate was $x_{UV} = 0.95$ and in the IR at 1540 nm, the transmission $x_{IR} = 0.75$. In calculations of efficiency, it is also important to note that the signal exits the cavity equally from both ends, thus only half of the signal energy is measured by the detector.

The external efficiency of the OPO, η_{ext} , depends on the output coupling efficiency, H , of the cavity, which in turn depends on the losses within the cavity. It is possible both to measure and calculate the magnitude of these losses as will be demonstrated. These measurements lead directly to a knowledge of the relative output coupling efficiencies of the signal and idler waves from the cavity.

The transmission of all the cavity elements was measured and found to be as follows. Firstly, the single pass loss of the crystal at 308 nm (the excimer wavelength) was ~13%. The assumption made in the following calculations is that the transmission of the LBO crystal at 308 nm and 385 nm is similar⁸. The transmission of the mirrors was tested using the OPO by a similar procedure to that used to measure the transmission of the pump deflector plates above. The transmission of the signal through the mirror was ~10% and of the idler, ~90%.

The energy in the signal and idler leaving the cavity in the forward direction, E_o , and the pump depletion, η_{int} , were measured as before. An additional measurement of the energy in the idler E_{im} was made by replacing two of the pump deflecting plates by a UV filter, RG460, which blocked the 308 nm and 385 nm radiation and was 90% transmitting for the idler. Using this information, it is possible to calculate the total energy immediately after the OPO, i.e. accounting for the losses of all the plates and filters. The energy in the signal, after the three plates, is given by

$$E_{s1} = E_o - \frac{(x_{\text{ir}})^2 E_{\text{im}}}{0.9}$$

The energy in the idler beam only, just after the OPO (i.e. allowing for losses at the pump beam deflection plate and the UV filter) is given by

$$E_I = \frac{E_{\text{im}}}{0.9x_{\text{ir}}}$$

The total two-way signal energy just after the OPO (i.e. allowing for losses at the three pump deflection plates), E_{s2} , is thus

$$E_{s2} = \frac{2E_{s1}}{(x_{\text{uv}})^3}$$

The total energy in the signal and idler having removed all extra-cavity losses is thus

$$E_T = E_{s2} + E_I$$

Using this equation, the external efficiencies of the signal and idler were calculated and are shown in figure 4.15.

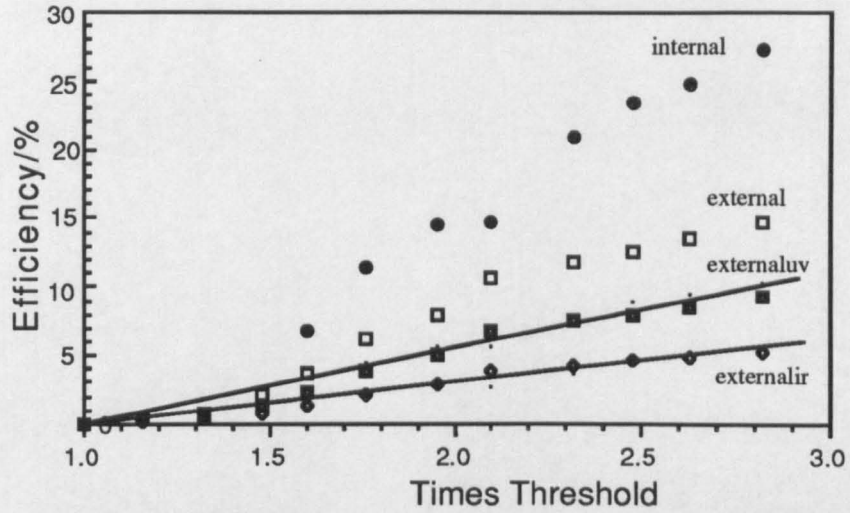


Figure 4.15. Internal and external efficiencies in UV resonant, NCPM LBO. KEY:- Filled circles = pump depletion, η_{int} ; open squares = total external efficiency, $\eta_{ext} = 0.55\eta_{int}$; filled squares = UV efficiency, $\eta_{extuv} = 0.33\eta_{int}$; open diamonds = IR efficiency, $\eta_{extir} = 0.22\eta_{int}$. The black lines represent the UV and IR efficiencies calculated from the pump depletion and a knowledge of the internal losses.

The output coupling efficiency, H , is defined as $\eta_{ext}/\eta_{int} = E_T/E_{pump}$. The individual output coupling efficiencies for the signal and idler may be defined as

$$H_{uv} = \frac{\eta_{extuv}}{\eta_{int}} = \frac{E_{s2}}{E_{pump}}$$

and

$$H_{ir} = \frac{\eta_{extir}}{\eta_{int}} = \frac{E_I}{E_{pump}}$$

respectively. The sum of H_{uv} and H_{ir} is H . Figure 4.15 shows the pump depletion, η_{int} , external efficiency, η_{ext} , and the external efficiencies of the signal and idler, η_{extuv} and η_{extir} respectively.

Theoretically, the external efficiency is related to the internal efficiency by the output coupling efficiency given by⁹

$$\eta_{\text{ext}} = \left[\frac{\omega_s}{\omega_p} \left(\frac{T}{T+L_s} \right) + \frac{\omega_i}{\omega_p} L_i \right] \eta_{\text{int}} = [H_{\text{uv}} + H_{\text{ir}}] \eta_{\text{int}} \quad (4.6)$$

where T is the mirror loss or output coupling and L_s is the intra-cavity loss for the signal in a cavity round trip. L_i represents the loss to the signal exiting the cavity. Inserting appropriate values into the equation gives

$$\begin{aligned} \eta_{\text{ext}} &= \left[0.8 \left(\frac{0.2}{0.2+0.26} \right) + 0.2 \times 0.9 \right] \eta_{\text{int}} \\ &= \left[(0.8 \times 0.417) + (0.2 \times 0.9) \right] \eta_{\text{int}} \\ &= [0.33 + 0.18] \eta_{\text{int}} = 0.51 \eta_{\text{int}} \end{aligned}$$

The calculated coupling efficiencies can be related to the measured values since

$$\eta_{\text{ext}} = (H_{\text{uv}} + H_{\text{ir}}) \eta_{\text{int}}$$

Measuring gradients from figure 4.15 it can be shown that the agreement is good (see η_{extuv} and η_{extir} in the figure caption). The output coupling efficiency, in terms of photon numbers can be calculated from measured data using $\omega_p/\omega_s \times H_{\text{uv}}$ and $\omega_p/\omega_i \times H_{\text{ir}}$ or, equivalently, from knowledge of the individual loss terms from $T/(T+L_s)$ and L_i . The non-resonant wave, which only contributes approximately half the energy, does in fact exit the cavity with an output coupling efficiency in photon numbers, of 90%. The resonant signal on the other hand is only coupled out with 42% efficiency, when considered in terms of photon numbers.

The results clearly show that the output coupling efficiency of the resonant wave is low in the presence of high intra-cavity losses. In this case, the uncoated crystal faces contribute a round trip loss of 26%. At the time of experimentation, suitable anti-reflection coatings for LBO were unobtainable. The available coatings were unable to withstand high pump energy densities. Under these circumstances, the crystal faces were left uncoated. Although the losses experienced by the resonant wave are large, the idler wave is generated on a single pass and leaves the cavity with very little loss. This then is an effective way of obtaining maximum energy in the desired wave.

4.10 IR Resonant NCPM LBO

Since the losses for the resonant wave are high within an OPO with uncoated crystal faces, generation of tunable ultraviolet light would best be performed by resonating the infrared wave. To this end, a new set of mirrors were used to replace the 370 nm to 420 nm mirrors used previously. The new mirrors were coated to be 90% reflecting between 1.4 μm and 1.6 μm . (The infrared wave is generated at 1.54 μm at normal incidence). The mirrors were also designed to be highly transmitting at 308 nm and 385 nm, which are the pump and signal wavelengths respectively.

Theoretical calculations of threshold and efficiency are independent of which wave is resonant, so they need not be repeated here (only in the case where both waves are resonant is the treatment modified). However, the calculation of the acceptance angle and acceptance bandwidth are altered, since both depend on the choice of resonant

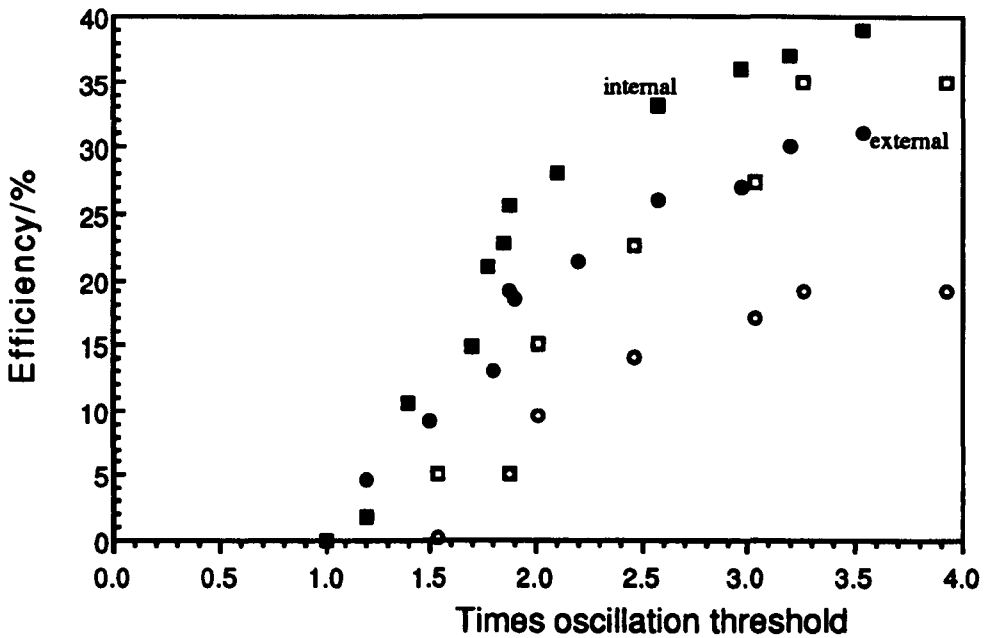


Figure 4.16. IR resonant NCPM LBO. Black squares: pump depletion, and black circles: external efficiency, and the white shapes represent the UV resonant data shown in figure 4.8 shown here for comparison. White squares = pump depletion, and white circles = external efficiency.

wave. The acceptance angle for the NCPM and yz geometries is shown in figure 3.9, for the case where the infrared wave is resonant. Note that the infrared wave is now the **signal** and the ultraviolet wave is the **idler** (refer to the note on nomenclature at the front of this thesis). The acceptance angle for NCPM LBO with an ultraviolet resonant cavity

is larger than that with an infrared resonant cavity (see figure 3.8). The tolerance to beam divergence of the IR resonant device is thus inferior to the UV resonant case.

The pump depletion, the external efficiency and the fraction of the energy in the IR were measured as before. Figure 4.16 shows the results graphically. The IR resonant pump depletion is slightly higher than the UV resonant pump depletion. This may be due to the newer, better quality mirrors used. The external efficiency in the IR resonant case is significantly higher than the UV resonant case, but, more importantly, the ratio of external to internal efficiencies in the IR resonant case is much higher than in the UV resonant case. From figure 4.16, it can be determined that the ratio $\eta_{\text{ext}}/\eta_{\text{int}}=0.78$ for the IR resonant cavity. The increased output coupling efficiency can be explained by looking at the cavity losses for the signal and idler. The output coupling losses for the IR resonant case can be calculated in the same way as for the UV resonant case. The external efficiency given by equation 4.6 now becomes

$$\begin{aligned}\eta_{\text{ext}} &= \left[0.2 \left(\frac{0.2}{0.2+0.26} \right) + 0.8 \times 0.9 \right] \eta_{\text{int}} \\ &= \left[(0.2 \times 0.417) + (0.8 \times 0.9) \right] \eta_{\text{int}} \\ &= [0.087 + 0.72] \eta_{\text{int}} = 0.81 \eta_{\text{int}}\end{aligned}$$

This value for $\eta_{\text{ext}}/\eta_{\text{int}}$ agrees well with the experimental value given above. By examining the output coupling efficiencies of the signal and idler separately, it is easy to see why resonating the IR wave results in higher external efficiencies. The photon output coupling efficiency for the idler is again 90% and for the signal only 42%. In terms of energy coupled out of the cavity, 72% of the energy is in the ultraviolet but less than 1% of the energy is in the infrared. Thus by resonating the infrared wave, over twice the energy in the ultraviolet has been extracted than was possible, under similar pumping conditions, when the ultraviolet wave was resonant. In general, these experiments show the penalty to be paid for having uncoated crystal faces within an otherwise efficient OPO cavity. In the absence of crystal coatings, however, resonating the unwanted wave is a useful means of obtaining higher external efficiencies from the other wave.

4.11 Inherent NCPM LBO Linewidths

In chapter 2.6, the relationships between the inherent linewidth of an OPO and the birefringence of the material, and between these and the tuning rate of the device were shown. From the tuning curves of NCPM LBO (figures 3.4 and 3.5), it can be seen that

the rate of tuning is not particularly great, with a rate of change of wavelength with angle of 0.16 nm° . This can be compared to BBO close to degeneracy, for example at 610 nm , where the linewidth is $\sim 10 \text{ nm}$ and the rate of tuning is 40 nm° (ref 2). It might be expected, therefore, that the inherent linewidth of NCPM LBO would be small. Figure 3.12 shows the calculated linewidth of NCPM LBO. Figure 4.17 shows a typical monochromator trace of the measured OPO linewidth, which was measured to be 0.08 nm . The trace was recorded by a plotter connected to a photomultiplier tube

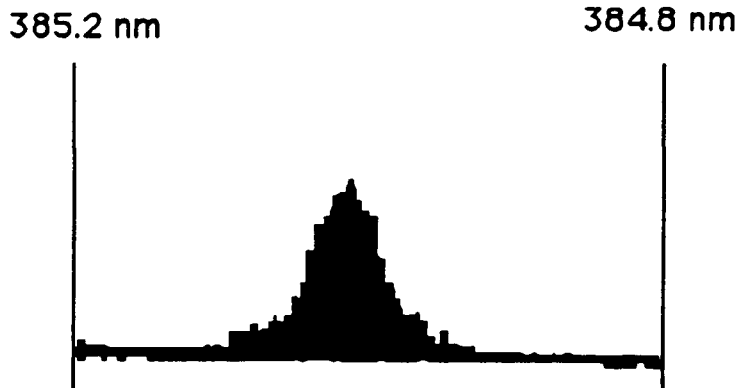


Figure 4.17. Spectrum of NCPM signal wave around 385 nm . The FWHM linewidth is 0.08 nm .

placed at the exit slit of the monochromator. The monochromator was scanned across a few nanometers around the peak of the ultraviolet wavelength. The laser was operating a 1 Hz repetition rate hence the spiked nature of the trace. The linewidth indicated by the trace is 0.08 nm FWHM. By checking the resolution of the monochromator with a HeNe laser, the trace was found to be limited by the resolution of the monochromator. It was thus necessary to measure the linewidth of the OPO using an interferometer. This was constructed using two plane, parallel mirrors similar to the ones used in the OPO cavity. They were mounted on gimbals to permit precise alignment and these in turn were mounted on translation stages. The mirror separation was continuously variable between 0 mm and 20 mm . The mirrors were fully illuminated by the ultraviolet light from the OPO via a diverging lens. The fringes formed in the interferometer were visible by fluorescence on a paper screen. A camera was used to capture the fringes on film. Again, the laser operated at 1 Hz and the camera shutter speed was set to 1 s thus ensuring that only one fringe set would be captured per frame. The OPO was operated with the ultraviolet wave resonant and at a few times threshold. The cavity length was 20 mm . For this cavity length the mode spacing can be shown to be 0.25 cm^{-1} (0.004 nm). The fringes shown in figure 4.18 are fluorescence fringes from a white paper screen placed after the interferometer. The interferometer mirror spacing was 5 mm . The free spectral

Figure 4.18 (shown overleaf)

Fringes from the interferometer. The NCPM OPO cavity length was 20 mm. The interferometer mirror spacing was ~5 mm. The finesse was ~10. The fringes are visible due to fluorescence from white card.

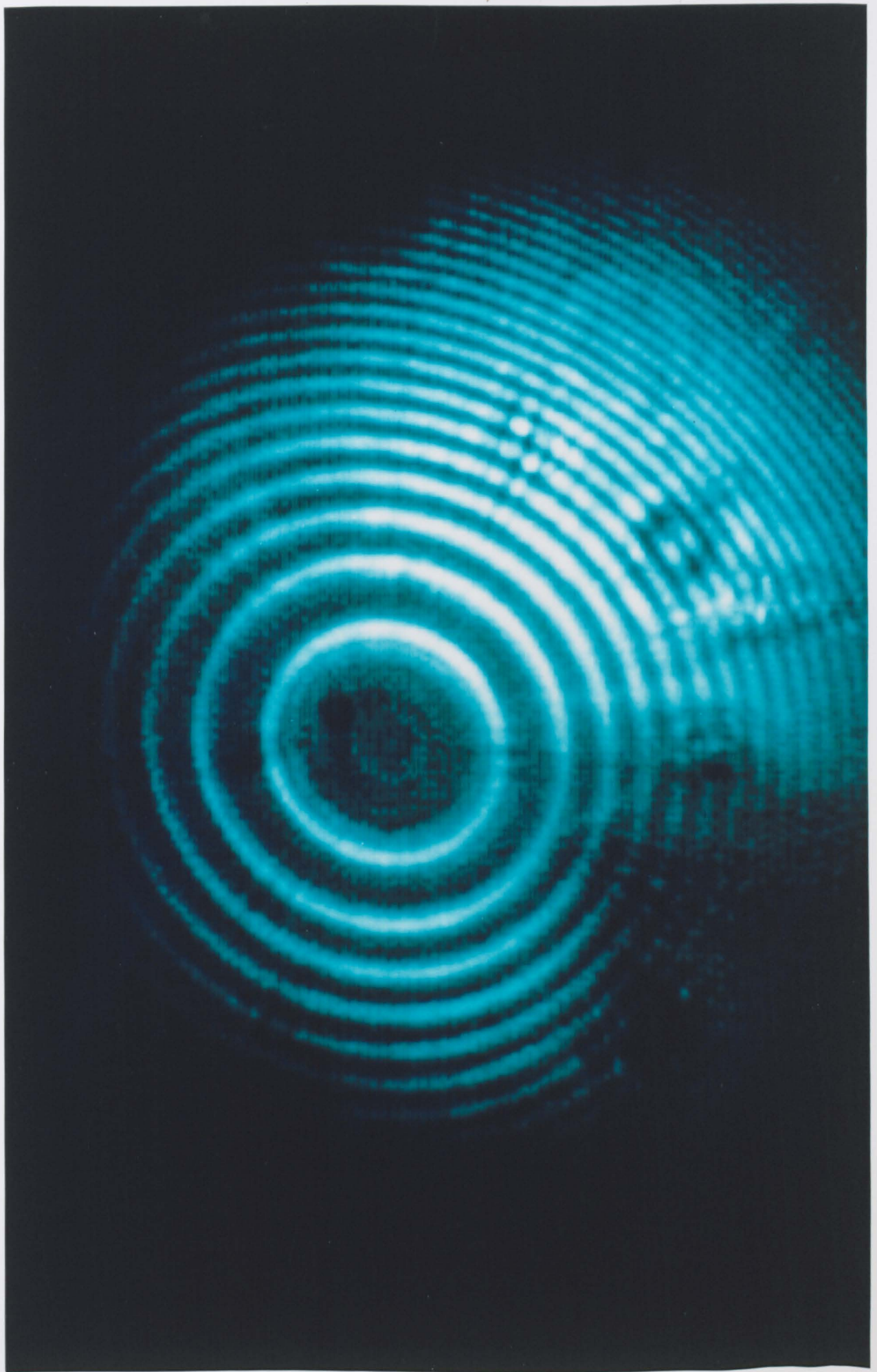


Figure 4.19 (see overleaf)
Oscillation on two axial modes. The OPO cavity length was 20 mm. The interferometer mirror spacing was ~5 and the finesse was ~10.

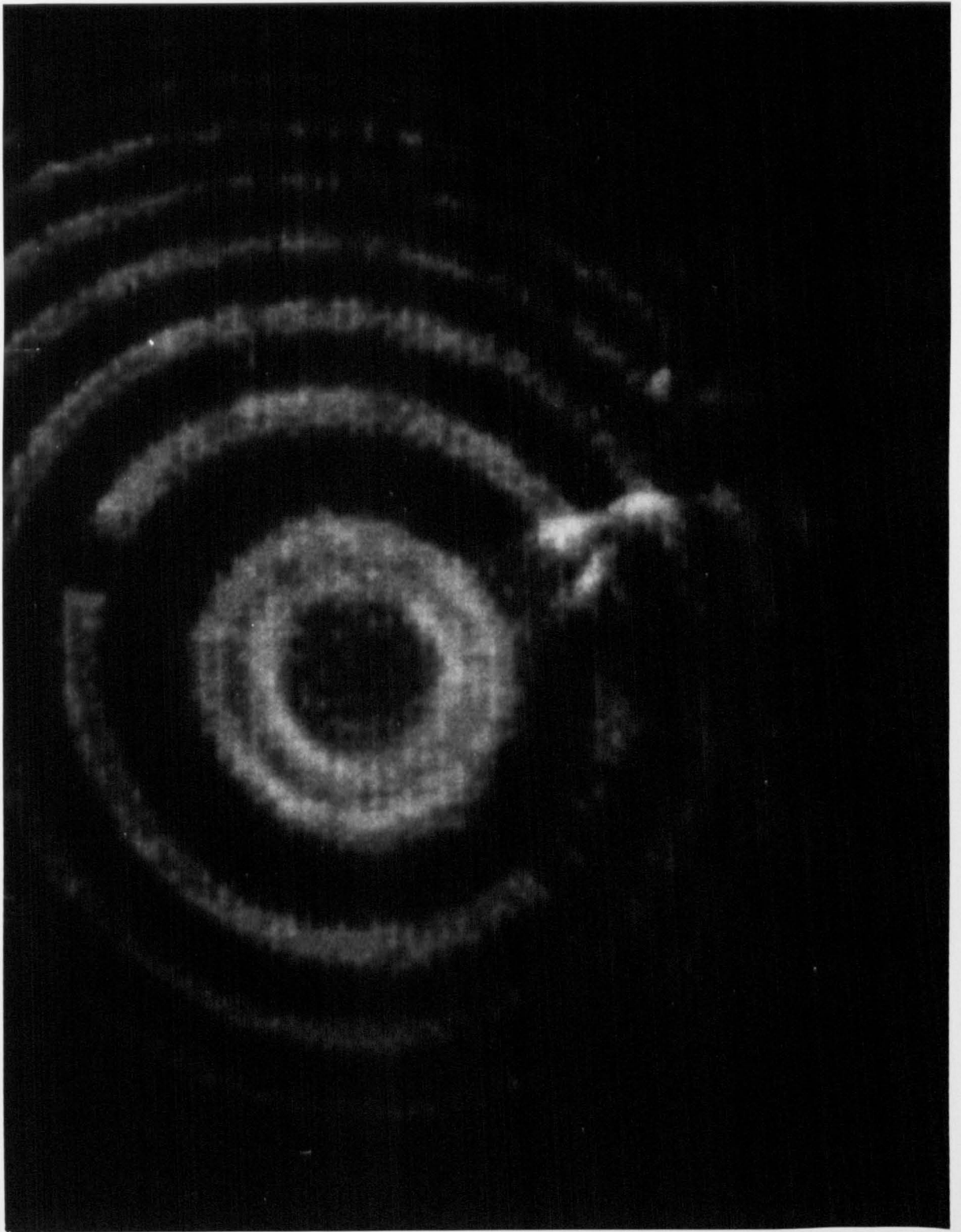
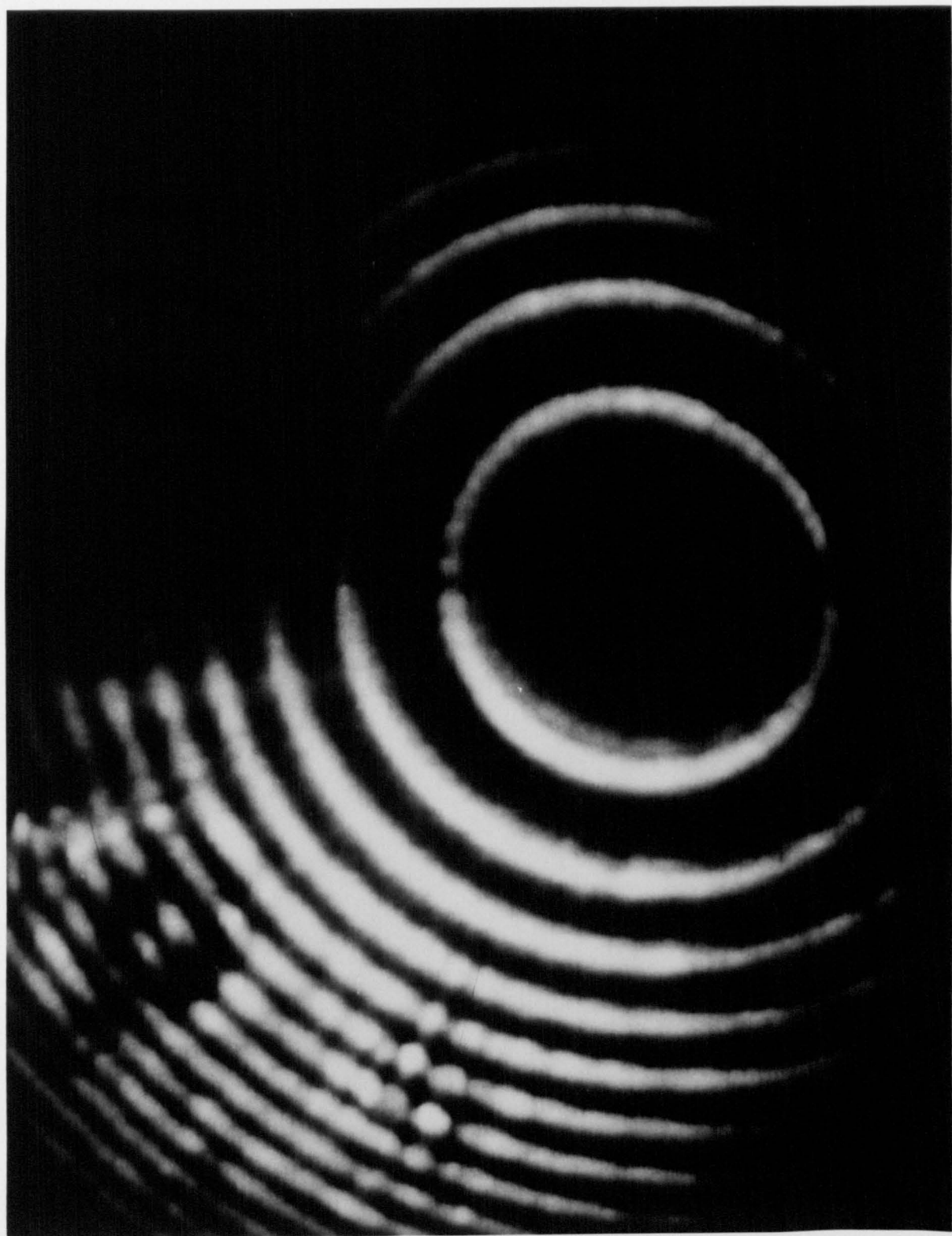


Figure 4.20 (shown overleaf)
Oscillation on one axial mode. The OPO cavity length was 20 mm. The interferometer mirror spacing was ~5 mm. The finesse was ~10.



range of the interferometer is 1 cm^{-1} and the finesse is greater than 15. It is thus theoretically capable of resolving detail down to 0.07 cm^{-1} (0.001 nm). The multiple fringe pattern in figure 4.19 is indicative of two axial modes oscillating. The frequency stability of the OPO however was not good and the oscillating modes hopped from shot to shot. On some shots only one axial mode was present. This is shown in figure 4.20.

Examination of figure 3.12 will show that the theoretically predicted NCPM linewidth is 0.11 nm , which is considerably greater than the measured linewidth of 0.008 nm (2 axial modes). The crystal was rotated off normal incidence by 1.6° to check if the linewidth was being affected by etalon effects from the crystal faces, however, fringes were still clearly visible. Other workers have observed linewidths in NCPM LBO that are narrower than predicted theoretically in references 5 and 10 of 0.02 nm and 0.003 nm respectively.

4.12 Type II yzLBO

4.12.1 Tuning Range

In chapter 3, the graphs of the phase-matching loci in the xz and yz planes were given and the common point of the NCPM geometry was identified. In the preceding sections, the study has concentrated on the NCPM geometry. However, both the xz and yz planes exhibit useful tuning ranges. The availability of a crystal cut for propagation at 40° to the

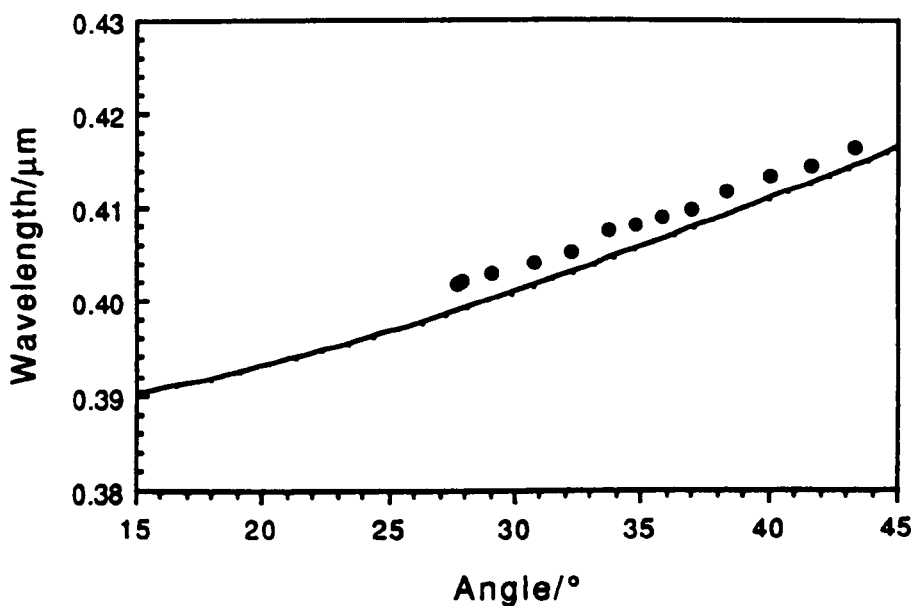


Figure 4.21. Measured tuning angle of yzLBO. KEY:- Solid line: theoretical tuning range, dots: measured tuning range.

z axis in the yz plane opened up the opportunity of studying this critically phase-matched type II geometry. The crystal was 15 mm long and had an aperture of $5 \times 5 \text{ mm}^2$.

The tuning range of the device was measured using the monochromator as before. The wavelength at normal incidence was measured to be 413 nm. The tuning range was limited to 416 nm on the long wavelength side by the increase in threshold. In the other direction, the tuning range was extended down to 402 nm. This was limited by the crystal aperture. In total, the crystal was rotated through an angle of 19° . The measured tuning range is shown along with the theoretically predicted tuning range in figure 4.21. The idler tuning range was measured to be $1.31 \mu\text{m}$ to $1.19 \mu\text{m}$.

4.12.2 Threshold

The effective non-linear coefficient in the yz plane is given by $d_{32}\cos\theta$ (see chapter 3.3). Therefore, a steady increase in threshold is to be expected as the propagation angle increases from zero. The threshold across the tuning range was measured, using the criterion of 2 shots in 10, as before. Figure 4.22 shows the measured variation. Again, there is a strong dip in threshold at normal incidence, which brings the threshold down to 0.37 Jcm^{-2} . Again this may be explained by the formation of an intra-cavity etalon

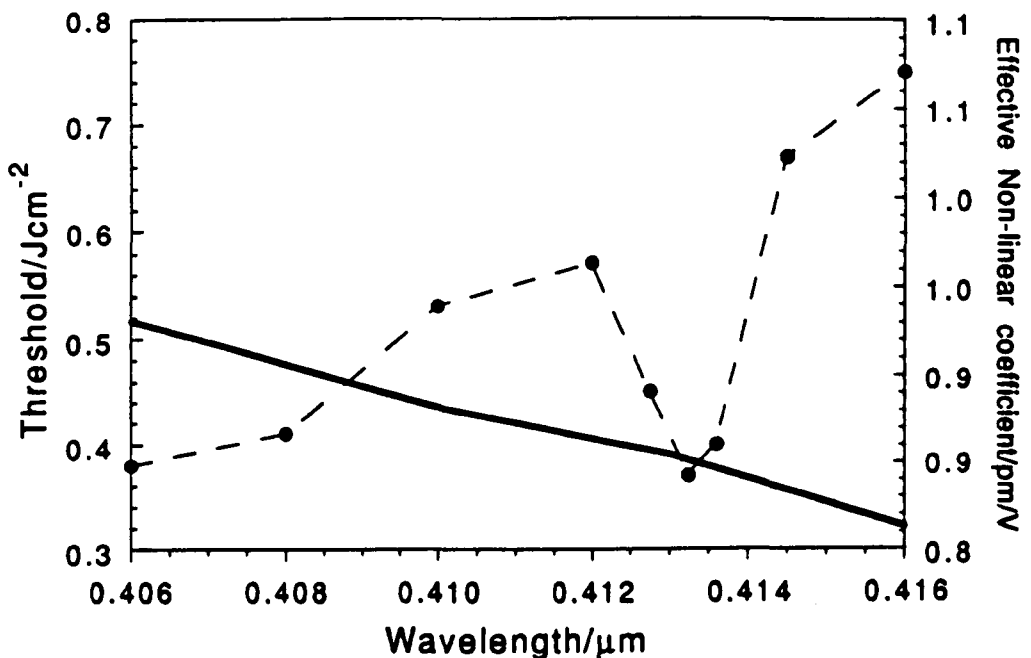


Figure 4.22. Variation of threshold across the observed tuning range, shown by the dots. The dashed line is interpolated through the data points. The variation in effective non-linear coefficient is shown by the solid line. A $4 \times 2 \text{ mm}^2$ beam size has been used. The normal incidence threshold was 25 mJ .

between the crystal faces and the cavity mirrors when the crystal is at normal incidence. From extrapolation of the surrounding points the threshold would be $\sim 0.6 \text{ Jcm}^{-2}$ in the absence of this effect, compared to 0.37 Jcm^{-2} . The threshold has thus been reduced by a factor of 1.6. This is slightly less than the 2.3 times predicted theoretically in section 4.4.2. The quality of the crystal surface and the parallelism of the two faces will clearly play a role in determining the magnitude of this etalon effect.

In the absence of the normal incidence effect, the threshold rises monotonically with wavelength from 0.38 Jcm^{-2} at 406 nm to 0.75 Jcm^{-2} at 418 nm. This explains why the tuning range is limited towards longer wavelengths. Figure 4.22 also shows the decrease in effective non-linear coefficient as the OPO is tuned away from the NCPM point (386 nm, $\theta=0^\circ$). There is clearly a correlation between the decreasing non-linear coefficient and the increasing threshold.

The effect of Poynting vector walk-off on threshold was also studied. Being a critical geometry the effect of beam size would be expected to be greater than that observed for the NCPM case. The walk-off angle at $\theta=40^\circ$ (normal incidence in this crystal) is $\rho =$

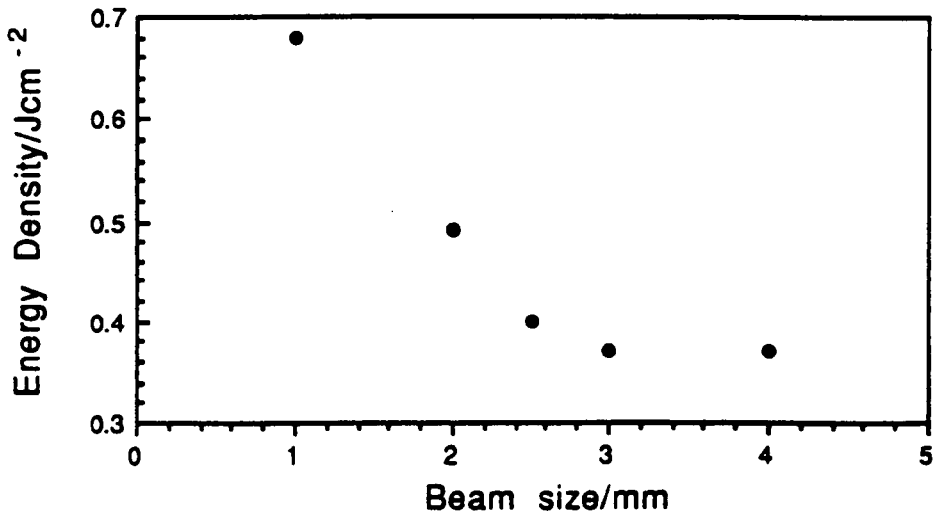


Figure 4.23. Threshold vs. beam size in yzLBO at normal incidence (413 nm)

0.5° (see chapter 3.7). The threshold was measured for various pump beam sizes using the 100 mJ Lambda Physik laser described at the beginning of this chapter. Collimated beams were used in each case. The results are shown in figure 4.23. The threshold for a 1 mm beam, measured in the plane of walk-off, was 0.68 Jcm^{-2} compared to only 0.37 Jcm^{-2} for the 3 mm beam at normal incidence. The walk-off angle at 40° can be shown to be 0.5° . Thus over the length of a 15 mm crystal, the extraordinary wave will walk-off

from the two ordinary waves by 0.15 nm. This has the effect of reducing the interaction between the three waves and hence the observed increase in threshold. This reduction in interaction also effects the efficiency of the device. Measurements of pump depletion at normal incidence were also taken. The maximum pump depletion of 8.5% was obtained using the 3 mm beam. The corresponding external efficiency was measured to be 4.8%, accounting for the signal exiting the cavity equally in both directions. This implies an output coupling efficiency of 56%, which is similar to the value observed for the NCPM OPO when the UV wave was resonant.

4.12.3 Linewidth

Linewidth measurements were also taken using a monochromator to scan across the gain bandwidth of the device. The linewidth was measured to be 0.15 nm across the tuning range, which is slightly greater than would be expected theoretically (see figure 3.12). A sample trace for the normal incidence is shown in figure 4.24. The OPO was operating at twice oscillation threshold, which might explain the increased linewidth, since linewidth increases with increasing number of times threshold.



Figure 4.24. Spectrum of yzLBO at 40°. The FWHM linewidth is 0.15 nm.

4.13 Conclusions

The new non-linear material LBO has been shown to operate in a potentially useful non-critically phase-matched geometry. This was the first reported demonstration of this LBO geometry. The non-linear coefficient used in this interaction is $d_{31}=0.8$ pm/V. The generated wavelengths are 385 nm and 1.54 μm . Tuning of the device has been observed by both angle tuning and temperature tuning. The angle tuning was limited by the small aperture of the crystal, which was only 3×3 mm². The measured temperature tuning range was 385.5 nm to 383 nm. This was limited by the maximum obtainable

temperature, which was governed by the temperature controller and oven. The temperature tuning rate was $-0.07 \text{ nm/}^\circ\text{C}$. Assuming a continued linear rate of change of wavelength with temperature, the OPO could realistically be tuned over the range 389-370 nm by changing the crystal temperature over the range -30°C to 250°C . Over the same temperature range, the infrared wave would tune from 1480 nm to 1838 nm.

The threshold of the device at normal incidence was observed to be $\sim 0.24 \text{ Jcm}^{-2}$, which permitted high pump depletions of 35% to be obtained. The effect of Poynting vector walk-off in the NCPM geometry was studied. It was shown that tight focusing left the threshold and the slope efficiency unchanged. A further discussion on the effects of walk-off is given in chapter 7.

The linewidth of the NCPM device was observed to be very narrow, only of the order of 1 or 2 axial modes, which was somewhat less than predicted. However, similar narrow linewidths have been observed by other workers (ref 5 and 10).

Angle tuning in the yz plane has also been explored using a crystal cut at 40° to the z axis in the yz plane. This displayed a greater tuning rate than the NCPM OPO. The roll-off in effective non-linear coefficient affected the threshold significantly with thresholds of 0.7 Jcm^{-2} at $\theta=40^\circ$ compared with 0.4 Jcm^{-2} at $\theta=28^\circ$. Walk-off was also observed to affect the threshold of the device when small pump beam sizes (less than 2.5 mm) were used. The linewidth of the critical geometry was measured to be 0.15 nm, close to the predicted linewidth of 0.12 nm given in chapter 3.

REFERENCES

- 1 M. Ebrahimzadeh, G. Robertson, M. H. Dunn and A. Henderson. Conference on Lasers and Electro-Optics (1990) postdeadline paper CPDP26
- 2 'Optical parametric oscillators pumped by a XeCl excimer laser'. Majid Ebrahimzadeh, PhD Thesis, St Andrews University (1991).
- 3 'Optical parametric oscillation threshold and linewidth studies'. J. Brosnan and Robert L. Byer. IEEE J. Quantum Electron. 15, 415 (1979).
- 4 'Lasers'. A. G. Seigman
- 5 'Blue parametric generation from temperature-tuned LiB_3O_5 '. Frank Hanson and David Dick. Opt. Lett. 16, 205 (1991).
- 6 'Measurements of noncritically phase-matched second-harmonic generation in a LiB_3O_5 crystal'. T. Ukachi, R. J. Lane, W. R. Bosenberg and C. L. Tang. Appl. Phys. Lett. 57, 980 (1990).

- 7 'Fundamentals of Optics'. Francis A. Jenkins and Harvey E. White. Pub. McGraw-Hill Book Company. Auckland N.Z. p526.
- 8 'New nonlinear-optical crystal: LiB_3O_5 '. Chuangtian Chen, Yicheng Wu, Aidong Jiang, Bochang Wu, Guiming You, Rukang Li and Shujie Lin. J. Opt. Soc. Am. B 6, 616 (1989).
- 9 'Lasers: a series of advances, vol4'. R. G. Smith. Eds A. K. Levine and A. J. DeMaria. Pub Marcel Dekker, New York (1976). p233.
- 10 'Lithium Triborate optical parametric oscillator pumped at 266 nm'. Y. Tang, Y. Cui and M. H. Dunn. Opt. Lett. 17, 192 (1992).

Type I LBO in the xy Plane

In chapter 3, the theoretical results for a broadly tunable OPO using LBO were presented. This chapter contains the experimental results relating to this device.

5.1 Experimental Set-up

The OPO presented in this chapter operated in a type I critical geometry in the xy plane. Using the simplification to the uniaxial convention, described in chapter 2.4, the phase-matching can be described as $e \rightarrow o+o$. Physically, this means that the signal and idler are polarised along the z axis and the pump wave is polarised in the xy plane.

The crystal was cut at an angle $\phi = 40^\circ$ to the x axis for propagation in the xy plane, and was 15 mm long with an aperture of $6 \times 3 \text{ mm}^2$. (For brevity this geometry will be called type I xyLBO or simply xyLBO). The crystal faces were uncoated for the same reasons as described for the NCPM device, i.e. the coating manufacturers were unable to coat the crystals over a suitably large wavelength range without placing severe restrictions on the optical damage threshold of the coatings. Sufficient energy was available from the laser that the theoretically predicted threshold could be reached without the need for anti-reflection coatings, whilst keeping the threshold sufficiently below the damage threshold of the mirrors and the crystal. The pump laser used was the Lambda Physik laser described in chapter 4.2, which was capable of delivering up to 100 mJ in a 17 ns pulse. Operating in the crystal geometry described above and with the pump laser operating at 308 nm the expected generated wavelengths at normal incidence are 399 nm and 1350 nm.

The mirrors selected for the OPO cavity were a pair of flat Suprasil substrates coated to be 90% reflecting between 370 nm and 420 nm and to be highly transmitting at the pump wavelength of 308 nm and at the idler wavelength of 1350 nm. Thus the OPO was designed to operate in a singly resonant configuration. The cavity mirrors were spaced 19 mm apart and on gimbal mounts to facilitate alignment of the OPO cavity.

The crystal was mounted on a rotation stage that permitted a large degree of rotation in the xy plane. The aperture of the crystal was cut such that the height of 6 mm was in the xy plane and the width of 3 mm was along the z axis. The large aperture in the

xy plane served two functions. Firstly it allowed large rotation angles to be achieved. Secondly, it allowed the beam size in the xy plane to be larger, which is a useful measure to reduce the effect of walk-off in this plane. (The pump beam polarisation of the laser was vertical and entered the crystal as an extraordinary wave in the xy plane).

The experimental set-up is shown in figure 5.1. The pump beam entered the OPO cavity via a gas cell attenuator (G), which controlled the energy of the pump, and a beam compressor. The beam compressor consisted of two fused silica

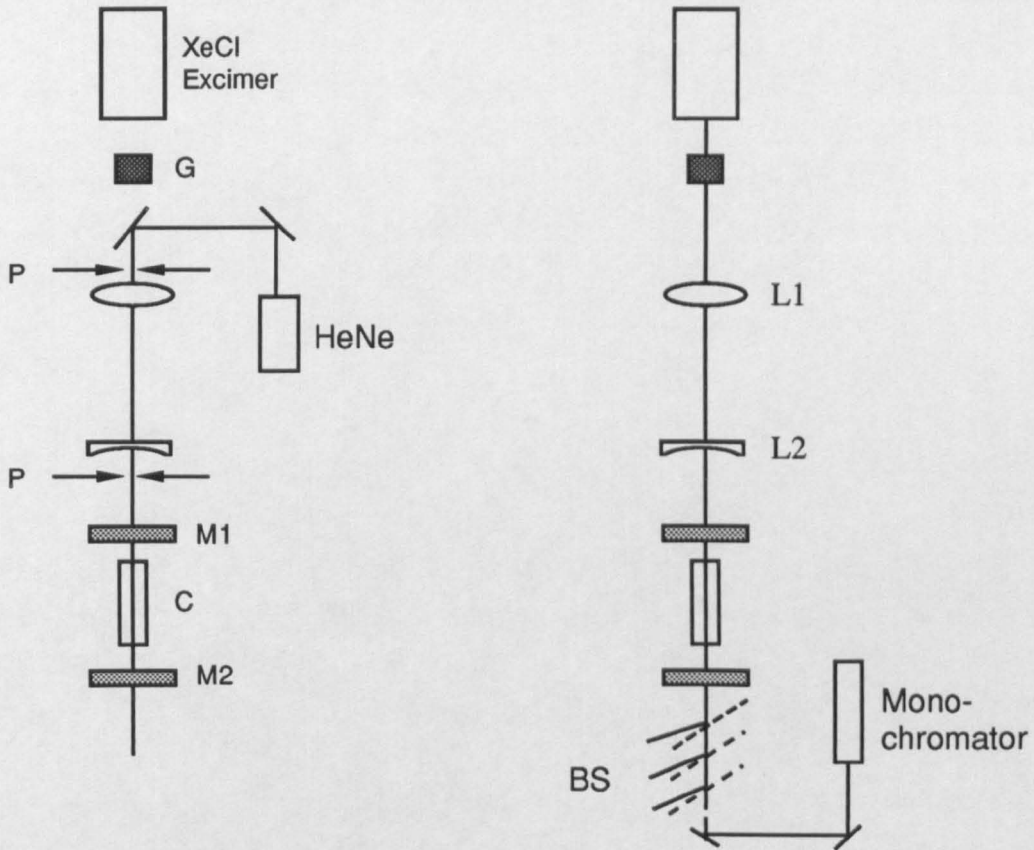


Figure 5.1. Experimental set-up. On the left the alignment process with the HeNe directed through the pin-holes (P) which are placed down the pump beam axis. On the right the OPO system with the monochromator. KEY:- G = gas cell attenuator, C = crystal, M1 & M2 = cavity mirrors, BS = pump beam deflecting plates. L1 & L2 = lenses

lenses in a Galilean telescope arrangement traversed in reverse. By changing the second lens for one of a different focal length and varying the separation between the two lenses, different beam sizes could be obtained, while still retaining collimation. The lenses of the beam compressor were not anti-reflection coated for the pump wavelength and the transmission of the lens system was ~ 0.83 . The maximum energy

measured at the pump laser was typically 80 mJ, thus the pump energy reaching the OPO was ~66 mJ. The pump laser beam had the dimensions 2 x 1 cm² and could be compressed to a collimated beam of the order of 0.8 x 0.4 mm².

The alignment of the OPO was carried out by placing pin-holes (P) in the beam, concentric with the hole in the centre of the excimer beam to define its path (The hole in the beam is caused by the arrangement of optics in the injection seeded laser, see figure 4.2). A HeNe laser beam was then used to mark the path of the excimer beam, by steering the HeNe beam through the pin-holes. Once the beam was aligned, it could be used to align the OPO crystal and cavity mirrors. Final alignment was achieved interferometrically by centring the fringes obtained from the two parallel cavity mirrors onto the pin-hole. This completed the alignment of the OPO. Three pump deflecting plates were placed in the beam, after the OPO, to separate the unwanted pump from the signal and idler beams. The plates were coated to be 90% reflecting at 308 nm when positioned at Brewster's angle.

5.2 Tuning Range

The crystal was set up as described above and the signal wavelength was monitored using a 1 m focal length monochromator (Monospek 100), as shown in figure 5.1. The monochromator was scanned around 400 nm until the blue light from the OPO was observed at the exit slit. The signal wavelength was measured to be 398.5 nm when the crystal was at normal incidence (i.e. $\phi = 40^\circ$) at 22°C. By changing the grating in the monochromator, the corresponding idler wave was measured to be at 1356 nm. These fit well with the expected wavelengths at 20°C of 399 nm and 1350 nm calculated from the Sellmeier equations (see figure 5.1). The temperature difference of 2°C would be expected to change the measured signal wavelength by -0.14 nm. Using the same mirror set, the OPO was tuned over the range 370 nm to 438.6 nm which covered the entire mirror reflectivity range. By using two other sets of mirrors with reflectivities of 90% in the ranges 420 to 480 nm and 450 nm to 550 nm, the tuning range was extended into the visible to 497 nm at the signal wavelength. The corresponding idler wavelength was measured to tune between 1356 nm and 810 nm. The tuning range was limited by the available aperture of the crystal. To cover this tuning range, the crystal was rotated through an external angle of 23°. The theoretically predicted tuning range is shown in figure 5.2 along with the experimentally measured results. From the figure, it can be seen that the crystal would have to be rotated through an additional internal angle of 6° to reach degeneracy. This angle, in terms of actual crystal rotation is ~9°.

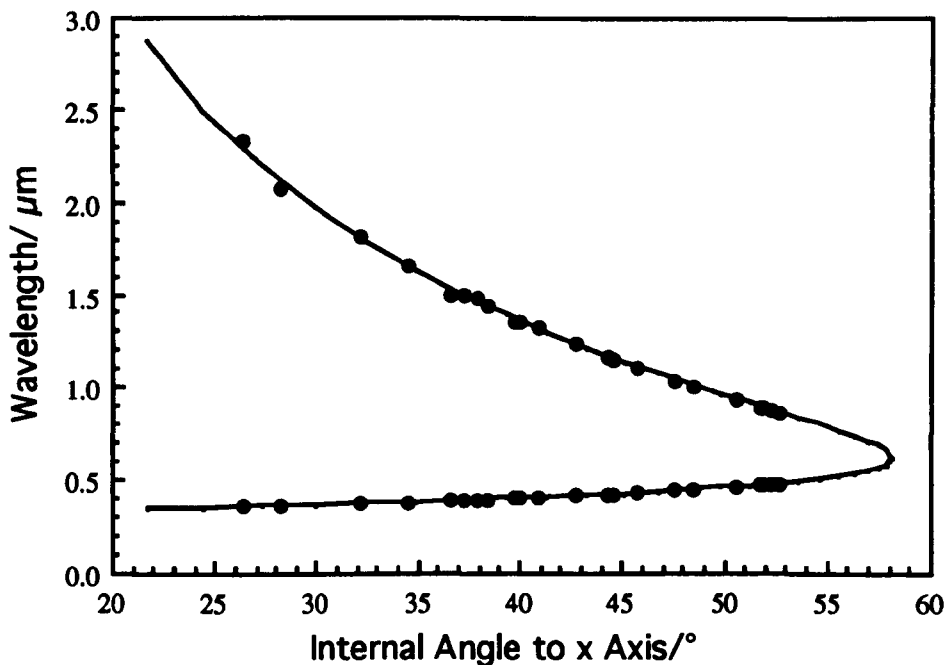


Figure 5.2. Theoretical and experimental tuning ranges of xyLBO

The tuning range was also extended into the UV using a set of mirrors designed to be 90% reflecting over the range 340 nm to 370 nm. The measured tuning range was extended down to 354 nm. In this case, the corresponding idler wavelength, although unmeasured, can be calculated to be 2.37 μm . To obtain this tuning range, from 398.5 nm at normal incidence down to 354 nm, the crystal was rotated through an angle of 22°. Again, the crystal aperture was the limiting factor in the tuning range. In total, the crystal was rotated through an angle of 43° and covered a tuning range of 354 nm to 2.3 μm , excluding the portion between 500 nm and 810 nm near to degeneracy. This is shown in figure 5.2 above. The angles of the measured wavelengths have been converted using Snell's law to the equivalent angles within the crystal, allowing for refraction at the crystal surface. The spectral region close to degeneracy could be accessed by using a larger crystal aperture, say of 9 mm, or by cutting the crystal at an angle of 46° instead of 40° and compromising the UV/IR coverage or by using two crystals cut at different angles.

5.3 Oscillation Threshold

The oscillation threshold of the xyLBO OPO was measured as a function of both beam size and wavelength. Firstly, the threshold was measured using a variety of pump beam sizes. The measurements were taken at 385 nm for comparison with the NCPM

geometry discussed in the previous chapter. The pump beam from the excimer was oriented such that the largest dimension was in the plane of walk-off. By using the beam compressor it was also possible to vary the beam size within the crystal. This allowed threshold measurements to be made for different beam sizes and observations to be made on how this affected the energy density threshold. The threshold was measured by first optimising the performance of the OPO at high pump energy densities and then reducing the pump energy until the OPO only oscillated on 1 in 5 shots (this was the criterion taken for determining threshold as described in chapter 4.4.2). Figure 5.3 shows the results of the experiment. The largest beam size was $5.2 \times 2.6 \text{ mm}^2$. This was limited by the energy available from the pump laser. To reach threshold with this beam size, a pump energy of 75 mJ (measured at the laser and which was only 62 mJ at the OPO due to losses at the lens surfaces) was required. At the time of experimenting, this was on the limit of the energy attainable from the laser ($\sim 80 \text{ mJ}$). At the other extreme, the beam sizes were limited by the lens combinations available. The smallest beam size was $0.8 \times 0.4 \text{ mm}^2$ and at this level the relative increase in threshold was $\sim 30\%$. In xyLBO, the walk-off angle is $\rho = 1.1^\circ$ (see chapter 3.7.1), which implies that the extraordinary beam will walk-off from the ordinary beams by 0.26 mm in a 15 mm crystal. This effect reduces the interaction between the three beams and becomes progressively more pronounced as the beam size decreases. These results will be discussed further in chapter 7 where the threshold results for all the materials studied in this thesis are brought together in a comparative study.

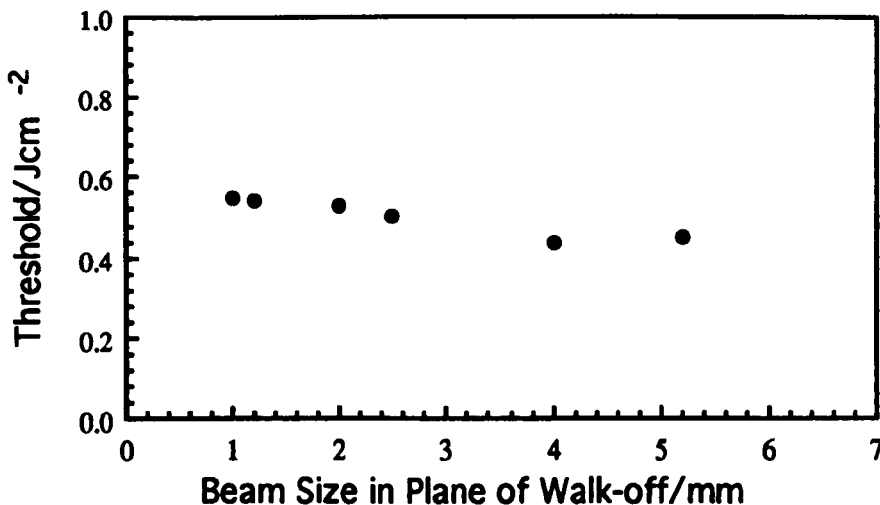


Figure 5.3. The variation in threshold with beam size. The beam sizes were measured in the vertical dimension, i.e. in the plane of walk-off.

In addition to the experiments on threshold carried out above, the variation in threshold was also measured across the attainable tuning range and this is shown in figure 5.4. The threshold was measured at various wavelengths across the tuning range in a similar manner to that described

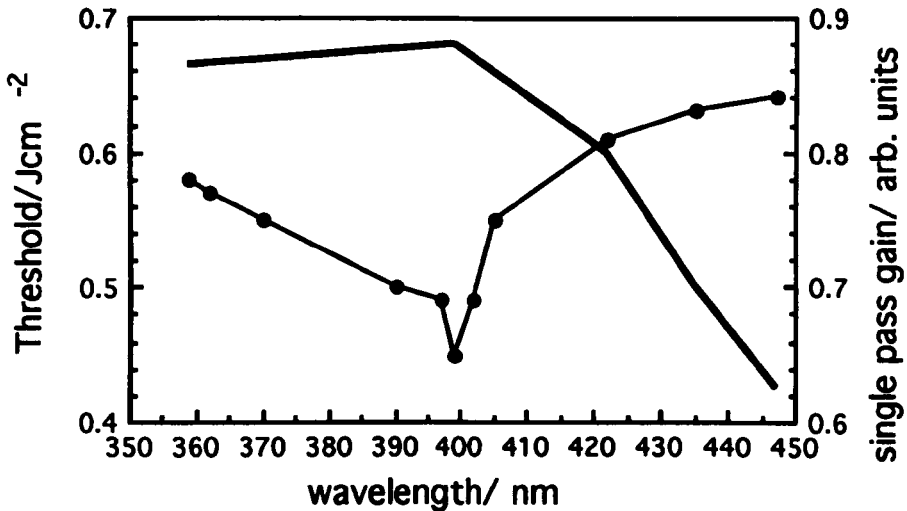


Figure 5.4. The variation in threshold across the tuning range, using a $4 \times 2 \text{ mm}^2$ beam. The dots represent measured thresholds, the thin joining line is to guide the eye. The thick line is the single pass gain expressed in arbitrary units.

above. The threshold measurements could not be extended above 498 nm or below 359 nm due to aperture clipping of the pump beam. From figure 5.4, it can be seen that there is a dip in the threshold at normal incidence. This is the same effect that was observed in NCPM LBO and yzLBO (refer to chapter 4.4.2 and 4.12.2) and is caused by the back reflections from the crystal faces being reflected off the cavity mirrors at normal incidence. It is difficult to measure the amount by which the threshold is reduced by this effect because there is an additional effect, due to the single pass gain, superimposed on it. Figure 5.4 also shows the theoretical single pass gain measured in arbitrary units as it varies across the tuning range. This is calculated from equation 2.9, for single pass gain given in chapter 2. The gain rolls off towards degeneracy because of the decrease in the effective non-linear coefficient, $d_{\text{eff}} = d_{32} \cos \phi$ ($\phi = 60^\circ$ at degeneracy). At degeneracy it has fallen to a value 0.65 times that of at normal incidence. Towards the UV/IR end of the tuning range, the single pass gain is reduced by the degeneracy factor present in the gain, i.e. $\omega_s \omega_i$, which becomes smaller as the separation in signal and idler wavelengths is increased. Fortunately, the peak gain occurs at normal incidence. Clearly there is a direct correlation between the increase in the threshold and the reduction in d_{eff} . The juxtaposition of the peak of the single pass gain with normal incidence makes it difficult to separate the individual effects.

The oscillation threshold model of Brosnan and Byer, which was discussed in chapter 2, allows a theoretical prediction of threshold to be made. With a pulse duration of 17 ns, a crystal length of 15 mm, an effective non-linear coefficient at 385 nm of 0.77pm/V and a mirror reflectivity, $R=0.9$, the threshold can be calculated to be 0.89Jcm^{-2} . The measured threshold at 385 nm using a beam sufficiently large to make walk-off effects negligible (e.g. $4 \times 2\text{mm}^2$) was 0.55Jcm^{-2} . As mentioned in chapter 2.9, the model often predicts a value for the oscillation threshold up to twice the value of the measured threshold. This may be due to double pass effects of the pump.

5.4 Pump Depletion vs. Beam Size

Following the measurements of threshold made in the last section, a series of experiments were carried out to measure the external efficiency and the pump depletion of the device when it was operating above threshold. The energy of the pump laser was again controlled using the gas cell attenuator (G) shown in figure 5.1. Various beam sizes were used in the experiments. These ranged from $4 \times 2\text{mm}^2$ to $1 \times 0.5\text{mm}^2$ and were achieved by changing the lens combination as before. The $5.2 \times 2.6\text{mm}^2$ beam size was not used because there was insufficient energy available to pump the OPO significantly above the oscillation threshold of $\sim 62\text{mJ}$. The results were all taken at normal incidence, so the generated waves were at 398.5nm and $1356\mu\text{m}$. The measured pump depletions are shown in figure 5.5. The maximum energy density used was $\sim 1.0\text{Jcm}^{-2}$ (measured at the OPO), which was set by the damage threshold of the cavity mirrors, except in the case of the $4 \times 2\text{mm}^2$ beam where the maximum pump energy density at the OPO was 0.75Jcm^{-2} , set by the maximum pump energy available (80mJ at the laser, 60mJ at the OPO). Although the lowest threshold was obtained with the $4 \times 2\text{mm}^2$ beam, the maximum pump depletion was obtained using the $3 \times 1.5\text{mm}^2$ beam size because higher energy densities could be obtained. The slope efficiencies obtained using the $3 \times 1.5\text{mm}^2$ and the $4 \times 2\text{mm}^2$ are essentially the same. As the beam sizes were decreased from $3 \times 1.5\text{mm}^2$ down to $1 \times 0.5\text{mm}^2$, there is an increase in threshold as described above and in addition there is a reduction in the slope efficiency. The reliability of the OPO pumped by the $1 \times 0.5\text{mm}^2$ beam was insufficient to obtain any efficiency results.

The observation of a significant reduction in oscillation threshold as the beam size decreases can be explained by two factors. Firstly, the compressed beam has a greater divergence, which results in a reduction in the single pass gain through the Δk term. This effect can also be regarded in terms of the reduced beam size, which results in a

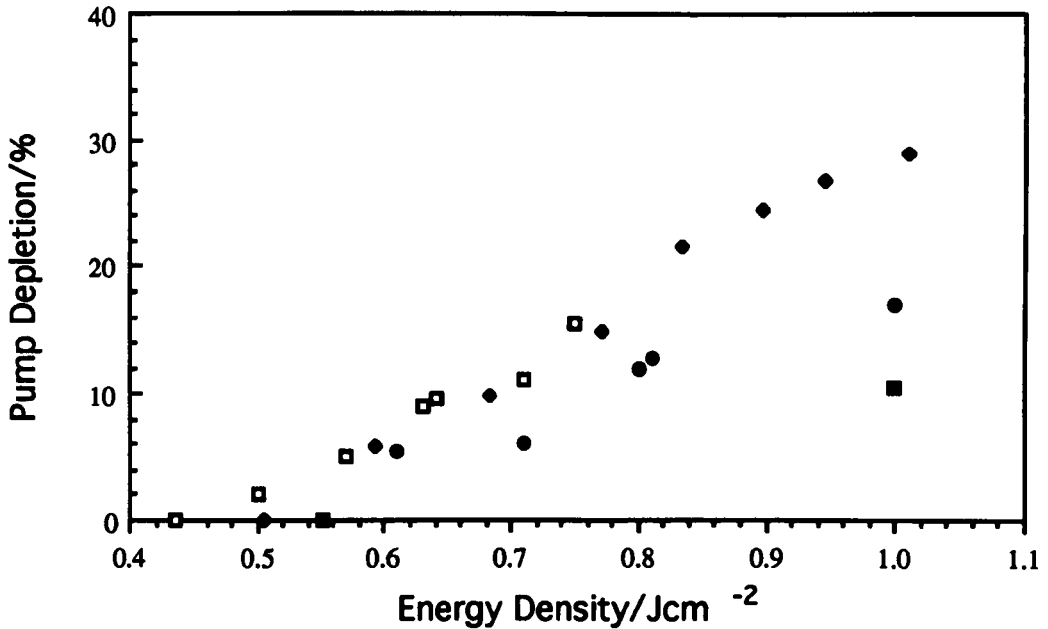


Figure 5.5. Pump depletions in xy LBO using various beam sizes. The results were taken at normal incidence (398.5 nm/ 1356 nm). KEY:- White squares:- 4 x 2 mm²; black diamonds:- 3 x 1.5 mm²; black circles:- 2.5 x 1.2 mm² and black squares:- 2 x 1 mm².

larger percentage of the pump beam walking-off from the generated signal and idler waves. This reduces the interaction between the three waves and thus the conversion efficiencies obtained. Secondly, the quality of the pump beam is reduced upon compression, as can be seen by the reduction in the damage threshold of the cavity mirrors in the presence of moderate energies confined to small spot sizes. It is, therefore, possible that one or other of these effects is responsible for the drop in slope efficiency as shown in figure 5.5.

5.5 Pump Depletion vs. Wavelength

The results in the previous section were taken at a fixed wavelength of 398.5 nm which corresponds to normal incidence in this particular crystal cut. It is, therefore, of interest to examine how the OPO performance varies across the tuning range when the beam size is constant. The optimum beam size for the energy available was, as shown previously, 3 × 1.5 mm² Figure 5.6 shows a graph of the pump depletion at four different wavelengths, taken

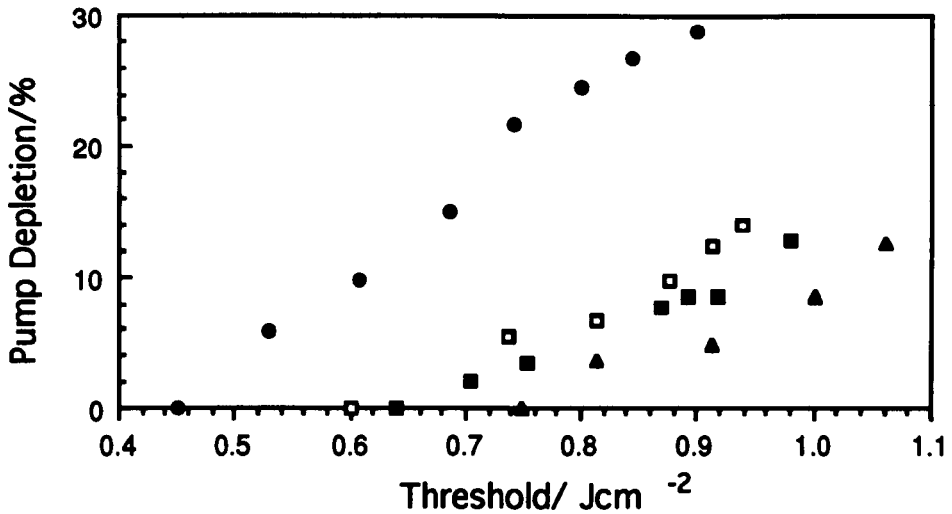


Figure 5.6. Pump depletions at four wavelengths across the tuning range. KEY:- open squares = 385 nm, circles = 399 nm, filled squares = 422 nm and triangles = 477 nm.

across the tuning range at 385 nm, 399 nm, 422 nm, and 447 nm, using a $3 \times 1.5 \text{ mm}^2$ pump beam. The highest pump depletion occurs at normal incidence, where the threshold and the intra-cavity loss are lowest due to the resonant effect of the crystal faces and the single pass gain is largest. At 385 nm, the maximum pump depletion is 12.5% at 1.4 times threshold. In the last chapter, the NCPM device, which also operated at 385 nm, produced pump depletions of only 8% at 1.4 times threshold. However, if the comparison is made in terms of pump energy instead of number of times threshold then the NCPM is far superior. This is due to the lower threshold of the NCPM device. The comparison of pump depletions between crystal geometries and further, between other crystals, is covered in chapter 7.

5.6 External Efficiency

In the previous chapter (section 4.9), it was shown that the external efficiency of the NCPM OPO differed from the pump depletion and that in some cases, this discrepancy could be significant. This discrepancy occurred as a result of the high losses experienced by the resonant wave. The large difference in the photon energies between the two generated waves in the NCPM geometry meant that a considerable 'improvement' in overall energy efficiency could be obtained by resonating the low frequency wave. Of course, the number of signal photons coupled out of the cavity did not depend on whether the cavity was resonant for the UV or IR, only that the signal photon energies differed in each case. The technique did, however, provide a useful way of efficiently extracting the desired wave from the cavity in the presence of high

intra-cavity losses. The same experiment was repeated for type I xyLBO using two sets of mirrors, the 370 nm to 420 nm set and the 1.4 nm to 1.6 μm set. Measurements of pump depletion and external efficiency are shown in figure 5.7 for operation at 385/1540 nm. Again, the discrepancy between the two (marked by the arrows) is clear and can be estimated by measuring the losses associated with each of the cavity elements. The mirror

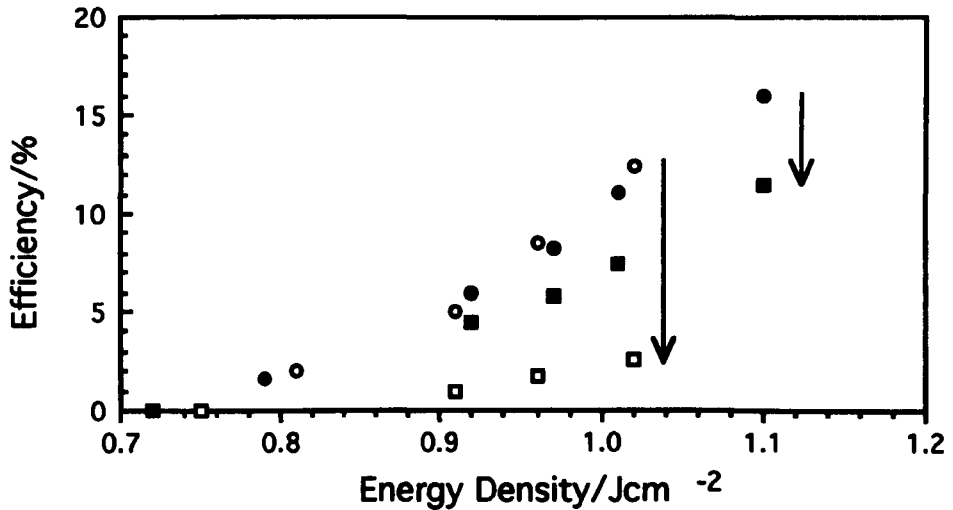


Figure 5.7. Internal and external efficiencies in xyLBO. Operation is at 385 / 1540 nm . With the IR wave resonant (BLACK) and UV resonant (WHITE) KEY:-circles = pump depletion, Squares = external efficiency. The arrows show the difference between internal and external efficiencies

losses are 10% each and the transmission loss of the crystal in a single pass is 13% due to Fresnel reflection losses. The external efficiency, η_{ext} , is related to the pump depletion, η_{int} , by¹

$$\eta_{\text{ext}} = \left[\frac{\omega_s}{\omega_p} \frac{T}{(T+L_s)} + \frac{\omega_i}{\omega_p} L_i \right] \eta_{\text{int}}$$

where T is the transmission loss through the mirrors for the signal wave, L_s is the round trip loss for the signal wave and L_i is the single pass loss for the idler. Inserting the appropriate values for the UV resonant case

$$\eta_{\text{ext}} = (0.8 \times 0.27 + 0.2 \times 0.9) \eta_{\text{int}} = 0.40$$

and for the IR resonant case

$$\eta_{\text{ext}} = (0.2 \times 0.27 + 0.8 \times 0.9)\eta_{\text{int}} = 0.77$$

The ratio $\eta_{\text{ext}}/\eta_{\text{int}}$ was measured experimentally for the UV and IR resonant cavities to be 0.25 and 0.71 respectively. The low UV resonant output coupling efficiency ($H=\eta_{\text{ext}}/\eta_{\text{int}}$) may possibly be explained by the poor quality of the UV mirrors.

5.7 Inherent Linewidth

The linewidth contributions attributable to gain bandwidth, pump beam divergence and pump beam linewidth were given for the xyLBO geometry in chapter 3. The linewidth is expected to vary from 10 nm at degeneracy to ~ 0.1 nm at 355 nm. Unfortunately, due to the limitation in tuning range imposed by the crystal aperture, the degeneracy point could not be accessed. The linewidth over the observable tuning range was measured using a 1 m focal length monochromator (Monospek 100). Over the wavelength range 480 nm to 380 nm, the linewidth varied from 0.3 nm to 0.2 nm. This can be compared to the theoretically predicted linewidth, calculated from the Sellmeier equations, which is shown in figure 5.8 along with the experimental data. As can be seen there is a reasonable agreement between the two.

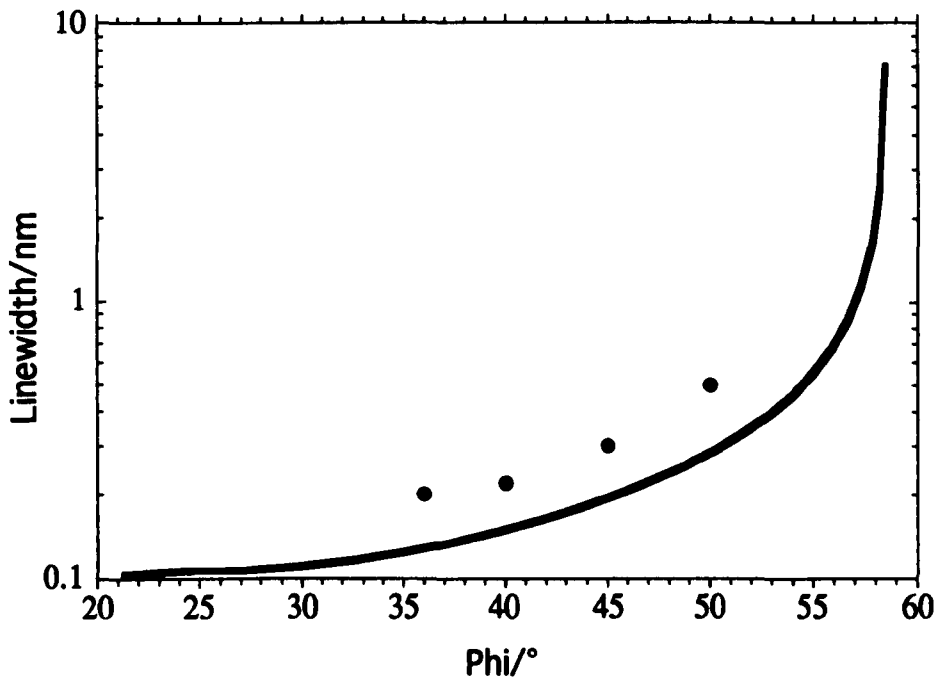


Figure 5.8 Theoretical and measured values of the linewidth in xyLBO. KEY:- circles indicate the measured linewidths, the solid line indicates the theoretical linewidth calculated using the Sellmeier equations.

5.8 Conclusions

The critically phase-matched LBO OPO operating in the xy plane displays a useful tuning range of 375 nm to 499 nm in the UV and blue, and of 1.72–0.80 μm in the infrared. The gap in this tuning range can probably be filled by using either a crystal with a larger aperture or a second crystal cut at say 46° . The linewidth of this device is of the order of 0.3 nm over the observable tuning range, although it would be expected to increase considerably on approaching degeneracy. The threshold of the device varies between 0.45 Jcm^{-2} and 0.65 Jcm^{-2} over the observable tuning range. At normal incidence, the threshold is 0.45 Jcm^{-2} . The threshold is not strongly dependent on the beam size used, varying only between 0.45 and 0.55 Jcm^{-2} over the range 4 mm to 1 mm at normal incidence. The threshold would be expected to rise significantly for beam sizes less than 1 mm because of the relatively small walk-off angle in this geometry. A comparative study of thresholds in materials is given in chapter 7.

REFERENCES

- 1 'Lasers a series of advances, vol 4'. R. G. Smith. Eds A K. Levine and A. J. DeMaria. Pub. Marcel Dekker, New York (1976). p 233.

Deuterated L-Arginine Phosphate

In this chapter theoretical and experimental results, on what is believed to be the first deuterated L-arginine phosphate (d-LAP) optical parametric oscillator, are presented.

6.1 Introduction

The non-linear optical material, d-LAP, is a monoclinic crystal with point group 2 and was first reported as such by Eimerl et al¹ in 1989. The crystal is also reported to have a single shot optical damage threshold, which is higher than that of fused silica², it is transparent down to 240 nm and possesses moderate non-linear coefficients making it an interesting choice for high power applications such as excimer pumping. In these respects, it is superior to non-linear materials like KDP and ADP, which display similar phase-matching ranges. The reported non-linear usage to date is confined to second harmonic generation reported by Eimerl et al³.

The properties noted above combine to make d-LAP an interesting material for a visible OPO. Initial experimentation with a non-critically phase-matched geometry proved the material to be highly resistant to single shot optical damage and moisture induced crystal degradation. Operation of the non-critically phase-matched geometry, which was cut for propagation along the z axis, proved unsuccessful due to lack of an adequate effective non-linear coefficient. To ensure successful operation of the second device, which is also described in this chapter, the crystal was cut for propagation along the direction of maximum effective non-linear coefficient. The calculation of this direction is outlined in the next section.

6.2 Linear and Non-linear Properties of d-LAP

6.2.1 Axis Systems

Being monoclinic, the crystallographic axes are not orthogonal and there is an angle of 98° between the a and c axes. Figure 6.1 shows the axis systems of d-LAP. The non-linear coefficient reporting frame, XYZ, (also called the piezoelectric axis system)

is oriented relative to the crystallographic axes (a , b , c) such that $a=X+8^\circ$, $b=Y$ and $c=Z$ as shown. In the XYZ system, the four independent non-linear coefficients are $d_{14}=d_{25}=d_{36}=-0.22\text{pm/V}$, $d_{16}=d_{21}=0.48\text{pm/V}$ and $d_{23}=-0.8\text{pm/V}$ (where the indices have the usual association with X, Y and Z).

The principal axes of the index ellipsoid, x , y , and z , which define the principal refractive indices, n_z , n_y and n_x are ordered such that $n_z > n_y > n_x$ and are related to the crystallographic axes by $a=x-27^\circ$, $b=y$ and $c=z-35^\circ$, when measured at 1064 nm. In d-LAP, the negative biaxial ellipsoid is used. This is the yzx axis system, where x is the polar axis, the angle θ is the polar angle and ϕ is the angle measured from y to z . The yzx axis system is subject to dispersion and rotates around the y axis. This rotation is however, thought to be small⁴ over the transparency range of the material, 350 nm to 1200 nm. Phase-matching calculations are carried out in the yzx system. To calculate the effective non-linear coefficient for these

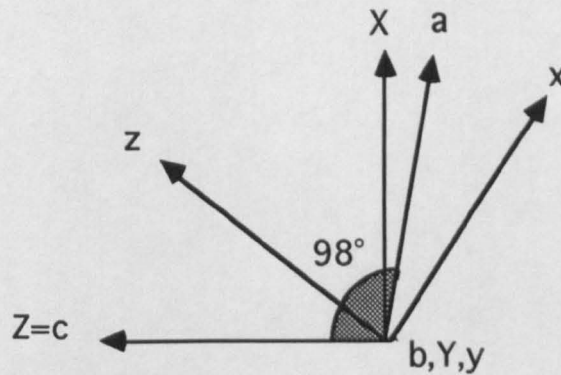


Figure 6.1. The axis systems of d-LAP. The crystallographic axes, a , b , and c , the non-linear coefficient reporting frame, X , Y and Z , and the principal axes of the index ellipsoid, x , y and z . The axes b , Y and y are out of the page. Both the yzx and XYZ axis systems are orthogonal axis sets.

phase-matching loci, it is necessary to rotate the XYZ axis system until it coincides with the yzx system.

6.2.2 Non-linear Coefficient

The two axis systems are shown in figure 6.2. Note that Z is the polar axis in the XYZ system and x is the polar axis in the yzx system. The rotation to transform $d_{ijk}^{(XYZ)}$ (the non-linear coefficient in the XYZ system) into $d_{lmn}^{(yzx)}$ (the non-linear coefficient in

the yzx negative biaxial system, as used by Roberts⁵, whose convention we follow), is achieved by a 3×3 rotation matrix, R_{ab} , thus

$$d_{lmn} = \Sigma(R_{li} \cdot R_{mj} \cdot R_{nk} \cdot d_{ijk})$$

where

$$R_{ab} = \begin{bmatrix} \cos\psi_1 \cos\psi_2 & \sin\psi_2 & -\sin\psi_1 \cos\psi_2 \\ -\cos\psi_1 \sin\psi_2 & \cos\psi_2 & \sin\psi_1 \sin\psi_2 \\ \sin\psi_1 & 0 & \cos\psi_1 \end{bmatrix}$$

R_{ab} represents a rotation through an angle, ψ_1 , about the Y axis until Z coincides with x (the two polar axes), followed by a rotation through an angle, ψ_2 , around the new Z axis until X coincides with y and Y with z . In d-LAP, the angles, ψ_1 and ψ_2 , are $+125^\circ$

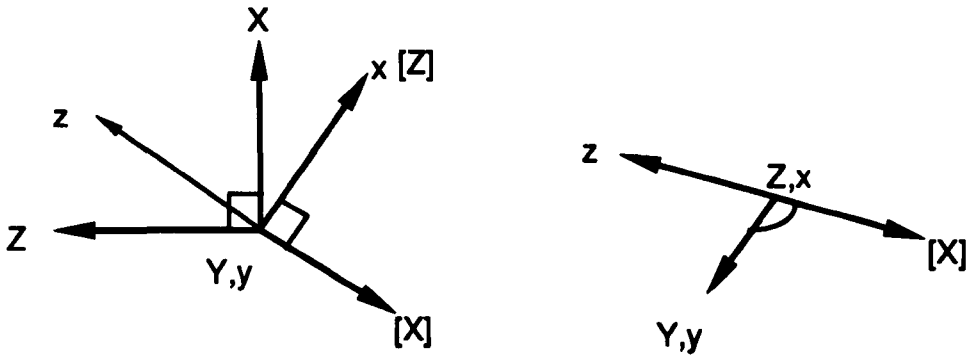


Figure 6.2. Rotation of the XYZ axis system to coincide with the yzx negative biaxial system. The axes of the non-linear coefficient are denoted by X, Y, Z . These are rotated through 125° about the Y axis and this intermediate state is denoted by $[X], Y$ and $[Z]$ (as shown in the diagram on the left). These are then rotated 90° about Z until $[X]$ coincides with y , and Y with z (as shown in the diagram on the right).

and $+90^\circ$ respectively. Transforming $d_{ijk}^{(XYZ)}$ to $d_{lmn}^{(yzx)}$ and adopting the contracted notation, $d_{l\mu}$, as described in chapter 2.2 gives

$$d_{l\mu}^{(yzx)} = \begin{bmatrix} 0.69 & -0.59 & 0.27 & 0.53 & 0 & 0 \\ 0 & 0 & 0 & 0 & 0.53 & -0.59 \\ 0 & 0 & 0 & 0 & 0.27 & 0.53 \end{bmatrix}$$

Multiplying the terms of $d_{\mu}^{(yzx)}$ by Miller's coefficient (see chapter 2.10) gives

$$d_{\text{eff}} = \begin{bmatrix} 0.803 & -0.690 & 0.308 & 0.611 & 0 & 0 \\ 0 & 0 & 0 & 0 & 0.626 & -0.700 \\ 0 & 0 & 0 & 0 & 0.306 & 0.610 \end{bmatrix}$$

for 308 nm pumping .

6.2.3 Phase-matching

The phase-matching calculations are carried out numerically using the Pascal program that is included in appendix B. d-LAP is a negative biaxial crystal so the phase-matching calculations are carried out in the yzx negative biaxial frame which has x as the polar axis with the angle, θ , measured from this axis towards the yz plane. The angle, ϕ , is an azimuthal angle measured in the yz plane and is positive when measured from y to z. By convention, the direction cosine matrices of chapter 2 are given in the yzx axis system. Hence, the equations for the two refractive indices, $n^{(1)}$ and $n^{(2)}$ must be written as

$$\frac{1}{n^{(1)2}} = \left[\left(\frac{a_x^{(1)}}{n_y} \right)^2 + \left(\frac{a_y^{(1)}}{n_z} \right)^2 + \left(\frac{a_z^{(2)}}{n_x} \right)^2 \right] \quad (6.1)$$

$$\frac{1}{n^{(2)2}} = \left[\left(\frac{a_x^{(2)}}{n_y} \right)^2 + \left(\frac{a_y^{(2)}}{n_z} \right)^2 + \left(\frac{a_z^{(2)}}{n_x} \right)^2 \right]$$

The direction cosines $a_i^{(1)}$ and $a_i^{(2)}$ are given by equation (2.14) in chapter 2. The calculation is performed (see the computer program in appendix B), by first calculating the angle between the optic axes and the x axis, Ω , from the values of the principal refractive indices at a set of specified wavelengths, λ_p , λ_s and λ_i , which are denoted in the program by the variables 'pump', 'ls' and 'li'. The angle, Ω , is then used to calculate the polarisation angle, δ , which in turn is used to calculate the direction cosines, a_{ij} . These are symbolised in the program by 'bjei'. The principal refractive indices are calculated from the Sellmeier data given in appendix A and are shown in table 6.1 for a set of three wavelengths. The index ellipsoid is near to being uniaxial with n_y and n_z being very similar. It is thus possible to identify n_x with n_e and $n_y \approx n_z$ with n_o . This is

Wavelength	n_x	n_y	n_z
308 nm	1.5434	1.6236	1.6393
430 nm	1.5176	1.5878	1.5976
1080 nm	1.4958	1.5581	1.5652

Table 6. 1. Principal refractive indices of d-LAP at three wavelengths.

useful later when dealing with Poynting vector walk-off as only the walk-off of the 'extraordinary-like' wave need be considered as it will be much greater than that of the 'ordinary-like' waves. The refractive indices can now be calculated for a given set of angles (θ , ϕ). The angles are changed in a repetitive loop until a minimum is found for

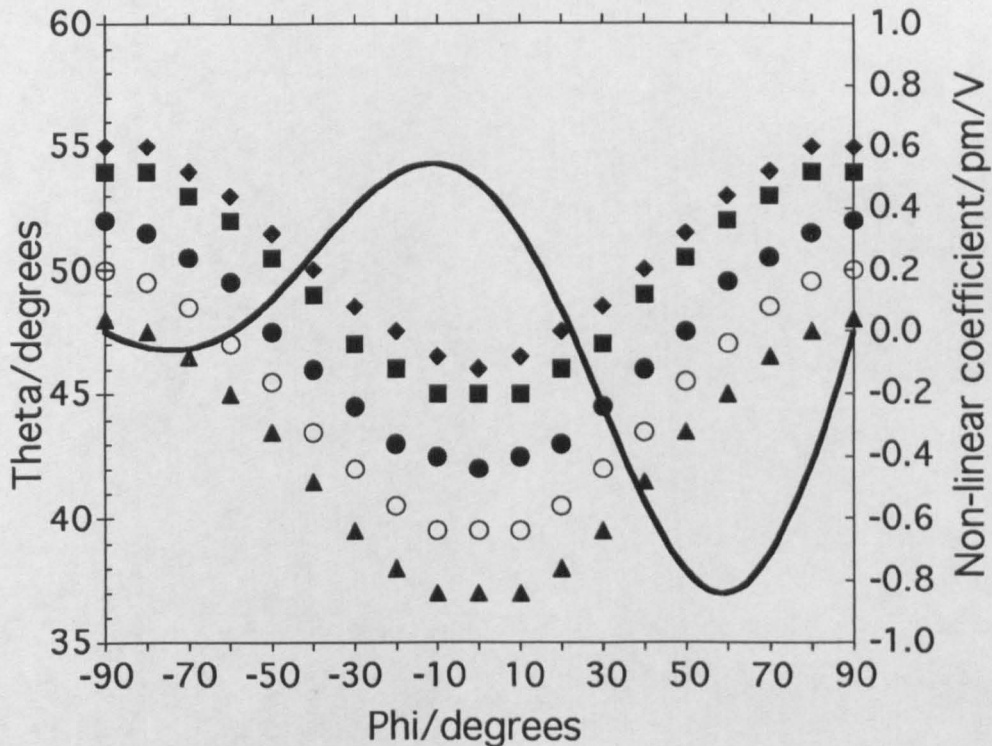


Figure 6.3. Type I phase-matching loci in d-LAP pumped at 308 nm.. The five symbol sets represent five phase-matching loci at five different signal wavelengths. The solid line represents the effective non-linear coefficient as it varies with the angle, ϕ , for the wavelength triplet (308, 430, 1085) nm. KEY:- triangles = (308, 410, 1238) nm, open circles = (308, 430, 1085) nm, filled circles = (308, 460, 932) nm, squares = (308, 520, 755) nm and diamonds = (308, 616, 616) nm (degeneracy).

the phase-mismatch, Δk . Only then is the effective non-linear coefficient calculated from the contributions of $d_{l\mu}$ using the equations given in chapter 2. This technique leads to the generation of phase-matching loci for a specified wavelength set ($\lambda_p, \lambda_s, \lambda_i$). Figure 6.3 shows 5 sets of phase-matching loci for type I phase-matching in d-LAP. Each set represents a different wavelength triplet as specified in the figure caption. The tuning range is limited by the infrared absorption edge at 1.3 μm (ref. 1) and so the maximum possible tuning range is 405 nm to 1.3 μm . The figure also shows the effective non-linear coefficient for the 430 nm locus. The maximum value of the non-linear coefficient occurs at $\theta = 48^\circ$ and $\phi = 60^\circ$. The variation of the non-linear coefficient with θ (not shown) over the range 45° to 55° is only -10%. The non-linear crystal was cut at this angle to access the maximum single pass gain.

6.2.4 Crystal Cut

Table 6.2 shows the various parameters affecting the performance of the device.

Acceptance Angle	Acceptance Bandwidth	Walk-off Angle	Non-linear Coefficient
0.24 mR cm	0.17 nm cm	57 mR	0.9 pm/V

Table 6.2. Parameters affecting OPO performance

The parameters are calculated in the same way as for LBO in chapters 4 & 5 and as outlined in chapter 2. The non-linear coefficient is similar to that of type I xyLBO, although the walk-off angle is greater, at around 57mR ($\sim 3^\circ$), for the 'extraordinary like' wave compared with only 1.1° for LBO. The acceptance angle and bandwidth are also less than those of LBO. It is the four parameters given in table 6.2 that decide the optimum length of the crystal. Table 6.3 shows the values of these parameters for various crystal lengths. It also shows the relevant parameters of the pump laser. The calculation for the expected threshold is made by putting appropriate values of crystal length into equation (2.26) in chapter 2. The loss is taken to be the Fresnel reflection loss which is the same in each case.

It is noted that the acceptance angle is always significantly less than the divergence of the excimer beam. Experience with BBO, which exhibits a similar acceptance angle, shows that the walk-off angle is a more indicative parameter when assessing the effect of the pump beam divergence and beam size on the threshold of the OPO. As a guide, a beam walk-off of 70% in BBO leads to a doubling of the oscillation

threshold*. The effect of walk-off can always be reduced by using larger beam sizes. However, this action is limited by the available crystal apertures and by the

Crystal Length/ mm	Expected Threshold / Jcm^{-2}	Acceptance Bandwidth/ nm	% Overlap of Beams at End of Crystal	Acceptance Angle/ mR
15	1.10	0.13	79%	0.16
20	0.82	0.09	71%	0.12
25	0.66	0.07	64%	0.10
30	0.56	0.06	57%	0.08
Excimer Laser	N.A.	0.0035	4 mm beam	1 mR (4mm beam)

Table 6.3. Comparison of expected OPO performance for different crystal lengths. The expected threshold is calculated by using the appropriate crystal length in the Brosnan and Byer model discussed in chapter 2. The expected beam overlap is calculated from the walk-off angle and crystal length. The last row contains data on the pump laser. (Linewidth, beam size (vertical dimension) and beam divergence)).

maximum pump energy available. Beam sizes in the 2 mm to 3 mm range are the most convenient given the pump energy available and thus a d-LAP crystal with a length greater than 30 mm is likely to exhibit large increases in threshold due to walk-off effects. The crystal used for the OPO experiments was $25 \times 5 \times 5 \text{ mm}^3$, which is a modest volume for a crystal of d-LAP.

6.3 OPO Set-up

The d-LAP crystal used in the experiments was $25 \times 5 \times 5 \text{ mm}^3$ and had uncoated entrance and exit faces. The vertical sides of the crystal were polished parallel to the plane formed by the pump beam propagation direction k and the 3 axis, as shown in figure 6.4. The polarisation angle δ shown in the figure is the angle between the polarisation eigenstate e^1 and $3-k$ plane. The definition of δ is given in chapter 2.4. An investigation of the optimum pump polarisation was never completed due to damage problems, which are described in this chapter.

* The experimental results will be shown in chapter 7 along with a more detailed study of walk-off effects in OPOs.

The system layout is shown in figure 6.5. The pump laser was a 308 nm excimer laser capable of delivering 17 ns pulses with energies of up to 100 mJ as is described in chapter 4. The energy of the pump pulses was controlled by the pressure of NO_2 gas in a fused silica cell. The polarisation of the laser was vertical, fixed by two polarisation plates, one between the two oscillators, the second after the output of the power oscillator. The beam was compressed from its original dimensions of $20 \times 10 \text{ mm}^2$ to a selection of different sizes via a beam compressor. The beam compressor was constructed from a 1m converging lens and an assortment of diverging lenses (15 cm, -20 cm and -25 cm). The converging lens was anti-reflection coated for 308 nm. The

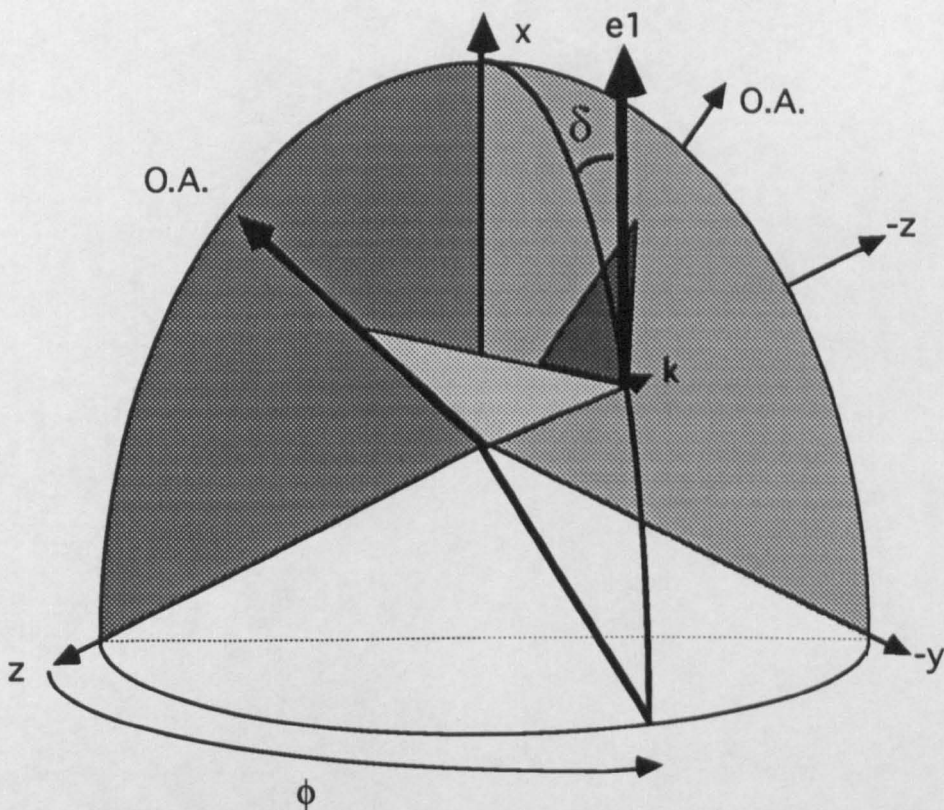


Figure 6.4. The polarisation angle, δ . The pump polarisation within the crystal is at an angle δ to the k - x plane in the negative biaxial frame yzx . The two optic axes (O.A.) are at an angle $\Omega=72^\circ$ measured from the z axis. The polarisation eigenmode, e^1 , is defined as the bisector of the two planes formed between the k vector and each of the optic axes., (the triangular planes shown shaded). The polarisation eigenmode, e^2 , is orthogonal to e^1 and k .

diverging lenses were uncoated because of the danger of damaging the coatings with the high energy densities used. The pump beam was carefully collimated before entering the OPO cavity. The cavity itself was constructed from two plane parallel mirrors, designed to transmit the 308 nm pump and to reflect only the signal beam. The OPO was designed to work as a singly resonant oscillator (SRO). From the theoretical phase-matching loci, the signal wavelength at normal incidence was concluded to be 430 nm. Mirrors with reflectivity of $\sim 90\%$ between 420 nm and 480 nm were selected. The crystal was mounted on a dual rotation stage, which allowed rotation about the vertical (i.e. about the pump beam polarisation direction) and at right angles to this in a horizontal plane. Vertical and horizontal translations were also possible to allow the aperture of the crystal to be aligned with the pump beam. Initially, the crystal was oriented with the pump beam propagation direction normal to the faces. The crystal was mounted open to the air and was not

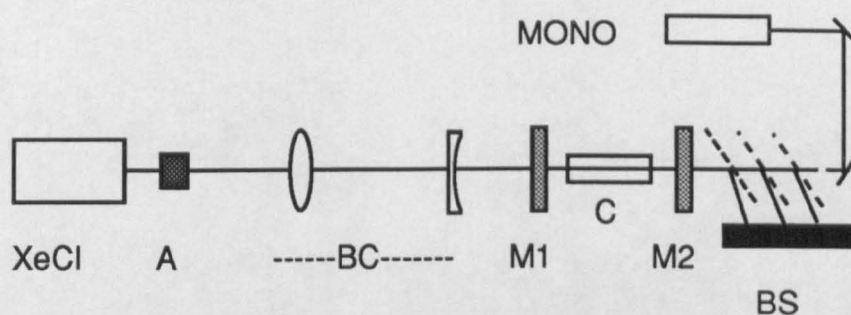


Figure 6.5. System layout. KEY:- XeCl = excimer laser, A = gas attenuator cell, BC = beam compressor (4–7 times), M1 & M2 = OPO mirrors, C = $25 \times 5 \times 5 \text{ mm}^3$ d-LAP crystal, BS = beam steering plates (x3) plus beam stop, and MONO = Monospek 1 m focal length monochromator.

contained within a hermetically sealed cell nor under phase-matching fluid. Since d-LAP is grown from an aqueous solution it is hygroscopic. However, experience with a previous piece of d-LAP (see section 6.1) had shown that the material did not suffer degradation from being exposed to the air in the laboratory. Since the penalty of keeping the crystal in a cell is to lengthen the cavity considerably, the decision was taken to mount the crystal in an open holder. The resultant cavity length was 30 mm, which allowed sufficient room for the crystal to be rotated. After the OPO cavity, a set of three dichroic plates were used to deflect the remainder of the pump beam. They were designed to be highly reflecting at 308 nm (p polarisation) and highly transmitting for wavelengths between 350 nm and $2.5 \mu\text{m}$ (s polarisation), when placed at

Brewster's angle . The alignment of the OPO was conducted in a similar way to that outlined in chapters 4 and 5 for LBO.

6.4 Experimental Results

The crystal growers had warned that there might be a damage problem with d-LAP when pumping at 308 nm. As a precaution, the experiments requiring the lowest energy densities were carried out first. The initial measurement taken was of the oscillation threshold at normal incidence for a $3 \times 1.5 \text{ mm}^2$ beam size. This was measured to be 0.39 Jcm^{-2} , which is approximately half that expected from the Brosnan and Byer model (0.66 Jcm^{-2}) (see table 6.3 above). The pump energy was 18 mJ at the front OPO mirror.

6.4.1 Tuning Range

Using the 1m focal length Monospek monochromator, the tuning range of the OPO was measured. At normal incidence, the signal wavelength was 413 nm. The corresponding idler was calculated to be 1211 nm. By turning the rotation stage in a plane defined by the pump polarisation and the propagation direction, the tuning range

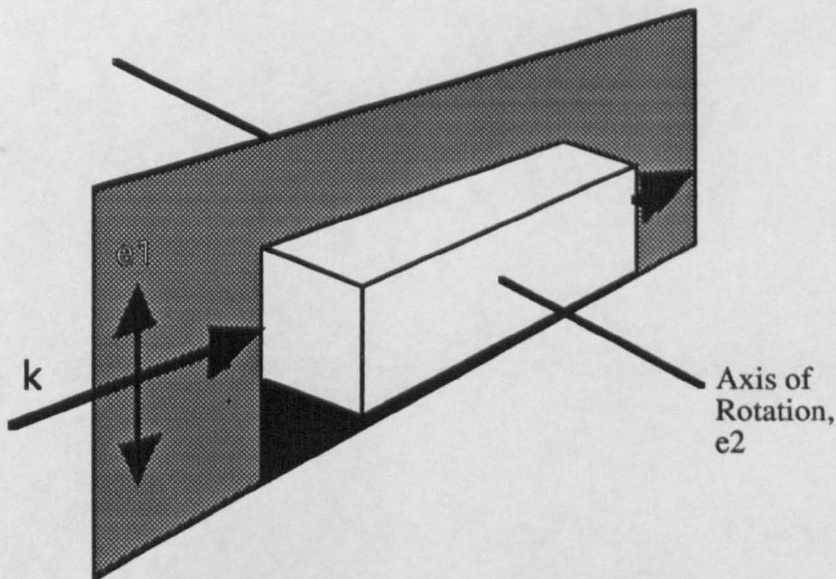


Figure 6.6. Rotation of the OPO crystal. The crystal was tuned in the plane formed by the pump wavevector k , and the polarisation eigenmode e^1 . This is approximately equivalent to saying that the rotation is about the e^2 signal (although the two are not exactly orthogonal due to dispersion).

of the device was measured. The crystal rotation is shown in figure 6.6. It is equivalent, in terms of the index ellipsoid reference frame, to keeping the angle, ϕ , constant and varying θ . The measured and theoretical tuning ranges are shown in figure 6.7. The measured tuning range is from 410 nm to 500 nm in the visible, with the corresponding idler wave covering the range 802 nm to 1.24 μm . To achieve this the crystal was rotated through an angle of 8° . The experimental results in the figure have been converted from external crystal angles to internal crystal angles using Snell's law, with the appropriate refractive index obtained from the Sellmeier equations. This allows a direct comparison between the measured and expected results. Clearly there is a discrepancy between the measured and expected wavelengths, which is nearly constant over the tuning range. At normal incidence, the measured wavelength was 413 nm, compared to the predicted wavelength of 430 nm. This may be due to a number of factors. Firstly, the crystal faces may not be polished perpendicular to the intended propagation direction, which in turn may not be correctly oriented. This would mean that normal incidence was not at $\theta=48^\circ$ and $\phi=60^\circ$ thus changing the phase-matching conditions. According to the crystal manufacturers (ref 4), this error could be as great as $\pm 0.5^\circ$. From the figure of the phase-matching

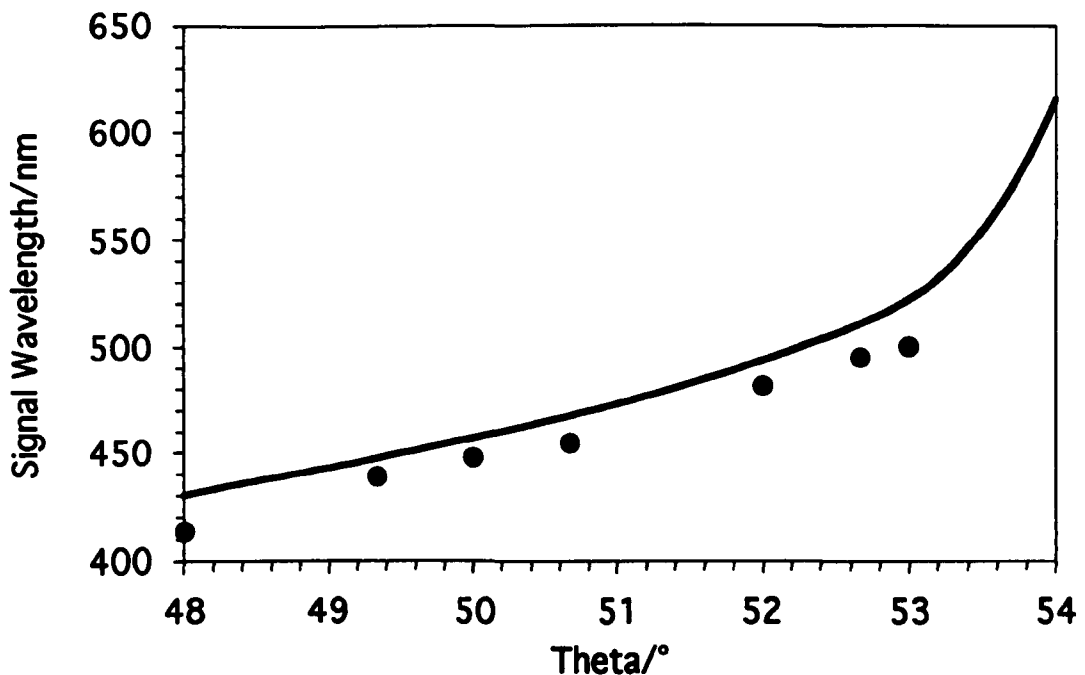


Figure 6.7. The tuning range of d-LAP rotated in the $k-e^l$ plane. The measured data is represented by the dots and the solid curve represents the theoretical tuning range.

loci, figure 6.3, it can be seen that 2° is the smallest error needed in the angle at which the crystal is cut to account for this wavelength discrepancy of 15 nm. Secondly, the index ellipsoid may rotate about the y axis over the transparency range. This is not taken into account in the theoretical calculations of the phase-matching loci. Thirdly, there may be a discrepancy in the Sellmeier data for d-LAP. This is quite common in new materials when there are few experimental results. In the cases of LBO and BBO, many revisions of the Sellmeier equations took place before satisfactory results were achieved across the tuning range, (see appendix A).

As a further exploration of the tuning capability of d-LAP, the crystal was rotated in a plane at right angles to the rotation described above. The measured tuning range is shown in figure 6.8 along with the theoretically predicted tuning range. The predicted range is based on the crude assumption that θ has been kept constant and ϕ has been varied during this rotation. As can be seen from the graph, the tuning rate in this direction is slower than that of the previous experiment. Again, there is discrepancy

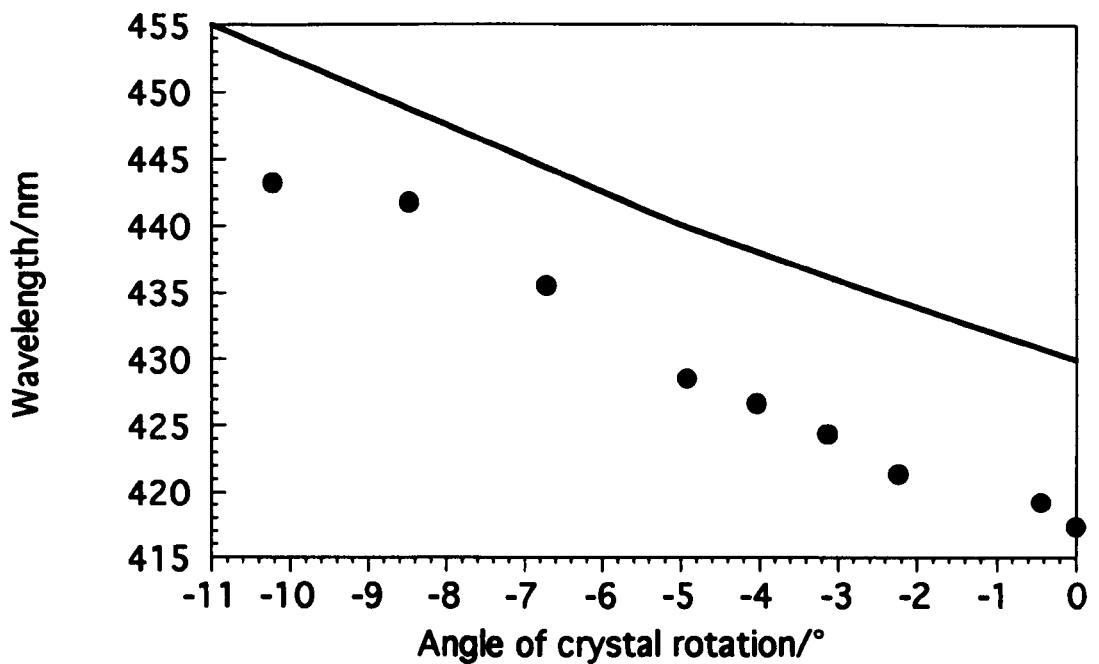


Figure 6.8. The tuning range of d-LAP about e^l . The dots show the measured signal wavelength against internal crystal angle. The solid line shows the theoretical approximation to this tuning range assuming that the rotation is similar to keeping θ constant.

between the measured and expected wavelengths of 17 nm at normal incidence. The same potential causes are still relevant, but in addition, in the experimental results, both angles (θ and ϕ) are changing to an extent, whereas the calculation assumes only ϕ changes.

It will be noticed in the two figures that there is no appreciable tuning to wavelengths shorter than 413 nm, (normal incidence). This is due to the absorption of the idler in d-LAP above 1.24 μm . The tuning range can, however, be extended further into the visible by combining the two rotations outlined above. This maximises the use of the crystal aperture. By performing the two rotations, a tuning range of 410 nm to 526 nm in the visible and 1.24 μm to 743 nm was achieved. In order to reach degeneracy, a further rotation, in a plane parallel to the pump polarisation (which gives the fastest tuning rate), of $\sim 2^\circ$ (external crystal angle) would be required. Due to the lack of tunability towards the UV, it would be better to obtain the crystal cut at a more central angle of $\theta = 52^\circ$ and $\phi = 60^\circ$. This would enable tuning across the entire range of 410 nm to 616 nm to be achieved with the corresponding idler wavelength tuning out to 1.24 μm .

6.4.2 Linewidth

The linewidth at normal incidence was measured using the monochromator. A photomultiplier tube was used to detect the light transmitted through the monochromator. The linewidth was measured to be 0.3 nm (FWHM) and a trace is shown in figure 6.9a. Using the linewidth equation derived in chapter 2, the linewidth at normal incidence can be calculated to be 0.2 nm. This is shown in the theoretical

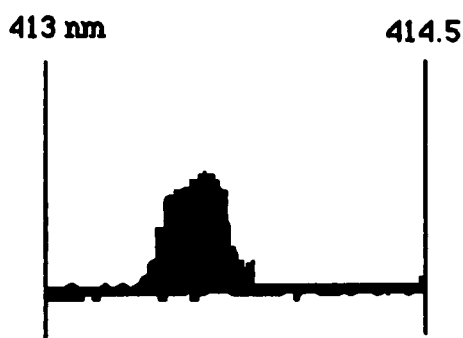


Figure 6.9a. Measured linewidth of d-LAP at normal incidence. FWHM linewidth = 0.3 nm.

plot of signal linewidth against wavelength given in figure 6.9b. By comparison BBO, which has a similar rate of tuning in the 413 nm region, has a calculated linewidth of 0.5 nm and a measured linewidth of 0.6 nm.

6.4.3 Oscillation Threshold

Measurements of the oscillation threshold were made using a Scientech power/energy meter to record the pump energy entering the OPO. Threshold was gauged by an arbitrary rule of successful oscillation on 1 shots in 5 pump pulses. Using this rule, the energy of the pump was steadily reduced, using the gas cell attenuator, until the oscillation threshold was reached. Due to the energy density of the laser, it was necessary to measure the laser energy immediately before the first lens, see figure 6.5. The loss encountered at the first lens of the beam compressor is negligible since it is

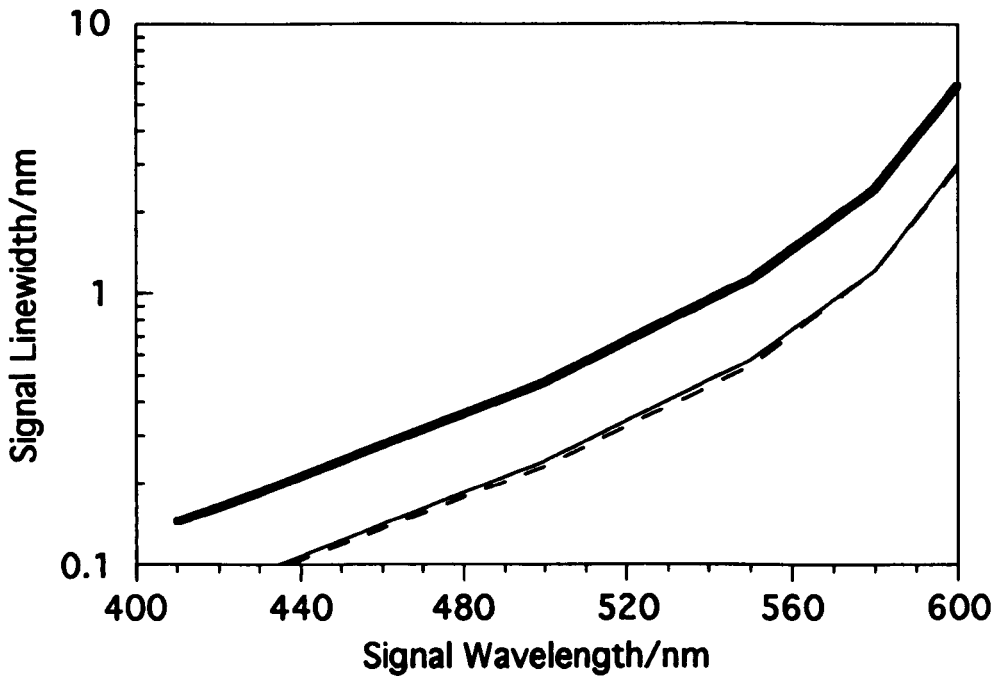


Figure 6.9b. Theoretical signal linewidth. The thin lines represent the two linewidth components dv_{s1} (solid) and dv_{s2} (dashed) and the thick line is the total signal linewidth. (see section 2.6).

anti-reflection coated at 308 nm. However, the second lens is not coated and losses of 4% per surface must be assumed. The measured threshold for normal incidence operation with a $5 \times 2.5 \text{ mm}^2$ beam was 0.3 Jcm^{-2} . This is approximately half the value

predicted by the Brosnan and Byer model (see chapter 2). This may be due to slight reflections of the pump or idler from the cavity mirrors. This makes the SRO assumption used in the Brosnan and Byer model invalid.

Since the beam is propagating in a critically phase-matched geometry, Poynting vector walk-off will be an issue effecting threshold. Figure 6.10 shows the measured variation in threshold with beam size. The various beam sizes were achieved by varying the lens combination, to produce collimated beams of the desired size. The upper limit on the beam size was set by the crystal aperture and the lower limit by the available lenses. The graph clearly shows the rise in threshold as the beam size

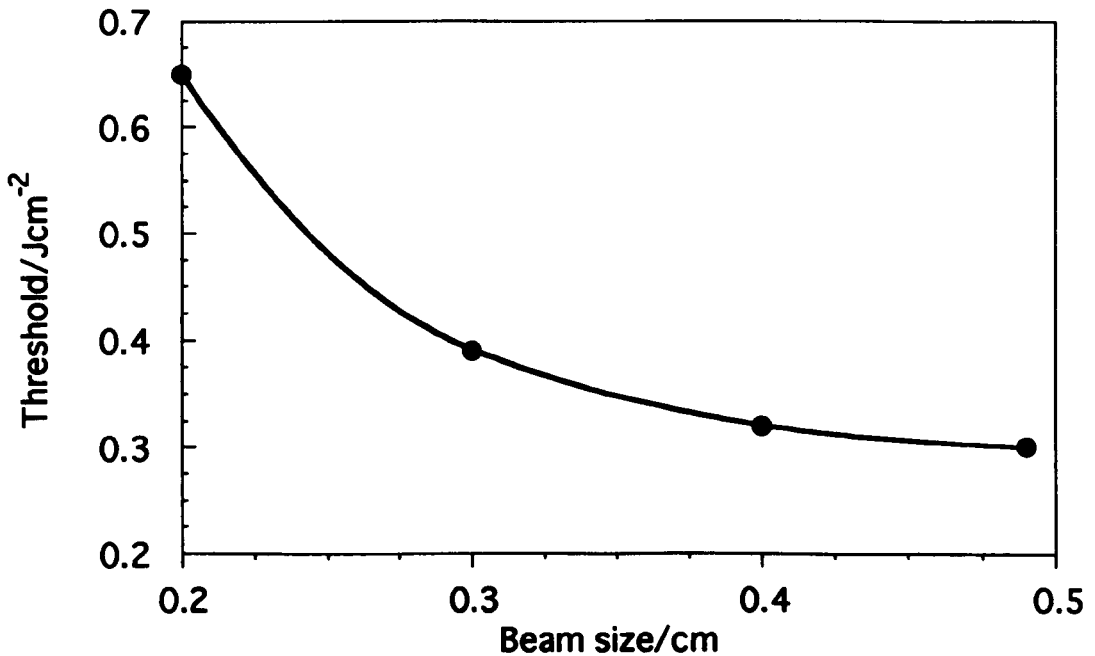


Figure 6.10. The variation of threshold with beam size. The solid line is a best fit through the experimental data.

decreases, which is an indication of how the presence of walk-off reduces the beam interaction area. As can be seen from figure 6.10, the increase in threshold is a factor of 2 when the beam size is decreased from 5 mm to 2 mm. Complete separation of the beams would occur when the beam width $W_B = W_W = l \tan \rho$. This happens for a beam of width, $W_W = 1.44$ mm. The reduction in threshold clearly becomes significant before the complete walk-off of the beams occurs. A comparison of the effect of walk-off on thresholds and pump depletions in various materials is given in chapter 7.

The above results are taken at normal incidence, which corresponds to 413 nm and 1211 nm for the signal and idler respectively. Further experiments were undertaken to measure the change in threshold over the tuning range of the device. Figure 6.11 shows the results taken at a number of discrete wavelengths. Rotating the crystal away from normal incidence, towards degeneracy, did not change the threshold significantly, although it was observed that towards the visible, the threshold began decreasing. Operation of the device further into the ultraviolet was not successful due to the sharp rise in threshold. The figure clearly shows a sharp rise in threshold as the OPO is tuned further into the

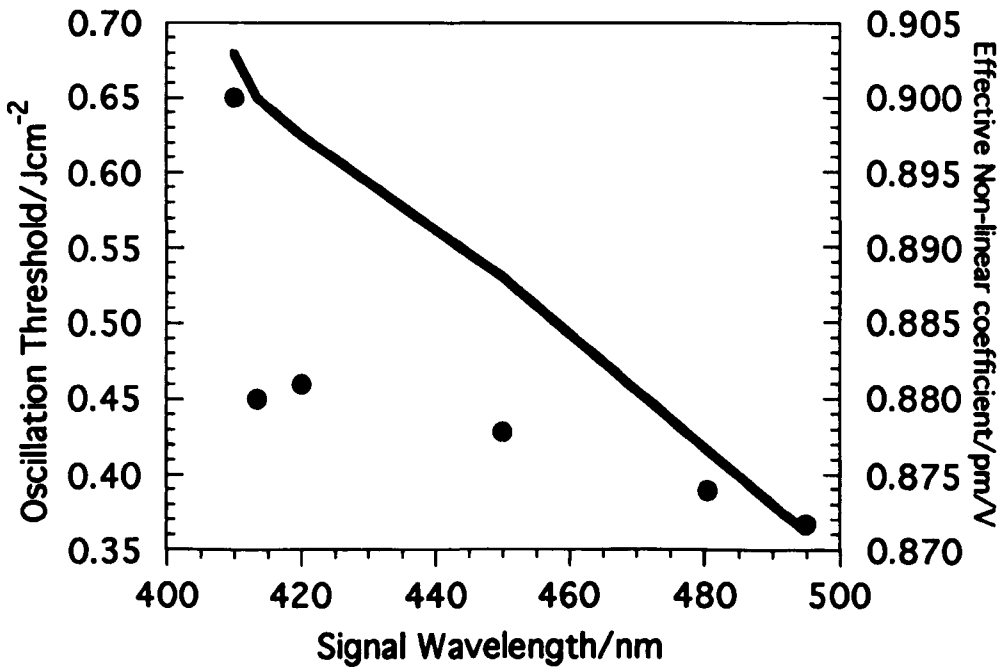


Figure 6.11. The variation of oscillation threshold with wavelength. The dots represent the measured threshold at various wavelengths across the tuning range. The solid line shows the variation in effective non-linear coefficient across this range.

UV, despite an increasing non-linear coefficient (also shown in the figure). The increased threshold is presumably due to the increase in absorption at the idler wavelength, caused by the known presence of the infrared absorption band at about 1.25 μm .

6.4.4 Multi-shot Damage

So far no sign of damage to the crystal had been observed. The pump energies used had been limited to less than 0.5 mJ, with the exception of an attempt to operate the device below 410 nm when the pump energy was increased to $\sim 1 \text{ Jcm}^{-2}$. While attempting to measure pump depletions, however, the device began to operate erratically and eventually failed completely. The maximum observed pump depletion was 5%. Damage appeared as brown streaks throughout the volume of the crystal that lay within the pumped region. It is suspected that the damage process is intrinsic to d-LAP and is not an impurity problem. With the data available from the experiments outlined above, it is not possible to say whether the damage was caused by an accumulated energy or an incident energy density process, or some combination of both. According to the manufacturers, the problem is only evident below 350 nm and so it may be possible to pump d-LAP at 351 nm using a XeF excimer laser without encountering the damage problem. Figure 6.12 shows the possible phase-matching loci

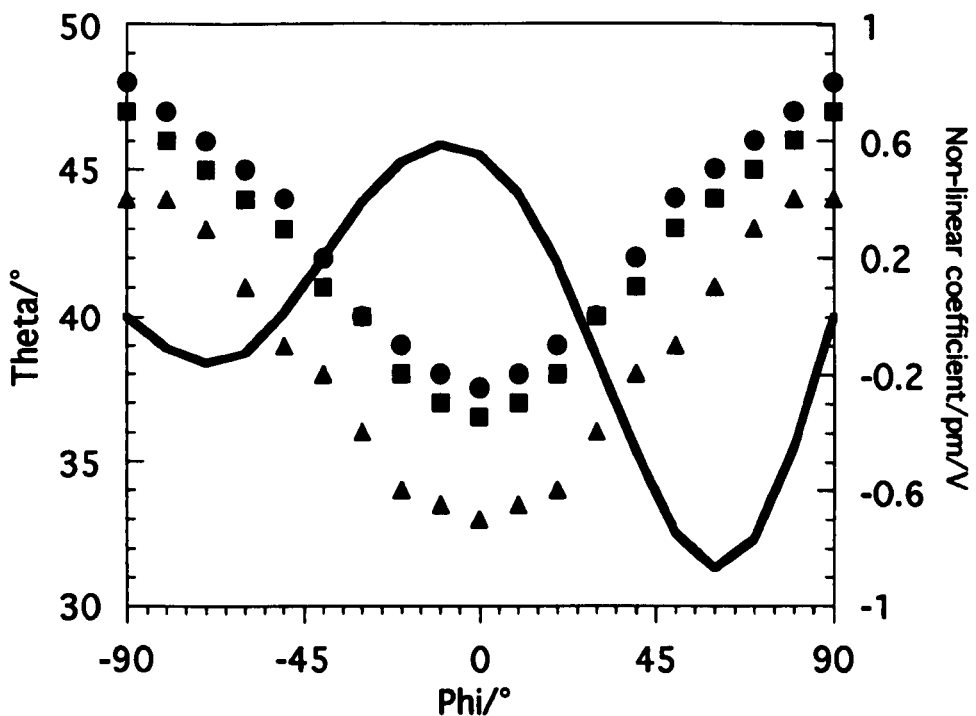


Figure 6.12. Possible phase-matching loci for 351 nm pumped d-LAP. The shapes represent three signal wavelengths and the solid line represents the effective non-linear coefficient as it varies with the angle ϕ . KEY:- triangles=520 nm, squares=600 nm and the circles = 702 nm (degeneracy). The tuning range is limited by the infrared absorption in d-LAP.

for a 351 nm pumped d-LAP OPO. Again the absorption band in the infrared limits the tuning range both in the infrared and ultraviolet. The predicted non-linear coefficient is also shown in figure 6.12. Its peak value of 0.9 pm/V is slightly larger than that for 308 nm pumping.

6.5 Conclusions

From the experiments carried out on this material, it seems that the inherent damage problem below 350 nm prohibits applications involving pump sources in this spectral region. It may however, be possible to construct an OPO pumped at 351 nm by an XeF excimer laser and achieve a tuning range of ~520 nm to 1.2 μm . It is likely that it will display similar characteristics to the 308 nm pumped version, in terms of thresholds and walk-off limitations. There also exists the possibility of using a tripled Nd:YAG system operating at 355 nm, to obtain an almost identical tuning range to the 351 nm option. Both of these would provide a cost effective method of producing tunable light in the 520 nm to 1.2 μm region. The availability of large apertures and large crystals may also be important in some applications. However, it seems unlikely that d-LAP will replace materials like KDP, LBO or BBO because of its restricted tuning range.

REFERENCES

- 1 'Deuterated L-Arginine Phosphate: A New Efficient Nonlinear Crystal'. D. Eimerl, S. Velsko, L. Davis, F. Wang, G. Loiacono, and G. Kennedy. IEEE J. Quantum Electron. QE-25, 179 (1989).
- 2 'Extremely high damage threshold of a new nonlinear crystal L-arginine phosphate and its deuterated compound'. Atsushi Yokotani, Takatomo Sasaki, Kunio Yoshida and Sadao Nakai. Appl. Phys. Lett. 55, 2692 (1989).
- 3 'Temperature-insensitive phase matching for 2nd-harmonic generation in deuterated L-arginine phosphate'. Charles E. Barker, David Eimerl and Stephan P. Velsko. J. Opt. Soc. Am. B. 8, 2481 (1991).
- 4 Private communication. D. Roberts. Cleveland Crystals Inc. 676 Alpha Drive, Highland Heights, Cleveland, Ohio. (1992).

- 5 'Simplified Characterisation of Uniaxial and Biaxial Nonlinear Optical Crystals: A Plea for Standardization of Nomenclature and Conventions'. D. Roberts. IEEE J. Quantum Electron. 28, 2057 (1992).

Comparison of Non-linear Materials

In the previous three chapters, the results of experiments on two materials, namely LBO and d-LAP, were presented. In this chapter, these materials are compared with BBO, another new and much documented non-linear material, which has proved popular in the field of OPOs since it was first reported by Chen¹. The focus of the comparison is on the utility of these materials for use in a broadly tunable, narrow linewidth OPO. The effect of walk-off in these materials is also studied.

7.1 Introduction

Thus far, four phase-matching geometries, in two new non-linear optical materials, have been reported but no direct comparison of the materials has been given. In table 1.2 in chapter 1, some key parameters were tabulated for LBO, d-LAP and BBO. In this chapter, experimental results from the three materials are brought together and their suitability for different applications is assessed. Results from previous chapters, as well as some new results, are presented in a way that allows direct comparison of thresholds, efficiencies and linewidths. These three parameters are of particular interest because the next two chapters are concerned with the efficient line-narrowing of OPOs. It has already been stated that the linewidth of an OPO, particularly near degeneracy, can be very large. Linewidths of greater than 10 nm are possible, and even with a linewidth of ~ 1 nm, the applications of the device are severely limited. It is, therefore, important to investigate schemes for effectively line-narrowing OPOs to the level of a single axial mode and to select the most suitable non-linear material.

This chapter takes the form of a dual comparison, between, firstly the materials and, secondly the pump sources. Recent work on diode pumped lasers has led to advances in all solid state OPO systems². To date, the energy available from the diode pumped lasers after tripling into the UV is low, ~ 3 mJ. The availability of only low pump energies means that small beam sizes within the crystal are necessary if the energy density required to reach oscillation threshold is to be attained. The use of small beam sizes however, increases the effect of Poynting vector walk-off, which, in turn, leads to a reduction in the interaction between the ordinary and the extraordinary waves. Since

LBO has both a smaller walk-off angle and non-linear coefficient than BBO, it might be expected that there would be a cross-over point in the performance of the two materials. This, in fact, is the case and the results are presented in this chapter. The excimer pumped system, being capable of producing both high and low energy pulses, is ideal for testing the performance of materials over a wide range of pumping energies. Experimentally, there is good continuity between the excimer pumped and the diode pumped thresholds, as will be seen.

7.2 A Review of Excimer Pumped BBO OPOs

In order to carry out the comparison between the three materials, it is first necessary to present some experimental results from the BBO OPO. BBO is a uniaxial material and its Sellmeier equations are given in Appendix A. It is characterised by a large birefringence, which leads to a broad tuning range, large walk-off angle and a small acceptance angle. It is transparent from 190 nm to 2600 nm and has a large non-linear coefficient. A list of BBO OPO experiments carried out to date was given in table 1.4.

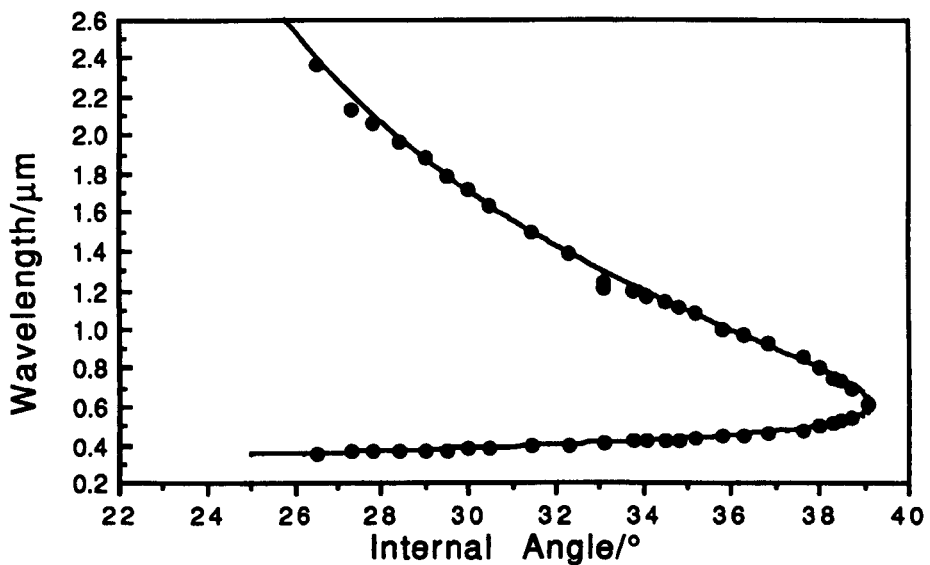


*Figure 7.1. Theoretical and measured tuning range of BBO when pumped at 308 nm.
KEY:-dots = measured tuning range; line = theoretical tuning range calculated using the Sellmeier equations in Appendix A.*

The crystal used for the experiments was a 20 mm long piece of β -BaB₂O₄ cut for propagation (at normal incidence) at 32° to the optic axis. The measured tuning range* for a BBO OPO, pumped by a XeCl excimer laser, is shown in figure 7.1. BBO has a larger birefringence than LBO and thus has a faster rate of tuning with angle. The tuning range extends from 355 nm to 2.3 μ m. This was obtained by rotating the crystal through an angle of only 10°. Associated with this fast rate of tuning, which is greatest near degeneracy, is a large linewidth, which is also greatest near degeneracy. This is shown in figure 7.2. The measured linewidth near to degeneracy is \sim 10 nm, which is close to the theoretically predicted linewidth, and falls rapidly as the OPO is tuned towards the UV/IR. The total linewidth is predominantly made up from the pump divergence component, $d\nu_{s2}$, due to the fast rate of change of wavelength with angle. The threshold of the device was measured to be typically \sim 0.15 Jcm⁻², which permits pumping at

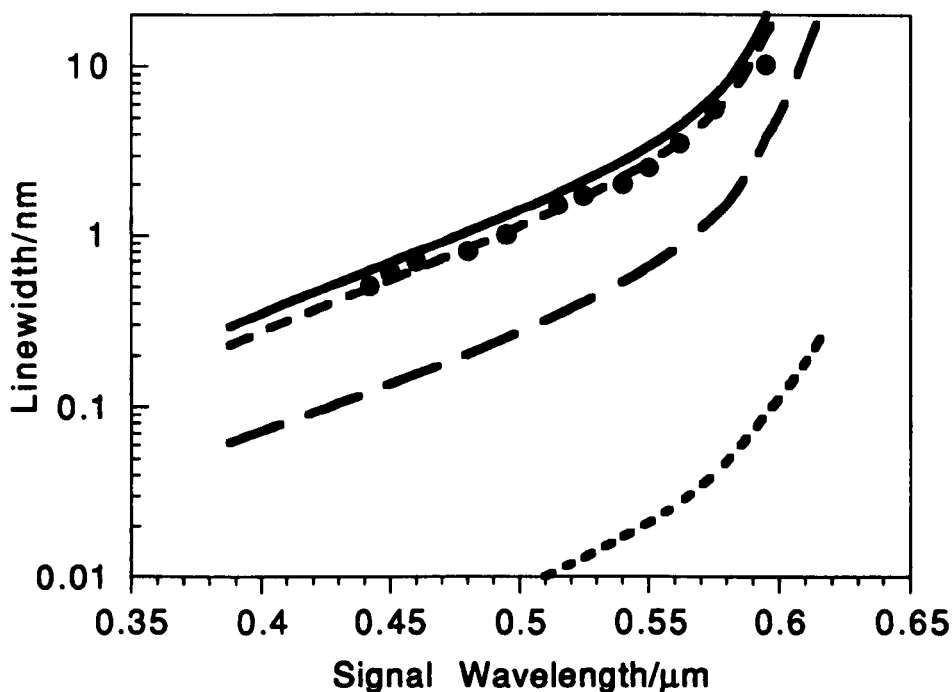


Figure 7.2. Theoretical and measured linewidth of BBO. KEY:- dots = experimental data, solid line = total theoretical linewidth, top dashed line = dn_{s2} component, middle dashed line = $d\nu_{s1}$ component and the bottom dashed line = $d\nu_{s3}$ component.

up to 7 times threshold without damage to either the crystal or the mirrors. The maximum pump depletion obtained was \sim 64% with a corresponding external efficiency

* The tuning range and linewidths were measured by M. Ebrahimzadeh and details can be found in his thesis, 'Optical Parametric Oscillators Pumped by Excimer Lasers'. St Andrews University 1989.

of 20%. The large discrepancy between the internal and external efficiencies is caused by the large Fresnel reflection losses of the crystal faces due to the high refractive indices of BBO. The high losses within the cavity reduce the output coupling efficiency, in the same way as in LBO (see chapters 4 & 5).

7.3 Comparison of Tuning Ranges

Figure 7.3 shows the tuning ranges of the various geometries and materials explored so far. The tuning range of type I BBO is the same as that of type I xyLBO. The measured xyLBO tuning range has a gap near degeneracy due to the crystal aperture. This is of no physical significance since it can be filled either by using a second crystal cut at a different angle or by using a crystal with a larger aperture.

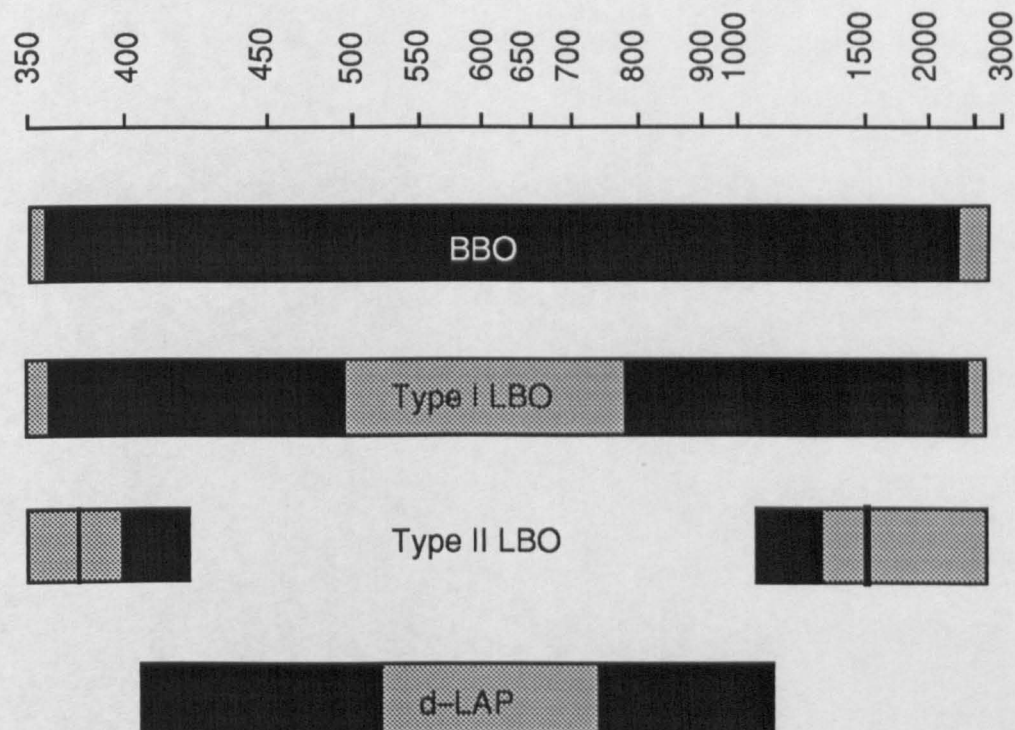


Figure 7.3. The tuning ranges of BBO, LBO and d-LAP. The grey areas represent wavelengths that are theoretically possible. The black areas represent achieved tuning ranges. The LBO NCPM tuning range is denoted by the two black lines on the type II LBO data.

d-LAP may also play a useful role in a broadly tunable, narrow linewidth device, although for excimer pumping at 308 nm, multi-shot damage is a problem.

The tuning range of the type II LBO geometry is confined to the UV and IR spectral regions and cannot be tuned over a large range. The NCPM tuning range is even more restricted and temperature tuning must be used to achieve even modest tunability. To cover 30 nm in the UV the temperature of the crystal must be raised by more than 300°C.

Thus from consideration of tuning ranges, it seems that only the type I xyLBO and type I BBO geometries are suitable for constructing a broadly tunable, narrow linewidth device. NCPM LBO and type II LBO do not possess the required tuning range and d-LAP suffers from damage problems when pumped below 350 nm .

7.4 Comparison of Thresholds

7.4.1 Excimer and Nd:YAG Pumped Systems

The results of oscillation threshold measurements for BBO, LBO and d-LAP are shown in figure 7.4. Included in this figure, with the excimer-pumped threshold results, are some data from an LBO OPO pumped by a tripled Nd:YAG laser pumped by a diode laser* . The beam sizes used by the diode pumped systems are necessarily smaller than that of the excimer system in order to reach threshold with the available energy. They provide a useful illustration of the rise in energy density threshold in critical LBO and NCPM LBO, which is not apparent with the beam sizes used in the excimer system.

The threshold results are plotted on a graph of energy density threshold in Jcm^{-2} versus energy threshold in mJ. Thus, straight lines drawn across the graph represent lines of constant beam area measured in cm^2 . The line marked on the graph is of special interest because experimentally it divides the excimer pumped OPO data from the diode pumped OPO data. To the left of the line marking $3 \times 10^{-3} \text{ cm}^2$, the white squares and black squares represent diode pumped LBO results for the type I critical geometry and the NCPM geometry respectively. The limitations on beam size for the diode pumped laser are due to the small pump energies available from this source, typically ~ 3 mJ. The limitation on beam size for the excimer system is governed by the reduction in beam quality upon compression of the beam below $1 \times 0.5 \text{ mm}^2$. At this compression level, the beam breaks up if propagated over any great distance. The line shown in figure 7.4 thus marks a practical division between two different OPO pumping options. The results obtained by the two systems are remarkably similar when the peak energy thresholds are compared.

* The diode pumped results are supplied courtesy of Y. Cui, St. Andrews University.

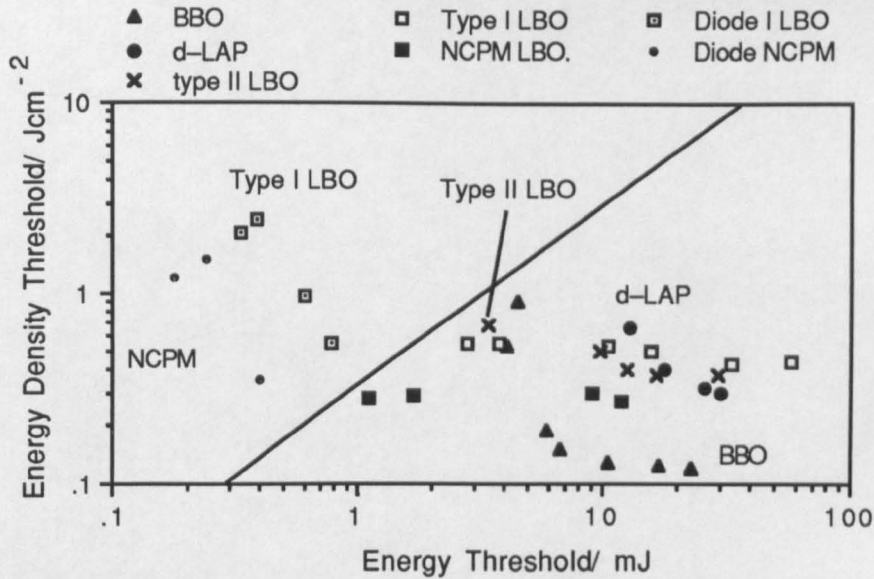


Figure 7.4. Oscillation thresholds in BBO, type I xy LBO, NCPM LBO, type II yz LBO and d-LAP. The diagonal line indicates a constant beam area of $3 \times 10^{-3} \text{ cm}^2$ which divides the excimer pumped results on the right from the diode pumped results on the left. The diode pumped thresholds are measured as peak energies. The curves through the points are to guide the eye.

From figure 7.4, it is clear that the energy density thresholds of d-LAP and BBO rise sharply as the energy available to reach threshold decreases. An effective upper limit on the energy density will be set by the damage threshold of either the crystals or the mirror coatings. The damage thresholds of LBO, BBO and d-LAP are higher than those of the mirror coatings so it is the latter that succumbs to damage first. This sets an upper limit of 1.0 Jcm^{-2} to 1.5 Jcm^{-2} for the excimer pumped OPO, (slightly higher peak energy densities have been used in the diode pumped system). The rapid increase in threshold in BBO and d-LAP is due to the effect of Poynting vector walk-off reducing the effective interaction length within the OPO. BBO and d-LAP both have large walk-off angles, 4.6° and 3.3° respectively. The effect of walk-off, for a given beam size, is greater in BBO and d-LAP than in LBO, because the walk-off angles in the LBO geometries are small, i.e. 1.1° (type I xy LBO), 0.5° (type II yz LBO) and 0° (NCPM geometry). The diode pumped data usefully illustrates the effect of walk-off in LBO. The rise in energy density threshold for the NCPM and critical type I LBO geometries is similar to those of BBO and d-LAP but it occurs at very much smaller spot sizes, which are unattainable with the excimer system. The increase in threshold in the type II LBO device occurs for a much larger beam size than would be predicted from the walk-off angle. In this geometry, the phase-matching is $o \rightarrow o+e$. Experimentally, the mode size of the signal and idler waves is often found to be smaller than the pump, thus the effect may be more pronounced when one of the generated waves is an extraordinary wave.

Figure 7.4 makes the point that there is no uniquely superior material for all applications and that the choice of material is strongly dependent on the energy requirements of the application and the pump energy available. Considering only the excimer results, the lowest energy density threshold available in the four geometries occurs in BBO, where thresholds are of the level of 0.15 Jcm^{-2} . Thresholds of this level are only attainable when pump energies of greater than 10 mJ are available. Below this energy, the energy density threshold rises sharply. From the opposite point of view, the lowest energy thresholds occur in LBO, at $\sim 1 \text{ mJ}$ for the NCPM geometry and $\sim 3 \text{ mJ}$ for the critical LBO geometry. Thus, when there is limited energy available, LBO is the favoured material. The cross-over point, in terms of pump energy, between the two critical geometries can be seen to be around 5 mJ or, in terms of beam size, for beams less than $1.8 \times 0.9 \text{ mm}^2$.

7.4.2 The Effect of Walk-off on Threshold

In chapter 2, the equivalence of walk-off and acceptance angle was postulated. The above experimental data provides interesting material with which to study this hypothesis. The results given above were explicable, in a qualitative way, by the effect of Poynting vector walk-off of the extraordinary wave (the pump wave in the type I geometries) from the other two waves. Table 7.1 lists the walk-off angles for the various

	BBO @ 400 nm	xyLBO @ 400 nm	d-LAP @430 nm	yz LBO @412 nm	NCPM LBO @385 nm
Walk-off angle, ρ	4.2°	1.1	3.3°	0.5	0°
Acceptance angle, $\Delta\theta$	0.12 mR	0.65 mR	0.2 mR	1.84 mR	57.4 mR*
$W_w = \rho L$	1.47 mm	0.29 mm	1.44 mm	0.13 mm	0
$W_\theta = \lambda/n\Delta\theta$	1.47 mm	0.29 mm	1.44 mm	0.13 mm	6 μm^*

Table 7.1. Walk-off and acceptance angles. The walk-off and acceptance angles are calculated at the same wavelength, shown at the top of each column. The crystal lengths were, 20 mm (BBO), 15 mm (xyLBO), 25 mm (d-LAP), 15 mm (yzLBO) and 16 mm (NCPM LBO). * The acceptance angle quoted is a second order acceptance angle. The first order acceptance angle becomes undefined at $\theta=0^\circ$

materials and geometries. These can be used, as outlined in chapter 2, to calculate the largest beam size, W_w , in a crystal of length, L , for which the extraordinary wave walks off completely from the other two waves.

The values of W_θ are also given. This is the width that a diffraction limited beam will have when the beam divergence equals the acceptance angle of the crystal. The values of W_w and W_θ for each material in the critical geometries are the same as expected from our discussion in chapter 2.8. The acceptance angle and Poynting vector walk-off are thus comparable ways of describing the same phenomenon. Although the walk-off angle of the NCPM geometry is zero, there exists a finite, second order acceptance angle which must be responsible for the increase in threshold when small beam sizes are used.

Figure 7.4 showed graphically the effect of walk-off on the oscillation thresholds of the various OPO geometries. If instead we take the ratio of the threshold at complete walk-off to the nominal threshold, we obtain, as shown in table 7.2, a roughly constant increase in threshold of ~ 2.3 times. Complete walk-off is deemed to have occurred when the pump beam size in the walk-off plane, W_b , equals the walk-off distance, $W_w (=l \tan \rho)$, which is shown for each geometry in table 7.2. The complete walk-off threshold,

Crystal	Walk-off Angle ρ	Crystal Length l	Walk-off Distance W_w	Complete Walk-off Threshold T_c	Nominal Threshold T_n	T_c/T_n
BBO	4.4°	20	1.47	0.35	0.16	2.2
xyLBO	1.1°	15	0.29	1.2	0.5	2.4
yzLBO	0.5°	15	0.13	unknown	0.37	N.A.
NCPM LBO	0°	16	0	N.A.	0.27	N.A.
d-LAP	3.3°	25	1.44	0.7	0.3	2.3

Table 7.2. The effect of walk-off on threshold. The walk-off distance $W_w = l \tan \rho$. The terms nominal threshold, T_n , and complete walk-off threshold, T_c , are explained in the text. The ratio T_c/T_n is roughly constant at 2.3 times.

T_c , for each of these beam sizes can then be read from figure 7.4. The nominal threshold, T_n , is taken to be the threshold when walk-off effects are small or negligible. In figure 7.4, these may be taken to be the thresholds corresponding to the largest beam sizes, since in all cases the thresholds approach a minimum asymptotically.

The ratio T_c/T_n , shown in the final column of table 7.2 suggests that the increase in threshold, if the extraordinary and ordinary waves of a type I, $e \rightarrow o+o$ interaction are allowed to separate completely, is approximately constant at 2.3 times. Thus a prediction of the effect of walk-off can be made from a knowledge of the walk-off angle, the crystal length and the likely beam sizes to be used. A similar prediction can be made using the acceptance angle instead of the walk-off angle, since in this case they give the same answers.

The type II yzLBO crystal was, unfortunately, not long enough to observe complete walk-off of the ordinary and extraordinary waves, so no value for T_c is given. Since the walk-off angle in this geometry is less than half that of the type I LBO geometry, it might be expected that the threshold would not increase significantly until the pump beam size was less than 0.6 mm (this is the turning point for type I LBO). However, the threshold is double the nominal threshold (0.37 Jcm^{-2}) when the pump beam is only 1 mm. Thus the threshold at complete walk-off (when the pump beam is 0.13 mm) is likely to be much greater than 2.3 times. As stated earlier, this may be due to the differences in mode sizes between the pump and generated waves. In general, the signal and idler are observed to have smaller beam sizes than that of the pump. Thus, if one of the generated waves is an extraordinary wave (in this case extraordinary wave is the one with the shorter wavelength), then the effect of walk-off, due to the smaller beam size, may be more pronounced.

Even in the absence of walk-off, the threshold of the NCPM geometry increases. The threshold reaches twice its nominal value when the pump beam size is $100 \mu\text{m}$. The value of W_θ given in table 7.1 was $6 \mu\text{m}$. Thus the increase in threshold is more rapid than would be expected for this geometry. Again consideration of signal and idler mode sizes and in addition the possibility that the beam quality may be reduced because of the tightly focused nature of the pump beam, may explain this.

7.5 Comparison of Efficiencies

In this section a comparison of the efficiency of each type of crystal is made. In particular the effect that walk-off has on the conversion efficiencies of the various devices is studied. This effect occurs in addition to the effect observed on the threshold.

Unfortunately, there are no efficiency results for d-LAP due to the optical damage problem encountered with this material.

7.5.1 NCPM vs. Type I Geometries

Figure 7.5 shows the pump depletion measured for NCPM LBO. The indication is that not only are the thresholds relatively constant with changing beam size but so also are the pump depletions. The beam sizes are limited in this experiment by the small aperture of this crystal, which is only $3 \times 3 \text{ mm}^2$. Note, however, that in figure 7.6, which shows the pump depletion for a range of beam sizes in type I xyLBO, there is a significant reduction in slope efficiency with decreasing beam size. This can be seen from the fact that the lines are not parallel. This can also be demonstrated by looking at the pump depletion in terms of number of times threshold. For the smallest beam size the pump depletion at 1.75 times threshold is $\sim 10\%$. In the case of the largest beam size, the pump depletion at 1.75 times threshold, is $\sim 20\%$. The reduction in peak pump depletion is therefore not totally explained by the increase in oscillation threshold. The walk-off decreases the pump depletion of the OPO, in addition to increasing the oscillation threshold. The maximum pump depletion is limited in each case by either the maximum pump energy available or by the 1.0 Jcm^{-2} to 1.5 Jcm^{-2} damage threshold limit of the OPO mirrors. So once again, the compromise between energy and energy density becomes apparent.

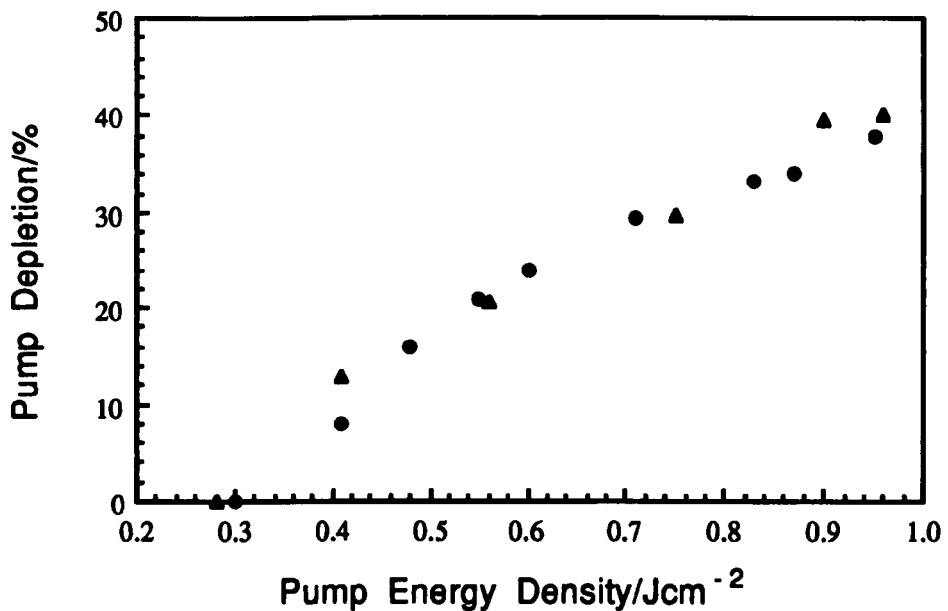


Figure 7.5. Pump depletion in non-critically phase-matched LBO. The circles represent the $2.5 \times 1.2 \text{ mm}^2$ beam size. The triangles represent the $1.1 \times 0.6 \text{ mm}^2$ beam size.

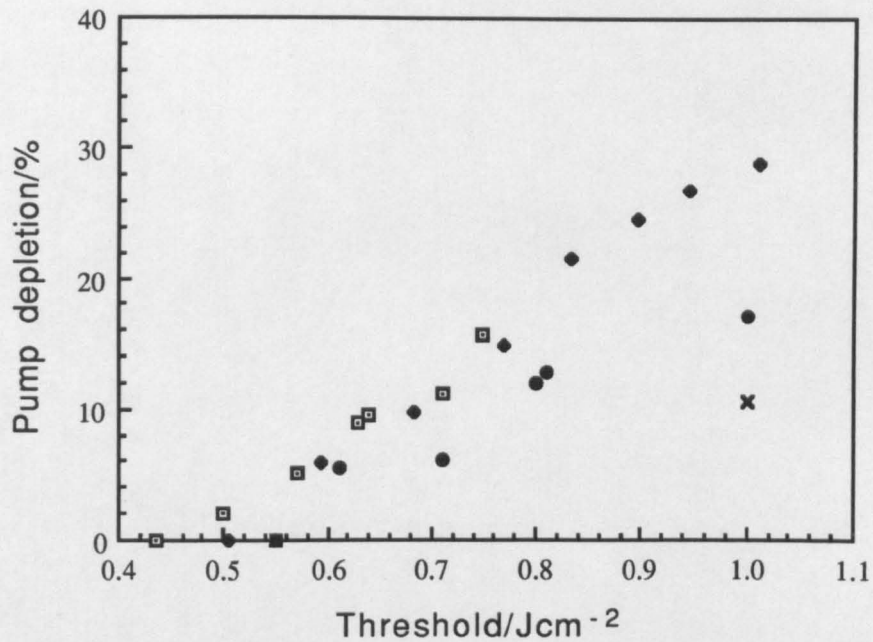


Figure 7.6. Pump depletion in type I *xyLBO*. Squares represent $4 \times 2 \text{ mm}^2$. Diamonds represent $3 \times 1.5 \text{ mm}^2$. Circles represent $2.5 \times 1.2 \text{ mm}^2$ and the cross represents $1.1 \times 0.6 \text{ mm}^2$.

7.5.2 *yzLBO*

The threshold of the type II geometry, cut at $\theta = 40^\circ$ in the *yz* plane, is considerably higher than that of the NCPM geometry due to the reduction in the effective non-linear coefficient. This increase agrees well with the theoretically predicted increase calculated from equation 2.24. As for the type I geometry, the threshold is now dependent on the beam size used. This is again due to the presence of Poynting vector walk-off. The walk-off angle at 40° is 0.5° . The beam sizes used during the experiments were $3 \times 1.5 \text{ mm}^2$, $2 \times 1 \text{ mm}^2$ and $1 \times 0.5 \text{ mm}^2$. The measured efficiencies are shown in figure 7.7. The effect of walk-off on this geometry is very similar to that of the type I LBO geometry although the walk-off angle of the former is only half that of the latter. A likely hypothesis is that the idler beam, which is an extraordinary wave in the type II geometry is somewhat smaller than the pump beam and thus more susceptible to walk-off. Measurements of the signal and idler mode size after the cavity tend to suggest that this might be the case.

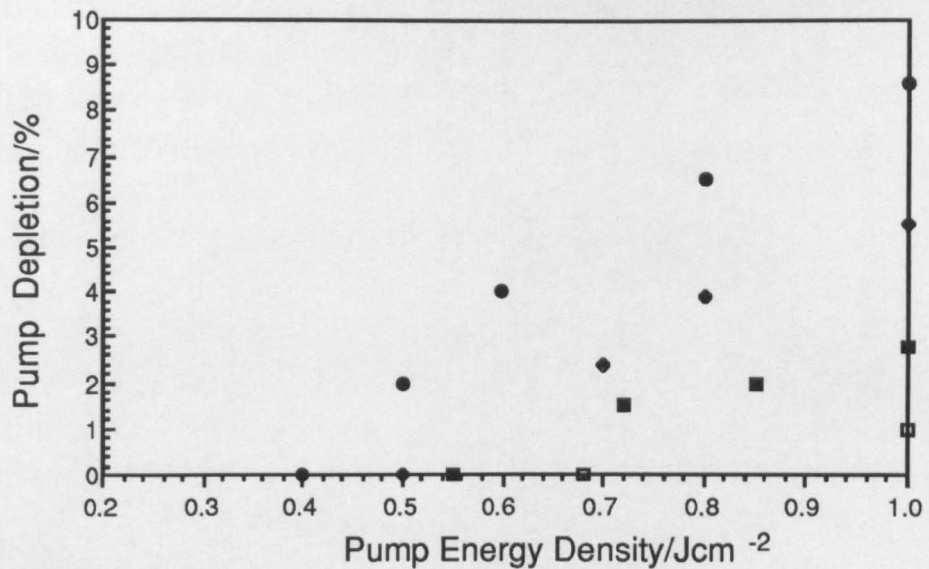


Figure 7.7. Pump depletions in yzLBO at 40° . The beam sizes are:- circles $4 \times 2 \text{ mm}^2$, diamonds $3 \times 1.5 \text{ mm}^2$, filled squares $2 \times 1 \text{ mm}^2$ and open squares $1.1 \times 0.6 \text{ mm}^2$.

7.5.3 Type I BBO

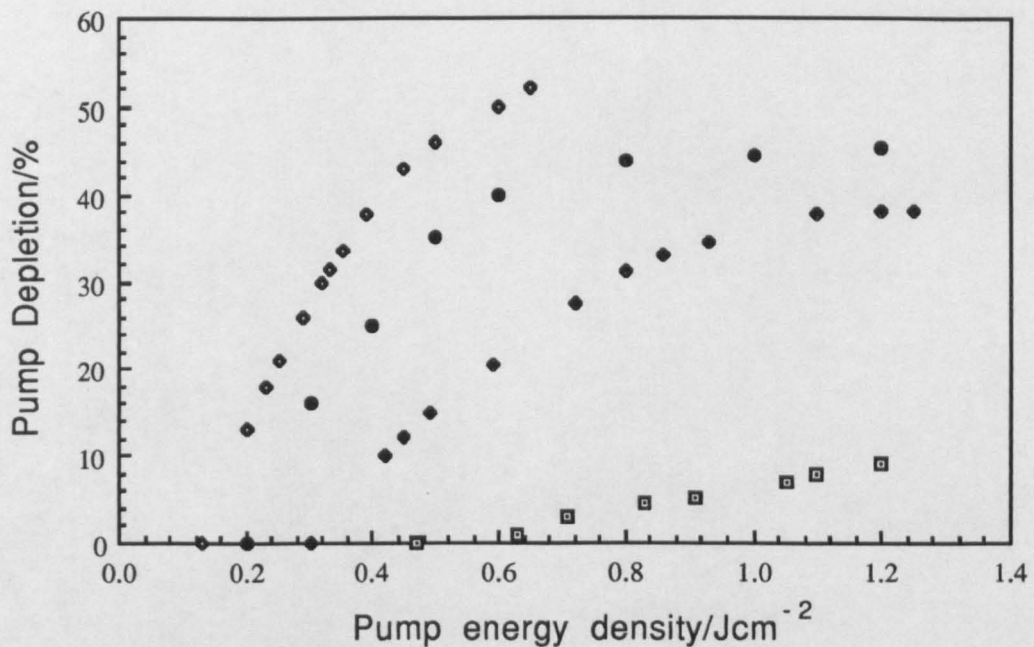


Figure 7.8. Pump depletion in BBO. Open diamonds represent $4 \times 2 \text{ mm}^2$. Circles represent $3 \times 2 \text{ mm}^2$. Filled diamonds represent $2.5 \times 1.2 \text{ mm}^2$ and squares represent $1.1 \times 0.6 \text{ mm}^2$.

Figure 7.8 shows the pump depletions for BBO. There is considerable increase in the threshold as the beam size decreases. Notice that it also exhibits a decrease in the slope efficiency as the beam size becomes smaller. This is even more marked than in the case

of type I LBO. Thus walk-off has a double effect on the performance of the OPO. Firstly, it increases the oscillation threshold and secondly, it reduces the slope efficiency. This double penalty severely limits the performance of the OPO when small beam sizes are used in critically phase-matched geometries.

7.6 Comparison of Inherent Linewidths

In chapter 2, the theoretical equations for the signal linewidth were given. There are contributions to the linewidth from firstly, the phase-matching bandwidth, $\Delta\nu_1$, secondly, the angular divergence of the pump, $\Delta\nu_2$, and finally, the pump bandwidth, $\Delta\nu_3$. Using the excimer pump system, where the pump bandwidth is small, the contribution to the signal linewidth from $\Delta\nu_3$ is also small. In general we have seen that the predicted and the measured linewidths are in good agreement. The

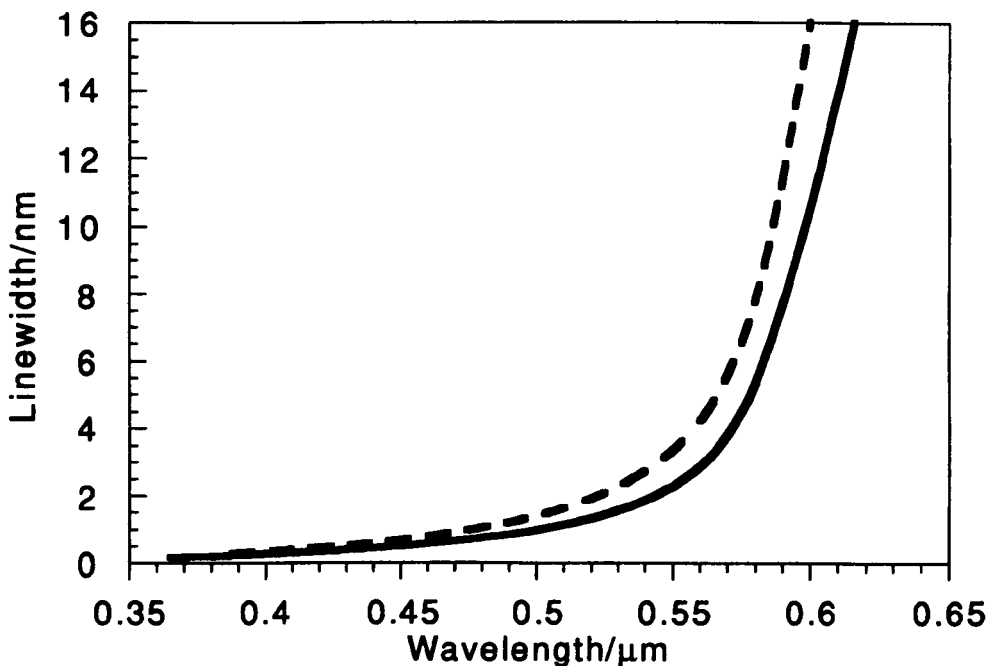


Figure 7.9. Theoretical comparison of linewidths in LBO and BBO. KEY:- dashed line = BBO, solid line = LBO.

linewidth of type I BBO is slightly larger than that of LBO across the tuning range. This is shown in figure 7.9. The contributions to linewidth are not, however, so straightforward. Figure 7.10 shows the contributions from the phase-matching bandwidth, $\Delta\nu_{s1}$, and from the pump beam divergence, $\Delta\nu_{s2}$. (The linewidth contribution from the pump bandwidth, $\Delta\nu_3$, is much smaller than the other two

components and is omitted. See figure 7.2 for BBO and figure 3.11 for LBO). From figure

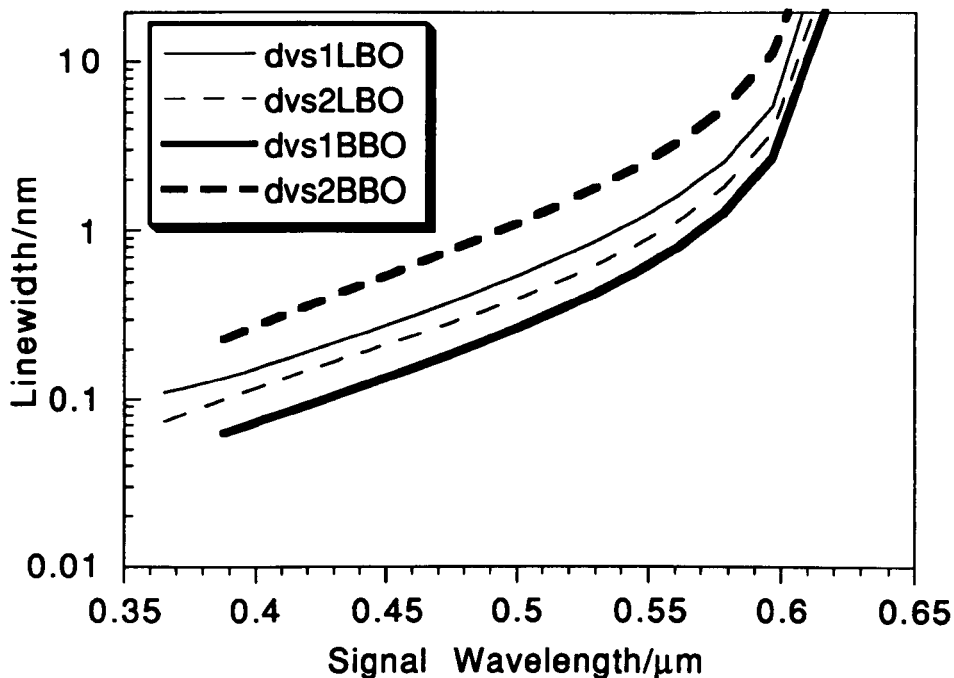


Figure 7.10. Theoretical comparison of linewidth components, dv_{s1} and dv_{s2} , for LBO and BBO. The third component, dv_{s3} , has not been shown since it is much smaller than the other two components.

7.10, it is clear that dv_{s1} in LBO is greater than in BBO. On the other hand, dv_{s2} is larger in BBO than in LBO. This might be expected since the rate of change of wavelength with angle is greater in BBO than in LBO. Thus for a given pump divergence, a larger spread of wavelengths in BBO would be expected. It is also worth noting that the two components, dv_{s1} and dv_{s2} , make similar contributions in LBO, whereas in BBO the majority of the linewidth is attributable to pump beam divergence.

7.7 Implications for Line-narrowing in OPOs

Finally, it is necessary to examine how the findings mentioned in the previous sections affect the choice of material when building a line-narrowed device. The intention of the experiments described in the following chapters is to construct a twin OPO system for a master /slave type operation. This will require splitting the pump energy and so the maximum realistic pump energy that will be attainable at each OPO will be ~ 40 mJ. At this level the lowest threshold will be in BBO at ~ 0.15 Jcm $^{-2}$. The threshold level in LBO, which has only a slightly narrower inherent linewidth than BBO, is ~ 0.55 Jcm $^{-2}$.

This would require much tighter focusing. The insertion of intra-cavity elements into the cavity may significantly increase the threshold of the device. With the damage threshold limit of the mirrors set at 1 Jcm^{-2} , the use of LBO may result in mirror damage problems. For this reason, the line-narrowed device was implemented using a BBO crystal.

REFERENCES

- 1 'Efficient High-Power Harmonic Generation in $\beta\text{-BaB}_2\text{O}_4$ '. C. Chen, Y. X. Fan, R. C. Eckardt and R. L. Byer. Conference on Lasers and Electro-Optics. (1986) paper THQ4.
- 2 'All-solid-state optical parametric oscillators tunable in the visible spectral region'. Y. Cui, M. H. Dunn, C. J. Norrie, W. Sibbett, B. D. Sinclair, Y. Tang, J. A. C. Terry. Conference on Lasers and Electro-Optics. (1992) paper CTuR1.

A Line-narrowed OPO

In this chapter, the topic of linewidth control using intra-cavity elements is explored. Background information and theory are presented along with experimental results on a single axial-mode BBO OPO. The topic of line-narrowing by injection seeding is addressed in the next chapter.

8.1 Introduction

A theoretical analysis by Kreuzer¹ in 1969 predicted that the steady-state linewidth of a singly resonant OPO (SRO) should be a single axial mode. Competition between oscillating modes under the gain bandwidth of the device leads to the extinction of all modes except the one experiencing lowest loss/highest gain. This will usually be the mode nearest to the wavelength where the momentum mis-match, Δk , is zero. Later experimental studies² showed that when an SRO reaches steady-state operation the linewidth of the signal is of the order of 1 cm^{-1} or less and the non-resonant wave linewidth approaches that of the pump. The steady state assumption may be true for CW systems or long pulse systems, but in the 5 ns to 20 ns regime, the OPO does not reach steady state oscillation and so the linewidth can be as broad as the gain bandwidth. The trade-off between tunability and linewidth in pulsed angle tuned systems has long been appreciated. We saw in the last chapter that the linewidth contribution due to the pump beam divergence is greatest in materials where the rate of tuning with angle is largest. Further, the linewidths of OPOs are often largest close to degeneracy, typically $\sim 10 \text{ nm}$, so the need for line-narrowing is apparent. As well as the parametric gain bandwidth and pump divergence, other factors that affect the OPO linewidth are the pump laser linewidth, the cavity geometry and the number of times above threshold that the OPO is being pumped.

Firstly with regard to pump linewidth, we saw in the last chapter that its contribution to OPO signal linewidth, in critical geometries, was typically two orders of magnitude less than the total linewidth. Experimentally, however, operation of an SRO with a single-axial-mode pump source leads to more stable operation in amplitude and frequency terms and can reduce the signal linewidth³. Secondly, the linewidth is affected by the cavity geometry. In a doubly resonant oscillator, it is possible that

operation on a single axial mode will occur even when a large gain bandwidth exists. This is because both generated waves are required to be resonant simultaneously in the cavity. Suitable mode pairs may be spaced many axial modes apart and moreover sufficiently far apart to exceed the gain bandwidth of the OPO. However, the instabilities due to the over-constrained resonator lead to mode and cluster hopping of the two generated beams. This in turn reduces the output power of the OPO. It is for this reason that SROs, although having higher thresholds, are preferred where possible.

Finally, the gain bandwidth is dependent on the pumping intensity and the greater the number of times above threshold, the more modes there will be above threshold and hence the greater will be the linewidth.

The total theoretical linewidth is calculated by determining the separation of the points where the gain has fallen to half of its peak value due to the contribution of all the above factors. This

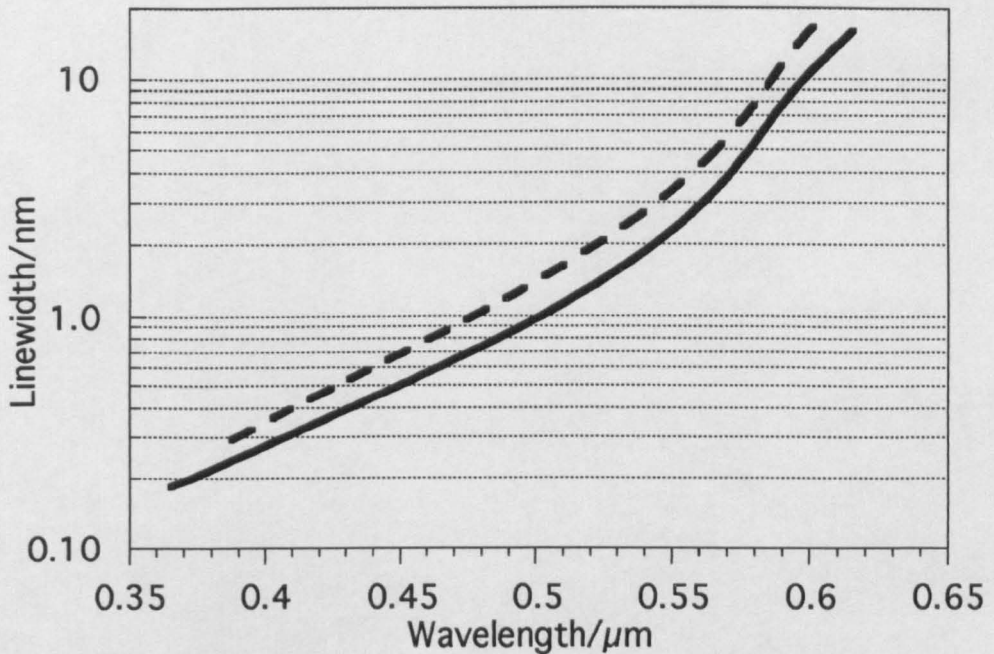


Figure 8.1. Comparison of BBO and LBO linewidths. KEY:-the dotted line represents the type I BBO linewidth and the solid line the type I xyLBO linewidth.

corresponds to a momentum mis-match over the crystal length of $\Delta kL = \pi$, as was shown in chapter 2, equation 2.19. The total theoretical linewidths for type I LBO and type I BBO are shown together in figure 8.1. In the last chapter, a comparison of the

two materials showed that although the linewidth of BBO is slightly larger than that of LBO, the significantly lower threshold of the former favoured it as the material of choice in an excimer pumped, line-narrowed system. Due to the large variation in linewidths across the tuning range of BBO, it is likely that different techniques will be required to line-narrow the device effectively. It is thus of interest at this point to examine the techniques used to date for line-narrowing OPOs.

8.2 Background

The first reported line-narrowed device was by Kreuzer in 1969 (ref 1). He demonstrated single mode operation of an OPO by placing a tilted etalon within the cavity. The output power was reduced to 25% of the broadband oscillator. Details of this experiment are shown in table 8.1 along with other experiments carried out to determine OPO linewidths. It is of interest to examine the linewidths across the tuning range of the various OPO geometries listed in the table. Some of the experiments merely state the linewidth of the broadband device and no attempt to line narrow the OPO has been made. The results for all non-critically phase-matched (NCPM) devices report narrow linewidths without any additional cavity elements. This is because the contribution to signal linewidth from the pump beam divergence is small in an NCPM device due to the slow angular tuning rate. The tuning ranges of these devices tend to be small as they rely on temperature tuning to alter the birefringence of the material. The type II geometries offer a compromise between the NCPM and type I geometries in the sense that they are moderately tunable and have narrow inherent linewidths. In some applications they may prove useful with or without any additional line-narrowing. Type I devices have the largest linewidths, typically in the range 2 nm to 10 nm at degeneracy and falling off sharply as the device is tuned away from the degenerate wavelength.

From the table, it can be seen that etalons have been used to line-narrow the OPO when the linewidth is already relatively narrow. Diffraction gratings have been used both for preliminary line-narrowing, in combination with etalons, or on their own depending on the initial conditions and the desired signal linewidth.

In practice, there are three techniques that are frequently used to line-narrow OPOs, namely gratings, etalons and injection seeding. The latter will be discussed in chapter 9. In the experiments detailed in table 8.1, gratings have been used to reduce the linewidth from ~10 nm down to fractions of a nanometer. This method of

Pump	Crystal	Phase matching	Tuning Range	Inherent Linewidth	Line-narrowing	Reference
532 nm	KTP	II	700–900 nm	Not Given	single mode	4
1.6 μm	LiNbO	Not Given	Not Given	0.5 nm	grating+prism+etalon; single mode	5
532 nm	Mg:LiNbO	NCPM	1007–1129 nm	single mode	DRO, single mode pump	6
308 nm	LBO	NCPM	383–387 nm	1–3 modes	None	7
266 nm	LBO	NCPM	312–314 nm	1–3 modes	None	8
355 nm	BBO	II	480–630 nm and 810–1360 nm	0.05–0.3 nm	None	9
1064 nm	LiNbO	Not Given	1.4–4.4 μm	0.7 nm @ 1.5 μm 11 nm @ 2.2 μm	2 mm, F=10 etalon; 4 etalon modes	10
355 nm	LBO	I	435–1922 nm	0.1 nm @ 400 nm 10 nm @ 700 nm	None	11
355 nm	BBO	I	420–2300 nm	0.15–10 nm	0.03 nm Littman grating	12
360 nm	BBO	I	406–3170 nm	1.5 nm @ 460 nm 3.5 nm @ 500 nm 18 nm @ 640 nm	Grating; 0.24 nm @ 500 nm	13
1830 nm	CdSe	II	2.2 μm 9.8–10.4 μm	1 nm	None	14
1064 nm	Proustite	Non co-linear	1.2–8.5 μm	2 nm @ 2.1 μm	None	15
308 nm	BBO	I	400–560 nm	single mode	Etalon	16
532 nm	CDA	I	854–1410 nm	5 nm @ 1064 nm	None	5

Table 8.1 Line-narrowing experiments in OPOs. Key to abbreviations. DRO= doubly resonant. NCPM= non-critical phase-matching. Shaded cells represent data not present in the reference.

line-narrowing causes a large increase in oscillation threshold, particularly, when operating at grazing incidence (Littman configuration), due to the low feedback from the grating. An alternative is to use an intra-cavity etalon. The limitation here is the minimum thickness to which a solid etalon can be made. Typically, this is $\sim 30\mu\text{m}$. At this thickness, the etalon is extremely fragile and its flatness is not usually guaranteed since warping of the substrate may occur after coating. A $30\mu\text{m}$ etalon has a free spectral range (FSR) of 166 cm^{-1} (or $\Delta\lambda = 6\text{ nm}$ at 616 nm). This may limit how close to degeneracy that the etalon may be used without the need for a diffraction grating for coarse selection. An alternative to the solid etalon is the deposited etalon. This is a multi-layer coating deposited onto a substantial substrate. The maximum thickness that can be laid down at present is $\sim 5\mu\text{m}$. Such an etalon would have an F.S.R = 1000 cm^{-1} (or $\Delta\lambda = 40\text{ nm}$ at 616 nm). This is greater than the linewidth of any OPO, even at degeneracy, and would be a useful replacement for the diffraction grating, permitting easier alignment and tuning.

The linewidth to which an etalon will narrow an OPO is governed by the FSR and the finesse, F . The maximum practical finesse is set by damage limitations of the etalon due to the intra-etalon field, $F_e \times E_{\text{cav}}$ (where E_{cav} is the field within the OPO cavity, which will be $F_{\text{cav}} \times E_{\text{ext}}$). A typical cavity finesse for the excimer system is ~ 5 and for an etalon, $F \sim 10$. Thus the field within the etalon can be as high as $50E_{\text{ext}}$. If the energy in the signal measured outside the cavity is $\sim 1\text{ mJ}$ then, for a $3 \times 1.5\text{ mm}^2$ beam, the internal field within the etalon will be greater than 1 Jcm^{-2} , which is greater than the optical damage threshold of the etalons.

The increase in effective cavity length, due to an etalon of finesse, F_e , is $D = dF_e$, where d is the etalon thickness, which may also be a factor in determining the maximum practical finesse.

8.3 Etalon Insertion Losses

Ideally, the insertion of an etalon should induce loss selectively; there should be one narrow band of wavelengths that are transmitted with 100% efficiency, with all other wavelengths within one FSR seeing high loss. If the etalon is chosen carefully, so that the OPO gain bandwidth is less than 1 etalon FSR, then the OPO will be effectively line-narrowed to a single narrow band of wavelengths. In practice, however, the transmission of the etalon is never 100%, even for the wavelength satisfying the condition $m\lambda = 2nd\cos\theta$, since there is a small portion of the beam that does not interfere due to the progressive beam walk-off which occurs with multi-passing of the

etalon when the angle θ is non-zero. The insertion loss due to this effect for an etalon tilted at an angle, θ , is given by the relation¹⁷

$$l = \frac{R}{(1-R)^2} \left[\frac{4\theta d}{\ln W} \right]^2 \quad (8.1)$$

where R is the reflectivity of the etalon mirrors and W the beam size. The loss can be estimated for a 30 μm etalon with a finesse of 10 as mentioned above (for such an etalon a tilt of 53 mR is required to tune through 1 FSR). When the etalon is tilted at 53 mR, the theoretical insertion loss, l , is 0.002%. For a thicker etalon, of say 2 mm, the angle required to tilt through one FSR is less, only 6 mR, and the corresponding loss, l , is 0.14%. The single pass insertion loss of an etalon is considerably smaller than both the output coupling losses, which are typically $\sim 10\%$, and the single pass loss associated with the uncoated crystal faces, typically $\sim 12\%$.

Any loss due to absorption or scattering, $(1-A)$, within the etalon will reduce the maximum transmission of the etalon, T_{max} from its theoretical peak of 100% to¹⁸

$$T_{\text{max}} = \frac{(1-R)^2 A}{(1-RA)^2} \quad (8.2)$$

which for a loss, $(1-A) = 1\%$ and a finesse of 10, gives a maximum transmission of 93%. Thus, the quality of the etalon is important if large intra-cavity losses are to be avoided.

8.4 Experimental Set-up

Experimentally, the added complication of a diffraction grating was avoided by restricting the line-narrowing of the signal beam to below 560 nm. In this regime, a 30 μm etalon, the thinnest solid etalon available, would be suitable to significantly reduce the linewidth of the OPO to ~ 0.6 nm. Then a combination of thicker etalons, 0.5, 1, and 2 mm could be used to further reduce the linewidth. Thus, the normal plane parallel cavity could be used with only minor modifications. The presence of the high energy pump field in the cavity would lead to damage problems with the etalons. For this reason it was necessary to introduce a beam steering plate into the cavity, as shown in figure 8.2. Using this arrangement, there is an area between M1 and the beam steering plate in which the etalons can be located. The beam steering plate is coated to be highly reflecting at 308 nm when oriented at Brewster's angle, $\sim 56^\circ$, and highly transmitting for the signal wave between 420 and 600 nm. The insertion of the

beam steering plate and the etalons will necessarily increase the cavity length and it is therefore of interest to measure the effect this has on

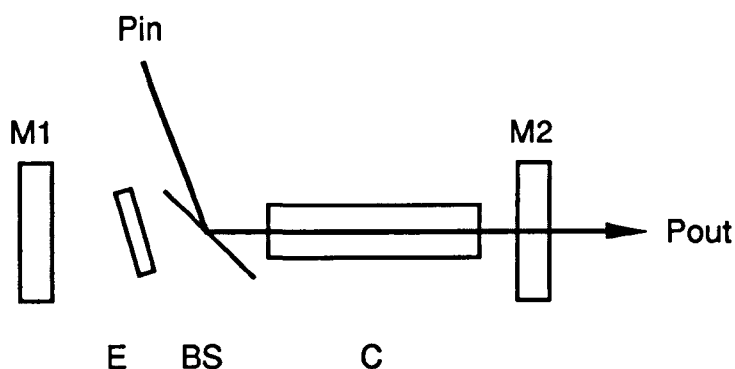


Figure 8.2 Experimental Set-up for line-narrowing of BBO OPO. KEY:- M1 & M2= mirrors, E = etalon, BS = beam steering plate, C= crystal, Pin= pump in, Pout = pump out.

the threshold of the device. To this end the threshold was measured for various cavity lengths between 28 mm and 160 mm and these points are shown in figure 8.3. Typically, cavity lengths of 60 mm to 100 mm are required to accommodate the beam

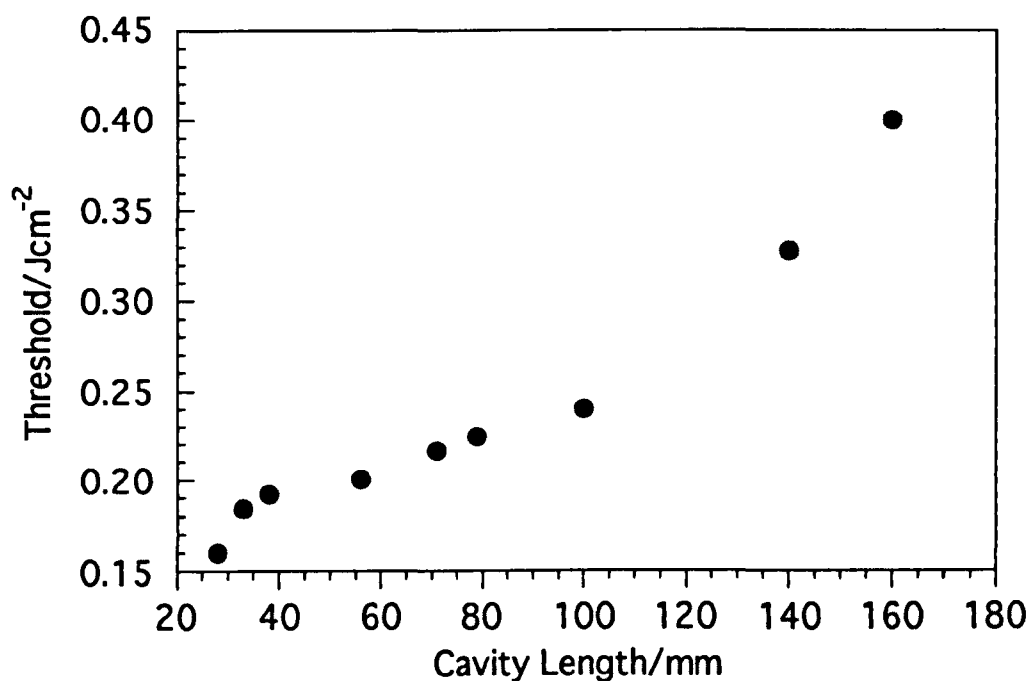


Figure 8.3. Threshold versus cavity length. The threshold is measured using a simple cavity design, with two plane mirrors and one crystal, operating at 500 nm.

steering plate and two etalons. The threshold increases by a factor of 1.5 when the cavity is lengthened from 28 mm to 100 mm. Using the Brosnan and Byer threshold equation given in chapter 2, the predicted increase in threshold due to this cavity length increase is 1.48, which is in satisfactory agreement with that observed experimentally. Clearly then, the increase in cavity length produces a small but significant increase in threshold of ~ 1.5 times, over and above any additional increases due to the line-narrowing process. In practice, thresholds can be expected to rise from 0.15 Jcm^{-2} to $\sim 0.25 \text{ Jcm}^{-2}$, due solely to the increase in cavity length.

The extended cavity can now be used for line-narrowing experiments. The etalons used were, 30 μm , 0.5 mm, 1 mm and 2 mm thick with reflectivities of 75% between the wavelengths of 420 and 600 nm. Over this range, they have a finesse, $F = 10$. The etalons were manufactured to a flatness of $\sim \lambda/50$ across the aperture and their coatings have an estimated damage threshold of $\sim 1 \text{ Jcm}^{-2}$ over the reflectivity range.

The etalons were mounted in plastic cells, which in turn were attached to a galvanometer scanner. The galvanometer was controlled by a voltage supply that allowed fine adjustment of the tilt angle of the etalon. To enable two etalons to be inserted into the cavity at one time, one etalon was suspended from a galvanometer mounted above the cavity and the other was inserted horizontally from the side of the cavity. The etalons could be inserted individually for testing and alignment. Firstly, the thin etalon was inserted into the pre-aligned cavity and tilted until the normal incidence or 'flash condition' was observed. In this position, the etalon operated like a mirror by reflecting or transmitting all the light along the cavity axis. When the etalon was tilted, light that did not satisfy the transmission condition, $m\lambda = 2nd\cos\theta$, was reflected from the cavity.

8.5 Experimental Results

Figure 8.4 shows the linewidth of the OPO operating with the various intra-cavity etalons inserted. The traces were obtained from a chart recorder connected to a photomultiplier tube (Hamamatsu 931B) which was set up to view the output slit of a monochromator (Monospec 1000). The first trace, 8.4(a), shows the inherent linewidth of the OPO, i.e. when the selection of oscillation wavelengths was controlled only by the phase-matching in the crystal. The measurements were taken around 480 nm where the inherent linewidth was measured to be 1 nm (FWHM). Figure 8.4(b) shows the effect of adding a 0.5 mm etalon to the cavity. The free spectral range of the etalon is 0.23 nm and the finesse is 10. The result is oscillation on five etalon modes.

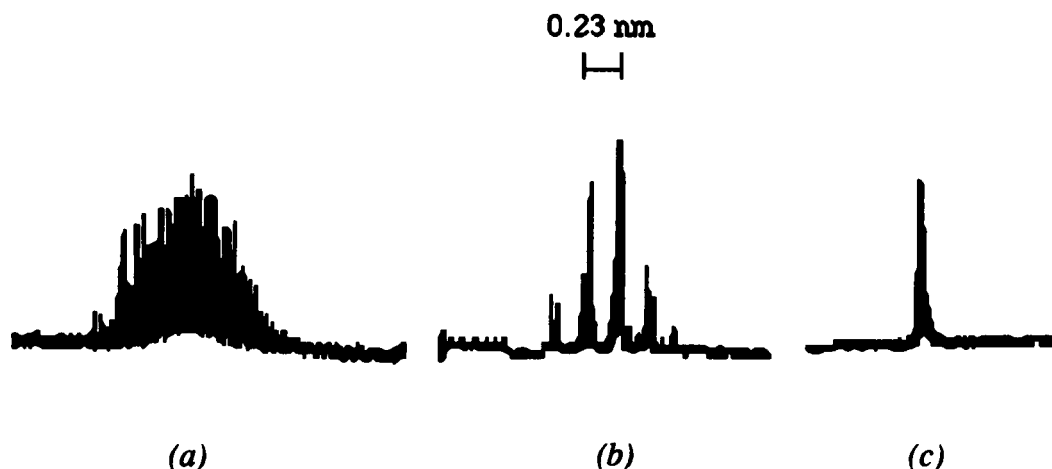


Figure 8.4. Line-narrowing using two intra-cavity etalons. The trace (a) shows the broadband linewidth, trace (b) shows the effect of the 0.5 mm ($F=10$) etalon and trace (c) was taken with both the 0.5 mm ($F=5$) and 30 μm ($F=10$) etalons in the cavity.

To achieve narrow linewidth operation on a single etalon peak, it was necessary to combine the 0.5 mm etalon with a 30 μm etalon. The result of this is shown in figure 8.4(c). The free spectral range of the 30 μm etalon is 3.9 nm and the finesse is 10. This reduces the gain bandwidth of the OPO to less than 0.4 nm, thus selecting a single transmission peak of the 0.5 mm etalon. The width of the peak was measured to be 0.06 nm FWHM, However, it appeared to be the same for the 0.5 mm, 1 mm and 2 mm etalon traces. This led to the possibility that the linewidths measured by the monochromator could be resolution limited.

To further study the linewidths, a Fabry Perot interferometer was constructed. This consisted of two plane parallel mirrors coated to be 95% reflecting between 450 and 550 nm. The mirrors were mounted in gimbal mounts one of which was placed on a translation stage to allow the mirror separation to be easily varied over a range of 10 mm. The signal beam from the OPO entered the interferometer via a -5 cm lens (L1). This illuminated the mirrors of the interferometer with divergent light. On leaving the interferometer, the light passed through a converging lens of 1 m focal length (L2) before being imaged onto a screen placed 1 m from the lens. This configuration is shown in figure 8.5. An 'EEV Photon' CCD camera was used to view the fringes and to capture them on a video frame store. The image could then be transferred to an Archimedes computer for analysis. Measurements of the pixel grey levels allowed intensity profiles of the fringe patterns to be made.

The interferometer mirror spacing was ~ 20 mm in each case (exact multiples of the etalon thicknesses were avoided to stop aliasing effects between cavity modes), which

implies an FSR of 0.25 cm^{-1} (which is equal to 0.0058 nm at 480 nm). The OPO cavity

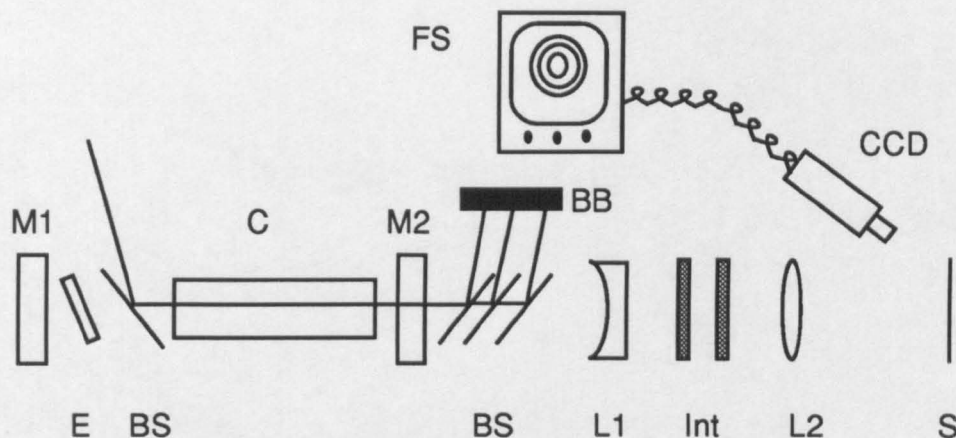


Figure 8.5. Monitoring the OPO linewidth with a Fabry Perot interferometer and a CCD camera. KEY:- M1 & M2 = mirrors, E= etalon, BS = beam steering plates, C= crystal, L1 & L2 = lenses, Int = interferometer, S= screen, CCD= CCD camera, FS = frame store and monitor. BB = beam block.

length was $\sim 60 \text{ mm}$ so the axial mode separation is $\sim 0.08 \text{ cm}^{-1}$ (which is equal to 0.00192 nm at 480 nm). Theoretically, the finesse of the interferometer, calculated using the mirror reflectivity, was ~ 60 . However, the mirror flatness is only $\sim \lambda/20$ across the aperture so an effective finesse of no more than 10 can be assumed. However, even with a finesse of 10, the individual cavity modes should be resolvable. Figure 8.6 shows the observed fringes from the OPO when operating with the $30 \mu\text{m}$ and 0.5 mm etalons. Multiple rings can clearly be seen indicating the presence of multiple axial modes. Further line-narrowing was achieved by replacing the 0.5 mm etalon with a 1 mm etalon. This resulted in operation on 1 or 2 axial modes as shown in figure 8.7. Single axial-mode operation was achieved by using the 2 mm etalon instead of the 1 mm etalon. Although single mode operation was achieved and was present on every shot, the fringes changed from shot to shot indicating that oscillation was not stable on any one mode. This is to be expected since no stabilisation or damping of the cavity was undertaken. Single axial-mode operation has been demonstrated across the tuning range from 420 nm to 560 nm . Figure 8.8 shows the single axial-mode operation.

Figure 8.6 (shown overleaf)
Multi-mode oscillation with a 0.5 mm etalon and a 30 μm etalon. The interferometer mirror spacing was ~ 20 mm. The finesse was ~ 10 . Oscillation is on three (or perhaps four) axial modes.



Figure 8.7 (shown overleaf)

Two axial mode operation. A 1 mm etalon has been used in addition to the 30 μm etalon to achieve oscillation on two modes. The interferometer spacing was 19 mm, the finesse was ~ 10 .

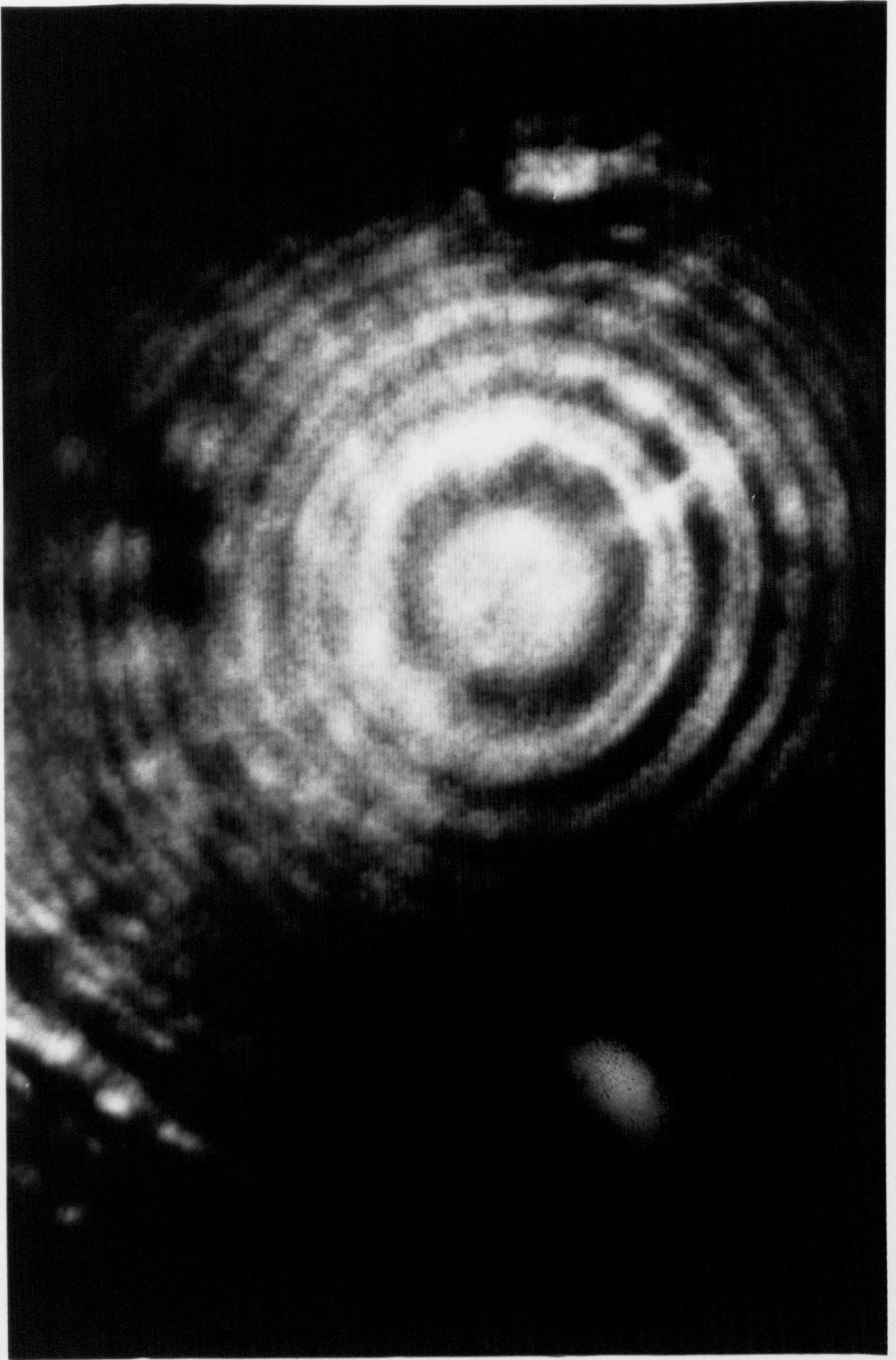
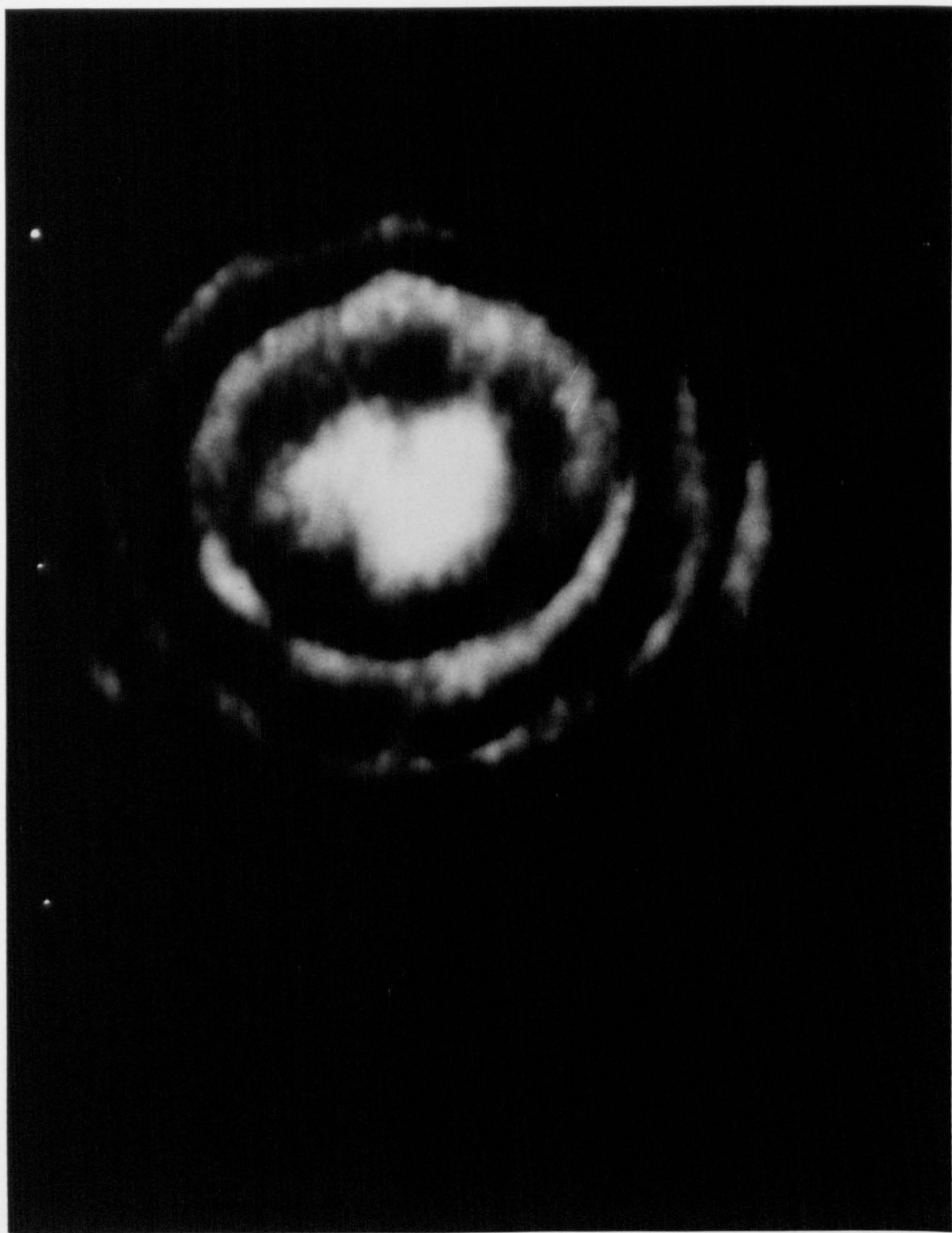


Figure 8.8

**Single axial mode operation of the BBO OPO.
A 2 mm etalon has been used with the 30 μm
etalon. The interferometer mirror spacing was
22 mm, the finesse was ~ 10 .**



8.6 Characterisation of the line-narrowed OPO

8.6.1 Threshold

Having obtained reliable, single axial-mode operation of the BBO OPO, it is important to examine the effect that the etalon has on the other aspects of the OPO performance. A series of threshold measurements were taken for each of the etalon combinations and the results are shown in table 8.2. The cavity mirror separation was kept constant at 60 mm and the same mirror set and pump beam size were used throughout, although the effective cavity length, L , varied because of the different etalon thicknesses. (The signal beam makes approximately F round trips of the etalon of thickness d , where F is the etalon finesse). The relative theoretical values were calculated from the threshold equation, (equation 2.26 in chapter 2), using the effective cavity length, L . These calculated thresholds are also shown in table 8.2. The OPO operating without an etalon is assigned a threshold of 1 and the thresholds of the other OPOs are measured relative to this. For single axial mode operation, the measured threshold is 1.5 times that of the broadband case. This is considerably more than would be expected purely from the effective increase in cavity length, dF_e . In absolute terms, the line-narrowed threshold is $\sim 0.3 \text{ Jcm}^{-2}$, which is twice the threshold of the short cavity broadband device.

Earlier in the chapter, the theoretical insertion losses of etalons were calculated and were shown to be extremely small relative to the output coupling and Fresnel losses within the cavity. If the etalon is assumed to be lossless, then the increase in threshold can be explained only by an increase in build-up time due to the effective cavity length increase $\sim Fd$ caused by the insertion of the etalon. The column, 'calculated threshold', in table 8.2 indicates the calculated threshold relative to the broadband case. Clearly, the experimental threshold increase is significantly more than can be explained by the increase in the effective cavity.

Etalon Combination	Relative Threshold	Calculated Threshold	Pump Depletion	O/P Coupling
No Etalon	1.0	1.00	27%	25%
0.5 mm + 30 μm	1.3	1.04	16%	10%
1 mm + 30 μm	1.4	1.05	11%	8%
2 mm + 30 μm	1.5	1.10	9%	6%

Table 8.2. Effect of etalons on OPO performance. All efficiency results were taken at 4 times oscillation threshold. All the cavities were 60 mm long.

8.6.2 Efficiency

The pump depletion of the line-narrowed OPOs was also studied. The undepleted pump that passes through the OPO is deflected off a dichroic mirror onto a power meter. The difference in transmitted pump energy between the oscillating and non oscillating cases can be measured for each of the etalon combinations. The pump depletion is defined as

$$\eta = \frac{E_n - E_o}{E_n}$$

where E_o and E_n are the measured transmitted energies of the oscillating and non-oscillating cavities, respectively. These results are summarised in table 8.2 above. The 2 mm and 30 μm etalon combination, which resulted in single axial-mode operation, had a pump depletion of 9% when measured at 4 times oscillation threshold ($\sim 1.2 \text{ Jcm}^{-2}$). The signal energy extracted usefully from the cavity was also measured and found to be 0.3 mJ, which corresponds to an output coupling efficiency of 6%. The efficiencies of the OPO with the other etalons are shown in table 8.2. (They are all taken at 4 times oscillation threshold).

With no etalon in the cavity, the pump depletion was 27%, of which 25% was usefully coupled out of the cavity. This tallies well with the expected performance of an OPO with Fresnel losses of 6.2 % per face and round-trip output coupling losses of 15%. The measured threshold of 0.2 Jcm^{-2} is approximately half that predicted by the Brosnan and Byer model (although the model predicts higher thresholds than are observed experimentally, in relative terms, the model is good at predicting threshold increases due to increased losses).

Experimentally, the effect of adding the intra-cavity etalons is three fold. Firstly there is an increase in the oscillation threshold (with contributions both from the etalons themselves and also from the necessary increase in cavity length). This is followed by a substantial drop in the pump depletion. Finally there is a reduction in the output coupling efficiency. This results in a drop in overall efficiency from 6.8% , broadband output, to 0.5% single axial-mode output.

8.6.3 Experimental Etalon Losses

Using a helium neon laser, the transmission of the four etalons was measured using the experimental set-up shown in figure 8.9. The diameter of the HeNe beam could be increased using the beam expansion telescope from 2.5 mm to 7 mm. The power in both the transmitted beam and the reflected beam was measured using a photodiode.

The transmission is calculated as the ratio of the power transmitted through the lens system and etalon, to the power transmitted solely through the lens system. Starting at normal incidence, the etalons were tilted through a few FSRs and the transmissions were measured. The maximum transmissions of the etalons was consistently measured to be in the region of 85–90%, see figure 8.10. When the etalon is inserted into the OPO cavity, the above loss can be regarded as an effective single pass loss. This large single pass loss is similar to the single pass Fresnel and output

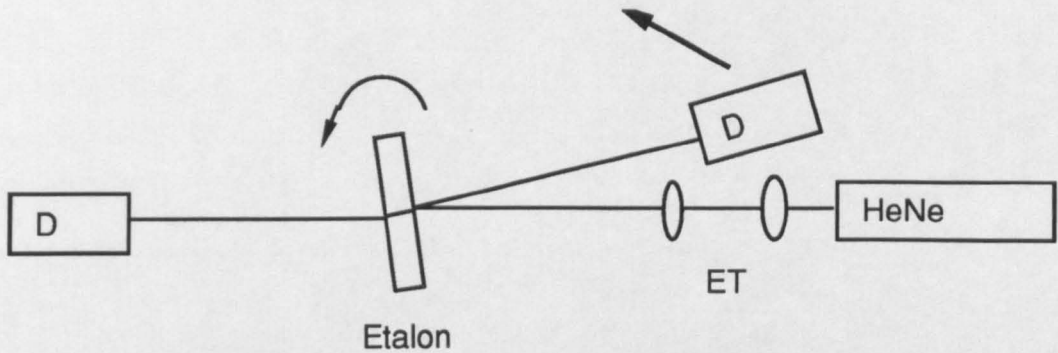


Figure 8.13. Measuring the transmission of the etalons. KEY:-D= photodiodes, ET = beam expansion telescope, HeNe = HeNe laser. An oscilloscope was used to compare the voltages of the reflected and transmitted light at various tilt angles of the etalon. The arrows indicate the direction of rotation.

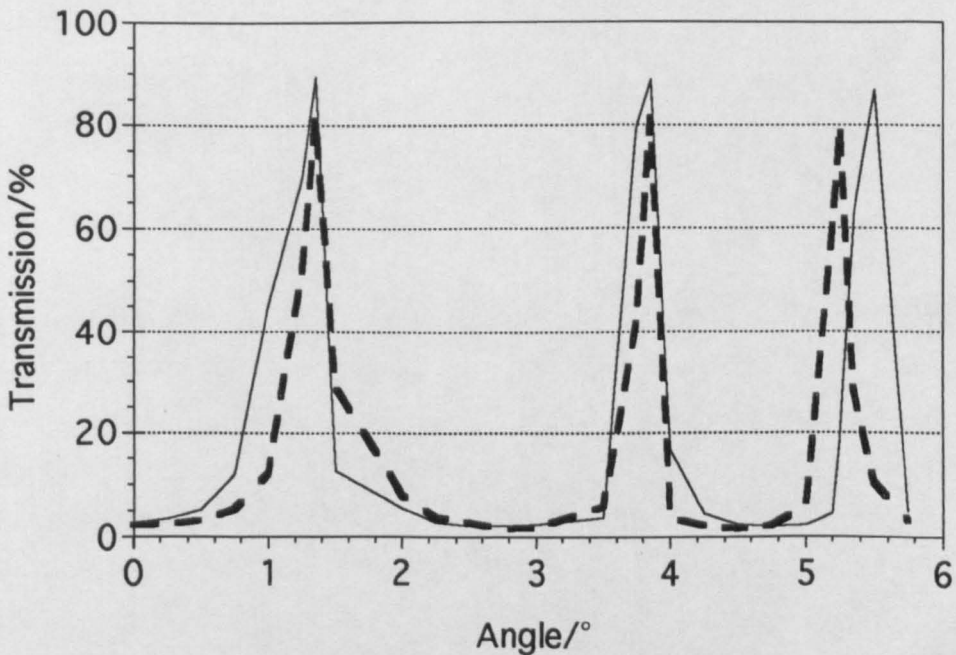


Figure 8.10. Transmission of the 0.5 mm etalon. The etalon was rotated by a galvanometer and the transmitted light was detected by a photodiode and the resultant voltage displayed on an oscilloscope. KEY:- the dotted line = 3.5 mm beam and the solid line = 2 mm beam.

coupling losses and is therefore a likely contributor to the increased thresholds and decreased efficiencies that have been observed. The power in the reflected beam was also measured at the angles corresponding to maximum transmission. From these measurements, the scattering and absorption losses were calculated. The reflected power was found to be ~8-13% of the incident power, implying that the scattering and absorption loss was ~2%. Using equation 8.2, the single pass absorption loss in the etalon substrate is 0.5%.

Table 8.3 shows the measured and calculated values of threshold and output coupling efficiency, using the measured etalon round-trip insertion losses of 25% per etalon. The calculated thresholds are now obtained by inserting the appropriate losses into the Brosnan and Byer model.

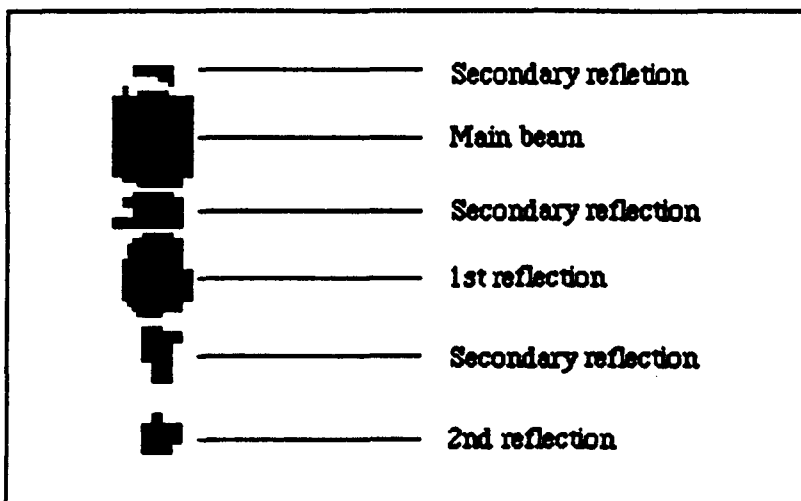
	Relative Threshold	Calculated Threshold	Measured O/P Coupling	Calculated O/P Coupling
No Etalon	1.0	1.00	25%	24%
0.5 mm + 30 μ m	1.3	1.60	10%	10.5%
1 mm + 30 μ m	1.4	1.63	8%	10.5%
2 mm + 30 μ m	1.5	1.70	6%	10.5%

Table 8.3 Comparison of measured and calculated thresholds and efficiencies with 25% etalon insertion loss.

The calculated values now predict more accurately (compared to table 8.2) the increases in threshold and the decreases in output coupling efficiencies seen experimentally.

The high reflection losses from the etalons was also noted by the 'multiple-spot' output of the OPO. The separation of the spots was directly related to the tilt of the etalon relative to the cavity axis and was a result of the high reflection loss of the etalons. The first bright reflection occurred at 2θ , where θ is the angle between the cavity axis and the normal to the etalon face. The next bright reflection occurred at 4θ . Between the bright spots were secondary reflections which were much weaker. For operation very close to normal incidence, the off-axis spots appeared bright; comparable with the central spot in intensity, presumably due to amplification on transit through the crystal. Figures 8.11a and 8.11b show the profile of the beams exiting the cavity. Measurement of the energy in these spots indicated that the first off-axis reflection contained ~1/10th of the energy in the central spot. The second off-axis reflection contained only ~1/100th of the central spot. Beyond this, measurement

Figure 8.11a (shown overleaf). An outline of the figure is shown below. The OPO was operating with an intra-cavity etalon tilted at $\sim 1^\circ$ from the cavity axis. The 1st reflection contains 1/10 of the energy in the main beam. The 2nd reflection contains 1/100 of the energy. The secondary reflections are much weaker and could not be measured.



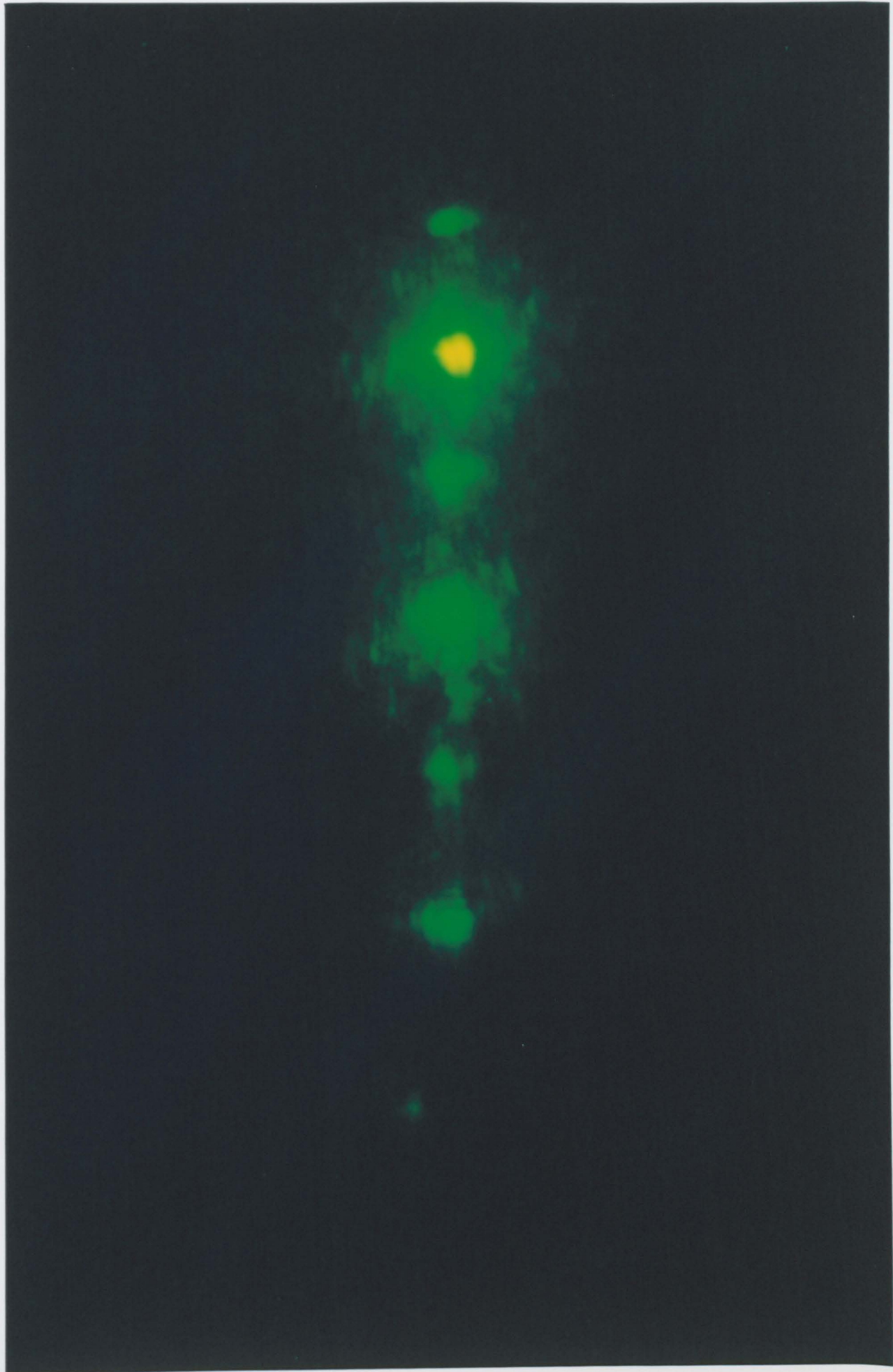
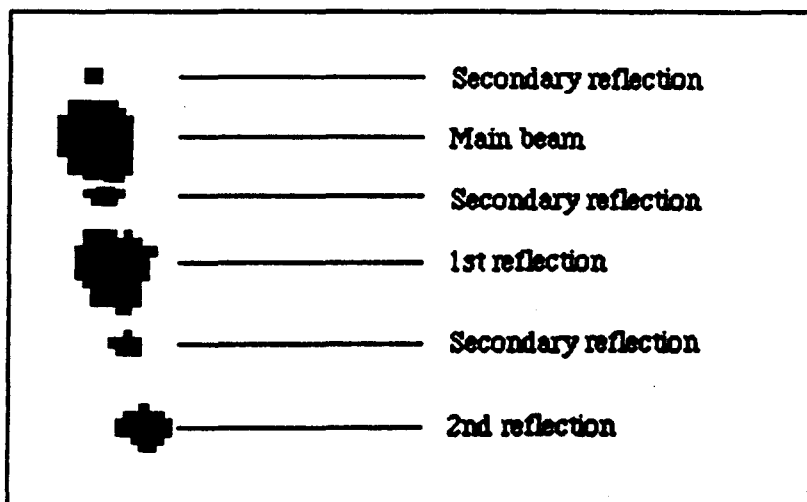
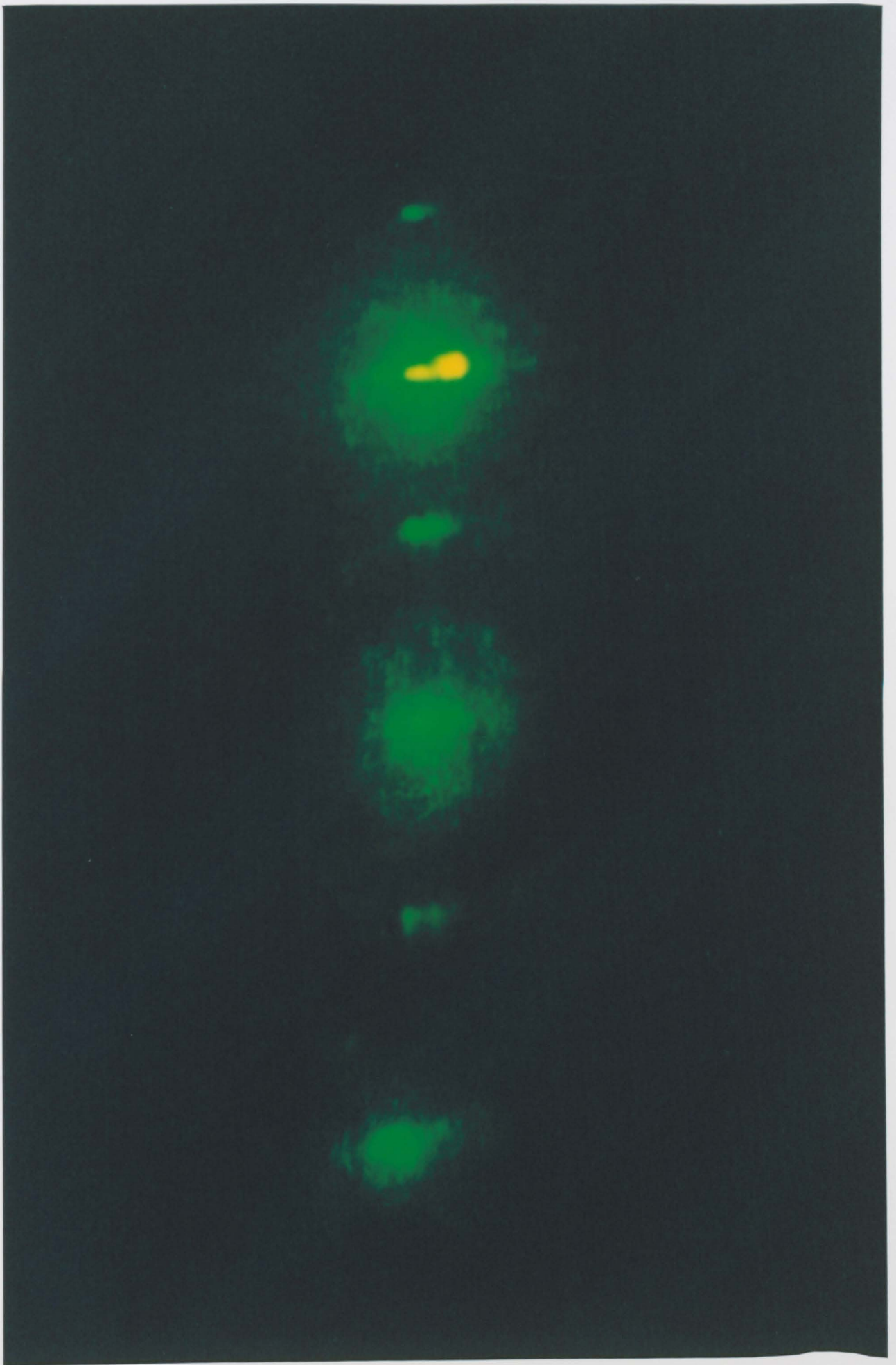


Figure 8.11 b (shown overleaf). An outline of the figure is shown below. The OPO was operating with an intra-cavity etalon tilted at $\sim 2^\circ$ from the cavity axis. The 1st reflection contains 1/10 of the energy in the main beam. The 2nd reflection contains 1/100 of the energy. The secondary reflections are much weaker and could not be measured.





was not possible, but it is reasonable to assume that this progression continues. Depending on the etalon tilt angle, up to five off-axis spots were visible to the eye at any one time. The ratio between the energies of the spots is similar to the measured loss of the etalons using the HeNe, i.e. ~10-15%. The reflections are most likely due to multiple reflections between the etalon and the OPO mirror.

Theoretically, the pump depletion should not be dependent on the increased losses within the cavity since operation is normalised to the number of times above threshold. The increased loss only has the effect of increasing the threshold. The reduction in the measured pump depletion (see table 8.2) can perhaps be explained by the signal beam divergence and the acceptance angle of the etalons. Measurements of signal beam divergence and pump depletion against number of times above threshold are shown in figure 8.12. The beam divergence increases as the

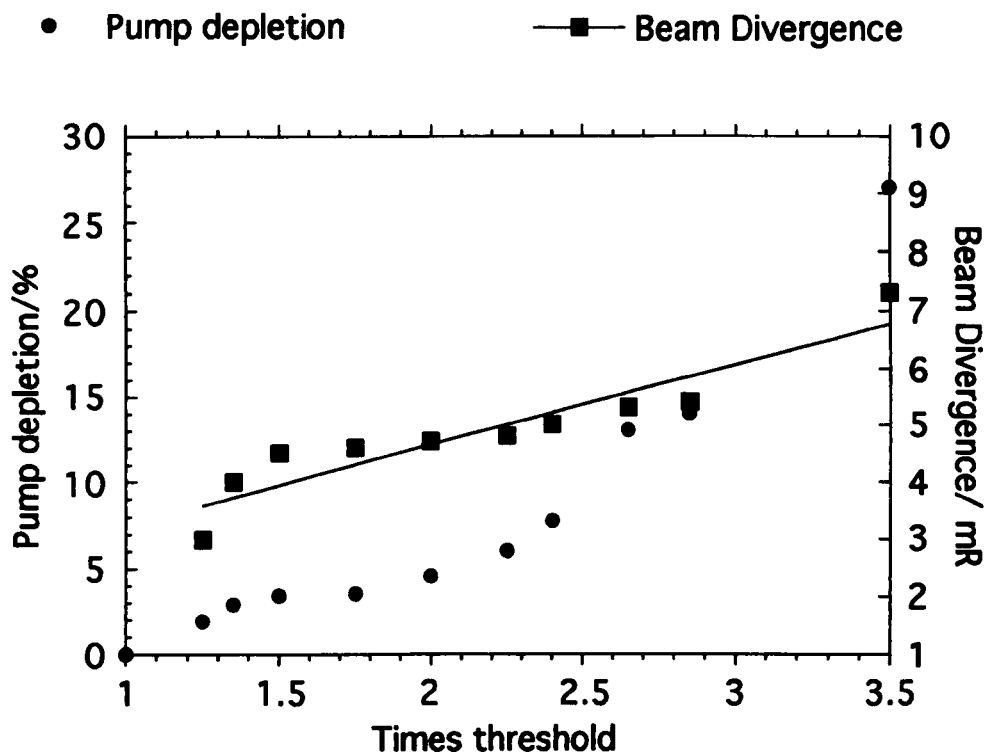


Figure 8.12. Beam divergence and pump depletion versus number of times above threshold. The solid line is a best fit through the beam divergence data.

number of times above threshold is increased from 3 mR near threshold to 7.3 mR at 3.5 times threshold. The measurements were taken under normal broad linewidth operation with no etalons in the cavity. If these values are compared to the acceptance angle of the etalons then the two values can be seen to be comparable. To calculate the

acceptance angles of the etalons the assumption was made that a loss discrimination of 30% or more will stop oscillation on the discriminated modes. Following the calculation through, the acceptance angles for the 0.5 mm, 1 mm and 2 mm etalons, tilted at 5 mR to the normal, can be shown to be 9.8 mR, 6.0 mR and 2.4 mR respectively. The acceptance angles of the etalons, therefore, impose a restriction on the signal beam divergence that is not present in the free running OPO cavity. In the unrestricted case, the large pump beam sizes permit a certain degree of non-collinearity in the signal and idler beams. Even with a pump beam divergence of 1 mR, pump depletions of greater than 60% have been observed in BBO where the acceptance angle is only 0.13 mR. The extra constraint introduced by the etalon acceptance angle prohibits the build-up of off-axis components of the signal and idler, which in turn means that part of the pump beam cannot be used. This leads to a decrease in the pump depletion.

Steps were taken to reduce the divergence of the signal beam by two methods. Firstly, a telescope consisting of two lenses, marked by 'BE' in figure 8.13, was incorporated in the cavity. The position of the telescope, between

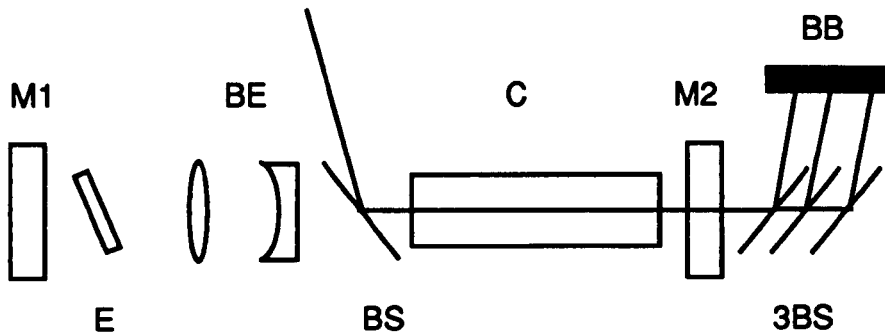


Figure 8.13. Telescopic cavity arrangement. M1 and M2 = mirrors, E = etalon, BE = beam expansion telescope, BS = beam steering plate, C = BBO crystal, BB = pump beam block. The solid line shows the path of the pump beam through the OPO.

the beam steering plate (BS) and the etalon (E) protected the delicate etalon coatings from the intense pump field. The telescope expanded the signal beam by a factor of two. Assuming a collimated beam, this would reduce the divergence at the etalon and would have the added advantage of reducing the energy density of the signal beam within the etalon. However, the lenses used were not anti-reflection coated and the increased round-trip loss of ~16%, in addition to the considerably lengthened cavity, increased the threshold dramatically from 0.3 Jcm^{-2} to 0.8 Jcm^{-2} . This limited the maximum number of times above threshold at which the OPO could be pumped due to mirror damage. As a result, only erratic behaviour was observed at about 1.5 times

threshold. When the telescope was removed, a reduction in the pump beam divergence was noticed, purely because of the increase in cavity length,. Thus, by operating the line-narrowed OPO with a 160 mm cavity, instead of the usual 60 mm length, it was possible to reduce the signal beam divergence. The beam divergence of the 60 mm cavity at three times threshold was 7.3 mR, compared with only 3.9 mR for the 160 mm cavity. It was also noticed that the threshold rose from 0.3 Jcm⁻² to 0.5 Jcm⁻² due to this length increase. Performance, in terms of pump depletion, with the 30 μm and 2 mm

Beam Size	Short Cavity		Long Cavity	
	@Threshold	3xThreshold	@Threshold	3xThreshold
4x2 mm	3.0 mR (2.0 mR)	7.3 mR (6.3 mR)	1.0 mR (0.0 mR)	3.9 mR (2.9 mR)
2x1 mm	1.8 mR (-0.2 mR)	3.9 mR (1.9 mR)	1.3 mR (-0.7 mR)	1.8 mR (-0.2 mR)

Table 8.4 Comparison of signal divergence in short and long cavities. The long cavity was 160 mm long and the short cavity was 60 mm long. Pump divergence = 1 mR. for the 4x2 mm² beam and 2 mR for the 2x1 mm² beam. The degree to which non-collinear phase-matching occurs in each of these cases may be estimated by subtracting the pump divergence from the signal (this is shown in brackets).

etalons was not significantly improved. This, however, proved to be the case even without etalons in the cavity. The restriction on non-collinear phase matching induced by the increased cavity length reduced the pump depletion in the same way as the acceptance angle of the etalon had done. A study of the effect of non-collinearity through the signal beam divergence is given in table 8.4. The pump beam sizes 4 x 2 mm² and 2 x 1 mm² were chosen as two representative examples (for the excimer system) of large and small beam sizes respectively. The results for both beam sizes show that the signal beam divergences at three times threshold are greater than the signal beam divergences at threshold. This is to be expected since more modes, further from Δk=0 will be above threshold. The signal beam divergences for the longer cavities are less than those of the short cavities. This is because the cavity length restricts the allowable spread in signal wavevectors, to those within the pump gain volume. The effect of the pump beam size should also be considered. The larger pump beam can permits a greater signal beam divergence, as expected. This result is perhaps obscured by the variation in the pump divergences between the two cases. By subtracting the pump beam divergences from the signal divergences, the remainder, due to non-collinearity, can be observed. The negative values indicate that the signal

has been constrained by the cavity to an angle less than the pump beam divergence and so part of the pump beam will be undepleted (spatially as opposed to temporally).

The large beam divergence of the signal is thus detrimental to the performance of the line-narrowed OPO. The divergence of the signal beam could not be easily reduced without increasing the threshold significantly. This is because the OPO relies on non-collinear phase-matching to overcome the restrictive acceptance angle in BBO. Clearly a pump source with a beam divergence less than the acceptance angle would be an interesting test of the hypothesis.

8.6.4 Tunability of the Line-narrowed OPO

So far, the discussion of the effects of the etalons has been restricted to the case where the etalon tilt is kept small, namely $\sim 3\text{mR}$. To achieve full tunability from the line-narrowed device, it is necessary to demonstrate that the etalons can be tuned through at least one FSR. The angle through which each etalon must be rotated, and the measured performance of the OPO under these conditions, are shown in table 8.5. Here, the increase in threshold is much greater.

Etalon	Angle for 1 FSR	Tilt	Relative Threshold
30 μm	53 mR	72 mR	1.3
0.5 mm	13 mR	31 mR	1.9
1 mm	9 mR	16 mR	2.3
2 mm	6 mR	15 mR	2.4
2 mm + 30 μm	N.A.	10 mR	2.8

Table 8.5. Relative change in threshold for etalon tilts greater than 3 mR

When both the 30 μm and the 2 mm etalons were in the cavity, the threshold increased to 0.56 Jcm^{-2} , which is 2.8 times that when there were no etalons in the cavity. Pump depletions of only $\sim 5\%$ were measured at 3 times threshold and the useful output energy was $\sim 0.1 \text{ mJ}$.

8.7 Conclusions

In this chapter, the characteristics of a single axial mode OPO have been presented. Under free running conditions, the linewidth of the OPO varied greatly across the large tuning range. In this study, the region close to degeneracy has been ignored as the emphasis of the work was on using etalons for line-narrowing. Manufacturing

restrictions limited the thinnest etalons available, which in turn limited the largest linewidth that could be controlled with a solid etalon. Below 580 nm, the OPO was successfully line-narrowed using two intra-cavity etalons. The etalons used were 30 μm and 2 mm thick and had finesses of 10. The OPO was successfully tuned between 420 nm and 560 nm, operating on a single axial mode. Operation was, however, not stable on any one mode and so stabilisation of the OPO cavity would be required to maintain oscillation to any one single axial mode.

The performance of the OPO was affected in three, non-beneficial ways by the insertion of the etalons. Firstly, the threshold increased. This was due to some extent, to the increased cavity length but more so by the large reflection losses from the etalons. It is possible that these losses were due to the flatness of the etalons, which are specified as flat to $\lambda/50$ across the aperture of 10 mm. However, due to the thinness of the substrates, the etalons may have become warped. Another explanation is the presence of damage on the etalon coatings due to the circulating signal field within the etalons. The damage observed was slight but its effect was difficult to quantify. Secondly, the pump depletion was reduced and it was postulated that this may have been due to the acceptance angle of the etalons limiting the non-collinearity of the signal beam. In BBO, the crystal acceptance angle is very small and the pump beam divergence is ~ 1 mR. To explain the high pump depletions obtained, it is necessary to assume that the non-collinearity of the signal beam allows off-axis interactions with the pump. This is borne out by the presence of large signal beam divergences. The signal divergence is greatly reduced both on the insertion of etalons and on the lengthening of the cavity. The pump depletion also falls. Thirdly, the output coupling efficiency drops. This can be explained by the increase in losses within the cavity. Clearly, there is a case for better quality etalons as this would reduce the effect on threshold and output efficiency, although the effect on pump depletion is likely to remain.

An attempt was also made to line-narrow an LBO OPO using the same etalons. The advantage of LBO over BBO is that the inherent linewidth is less, meaning that ideally the etalons used can be thinner and the finesses less. In reality, the significantly higher threshold of the device made it impractical to line-narrow. An increase in the threshold of over 2 times put the pump energy density in the region of mirror damage and the operation was erratic. The main motivation of the experiment was to measure the difference that a much larger acceptance angle, and therefore reduced dependence on non collinear phase matching, would have on the performance of the device. Unfortunately, this could not be tested.

REFERENCES

- 1 'Single Mode Oscillation of a Pulsed Singly Resonant Optical Parametric Oscillator'. L. B. Kreuzer. *Appl. Phys. Lett.* 15, 263 (1969).
- 2 'Lasers: a series of advances, vol 4'. R. G. Smith. Eds A. K. Levine and A. J. Maria. Pub Marcel Dekker, New York (1976). p293.
- 3 Visible BaB₂O₄ Optical Parametric Oscillator pumped at 355 nm by a single-axial-mode Pulsed Source'. Y. X. Fan, R. C. Eckardt and R. L. Byer. *Appl. Phys. Lett.* 53, 2014 (1988).
- 4 'Single-frequency optical parametric oscillator'. W. R. Bosenberg and D. R. Guyer. *Appl. Phys. Lett.* 61, 387 (1992).
- 5 Optical Parametric Oscillation Threshold and Linewidth Studies'. Stephen J. Brosnan and Robert L. Byer. *IEEE J. Quantum Electron.* 15, 415 (1979).
- 6 'Efficient, single-axial-mode operation of a monolithic Mg:LiNbO₃ optical parametric oscillator'. C. D. Nabors, R. C. Eckardt, W. J. Kozlovsky and R. L. Byer. *Opt. Lett.* 14, 1134 (1989).
- 7 Efficient ultraviolet LiB₃O₅ optical parametric oscillator'. Majid Ebrahimzadeh, Gordon Robertson and Malcolm H. Dunn. *Opt. Lett.* 16, 767 (1991).
- 8 'Lithium triborate optical parametric oscillation pumped at 266 nm'. Y. Tang, Y. Cui and M. H. Dunn. *Opt. Lett.* 17, 192 (1992).
- 9 'Type II phase matching in a β -barium borate optical parametric oscillator'. W. R. Bosenberg and C. L. Tang. *Appl. Phys. Lett.* 56, 1819 (1990).
- 10 'A 1.4-4 μm high-energy angle-tuned LiNbO₃ parametric oscillator'. R. L. Herbst, R. N. Fleming and R. L. Byer. *Appl. Phys. Lett.* 25, 520 (1974).
- 11 'Visible optical parametric oscillation in LiB₃O₅'. Yunping Wang, Zuyan Xu, Daoqun Deng, Wanhua Zheng, Baichang Wu and Chuangtian Chen. *Appl. Phys. Lett.* 59, 531 (1991).
- 12 High-efficiency and narrow-linewidth operation of a two-crystal β -BaB₂O₄ optical parametric oscillator'. W. R. Bosenberg, W. S. Pelouch and C. L. Tang. *Appl. Phys. Lett.* 55, 1952 (1989).
- 13 Visible optical parametric oscillation in synchronously pumped beta-barium borate'. S. Burdulis, R. Grigonis, A. Piskarskas, G. Sinkevicius, V. Sirutkaitis, A. Fix, J. Nolting and R. Wallenstein. *Opt. Comm.* 74, 398 (1990).
- 14 'Singly Resonant CdSe Infrared Parametric Oscillator'. R. L. Herbst and R. L. Byer. *Appl. Phys. Lett.* 21, 189 (1972).
- 15 'Singly resonant proustite parametric oscillator tuned from 1.22 to 8.5 μm '. D. C. Hanna, B. Lunther-Davies and R. C. Smith.
- 16 Efficient, single-axial mode oscillation of a beta barium borate optical parametric oscillator pumped by an excimer laser'. Gordon Robertson, Angus Henderson and Malcolm H. Dunn. *Appl. Phys. Lett.* 62, 123 (1993).
- 17 'Tunable single mode operation of gas lasers using intracavity tilted etalons'. M. Hercher. *Appl. Opt.* 8, 1103 (1969).
- 18 *Optical Electronics*' Amnon Yariv. CBS Publishing, New York p92.

Injection Seeding

In this chapter, the line-narrowed OPO developed in the previous chapter is used as a seeding source to control the linewidth of an optical parametric oscillator (OPO) and an optical parametric amplifier (OPA).

9.1 Introduction

In the last chapter, a single-axial-mode OPO that was tunable from 420 nm to 560 nm was demonstrated. Theoretically, this range could be extended below 420 nm to 355 nm since the inherent linewidth of the signal decreases as the wavelength decreases, making the task of line-narrowing simpler. The range between 560 nm and degeneracy at 616 nm requires the use of a diffraction grating with an associated increase in oscillation threshold.

The increase in threshold and the reduction in pump depletion and output coupling efficiency means that the output energies from the line-narrowed OPO are greatly reduced. This can be explained by the increase in cavity length required to house the etalons, the large insertion loss of the etalons, ~10%, and the restriction placed on non-collinear phase-matching within the cavity. It seems likely that, even with improved etalons and reduced pump beam divergence, there would still be a significant drop in the output energy. It is thus of interest to investigate the alternative line-narrowing strategy of injection seeding. Any light source with the desired spectral and coherence properties may be used. Suitable seeding sources are dye lasers, tunable solid state lasers (such as Ti:sapphire) or fixed frequency lasers (such as helium neon lasers).

Fixed frequency lasers confine the operation of the OPO to a single pair of wavelengths², one of which is the seed laser wavelength. If, however, the other wavelength is of practical use, this may prove to be a useful way of generating it. The use of a dye laser means that many laser dyes³ are required to cover a large wavelength range, removing the advantage of a solid state device. Other tunable sources⁴ can be used in a similar way to the fixed frequency lasers, to seed on either wave, however, the use of a laser seed source will limit to some extent the tunability of the OPO. The

only source that is as broadly tunable as the BBO (or LBO) OPO is another similar OPO. For this reason the OPO and the OPA described in this chapter are seeded by another BBO OPO that has been line-narrowed by intra-cavity etalons.

In an singly resonant oscillator (SRO), there will be a set of modes under the gain bandwidth, centred on $\Delta k = 0$, that will experience gain in the presence of a strong pump field (see equation 2.9) The radiation in these pumped modes builds up exponentially from its initial level, which is usually noise. In this simple model, the effects of pump depletion are ignored in the initial stages. The various modes build up at a rate that depends on their value of Δk . The mode nearest $\Delta k=0$ experiences the highest gain. In a simple model, it can be assumed that steady state oscillation will occur on the first mode to reach 10% of the pump intensity. If a signal is injected into the cavity during the build-up time of the OPO, at some power density level above the noise level of the cavity modes, then it too will experience exponential gain. Assuming that the injection signal is not at $\Delta k=0$, then it will experience less gain than modes nearer $\Delta k=0$. However, since it starts from a higher power density level than the surrounding modes, it is possible that it will reach 10% of the pump intensity first. In this case, injection seeding will be successful and the OPO will oscillate on the injected mode. The other modes will still experience gain but at a reduced level due to the pump depletion caused by the injected mode. Eventually, the mode nearest $\Delta k=0$ will grow to a level where it too can deplete the pump. At this point, control of the injection seeded mode will cease and the OPO will revert to free running oscillation. It is clear then that injection seeding of a pulsed OPO provides only temporary control over frequency and coherence characteristics. In this sense, it is important to seed the OPO at a wavelength close to that dictated by the $\Delta k=0$ phase-matching condition in order to maximise the period of control and at a sufficiently high energy level to control the mode of oscillation.

9.2 Historical Perspective

Injection seeding was first reported by Bjorkholm and Danielmeyer⁵ in 1960, to control the output characteristics of an LiNbO_3 OPO that was pumped by a ruby laser at 693 nm and injection seeded by an Nd:YAG laser at 1.064 μm . The use of fixed frequency lasers, such as Nd:YAG lasers as a seeding sources, clearly means that the OPO will not be tunable. Work by Abdullin et al⁶ used a non-critically phase-matched barium sodium niobate OPO to injection seed a lithium niobate OPO. The seed source was tunable from 0.75 μm – 1.8 μm and could thus be used to seed the entire short wavelength tuning range of the OPO. Injection signal energies of $\sim 0.5\mu\text{J}$ were

sufficient to control the spectral properties of the seeded OPO. Other tunable seeding sources that have been reported are colour centre lasers (ref 4) and pulsed dye lasers⁷. Both of these provide limited tunability over a small portion of the OPO tuning range.

In references 2 to 6, the injection signal energy required to successfully injection seed the OPO was in the range 0.5–20 μJ and a reduction in oscillation threshold was observed. OPOs with pulse durations of between 5 and 10 ns have been successfully injection seeded. For comparison, the expected injection signal energy from the BBO OPO, to be used as a master oscillator, will be $\sim 300 \mu\text{J}$ and the pulse duration of the excimer and OPO are 17 ns (FWHM) and 12 ns (FWHM), respectively.

9.3 Injection Seeding Experimental Set-up

The injection seeding source, as mentioned earlier, was the line-narrowed BBO OPO discussed in chapter 8. In order to maintain a reasonable threshold, the OPO was initially line-narrowed using only one etalon. The resulting signal and idler would thus be many axial modes wide and so the need for cavity length matching of the two cavities would not be necessary. The intention was to demonstrate control of the linewidth of the second OPO before preceding to line narrow the first OPO any further. The experimental set-up is shown in figure 9.1. The excimer beam was split 50:50 at the beam splitter (BSP) to give equal pump beams for both cavities.

One half of the beam was directed through a beam compressor comprising of a 1.5 m lens (L1) and a -240 mm lens (L2). The focused beam had an area of $3 \times 1.5 \text{ mm}^2$. A beam steering plate (BS1) was used to introduce the pump beam into the line-narrowed OPO cavity (master oscillator). The beam steering mirror was coated on one side to be highly reflecting at the pump wavelength, 308 nm, and transmitting for the signal wave between 350 and 620 nm. The mirror was Brewster angled to reduce the insertion loss.

The other half of the pump beam was directed into the second OPO (slave oscillator) via a second beam compressor identical to the first. A beam steering plate, BS2, coated for the same wavelengths as BS1, was used to direct the pump beam into the slave OPO cavity. This plate was mounted outside the cavity to keep the OPO cavity as short as possible. The collinear alignment of the injection signal and the pump beam was achieved using the signal steering mirrors, SM1, and SM2. A 25 cm focal length lens, L5, was used to shape the injection signal beam before it entered the slave OPO cavity.

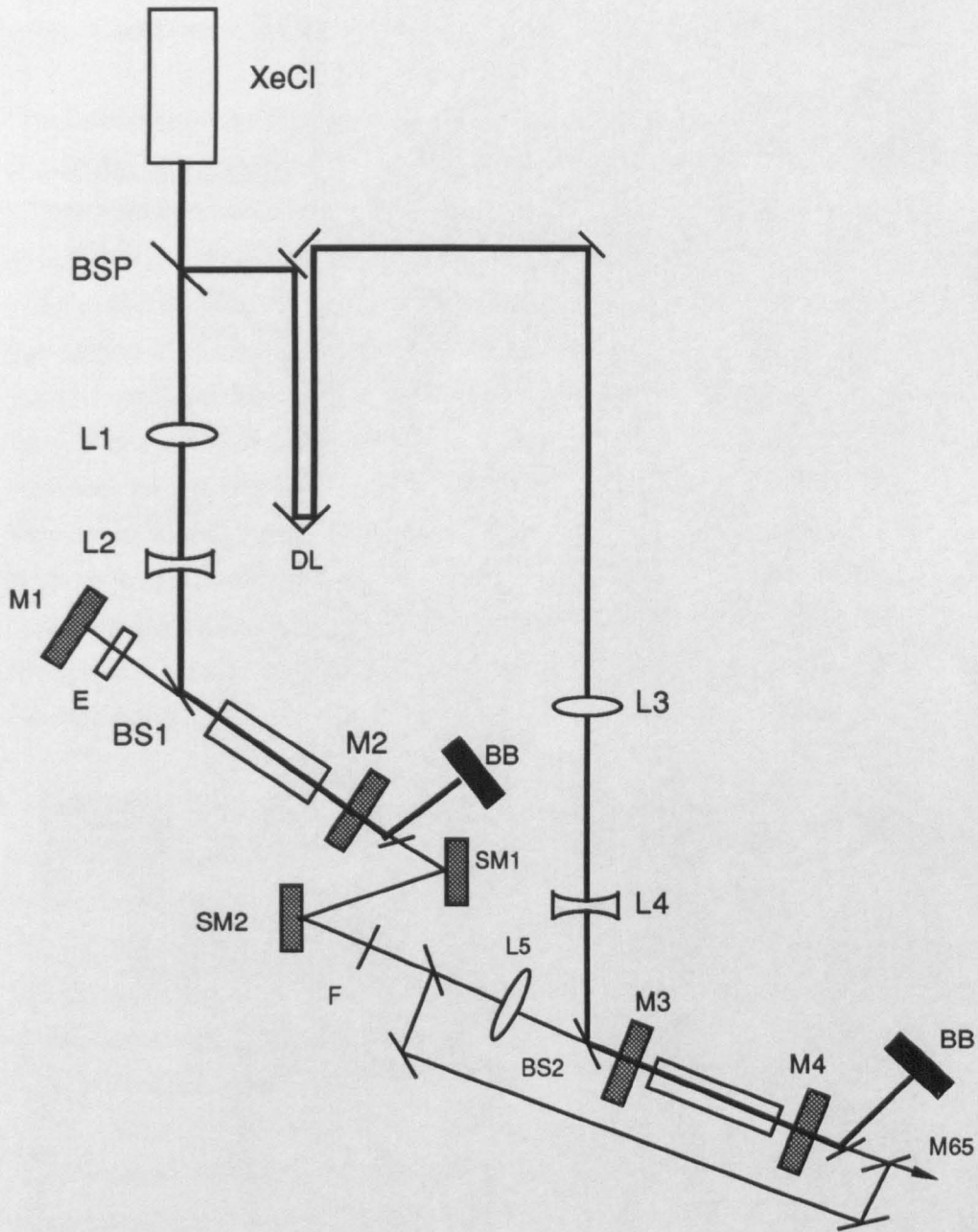


Figure 9.1. Injection seeded OPO experimental set-up. KEY:- BB = beam block, BSP= beam splitter, BS1 & BS2 = beam steering plates, DL= delay loop, E= etalon, F= filter, L1 & L3 = 1.5 m focal length lenses, L2 & L4 = -240 mm focal length lenses. L5 = 25 cm focal length lens, M1-4 = cavity mirrors, M65 = 65% reflecting mirror. SM1 & SM2 = signal beam steering mirrors. The final output is directed into a monochromator.

The master OPO was line-narrowed using one etalon. The OPO mirror, M1, was highly reflecting for the signal wave between 400 and 600 nm. All the signal and idler

energy thus left the cavity via, M2, an output coupler of ~5%. By selecting an appropriate filter, F, either the signal or idler wave could be blocked.

To ensure that the injection signal was present within the cavity of the slave OPO during the build-up time, it was necessary to introduce a delay between the two OPOs. The required duration of this delay was the sum of the build-up time of the master OPO plus the transit time between the two OPOs. The transit times between the pump laser and the OPOs were the same (omitting the delay loop, DL). The build-up time of the line-narrowed master OPO was measured, using a photodiode to monitor the temporal pump depletion, to be 3 ns to 4 ns and the transit time was 1.5 ns. The delay between the OPOs should thus be ~4.5 ns to 5.5 ns, taking the extreme cases. The delay was introduced by constructing a delay loop, DL, into the pump path of the second OPO. Two beam steering mirrors placed at right angles to each other acted as a retro-reflector in the horizontal plane. The mirrors were placed on a sliding rail which allowed the path length between the pump laser and the slave OPO to be varied by up to 2 m. The OPOs were positioned such that the delay between the two devices could be varied from 2 ns to 8 ns.

To monitor the linewidth of the OPOs, a Monospek monochromator was used. A glass plate was used to divert 4% of the signal/idler beam from the master OPO, into the monochromator via the 65% reflecting mirror, M65. The mirror was aligned such that the beams from both OPOs were collinear on entering the monochromator. Using this set-up, it was possible to monitor the wavelength of both OPOs simultaneously. A CCD array could be used to monitor the spectral content of the two beams on leaving the exit slit of the monochromator.

Alignment of the system was achieved by initially operating the two OPOs independently and tuning both to the same wavelength. The delay was initially set at ~5 ns. The master OPO was then line-narrowed using an etalon. The resultant signal or idler beam was collimated and steered into the slave OPO. A filter was used to remove the unwanted wave. Observation of the linewidth of the signal wave from the slave OPO indicated whether injection seeding had occurred. The temporal overlap was optimised by varying the delay between the OPOs. The spatial overlap was also changed as required, using the beam steering mirrors and the collimating optic (L5).

The line-narrowed OPO was pumped with ~35 mJ in a $4 \times 2 \text{ mm}^2$ beam. The cavity was 60 mm long and the threshold was 0.3 Jcm^{-2} . The signal and idler energies from this OPO were 0.1 mJ and 0.05 mJ respectively. The pump beam of the slave OPO

was identical to that of the line-narrowed device. The slave OPO cavity was ~ 25 mm long, and the threshold was 0.16 Jcm^{-2} . This OPO was thus operating at ~ 3 times threshold and the OPO output energy was measured to be $\sim 1 \text{ mJ}$.

9.4 Injection Seeding Results.

Initially, the performance of the injection seeding was optimised for spatial and temporal overlaps within the crystal. For seeding to be effective, it was only necessary that the injection signal be present during the build-up time of the slave OPO. The

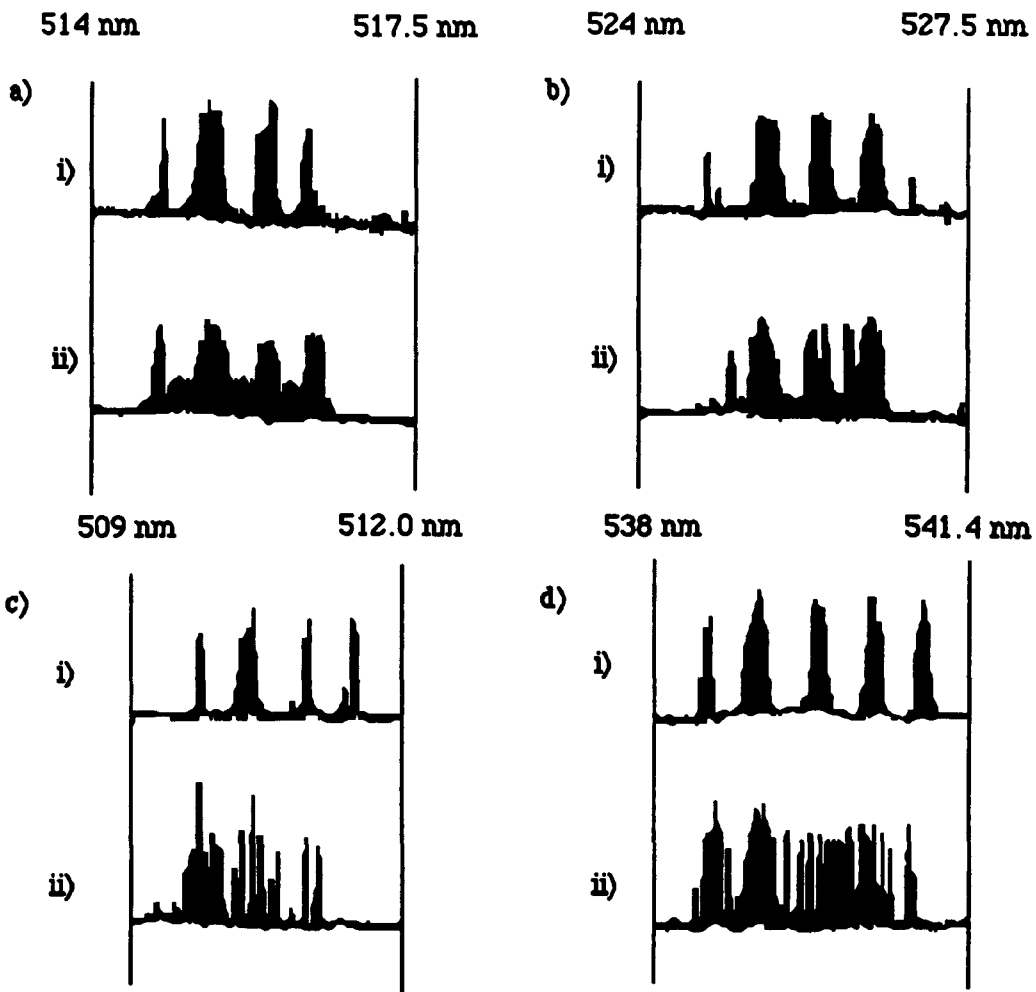


Figure 9.2. Variation in spectral control with delay. The traces show (i) the seeding and (ii) the seeded spectral outputs for four different delays. (a) 4 ns, (b) 6 ns and (c) 7.2 ns, (d) 9 ns. Seeding is most effective in the 4-6 ns region. The etalon used to line-narrow the OPO was a 0.2 mm thick with a finesse of ~ 4.5 .

temporal overlap was found to be insensitive to the exact overlap between the pump and injection signal. Since the injection signal was ~ 12 ns long and the build-up time was ~ 5 ns then it is clear to see why the seeding was insensitive to the temporal overlap. Figure 9.2 shows the spectra of the OPOs with various delays. The best seeding performance was found to be when the delay between the two OPOs was in the range 4 ns to 6 ns. The spatial overlap, however, was much more critical. A diverging beam of ~ 1 mR was found to work best with the injection signal beam area as closely matched to the pump beam as possible. The threshold of the slave OPO was observed to drop by a factor of 10% when injection seeding occurred. It was also necessary to have the wavelengths of the two OPOs matched to within half of the OPO inherent linewidth.

Figure 9.3a(i) shows the linewidth of master OPO under normal free running conditions, which is the same as the free running linewidth of the slave OPO. The OPO was oscillating at 526 nm/743 nm with the lower wavelength resonant. The linewidth was ~ 2.2 nm FWHM. Figure 9.3a(ii) shows the linewidth of the master OPO with a 0.2 mm, etalon of finesse 5 in the cavity. The linewidth was reduced to 4 peaks at 526 nm. The 526 nm radiation was used to injection seed the slave OPO, which was also set to oscillate at 526 nm/743 nm. Figure 9.3a (iii, iv & v) show examples of the measured linewidth of the signal wave at 526 nm from the slave OPO. Clearly a certain degree of control has been exerted over the spectral properties of the slave OPO. It should be remembered that it takes in the region of 100 shots to take each trace and hence the reliability of the seeding is quite good. However, there is clearly a broadening of the individual peaks and there are a few shots where seeding has not been successful. This is indicated by the existence of sharp lines between the 4 main peaks. Figure 9.3b shows more examples of injection seeding taken at 511 nm. The seed beam characteristics are similar.

The experiments were repeated using the idler beam from the master OPO to injection seed the slave OPO. The first oscillator was resonant for the lower wavelength as before and an intra-cavity etalon ($30 \mu\text{m}$, $F=10$) selected a single 0.4 nm peak from within the gain bandwidth. The linewidth of the idler was then measured to be 0.5 nm and this is shown in figure 9.4. This was used to seed the non-resonant wave in the slave OPO. The results are shown in figure 9.4. Clearly a similar performance is achieved using this method.

The above results show that injection seeding is taking place within the slave OPO. However, the slave OPO does not reproduce the linewidth of the master OPO

satisfactorily. This may be due to inadequate mode-matching between the pump beam and the injection signal. This would required careful matching of both the beam sizes and the beam divergences. In addition, the injection signal beam and the pump beam may not overlap sufficiently, either spatially or temporally, within the slave OPO. As a result,

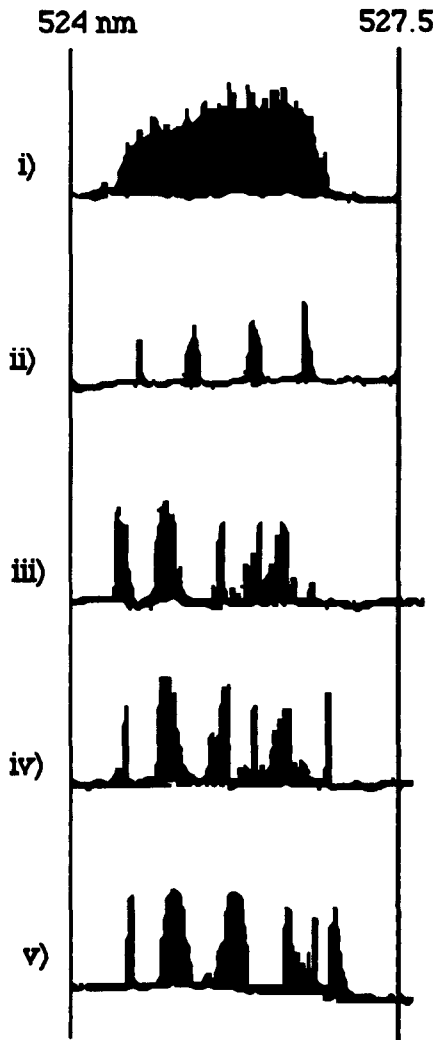


Figure 9.3a

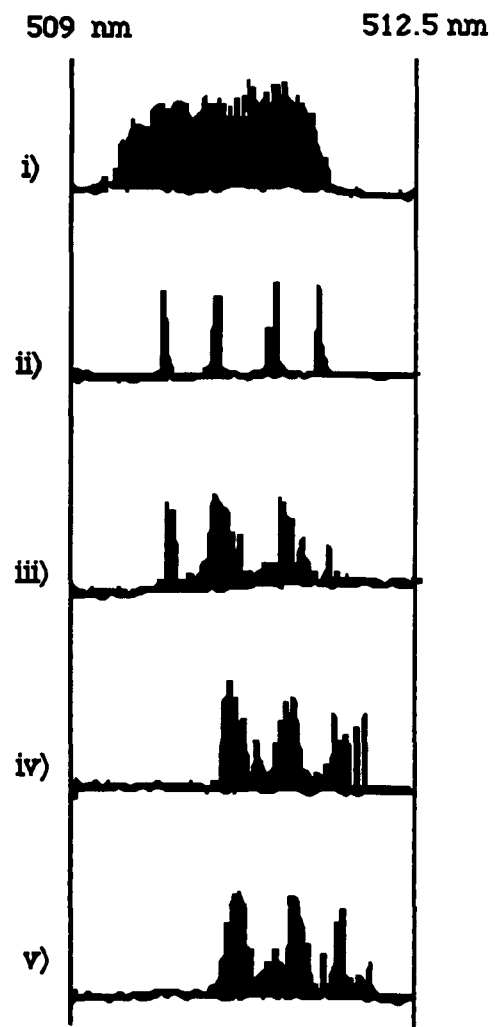


Figure 9.3b

Figure 9.3 Injection seeding of a BBO OPO. The wavelength range of the scans are shown at the top of each figure. The vertical scales are in arbitrary units of intensity.

In both figures, trace (i) represents the inherent linewidth of the OPO. Trace (ii) depicts the spectral output of the first OPO when line-narrowed with a 0.2 mm, $F=5$, etalon. The remaining traces, iii, iv, and v, are representative of the spectral output of the second OPO in the presence of the injection signal.

a portion of the gain volume may not be controlled by the injection signal. An alternative to an injection seeded OPO is to use an optical parametric amplifier (OPA) as shown in figure 9.4. This option is explored further in the next section.

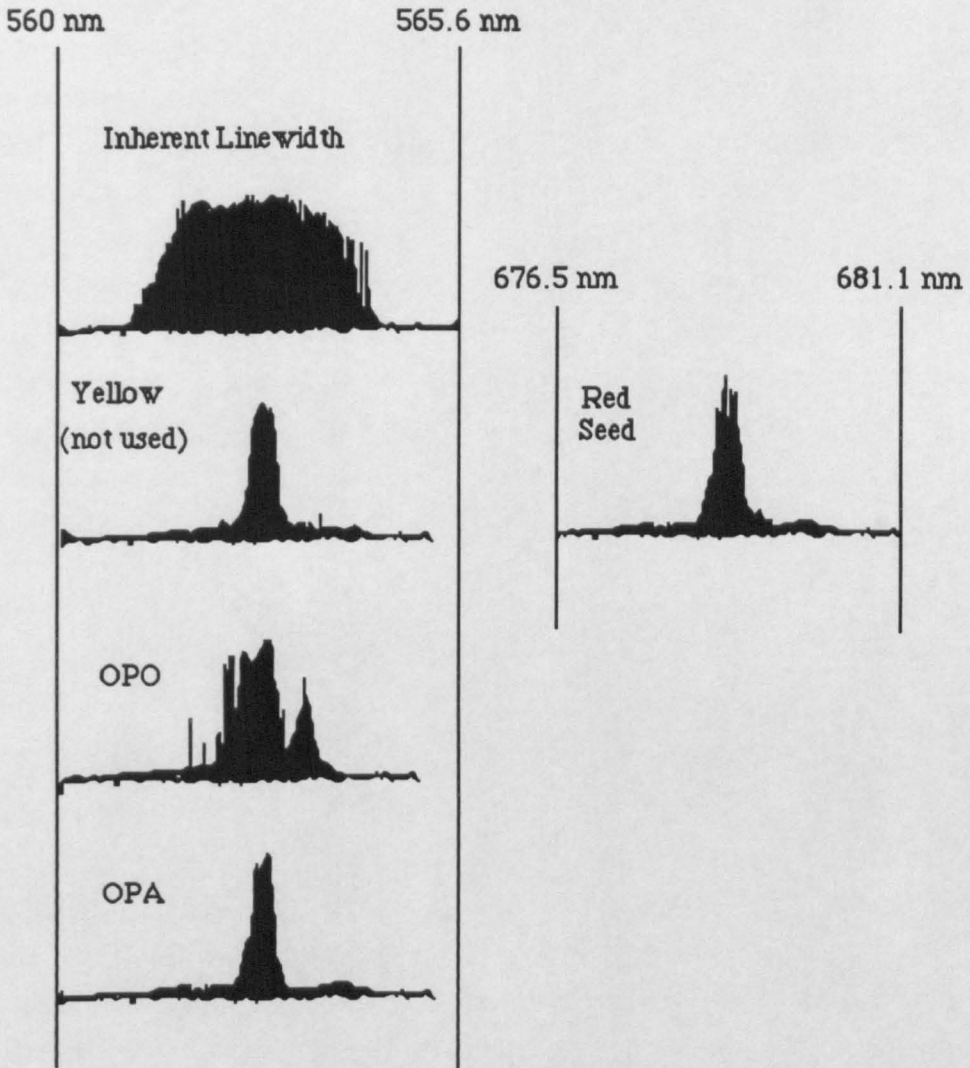


Figure 9.4. Injection seeding using the idler from the line-narrowed OPO. The inherent linewidth of both OPOs is shown. The master oscillator was line-narrowed using a $30\ \mu\text{m}$ etalon with a finesse of 10. The yellow and red waves from this OPO are shown.

The yellow wave was blocked using a filter and the red wave was used to seed the slave oscillator. The spectrum of the yellow wave from the slave oscillator is shown (marked OPO). The linewidth of this wave is broader than that of the yellow output of the master oscillator. This is similar to previous examples. In addition the output of an OPA, seeded with the same red beam, is shown. Clearly the reproduction of the linewidth is far superior.

9.5 Optical Parametric Amplifier

9.5.1 Introduction

Under normal conditions, the signal and idler waves are generated initially from noise. In the situation described above, the signal wave of the slave OPO is generated from a seeding signal, which is injected into the cavity during the build-up period of the OPO. This is apparent in practice since the signal and idler assume the same characteristics as the injection signal. The seeded slave OPO, therefore, no longer builds up from noise and the threshold is subsequently lowered. However, given sufficient single pass gain, it is possible to amplify the injection signal on a single pass, creating idler photons in the process. It is a simple matter to calculate the expected single pass gain in the crystal from the measured OPO threshold and knowledge of the pump pulse duration, and the lengths of the non-linear crystal and the OPO cavity. The single pass gain $G = \cosh^2(\Gamma L)$ where $\Gamma^2 = K S_p^2$. S_p^2 is the pump intensity. K can be calculated both theoretically as defined in chapter 2 and experimentally thus,

$$K = \frac{2.25\tau}{J_0 L^2} \left\{ \frac{1 \ln(P_N/P_Q)}{2\tau c} + 2\beta L - 0.5 \ln R + \ln 2 \right\}^2 \quad (9.1)$$

For the BBO OPO, these parameters have the following values: $J_0 = 1600 \text{ Jm}^{-2}$, $L = 20 \text{ mm}$, $l = 25 \text{ mm}$, $\tau = 17 \text{ ns}$, $\beta = 0.22$ and $R = 0.9$. On inserting these values into equation 9.1, $K = 6.45 \times 10^{-8}$. For a 17 ns pump pulse with an energy of 30 mJ in a $3 \times 1.5 \text{ mm}^2$ beam, the single pass gain, G , is 150. Thus theoretically, the pump should be completely depleted for injection signal energies of $\sim 0.2 \text{ mJ}$. It is, however, important that there is a perfect spatial, temporal and spectral overlap between the pump field and the injection signal beam. In designing the OPO/OPA system, it was important to have maximum control over these parameters.

9.5.2. Experimental Set-up

The experimental set-up is shown in figure 9.5. The line-narrowed OPO is identical to the one used in sections 9.3 and 9.4 for the injection seeding experiments. The signal (or idler) from the line narrowed BBO OPO was directed into the OPA crystal via two beam steering mirrors (B). Filters were used to block out either the unwanted signal or idler. The collimating optics (CO) consisting of two lenses, one convergent and one divergent, which were used to shape the injection signal beam. Initially, the OPA was operated as an OPO to select the wavelength of oscillation. The OPO mirrors were then

removed to form an OPA. The maximum line-narrowed seeding energy at the OPA crystal was 0.3 mJ. The delay between the OPO and the OPA was 4 ns, the same as used in the injection seeding experiment. Initial alignment was simplified by the presence of non-collinear phase-matching, which generated off-axis light when the OPA was not perfectly aligned. The OPA crystal could then be rotated to a position where a single tight spot of light exited the cavity. Although only the pump and

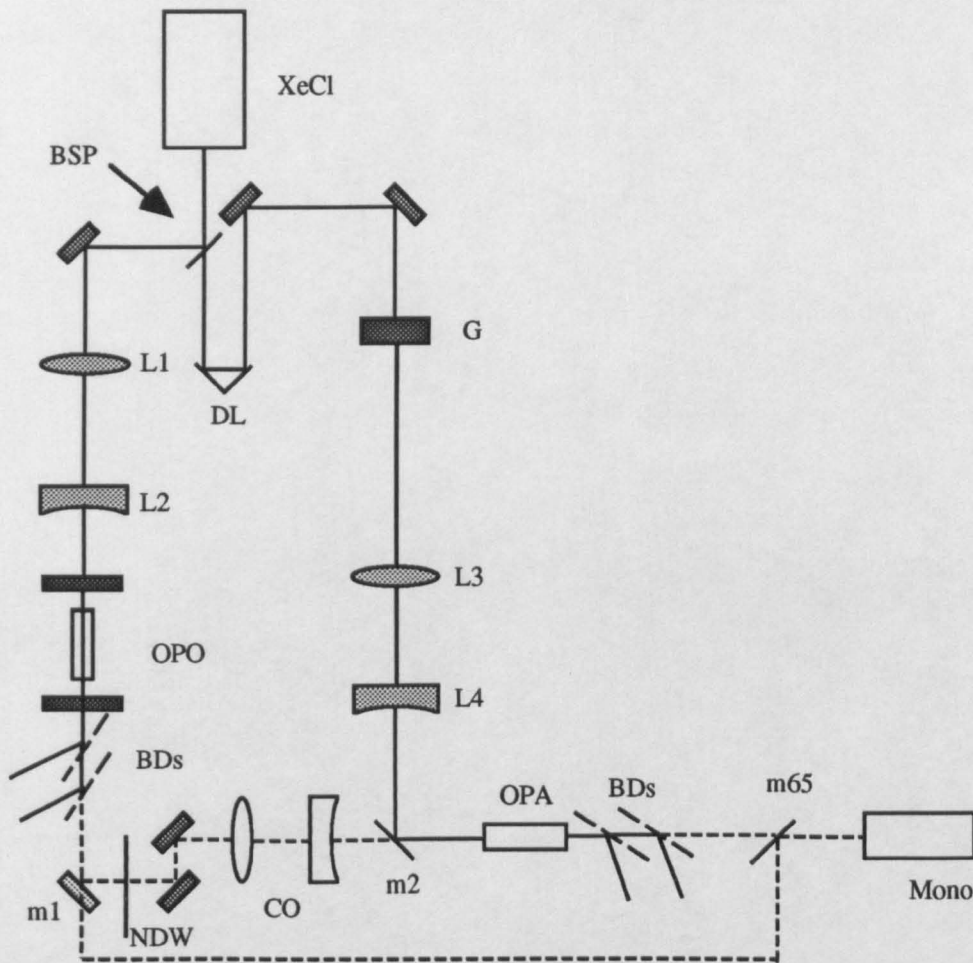


Figure 9.5. Oscillator (OPO)/ amplifier (OPA) system layout. KEY:- Beam steering plates (BDs), 50% beam splitter (BSP), collimating optics (CO), delay loop (DL), gas cell attenuator (G), lenses (L1, L2, L3 and L4), mirror, highly reflecting 600-1000 nm (m1), pump mirror, highly transmitting 400-1000 nm (m2), mirror, 65% reflecting 450-550 nm (m65), monochromator (mono), neutral density wheel (NDW).

injection signal beams entered the OPA crystal, an idler wave was observed, in addition to the pump and amplified signal, at the crystal exit face, indicating that parametric amplification had occurred.

9.6 Optical Parametric Amplifier Results

9.6.1 Linewidth Control

Figure 9.6a(i) shows the line-narrowed spectrum of the OPO around 525 nm. To be sure that the light measured from the OPA was not actually the injection signal from the OPO, the linewidth of the OPA idler was monitored instead. The red wavelength, at ~740 nm, was used to seed the OPA. The spectrum of light generated in the OPA at

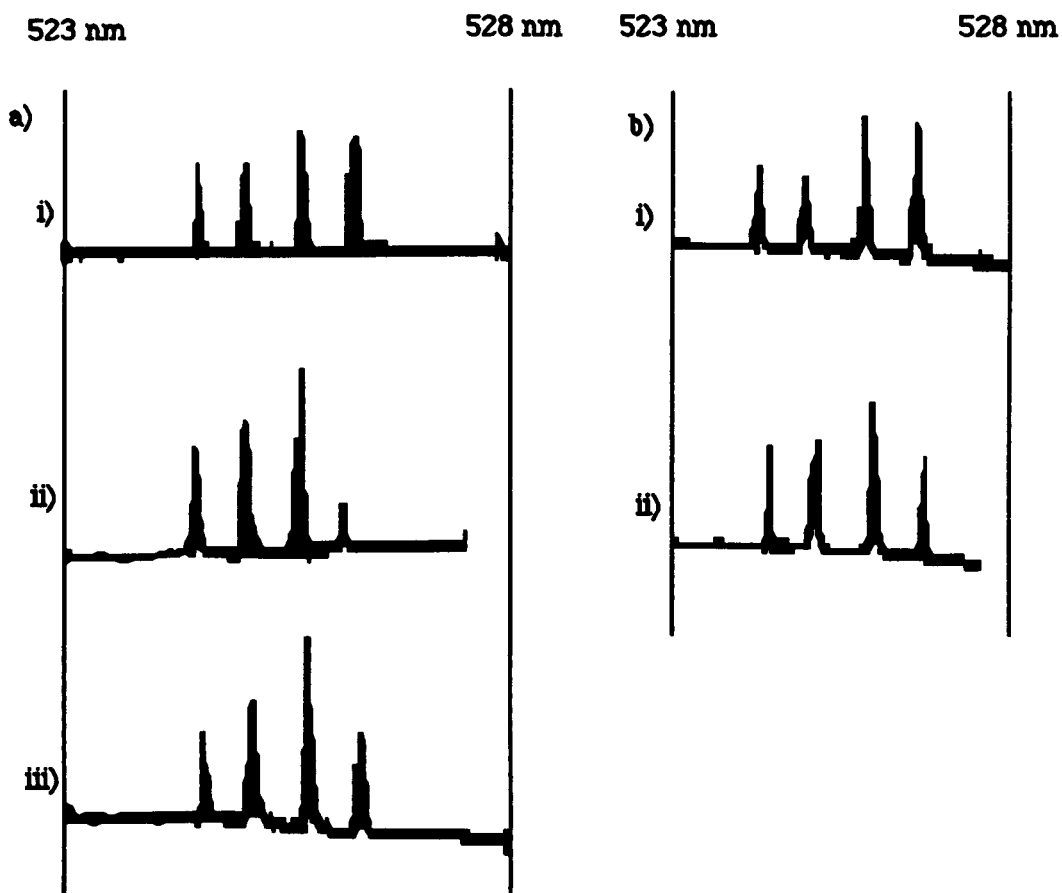


Figure 9.6. Spectral output from the OPA.. The wavelength ranges of the scans were 523 nm to 528 nm as shown at the top of the figure. In both 9.6(a) and (b) the trace (i) shows the spectrum of the seeding beam and the other traces show the spectrum of the OPA.

~525 nm was then measured using a monochromator, see figure 9.6a (ii & iii). The OPA was observed to faithfully reproduce the injection signal linewidth.

Optimisation of the OPA was achieved by varying the temporal, spatial and spectral overlaps within the OPA crystal. In order to maximise the potential injection signal energy, the optimisation process was carried out using a broadband OPO. In the case of the injection seeded OPO it was necessary to have the seeding beam present during the build-up time of the second OPO. In the case of the OPA it is necessary that the peak of the injection signal pulse overlaps with the peak of the OPA pump pulse. It is apparent that the delay between the OPO/OPA combination will be longer than that of the OPO/OPO combination. Figure 9.7 shows a graph of OPA output energy versus delay between the OPO and the OPA. The delay is defined purely in terms of the additional transit time inserted between the pump laser and the

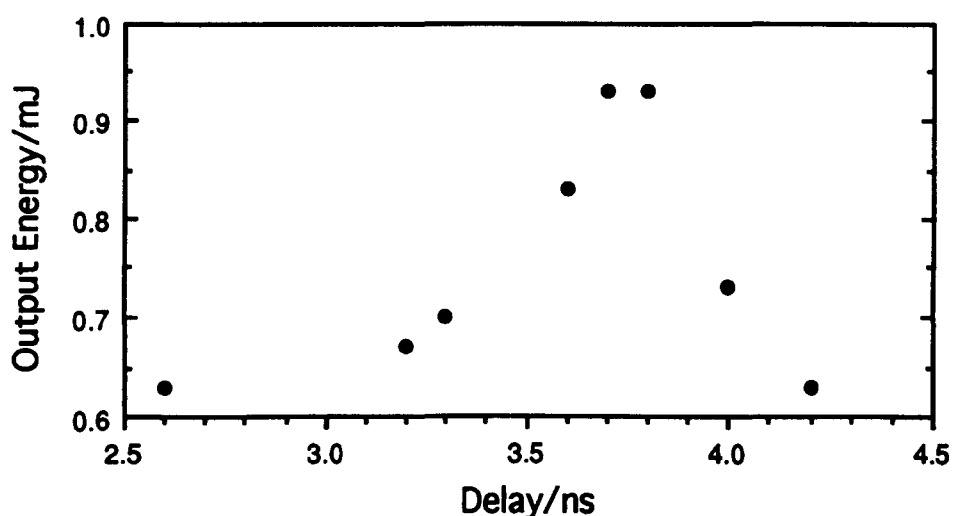


Figure 9.7. OPA output energy vs. delay between the OPO and OPA.

OPA to compensate for the build-up time of the OPO. The delay due to the transit time between the OPO and OPA was accounted for in the initial pump beam path lengths. Comparison of the build-up time and the delay show that for maximum gain, the injection signal must be present at the peak of the pump pulse.

9.6.2 OPA Performance

A study of the OPA performance for various pump and signal energies was undertaken. A gas cell attenuator was placed at position G in figure 9.5. This allowed control over the pump energy, and hence the gain in the OPA crystal, without affecting the gain of the OPO. The injection signal energy was kept constant at 0.2 mJ. Figure 9.8 shows the results. Clearly the output energy is linearly related to the pump intensity

within the crystal. There is no sign of any saturation of the OPA gain. Thus greater pump energy densities should increase the single pass gain of the device.

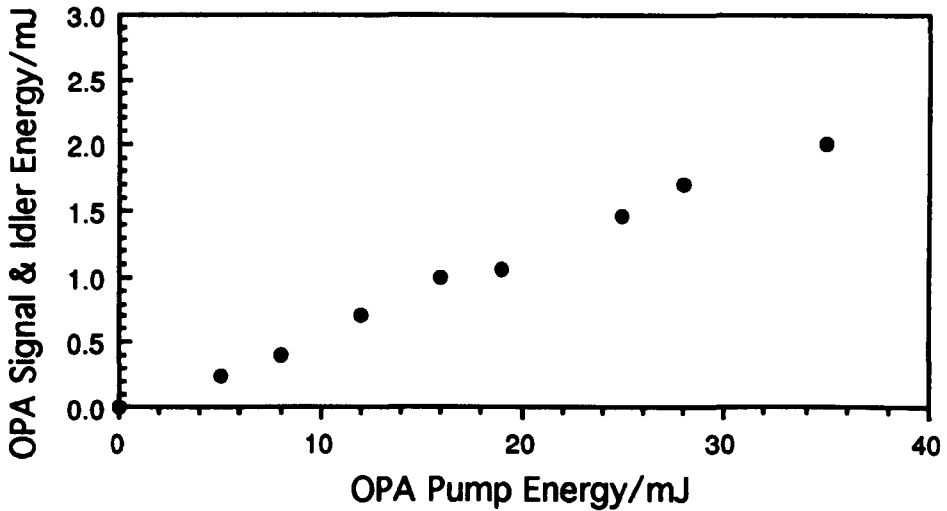


Figure 9.8. OPA output energy vs. OPA pump energy. (Injection signal kept constant at 0.2 mJ)

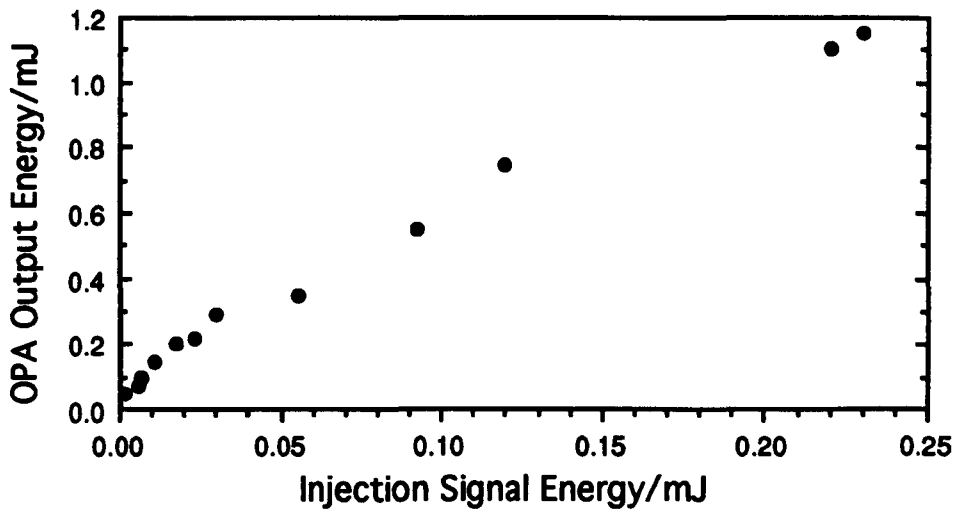


Figure 9.9. OPA output energy vs. injection signal energy. (Pump energy constant at 20 mJ)

The dependence of the OPA output energy on the injection signal strength was also measured. The pump energy to both the OPO and the OPA was kept constant at 20 mJ. The injection signal energy was controlled by a neutral density wheel (indicated by NDW in figure 9.5) placed between the OPO and the OPA. The injection signal energy

was decreased from a maximum of 0.23 mJ to 0 mJ as shown in figure 9.9. Again, the gain is linear with injection signal intensity.

Finally, a study of the effect of the injection signal beam profiles was made. The injection signal had a beam divergence of 5 mR and a beam size at the OPO of $\sim 2 \times 1$ mm². Various lenses were used to control the beam size and divergence. Maximum gains of ~ 15 were observed when the beam was focused into the cavity using a 25 cm lens.

9.7 Conclusions

An injection seeded OPO and an OPA have been studied. The injection seeded OPO was observed to have a 10% lower threshold than the unseeded OPO. The seeding beam, which had an energy per pulse of ~ 0.1 mJ, proved partially successful in controlling the linewidth of the slave OPO. A broadening of the spectral features of the injection signal by the slave oscillator was observed.

The OPA was seen to reproduce closely the linewidth of the seed source. Single pass gains of up to 15 were observed. This is significantly less than the predicted single-pass gain of 150. Optimisation of the spectral and temporal characteristics of the system suggest that the lack of exact spatial overlap between the pumped volume in the OPA and the input signal from the oscillator is the most likely cause of the reduced gain. (The quality of the OPO beams were insufficient to 'mode-match' the injection signal with the OPA pump beam).

REFERENCES

- 1 'Efficient, Single Axial Mode Oscillation of a Beta Barium Borate Optical Parametric Oscillator pumped by an Excimer Laser'. Gordon Robertson, Angus Henderson and Malcolm H. Dunn. *Appl. Phys. Lett.* 62, 123 (1993).
- 2 'Frequency control of a pulsed optical parametric oscillator by radiation injection'. J. E. Bjorkholm and H. G. Danielmayer. *Appl. Phys. Lett.* 15, 171 (1969).

- 3 'Continuously tunable, injection-seeded β -barium borate optical parametric oscillator: Spectroscopic applications'. J. G. Haub, M. J. Johnson, B. J. Orr, R. Wallenstein. *Appl. Phys. Lett.* 58, 1718 (1991).
- 4 'High power injection seeded optical parametric oscillator'. D. C. Hovde, J. H. Timmermans, G. Scoles and K. K. Lehmann. *Opt. Comm.* 86, 294 (1991).
- 5 'Frequency Control of a Pulsed Optical Parametric Oscillator by Radiation Injection'. J. E. Bjorkholm and H. G. Danielmeyer.
- 6 'Investigation of the spectral and energy characteristics of a pulsed optical parametric oscillator operating in the regime of external signal injection'. U. A. Abdullin, G. P. Dzhotyan, Yu. E. D'yakov, B. V. Zhdanov, V. I. Pryalkin, V. B. Sobolev and A. I. Kholodnykh. *Sov. J. Quantum Electron.* 14, 538 (1984).

Conclusions

10.1 Summary

In this thesis, new non-linear materials have been studied for their suitability as gain media in pulsed optical parametric oscillators (OPOs). These materials were LiB_3O_5 (LBO), deuterated L-arginine phosphate (d-LAP) and $\beta\text{-BaB}_2\text{O}_4$ (BBO).

In chapter 4, the non-critically phase-matched geometry in LBO was investigated for the first time. It proved to have a relatively low threshold, typically $\sim 0.3 \text{ Jcm}^{-2}$ for a 16 mm crystal. The threshold was found to be independent of beam size due to the absence of walk-off in this geometry. The device was both temperature and angle tunable. The former was limited by the maximum temperature obtainable by the oven and the latter by the small crystal aperture. This particular geometry also displayed a very narrow inherent linewidth of only a few axial modes. The OPO was operated originally with the cavity resonant for the UV wave and then later with the IR wave. The latter was found to be more efficient at coupling out the UV wave, as expected, due to the reduced losses for this wave. Calculations of losses within the cavities were found to be consistent with observed performance.

The angle tuning range obtained using the NCPM LBO crystal was extended by using a second crystal which was cut for propagation in the yz plane and which had the same d_{ij} as the NCPM geometry. Cut at 40° to the z axis the tuning rate of this geometry was faster and the linewidth broader. The threshold was dependent on the pump beam size due to the increased walk-off and the decreased acceptance angle in this geometry. For a $4 \times 2 \text{ mm}^2$ beam, the threshold was found to be $\sim 0.37 \text{ Jcm}^{-2}$ compared to 0.68 Jcm^{-2} for a $1 \times 0.5 \text{ mm}^2$ beam.

In chapter 5, another phase matching geometry in LBO was explored. This type I critically phase-matched OPO displayed a very large tuning range from 355 nm to $2.3 \mu\text{m}$, omitting only the portion near degeneracy. This portion could not be accessed due to the limited crystal aperture. The linewidth over the observable tuning range was $\sim 2 \text{ nm}$ to 3 nm , as predicted theoretically.

The threshold of the device was dependent on both the wavelength of operation and the pump beam size used. The variation with wavelength correlated with the change in single pass gain over the tuning range. The peak gain was at $\phi=40^\circ$ which corresponded to the minimum threshold of $\sim 0.42 \text{ Jcm}^{-2}$ using a $3 \times 1.5 \text{ mm}^2$ beam at normal incidence. The Fresnel reflection losses were reduced at normal incidence due to the on resonance feedback from the crystal faces into the cavity. This reduced loss within the cavity made the threshold at normal incidence lower than the threshold at slight angles. The threshold away from normal incidence was in the region of 0.5 Jcm^{-2} to 0.6 Jcm^{-2} . When smaller beam sizes, typically $\sim 1 \text{ mm}$, were used, the threshold rose by a factor of 1.3. This was due to the walk-off present in the critical geometry.

The second material to be explored was deuterated L-arginine phosphate (d-LAP). The results for this OPO, believed to be the first d-LAP OPO, were presented in chapter 6. The tuning range was limited in both the IR and UV by the IR absorption cut-off at $\sim 1.3 \mu\text{m}$. The crystal aperture was insufficient to permit tuning as far as degeneracy and so the observed tuning range was 410 nm 500 nm and 802 nm to $1.2 \mu\text{m}$. Being a critical geometry the threshold was again dependent on the beam size used. The threshold was $\sim 0.3 \text{ Jcm}^{-2}$ for beams sizes greater than 5 mm rising to $\sim 0.6 \text{ Jcm}^{-2}$ for beam sizes $\sim 2 \text{ mm}$.

Unfortunately a severe optical damage problem was discovered in d-LAP during the efficiency measurements and only a 5% pump depletion was recorded before oscillation ceased. From the experimental evidence, it is impossible to say whether the damage was induced by high incident energy densities or from prolonged exposure to lower energy levels. The damage took the form of brown streaks formed along the pumped volume.

The third material to be explored was BBO. Much work has previously been reported on BBO and so this study concentrated on the suitability of BBO in a line-narrowed OPO compared to the suitability of LBO and d-LAP. The threshold of the BBO device was observed to be much lower than that of the other two materials provided that the beam sizes used were large enough to overcome the walk-off effect. The large birefringence of BBO, which accounts for the broad tunability, also ensures that the walk-off angle of BBO is large and the acceptance angle is small. Thus the ability to use large beams with BBO is an advantage and this was no problem with the excimer laser. The linewidth of BBO is largest at degeneracy where it rises to a value of $\sim 15 \text{ nm}$. At this level, it would be necessary to use a diffraction grating to reduce the linewidth to a level where a solid etalon could be used. To avoid this complication the line-narrowing

experiments were restricted to below 560 nm. Line-narrowing was successful and single axial mode oscillation was achieved. The penalty in terms of threshold was an increase of 1.5 times over the broadband case. Full tunability could be achieved but only with the additional penalty of a further increase in threshold. The output energy also dropped considerably and thus led to the idea of constructing an injection seeded OPO. This OPO was seeded by the light from the line-narrowed OPO which was operating just above threshold. In practice, the seeded OPO did not produce the same narrow linewidths as the seeding source and total linewidth control could not be achieved. Instead an OPA was constructed. Here, single pass gains of up to 20 were observed and the linewidth of the OPO was faithfully reproduced.

10.2 Conclusions

In this thesis an NCPM LBO OPO and a d-LAP OPO have been demonstrated for the first time. Characterisation of these devices along with work on a type I LBO OPO and a type I BBO OPO has led to the demonstration of a single axial mode BBO device.

The new non-linear materials, BBO, LBO and d-LAP have produced significant advances in OPO performance compared to the older materials like KDP, not just because of their vast tuning ranges, but also because of their superior non-linear coefficient, damage threshold product. Table 10.1 shows non-linear coefficient, damage threshold products for a variety of non-linear materials.

BBO	d-LAP	LBO	Urea	KTP	KNbO ₃	LiNbO ₃	KDP	LiIO ₃	BSN
41.4	22.5	12	6.5	5.2	2.5	1.7	1.1	0.42	0.05

Table 10.1. Non-linear coefficient, damage threshold products¹ in $\text{GWcm}^{-2}\cdot\text{pm/V}$. The new non-linear materials BBO, d-LAP, LBO and Urea have the highest products, while the older, 'traditional' materials such as KDP and Barium Sodium Niobate have the smallest.

The three materials used in this thesis lie at the extreme left of the table, indicating their superiority over the older materials.

Even though the new materials show a vast improvement over the older materials, there is still no one outstanding material for all applications. The characterisation work in this thesis highlights the limitations of the new non-linear materials in terms of tuning range, linewidth and in particular the effect of Poynting vector walk-off on threshold. These parameters affect the choice of material used in any application. BBO is unsuitable if

only low pump energies are available, since the effect of tight focusing is an increase in threshold. However, when ample energy is available, the large non-linear coefficient ensures that BBO is the material of choice. When only low pump energies are available, non-critically phase-matched geometries such as the type II z-cut geometry in LBO is particularly useful. The absence of walk-off allows tight focusing to be employed without a substantial rise in threshold. Each material, thus, has its own niche depending upon the pump energy available.

Current research into diode-pumped systems (see figure 7.4) shows that the oscillation thresholds of these devices are positioned on the left-most portion of the curve where the effect of Poynting vector walk-off is greatest. At the 3 mJ pumping level, the successful operation of LBO OPOs is possible and respectable pump depletions of 50% can be achieved. Higher pump energies of 10 mJ to 20 mJ will allow intracavity elements, such as etalons, to be used. In the near future a compact, tunable, commercial OPO based on LBO may be available through the use of diode pumped technology.

The large non-linear coefficient and large tuning range of BBO make it an attractive material for high energy applications, where the effect of Poynting vector walk-off can almost be eliminated by using large aperture beams. The OPO is an easily scalable device since little or no pump absorption occurs. Heat dissipation is therefore not a problem. The use of large beam sizes allows large pump energies to be converted to broadly tunable output. The maximum energy is limited only by the available crystal aperture.

Extremely large crystal apertures can be obtained by using d-LAP, which can be easily grown in very large volumes. Single crystals as large as $8 \times 6 \times 3 \text{ cm}^2$ have been grown by Cleveland Crystals². Coupled with the high damage threshold of d-LAP, this makes an interesting option for very high energy conversion.

There is no doubt about the desirability of a broadly tunable coherent source capable of accessing the UV, visible and IR simply by rotating a crystal. However, the problem of broad linewidth operation across much of the tuning range limits the applications of the OPO. Demonstration of a single axial mode BBO OPO, capable of a broad tuning range, as reported in this thesis, is important in the continuing development of the device.

Insertion of line-narrowing elements within the OPO cavity resulted in the reduction of efficiency of the device. The device studied in this thesis had uncoated crystal and lens surfaces and the lossy cavities inevitably resulted in additional losses not associated with the line-narrowing elements. However, it seems likely that the action of line-narrowing

the OPO will result in reduced efficiency due to problems with the signal beam divergence and increased cavity lengths. As a result, the master/slave oscillator is an attractive option for producing a highly efficient, narrow linewidth device. (The recent development of a high energy, broadly tunable, line-narrowed master/slave OPO system by Spectra Physics³, confirms the findings of this thesis in the use of BBO for high energy applications).

10.3 Future Work

The focus of future work on the excimer system should be concerned with the optimisation of the OPO/OPA system. Theoretical single pass gains of ~ 150 are predicted and current efforts fall well short of this value. Improvement in the beam quality of the OPO should result in substantial enhancement of the pump beam/signal beam overlap in the OPA. This seems to be the most likely cause of the low gains observed. Improvement in the performance of the master OPO may be achieved by the use of crystal coatings and better quality etalons.

The primary concern must be with the beam quality of the seeding source. At present, the master oscillator beam is highly divergent and the spatial mode structure is complex. As an initial test of the effect of the spatial mode quality on the performance of the OPA, an experiment using an excimer pumped dye laser would prove useful. This should indicate the gain that can be expected if the beam quality of the OPO was improved.

Following successful demonstrations of high gain in the OPA, work improving the beam quality of the OPO would be necessary. A curved mirror cavity will be required to control the transverse mode structure of the OPO. In addition, spatial filtering of the OPO output may be necessary to provide a high quality injection signal mode profile.

The OPO crystal should be anti-reflection coated for the signal wavelength. The benefits, in terms of performance, are likely to be dramatic. We saw, in chapters 4, 5 and 6 that at normal incidence, where the on-axis reflection from the crystal faces effectively removed the Fresnel losses, the oscillation threshold was reduced by a factor of 1.6. In addition, the pump depletion and output coupling efficiency are likely to be improved.

The OPO should be line-narrowed, initially, using a $5 \mu\text{m}$ (or thicker if possible) deposited etalon with a finesse of 20. The OPO should be line-narrowed to around 2 nm

(FWHM) from 15 nm (FWHM) at degeneracy. Care will be required because of the high finesse of the etalons. Optical damage of the etalon coatings may occur due to high intra-cavity optical fields. A 60 μm solid etalon with a finesse of 10 could then be used to line-narrow the OPO to around 0.3 nm, and finally a 2 mm etalon with a finesse of 10 could be used to select a single axial mode, as described in chapter 8.

Real-time monitoring of the delay between the OPO and the OPA is required to determine if the injection signal and the OPA pump pulse are temporally overlapped. Also, real-time measurement of the OPA linewidth is necessary to ensure that the spectral overlap of the OPO and OPA is optimised. A wavemeter could be used to monitor a portion of the OPA output. Such a set-up would be beneficial in a practical system to provide a real-time measurement of the linewidth.

The expected single pass gain for a pump energy of 30 mJ in a $3 \times 1.5 \text{ mm}^2$ beam is 150. This is calculated using the measured threshold of the OPO (equation 9.1), and should thus provide a good estimate of the gain with near perfect spectral and spatial overlap of the pump and injection signal. In practice, if a gain of 100 could be achieved in the OPA then over 10 mJ of single axial mode light could be obtained across the range 354 nm to 616 nm. An investigation of the linewidth of the idler in the OPO and the non-seeded wave in the OPA would be required before statements about the linewidth across the entire tuning range can be made.

The exceptional tuning ranges, narrow linewidths and high output energies possible from OPO systems should make them strong rivals to other more established methods of generating tunable coherent light. In the near future, their full potential in major spectroscopy applications may be realised .

REFERENCES

- 1 'Handbook of Non-linear Optical Crystals'. V. G. Dmitriev, G. G. Gurzadyan, D. N. Nikogosyan. Springer Series in Optical Science.
- 2 'Deuterated L-Arginine Phosphate: A New Efficient Nonlinear Crystal'. D. Eimerl, S. Velsko, L. Davis, F. Wang, G. Loiacono and G. Kennedy. IEEE J. Quantum Electron. 25, 179 (1989).
- 3 'MOPO-700 Series Tunable Optical Parametric Oscillator Systems'. Spectra Physics. 1250 West Middleview Rd. Mountain View CA. 94042 USA.

Appendix A

Sellmeier equations for the three non-linear materials described in this thesis. The equations take the form

$$n^2 = a + \frac{b}{\lambda^2 + c} + d\lambda^2$$

A1 Lithium Borate

The following is a chronological list of the Sellmeier equations that have been generated for lithium borate (LBO). The quality of fit to the measured values is discussed in chapter four.

The first set were published by Chen *et al*¹ in April 1989. They are calculated from refractive index data measured at 16 wavelengths between 1.064 μm and 0.2537 μm . The wavelengths, λ , are all in microns.(eqn A1),

	a	b	c	d
x	2.4517	0.01177	-0.00921	-0.00960
y	2.5279	0.01652	0.005459	-0.01137
z	2.5818	0.01414	-0.01186	-0.01457

Corrections to the above equations were made by Wu *et al*² in October 1989, by measuring phase-matching angles in LBO with a Nd:YAG laser and a Rhodamine 6G dye laser as pump sources. This lead to the following equations, (eqn A2),

	a	b	c	d
x	2.4517	0.01177	-0.00851	-0.0096
y	2.5278	0.01652	0.005459	-0.01137
z	2.5818	0.01414	-0.01192	-0.01457

Using Chen's data, Hanson and Dick recalculated the Sellmeier equations neglecting the lowest wavelength data, (eqn A3),

	a	b	c	d
x	2.45768	0.0098877	-0.026095	-0.013847
y	2.52500	0.017123	0.021414	-0.016293
z	2.8488	0.012737	-0.021414	-0.016293

Chen then published another set of refined equations, (eqn A4)

	a	b	c	d
x	2.45316	0.01150	-0.01058	-0.0185
y	2.53969	0.01249	-0.01339	-0.02029
z	2.58515	0.01412	-0.00467	-0.01850

Kato then published another set of Sellmeier equations using Chen's original data, along with data from experiments on second harmonic generation and sum frequency mixing at 1064 nm. (eqn A5)

	a	b	c	d
x	2.4542	0.01125	-0.01135	-0.01388
y	2.5390	0.01277	-0.01189	-0.01848
z	2.5865	0.01310	-0.01223	-0.01861

A2 Deuterated L-Arginine Phosphate

The following Sellmeier equations were calculated and published by Eimerl et al (IEEE J. Quantum Electron. 25, 179 (1989)) for d-LAP.

	a	b	c	d
x	2.2352	0.0118	-0.0146	-0.00683
y	2.4313	0.0151	-0.0214	-0.0143
z	2.4484	0.0172	-0.0229	-0.0115

A3 β -Barium Borate

The following Sellmeier equations were published by Kato (IEEE J. Quantum Electron. 22, 1013 (1986)) for the uniaxial material BBO.

	a	b	c	d
o	2.7359	0.01878	-0.01822	-0.01354
e	2.3753	0.01224	-0.01667	-0.01515

APPENDIX B

```

PROGRAM Criticallbo;
{ calculates the tuning curve of xyLBO for a given wavelength using new Sellemeier }
{ equations calculated by Kato. The phase matching is e>o+o. }
USES
SANE;
CONST
light = 2.997e8;
pi = 3.1415;
increment = 1e14;
length = 15e-3;
L = 15e-3;
divergence = 1e-3;
dvp = 6e9;
VAR
wp, a, b, c, ws, wi, dndt, dw, dnsdls, dws1, dws3 : real;
dnpdlp, dndli, bottom, top, dtheta, tsqt, cth : real;
theta, pump, ls, li, ns, ni, np, np2, nyp, nxp, cst : real;
dls1, dndtheta, dws2, dls2, dls3, bracket, rho : real;
dndls, dndli, dndlp : real;
i, j : integer;
f : text;
textname : STRING;
BEGIN
{ * open files * }
textname := newfilename('name for new text file? ');
IF textname <> " THEN
rewrite(f, textname);
write('enter pump wavelength in microns ');
readln(pump);
a := 2 * pi * light;
wp := a / (pump * 1e-6);
ws := wp / 2;
REPEAT
BEGIN
{ * calculate wavelengths * }
wi := wp - ws;
b := ws * 1e-6;
ls := a / b;
c := wi * 1e-6;
li := a / c;
{ * calculate refractive indices * }
ns := sqrt(2.5865 + (0.01310 / (sqr(ls) - 0.01223)) - (0.01861 * sqr(ls)));
ni := sqrt(2.5865 + (0.01310 / (sqr(li) - 0.01223)) - (0.01861 * sqr(li)));
np := ((ws * ns) + (wi * ni)) / wp;
nyp := (2.5390 + (0.01277 / (sqr(pump) - 0.01189)) - (0.01848 * sqr(pump)));
nxp := (2.4542 + (0.01125 / (sqr(pump) - 0.01135)) - (0.01388 * sqr(pump)));
np2 := 1 / sqr(np);
nyp := 1 / nyp;
nxp := 1 / nxp;
tsqt := -(np2 - nyp) / (np2 - nxp);
cth := sqrt(tsqt);
theta := arctan(cth);
{ * calculate the acceptance angle dtheta * }
top := (nxp - nyp) * cos(theta) * sin(theta);
bottom := (nxp * sqr(cos(theta))) + (nyp * sqr(sin(theta)));
bottom := sqrt(bottom * bottom * bottom);

```

```

IF bottom <> 0 THEN
  dndt := top / bottom;
  dtheta := (pump * 1e-6) / (length * dndt);
  top := (pump * 1e-6) / (np * dtheta);
  writeln('answer=', top, np, dtheta);
(* calculate the acceptance bandwidth *)
  dndli := -li * (0.01310 / (sqr(sqr(li) - 0.01223))) - (0.01861 * li);
  dndlp := -pump * (0.01125 / (sqr(sqr(pump) - 0.01135))) - (0.01388 * pump);
  dw := 1 / (length * ((np - ni) - (pump * dndlp / np) + (li * dndli / ni)));
(* walk-off *)
  rho := dndt / np;
(* calculation of linewidth *)
  dndls := -ls * (0.01310 / (sqr(sqr(ls) - 0.01223))) - (0.01861 * ls);
  dndli := -li * (0.01310 / (sqr(sqr(li) - 0.01223))) - (0.01861 * li);
  dndlp := -pump * (0.01125 / (sqr(sqr(pump) - 0.01135))) - (0.01388 * pump);
  IF ni <> ns THEN
    BEGIN
(* *****dls1***** )
      bracket := ((ni - ns) + ((ls / ns) * dndls) - ((li / ni) * dndli));
      dws1 := (light / L) * (1 / bracket);
      dls1 := sqr(ls * 1e-6) * dws1 / light;
      dls1 := dls1 * 1e9;
      writeln('dls1 = ', dls1);
(* *****dls2***** )
      top := (nyp - nxp) * cos(theta) * sin(theta);
      bottom := (nxp * sqr(cos(theta))) + (nyp * sqr(sin(theta)));
      bottom := sqrt(bottom * bottom * bottom);
      dndtheta := top / bottom;
      dws2 := 0.5 * (light / (pump * 1e-6)) * dndtheta * divergence / bracket;
      dls2 := sqr(ls * 1e-6) * dws2 / light;
      dls2 := dls2 * 1e9;
      writeln('dls2= ', dls2);
(* *****dls3***** )
      dls3 := dvp * ((np - ni) + ((pump / np) * dndlp) - ((li / ni) * dndli)) / bracket;
      dls3 := sqr(ls * 1e-6) * dls3 / light;
      dls3 := dls3 * 1e9;
      writeln('dls3= ', dls3);
    END;
(* print out results *)
    theta := theta * 180 / pi;
    write(theta : 8 : 5, 'accept=', dtheta : 8 : 5, 'rho=', rho : 8 : 5);
    writeln(f, theta : 8 : 5, chr(9), ls : 8 : 5, chr(9), li : 8 : 5, chr(9), dw : 8 : 5,
      chr(9), dtheta : 8 : 5, chr(9), dls3 : 8 : 5, chr(9));
    ws := ws + increment
  END;

  UNTIL (li < 0.350) OR (ls < 0.350);
END.

```

PROGRAM LBOyz;

{ calculates the tuning curve of xyLBO for a given wavelength using Sellemeier }

{ equations listed in appendix A. The phase matching is o>o+e. }

USES

SANE;

CONST

light = 2.997e8;

pi = 3.1415;

L = 15e-3;

dvp = 6e9;

VAR

wp, a, b, c, ws, wi, tsqt, cth, theta, pump, ls, li : real;

ns, ni, np, ns2, nys, nzs, cst, increment, factor : real;

dnpdlp, dnsdls, dnidli, dw, dws, length : real;

dls1, dls2, dls3, dndli, dndlp, dndls, bracket : real;

dws1, dws2, dws3, top, bottom, dtheta, dndtheta, rho : real;

i, j, equation : integer;

f : text;

textname : STRING;

BEGIN

{* open files *

increment := 9e12;

length := 15e-3;

textname := newfilename('name for new text file? ');

IF textname <> " THEN

rewrite(f, textname);

write('enter pump wavelength in microns ');

readln(pump);

write(' which set of Sellemeier equations do you wish to use?');

readln(equation);

write('enter increment decrease factor, about 1.5 ');

readln(factor);

a := 2 * pi * light;

wp := a / (pump * 1e-6);

ws := a / (420e-9);

REPEAT

BEGIN

{* calculate wavelengths *

wi := wp - ws;

b := ws * 1e-6;

ls := a / b;

c := wi * 1e-6;

li := a / c;

IF equation = 1 THEN

BEGIN

{* calculate refractive indices using equation A1 *

np := sqrt(2.4517 - (0.01177 / (0.00921 - sqrt(pump))) - (0.0096 * sqrt(pump)));

ni := sqrt(2.4517 - (0.01177 / (0.00921 - sqrt(li))) - (0.0096 * sqrt(li)));

nys := (2.5279 + (0.01652 / (0.005459 + sqrt(ls))) - (0.01137 * sqrt(ls)));

nzs := (2.5818 - (0.01414 / (0.01186 - sqrt(ls))) - (0.01457 * sqrt(ls)));

END;

IF equation = 2 THEN

BEGIN

{* calculate refractive indices using equation A2 *

np := sqrt(2.4517 + (0.01177 / (sqrt(pump) - 0.00851)) - (0.0096 * sqrt(pump)));

ni := sqrt(2.4517 + (0.01177 / (sqrt(li) - 0.00851)) - (0.0096 * sqrt(li)));

nys := (2.5278 + (0.01652 / (sqrt(ls) + 0.005459)) - (0.01137 * sqrt(ls)));

nzs := (2.5818 + (0.01414 / (sqrt(ls) - 0.01192)) - (0.01457 * sqrt(ls)));

END;

IF equation = 3 THEN

BEGIN

{* calculate refractive indices using equation A3 *

np := sqrt(2.45768 - (0.0098877 / (0.026095 - sqrt(pump))) - (0.013847 * sqrt(pump)));

ni := sqrt(2.45768 - (0.0098877 / (0.026095 - sqrt(li))) - (0.013847 * sqrt(li)));

```

nys := (2.5250 - (0.017123 / (-0.0060517 - sqrt(ls))) - (0.0087838 * sqrt(ls)));
nzs := (2.58488 - (0.012737 / (0.021414 - sqrt(ls))) - (0.016293 * sqrt(ls)));
END;
IF equation = 4 THEN
BEGIN
(* calculate refractive indices using equations A4 *)
np := sqrt(2.45316 + (0.01150 / (sqrt(pump) - 0.01058)) - (0.0185 *
sqrt(pump)));
ni := sqrt(2.45316 + (0.01150 / (sqrt(li) - 0.01058)) - (0.0185 * sqrt(li)));
nys := (2.53969 + (0.01249 / (sqrt(ls) - 0.01339)) - (0.02029 * sqrt(ls)));
nzs := (2.58515 + (0.01412 / (sqrt(ls) - 0.00467)) - (0.01850 * sqrt(ls)));
END;
IF equation = 5 THEN
BEGIN
(* calculate refractive indices using equations A5 *)
np := sqrt(2.4542 + (0.01125 / (sqrt(pump) - 0.01135)) - (0.01388 *
sqrt(pump)));
ni := sqrt(2.4542 + (0.01125 / (sqrt(li) - 0.01135)) - (0.01388 * sqrt(li)));
nys := (2.5390 + (0.01277 / (sqrt(ls) - 0.01189)) - (0.01848 * sqrt(ls)));
nzs := (2.5865 + (0.01310 / (sqrt(ls) - 0.01223)) - (0.01861 * sqrt(ls)));
END;
(* calculate phase-matching angle theta *)
ns := ((wp * np) - (wi * ni)) / ws;
ns2 := 1 / sqrt(ns);
nys := 1 / nys;
nzs := 1 / nzs;
tsqt := -(ns2 - nys) / (ns2 - nzs);
IF tsqt > 0 THEN
BEGIN
cth := sqrt(tsqt);
theta := arctan(cth);
(* Acceptance Bandwidth *)
dndli := -li * (0.01310 / (sqrt(sqrt(li) - 0.01223))) - (0.01861 * li);
dndls := -ls * (0.01125 / (sqrt(sqrt(ls) - 0.01135))) - (0.01388 * ls);
dndlp := -pump * (0.01125 / (sqrt(sqrt(pump) - 0.01135))) - (0.01388 * pump);
dw := 1 / (length * ((np - ns) - (pump * dndlp / np) + (ls * dndls / ns)));
(* Signal Linewidth *)
dndls := -ls * (0.01125 / (sqrt(sqrt(ls) - 0.01135))) - (0.01388 * ls);
dndli := -li * (0.01310 / (sqrt(sqrt(li) - 0.01223))) - (0.01861 * li);
dndlp := -pump * (0.01125 / (sqrt(sqrt(pump) - 0.01135))) - (0.01388 * pump);
IF ni <> ns THEN
BEGIN
(* *****dls1***** *)
bracket := ((ni - ns) + (ls / ns) * dndls) - ((li / ni) * dndli);
dws1 := (light / L) * (1 / bracket);
dls1 := sqrt(ls * 1e-6) * dws1 / light;
dls1 := dls1 * 1e9;
writeln('dls1 = ', dls1);
(* *****dls2***** *)
top := (nzs - nys) * cos(theta) * sin(theta);
bottom := (nys * sqrt(cos(theta))) + (nzs * sqrt(sin(theta)));
bottom := sqrt(bottom * bottom * bottom);
dndtheta := top / bottom;
dws2 := 0.5 * (light / (pump * 1e-6)) * dndtheta * divergence / bracket;
dls2 := sqrt(ls * 1e-6) * dws2 / light;
dls2 := dls2 * 1e9;
writeln('dls2 = ', dls2);
(* *****dls3***** *)

```

```

dls3 := dvp * ((np - ni) + ((pump / np) * dndlp) - ((li / ni) * dndli)) / bracket;
dls3 := sqrt(ls * 1e-6) * dls3 / light;
dls3 := dls3 * 1e9;
writeln('dls3= ', dls3);
IF dndtheta < 0 THEN
dtheta := ((ns * ls * 1e-6) / (np * length * dndtheta));
writeln(ns : 8 : 5, ls : 8 : 5, np : 8 : 5, length : 8 : 5, dndtheta : 8 : 5);
dtheta := dtheta * 1e3;
rho := dndtheta / ns;
rho := rho * 180 / pi;
writeln('acc angle= ', dtheta : 8 : 5, ' walk-off angle = ', rho : 8 : 5);
END;
{ * print out * }
dws := sqrt(ls) / ((length * 1e3) * ((ns - ni) - (ls * dnsdls) + (li * dndli)));
theta := theta * 180 / pi;
write(theta : 8 : 5, 'ls=', ls : 8 : 5, 'dw=', dw : 8 : 5);
writeln(f, theta : 8 : 5, chr(9), ls : 8 : 5, chr(9), rho : 8 : 5, chr(9), dtheta : 8 : 5,
chr(9));
END;
IF theta < 11 THEN
increment := increment / factor;
ws := ws + increment;
END;
UNTIL (li < 0.350) OR (ls < 0.350) OR (theta < 0);
END.

```

```

PROGRAM dlap;
{ calculates the phase-matching and non-linear coefficient in dlap }
{ for a given signal wavelength using the Sellmeier equations in appendix A }
CONST
Pi = 3.14159;
omega = 1.2217;
{ Non-linear coefficients }
d11 = 0.803;
d12 = -0.69;
d13 = 0.308;
d14 = 0.611;
d25 = 0.626;
d26 = -0.7;
d35 = 0.306;
d36 = 0.61;
pump = 0.351;
small = 0;
divergence = 1e-3;
length = 25e-3;
light = 3e-8;
VAR
ls, li, phi, theta, p, t, yy, xx, tn2d, delta : real;
b1e1, b2e1, b3e1, b1e2, b2e2, b3e2 : real;
A, B, C, D, E, F, G, H, de, dndls, dndli : real;
dws1, dls1, dls2, dws2 : real;
nxp, nxs, nxi, nyp, nys, nyi, nzp, nzs, nzi : real;
n1, n2, n3, l, dk, previous, top, bottom, dndtheta, bracket : real;
flag : integer;
q : text;
textname : STRING;

```

```

FUNCTION tan (value : real) : real;
BEGIN
tan := sin(value) / cos(value);
END;
BEGIN
{ * open files * }
    textname := newfilename('name for new text file? ');
    IF textname <> " THEN
    rewrite(q, textname);
    write('Input signal wavelength, in microns ');
    read(ls);
    li := 1 / ((1 / pump) - (1 / ls));
    phi := -90;
    p := phi * pi / 180;
    REPEAT
    theta := 60;
    t := theta * pi / 180;
    flag := 1;
    previous := 100000;
{ calculate the polarisation angle delta }
    REPEAT
    yy := -cos(t) * sin(2 * p);
    xx := small + (sqr(cos(p))) - ((sqr(cos(t))) * (sqr(sin(p)))) + ((sqr(tan(omega)))
* (sqr(sin(t))));
    tn2d := yy / xx;
    delta := (arctan(tn2d)) / 2;
{ calculate the direction cosines }
    b1e1 := (-1 * cos(t) * cos(p) * cos(delta)) + (sin(p) * sin(delta));
    b2e1 := (-1 * cos(t) * sin(p) * cos(delta)) - (cos(p) * sin(delta));
    b3e1 := sin(t) * cos(delta);
    b1e2 := (-1 * cos(t) * cos(p) * sin(delta)) - (sin(p) * cos(delta));
    b2e2 := (-1 * cos(t) * sin(p) * sin(delta)) + (cos(p) * cos(delta));
    b3e2 := sin(t) * sin(delta);
{ (e1,e2,e2 phasematching)
{ Principal refractive indicies }
    a := 2.2352;
    b := 0.0118;
    c := -0.0146;
    d := -0.00683;
    nxp := sqrt(a + (b / (sqr(pump) + c)) + (d * (sqr(pump))));
    nxs := sqrt(a + (b / (sqr(ls) + c)) + (d * (sqr(ls))));
    nxi := sqrt(a + (b / (sqr(li) + c)) + (d * (sqr(li))));
    a := 2.4313;
    b := 0.0151;
    c := -0.0214;
    d := -0.0143;
    nyp := sqrt(a + (b / (sqr(pump) + c)) + (d * (sqr(pump))));
    nys := sqrt(a + (b / (sqr(ls) + c)) + (d * (sqr(ls))));
    nyi := sqrt(a + (b / (sqr(li) + c)) + (d * (sqr(li))));
    a := 2.4484;
    b := 0.0172;
    c := -0.0229;
    d := -0.0115;
    nzp := sqrt(a + (b / (sqr(pump) + c)) + (d * (sqr(pump))));
    nzs := sqrt(a + (b / (sqr(ls) + c)) + (d * (sqr(ls))));
    nzi := sqrt(a + (b / (sqr(li) + c)) + (d * (sqr(li))));
{ phasematching (l is a temporary variable)
    l := (sqr(b1e1 / nyp)) + (sqr(b2e1 / nzp)) + (sqr(b3e1 / nxp));

```

```

n3 := 1 / (sqrt(l));
l := (sqr(b1e2 / nys)) + (sqr(b2e2 / nzs)) + (sqr(b3e2 / nxs));
n2 := 1 / (sqrt(l));
l := (sqr(b1e2 / nyi)) + (sqr(b2e2 / nzi)) + (sqr(b3e2 / nxi));
n1 := 1 / (sqrt(l));
dk := abs((n3 / pump) - (n2 / ls) - (n1 / li));
IF (previous > dk) AND (flag = 1) THEN
flag := -1;
IF (previous < dk) AND (flag = -1) THEN
flag := 0;
IF (previous = dk) THEN
flag := 0;
theta := theta - 1;
t := theta * pi / 180;
previous := dk;
UNTIL flag = 0;
theta := theta + 1;
{ * Effective Non-linear coefficient * }
A := b1e1 * (d11 * b1e2 * b1e2);
B := b1e1 * (d12 * b2e2 * b2e2);
C := b1e1 * (d13 * b3e2 * b3e2);
D := b1e1 * (d14 * ((b2e2 * b3e2) + (b3e2 * b2e2)));
E := b2e1 * (d25 * ((b1e2 * b3e2) + (b3e2 * b1e2)));
F := b2e1 * (d26 * ((b1e2 * b2e2) + (b2e2 * b1e2)));
G := b3e1 * (d35 * ((b1e2 * b3e2) + (b3e2 * b1e2)));
H := b3e1 * (d36 * ((b1e2 * b2e2) + (b2e2 * b1e2)));
de := A + B + C + D + F + G + H;
writeln(ls, ' ', li, ' phi= ', phi, ' theta=', theta, ' deff= ', de);
{ * calculation of linewidth * }
dndls := -ls * (0.0151 / (sqr(sqr(ls) - 0.0214))) - (0.0143 * ls);
dndli := -li * (0.0151 / (sqr(sqr(li) - 0.0214))) - (0.0143 * li);
IF n1 <> n2 THEN
BEGIN
{ * *****dls1***** }
bracket := ((n1 - n2) + ((ls / n2) * dndls) - ((li / n1) * dndli));
dws1 := (light / length) * (1 / bracket);
dls1 := sqr(ls * 1e-6) * dws1 / light;
dls1 := dls1 * 1e9;
writeln('dws1= ', dws1, ' bracket= ', bracket, ' dls1= ', dls1);
{ * *****dls2***** }
top := (nzp - nxp) * cos(t) * sin(t);
bottom := (nzp * sqr(cos(t))) + (nxp * sqr(sin(t)));
bottom := sqrt(bottom * bottom * bottom);
dndtheta := top / bottom;
writeln('top= ', top, ' bottom= ', bottom, ' dndtheta= ', dndtheta);
dws2 := 0.5 * (light / (pump * 1e-6)) * dndtheta * divergence / bracket;
dls2 := sqr(ls * 1e-6) * dws2 / light;
dls2 := dls2 * 1e9;
writeln('dws2= ', dws2, ' dls2= ', dls2);
{ * *****dls3***** }
dls3 := dvp * ((np - ni) + ((pump / np) * dndlp) - ((li / ni) * dndli)) / bracket;
dls3 := sqr(ls * 1e-6) * dls3 / light;
dls3 := dls3 * 1e9;
{ * print out * }
writeln('dls3= ', dls3);
writeln(q, theta : 8 : 5, chr(9), ls : 8 : 5, chr(9), li : 8 : 5, chr(9), de : 8 : 5,
chr(9), dls1 : 8 : 5, chr(9));
END;

```



```

    phi := phi + 10;
    p := phi * pi / 180;
    UNTIL phi = 100
END.

```

```

PROGRAM BBO;
{ calculates the tuning curve of BBO for a given wavelength using the Sellemeier }
{ equations in appendix A. The phase matching is e>o+o. }
USES
SANE;
CONST
light = 2.997e8;
pi = 3.1415;
increment = 1e14;
L = 0.02;
divergence = 1e-3;
dvp = 6e9;
VAR
wp, a, b, c, ws, wi, tsqt, cth, theta, rho : real;
pump, ls, li, ns, ni, np, np2, nyp, nxp, cst : real;
dndls, dndli, dws1, dws2, dws3, dls1, dndtheta, bottom, dls2 : real;
dnpdlp, dls3, dw, dnidli, dndlp, bracket, top, dtheta, dndt : real;
i, j : integer;
f : text;
textname : STRING;
flag : boolean;
PROCEDURE inputdata (VAR textname : STRING;
VAR f : text;
VAR pump : real);
BEGIN
textname := newfilename('name for new text file? ');
IF textname <> " THEN
rewrite(f, textname);
write('enter pump wavelength in microns ');
readln(pump);
END;
{ ***** }
PROCEDURE outputdata (VAR theta, ls, li, dls : real;
VAR f : text);
CONST
pi = 3.1415;
BEGIN
theta := theta * 180 / pi;
write(theta : 8 : 5, ls : 8 : 5, li : 8 : 5);
writeln(f, theta : 8 : 5, chr(9), ls : 8 : 5, chr(9), li : 8 : 5, chr(9), dtheta : 8 : 5, chr(9), dw
: 8 : 5, chr(9), dls3 : 8 : 5, chr(9));
ws := ws + increment
END;
{ ***** }
PROCEDURE walkoffcalc (VAR nyp, nxp, theta : real);
VAR
rho : real;
BEGIN
rho := arctan((nyp / nxp) * tan(theta)) - theta;
write(' walk-off angle ', rho, ' rad')
END;
{ ***** }
BEGIN

```

```

flag := true;
inputdata(textname, f, pump);
a := 2 * pi * light;
wp := a / (pump * 1e-6);
ws := wp / 2;
REPEAT
BEGIN
(* calculate wavelengths *)
wi := wp - ws;
b := ws * 1e-6;
ls := a / b;
c := wi * 1e-6;
li := a / c;
(* calculate refractive indices *)
ns := sqrt(2.7359 + (0.01878 / (sqr(ls) - 0.01822)) - (0.01354 * sqr(ls)));
ni := sqrt(2.7359 + (0.01878 / (sqr(li) - 0.01822)) - (0.01354 * sqr(li)));
np := ((ws * ns) + (wi * ni)) / wp;
nyp := (2.7359 + (0.01878 / (sqr(pump) - 0.01822)) - (0.01354 * sqr(pump)));
nxp := (2.3753 + (0.01224 / (sqr(pump) - 0.01667)) - (0.01516 * sqr(pump)));
np2 := 1 / sqr(np);
nyp := 1 / nyp;
nxp := 1 / nxp;
(* calculate phase-matching angle *)
tsqt := -(np2 - nyp) / (np2 - nxp);
cth := sqrt(tsqt);
theta := arctan(cth);
(* acceptance bandwidth *)
dndli := -li * (0.01878 / (sqr(sqr(li) - 0.01822))) - (0.01354 * li);
dnpdlp := -pump * (0.01224 / (sqr(sqr(pump) - 0.01667))) - (0.01516 * pump);
dw := 1 / (L * ((np - ni) - (pump * dnpdlp / np) + (li * dndli / ni)));
(* acceptance angle *)
top := (nxp - nyp) * cos(theta) * sin(theta);
bottom := (nxp * sqr(cos(theta))) + (nyp * sqr(sin(theta)));
bottom := sqrt(bottom * bottom * bottom);
IF bottom < 0 THEN
dndt := top / bottom;
dtheta := (pump * 1e-6) / (L * dndt);
(* calculation of linewidth *)
dndls := -ls * (0.01878 / (sqr(sqr(ls) - 0.01822))) - (0.01354 * ls);
dndli := -li * (0.01878 / (sqr(sqr(li) - 0.01822))) - (0.01354 * li);
dndlp := -pump * (0.01224 / (sqr(sqr(pump) - 0.01667))) - (0.01516 * pump);
IF ni < ns THEN
BEGIN
(* *****dls1***** *)
bracket := ((ni - ns) + ((ls / ns) * dndls) - ((li / ni) * dndli));
dws1 := (light / L) * (1 / bracket);
dls1 := sqr(ls * 1e-6) * dws1 / light;
dls1 := dls1 * 1e9;
writeln('dws1= ', dws1, ' bracket= ', bracket, ' dls1= ', dls1);
(* *****dls2***** *)
top := (nyp - nxp) * cos(theta) * sin(theta);
bottom := (nxp * sqr(cos(theta))) + (nyp * sqr(sin(theta)));
bottom := sqrt(bottom * bottom * bottom);
dndtheta := top / bottom;
writeln('top= ', top, ' bottom= ', bottom, ' dndtheta= ', dndtheta);
dws2 := 0.5 * (light / (pump * 1e-6)) * dndtheta * divergence / bracket;
dls2 := sqr(ls * 1e-6) * dws2 / light;
dls2 := dls2 * 1e9;

```

```
writeln('dws2= ', dws2, 'dls2= ', dls2);
{ * *****dls3***** }
dls3 := dvp * ((np - ni) + ((pump / np) * dndlp) - ((li / ni) * dndli)) / bracket;
dls3 := sqr(ls * 1e-6) * dls3 / light;
dls3 := dls3 * 1e9;
writeln('dls3= ', dls3);
writeln('np= ', np);
END;
IF flag THEN
walkoffcalc(nyp, nxp, theta);
outputdata(theta, ls, li, dls3, f);
END;
UNTIL (li < 0.350) OR (ls < 0.350);
END.
```